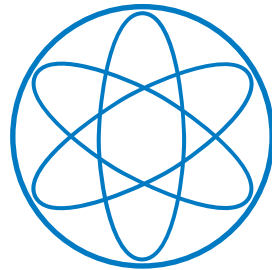


FAKULTÄT FÜR PHYSIK



**New Brightness Enhanced
Positron Microbeam for Spatially
Resolved Doppler Broadening
Spectroscopy at NEPOMUC**

DISSERTATION

VON

THOMAS MICHAEL GIGL



TECHNISCHE UNIVERSITÄT MÜNCHEN

TECHNISCHE UNIVERSITÄT MÜNCHEN

Fakultät für Physik
Lehrstuhl E21 für Experimentalphysik

**New Brightness Enhanced Positron
Microbeam for Spatially Resolved Doppler
Broadening Spectroscopy at NEPOMUC**

Thomas Michael Gigl

Vollständiger Abdruck der von der Fakultät für Physik der Technischen Universität München zur Erlangung des akademischen Grades eines

Doktors der Naturwissenschaften (Dr. rer. nat.)

genehmigten Dissertation.

Vorsitzender: Prof. Dr. Martin Zacharias

Prüfer der Dissertation:

1. Priv.-Doz. Dr. Christoph Hugenschmidt
2. Prof. Dr. Günther Dollinger

Die Dissertation wurde am 18.09.2018 bei der Technischen Universität München eingereicht und durch die Fakultät für Physik am 22.10.2018 angenommen.

Abstract

Within the scope of this thesis, a new coincident Doppler broadening spectrometer (CDBS *upgrade*) was designed, established and successfully set into operation at the high-intensity positron source NEPOMUC located at the research neutron source Heinz-Maier Leibnitz (FRM II) at the Technical University of Munich (TUM). The implementation of a new positron microbeam enables high-resolution lateral and depth dependent measurements of the Doppler broadened 511 keV photo peak of the positron-electron annihilation radiation. This technique provides a non-destructive evaluation of the defect distribution and the chemical composition at the annihilation site.

For this purpose, various new components were developed and implemented in the new CDB spectrometer. In order to facilitate the optimization of the beam parameters at the beginning of each beamtime, three new beam monitors were employed for beam adjustment. A key part was the implementation of a brightness enhancement system comprising a focusing unit and a 100 nm thin Ni(100) single crystal foil used in transmission geometry. In order to maximize the re-moderation efficiency of the Ni foil, comprehensive studies were carried out. Additionally, two electrostatic lens systems were developed for beam guidance and focusing. Their geometry and the appropriate values of the high voltages applied to the electrodes were determined and optimized by simulations. The first lens system focuses the re-moderated beam provided by NEPOMUC onto the Ni(100) re-moderation foil. Subsequently, the second lens system forms the re-emitted positrons to a beam and focusses them onto the sample. With the help of the new re-moderation system, a minimal beam diameter of 50 μm can be achieved. Using an additional aperture in front of the re-moderation foil this value can be further reduced to 33 μm .

The positron microbeam was successfully set in routine operation. Its capability of investigating the defect- and elemental distribution was first demonstrated on a laser beam and a friction stir welded AlCu alloy. The properties of such an age hardening alloy are known to be significantly influenced by a combination of solution annealing, cooling, cold working and subsequent artificially ageing at elevated temperatures. Hereby, the presence of Cu precipitates are crucial for influence the strength of the alloy. The formation of precipitates and the defect distribution were analysed with the CDBS *upgrade* microbeam. As a result, a significantly higher Cu signal was

detected in the base material with respect to the weld nugget. This is attributed to the enhanced solubility of the Cu precipitates at elevated welding temperatures and subsequent rapid cooling. Additionally, a newly developed in-situ tension testing machine was implemented. Its ability to record stress strain curves while performing DBS measurements was firstly demonstrated on a laser beam welded stainless steel sample. Hereby, its defect distribution could be related to the rupture zone located between both heat affected zones. Furthermore, for the first time the grains of an annealed polycrystalline Pt foil was investigated with the positron microbeam. The grain structure formed during an annealing process could be clearly identified due to a significant change in the S-parameters of different grains.

Zusammenfassung

Im Rahmen dieser Arbeit wurde ein neues koinzidentes Dopplerverbreiterungs-Spektrometer (CDBS) an der hochintensiven Positronenquelle NEPOMUC der Forschungsneutronenquelle Heinz-Maier Leibnitz der Technischen Universität München entwickelt, aufgebaut und erfolgreich in Betrieb genommen. Das CDBS ermöglicht lateral hochaufgelöste und tiefenabhängige Defektspektroskopie über die Messung der Dopplerverbreiterten Photolinie der Annihilationsstrahlung von Positronen mit Elektronen. Dieses Verfahren erlaubt die zerstörungsfreie Untersuchung der Fehlstellen- und Elementverteilungen am Annihilationsort.

Um dieses Vorhaben zu realisieren, wurden für das Spektrometer diverse neue Komponenten entwickelt und implementiert. Zur einfacheren Optimierung der Strahlparameter, kamen drei neue Strahlmonitore, zwei Mikrokanalplatten-Strahlmonitore sowie ein einzelner Phosphorschirm zur Strahljustage am Probenort zum Einsatz. Kernstück der Arbeit war die Implementierung einer Transmissions-Remoderationseinheit in Form einer 100 nm dünnen einkristallinen Ni(100) Folie zur Brillianzerhöhung des Positronenstrahls. Im Vorfeld wurden hierzu umfangreiche Untersuchungen an der Ni(100) Folie durchgeführt um deren Remoderationseffizienz zu maximieren. Zur Strahlführung und -fokussierung wurden zwei elektrostatische Linsensysteme entwickelt. Die Geometrie sowie auch die Spannungen der Elektroden der Linsensysteme wurden hierfür durch umfangreiche Simulationen optimiert. Eines der Linsensysteme fokussiert den remodierten Strahl von der Positronenquelle NEPOMUC auf die Ni(100) Folie. Ein weiteres dient zur Strahlformung und -fokussierung der reemittierten Positronen auf die Probe. Durch den Einsatz der Remoderationseinheit kann ein minimaler Strahldurchmesser von 50 μm erreicht werden. Eine zusätzliche Blende vor der Remoderationsfolie reduziert diesen Wert weiter auf 33 μm .

Zum ersten Mal wurde dieser neue Positronenmikrostrahl zur Untersuchung der Defekt- und Elementverteilung in Laser- und Rührreibschweißnähten einer ausscheidungshärtenden AlCu Legierung erfolgreich im Regelbetrieb eingesetzt. Die Festigkeit solcher Legierungen lässt sich signifikant durch eine Kombination von Wärmebehandlung, Abschrecken, Umformen und anschließendem Auslagern bei erhöhten Temperaturen beeinflussen. Im Falle von AlCu Legierungen sind die sich dabei bildenden Cu Ausscheidungen von größter Bedeutung. Deren Bildung und die Defektverteilung wurden mit dem

neuen Mikrostrahl des CDBS *upgrade* analysiert. Hierbei konnte ein signifikant höheres Cu Signal im Ausgangsmaterial als in der Schweißnaht nachgewiesen werden. Dies kann der erhöhten Löslichkeit der Cu Ausscheidungen bei hohen Schweißtemperaturen und dem nachfolgenden raschen Abkühlen zugeschrieben werden.

Darüber hinaus wurde mit einer neu entwickelten in-situ Zugmechanik das Verhalten einer Edelstahl-Laserschweißnaht während der Durchführung eines Zugversuches erstmalig studiert. Die Bruchstelle konnte hierbei in Relation zur Defektverteilung gesetzt und in einem Bereich zwischen den Wärmeinflusszonen lokalisiert werden.

Des Weiteren wurde mit dem Positronenmikrostrahl erstmals demonstriert, dass sich die Kristallite in einer wärmebehandelten Pt Folie durch ihre Unterschiede im S-Parameter orts aufgelöst darstellen lassen.

Abbreviations

ACAR	angular correlation of annihilation radiation
AFM	atomic force microscopy
BM	beam monitor
CDB	coincident Doppler broadening
CDBS	coincident Doppler broadening spectrometer
DBS	Doppler broadening spectroscopy
DSP	digital signal processor
FRM II	research neutron source Heinz-Maier Leibnitz
FSW	friction stir welding
FWHM	full width at half maximum
GP	Guinier-Preston
HAZ	heat affected zone
HPGe	high purity germanium
HV	high voltage
IWB	institute for machine tools and industrial management
LBW	laser beam welding
LINAC	linear accelerator
LLNL	Lawrence Livermore national laboratory
MCP	micro channel plate
NEPOMUC	neutron induced positron source Munich
PAES	positron annihilation induced Auger electron spectrometer
PALS	positron annihilation lifetime spectroscopy
PAS	positron annihilation spectroscopy
PLEPS	pulsed low energy positron system

Ps	positronium
PSD	phase space density
PSV	phase space volume
RHEED	reflection high-energy electron diffraction
ROI	region of interest
SEM	secondary electron microscope
SPM	scanning positron microscope
SSSS	supersaturated solid solution
STM	scanning tunnelling microscopy
TEM	transmission electron microscopy
TMAZ	thermo-mechanically affected zone
TRHEPD	total-reflection high-energy positron diffraction
TUM	Technische Universität München
TWI	the welding institute
UHV	ultra high vacuum
UTS	ultimate tensile strength
XPS	x-ray induced photo electron spectroscopy

Contents

Abstract	v
Zusammenfassung	vii
Abbreviations	ix
1 Introduction	1
2 Theory of Positron Physics	5
2.1 Positrons in Solid State Physics	5
2.1.1 Properties of the Positron	5
2.1.2 Positron Sources	6
2.1.3 Positrons in Matter	11
2.2 Positron Moderation and Beam Formation	15
2.2.1 Purpose of Moderation	15
2.2.2 Positrons at the Surface	18
2.3 Beam Guidance and Focusing of Charged Particles	19
2.3.1 Movement of Charged Particles in Electromagnetic Fields	19
2.3.2 Magnetic Beam Guidance	21
2.3.3 Focusing of Charged Particles in Electromagnetic Fields	25
2.4 Brightness Enhancement of Positron Beams	34
2.4.1 Definition of the Brightness	35
2.4.2 Liouville's Theorem	35
2.4.3 Re-moderation of Positrons	37
3 Doppler Broadening Spectroscopy of the Positron Annihilation Line	41
3.1 Positron as Probe for Open Volume Defects	41
3.2 Principle of Doppler Broadening Spectroscopy	42
3.3 High-Resolution γ -Detection	47
3.3.1 Working Principle of HPGe-Detectors	47
3.3.2 Spectrum of Positron Annihilation Radiation	48

3.4	Data Evaluation in PAS	50
3.4.1	Doppler Broadening Spectroscopy - DBS	50
3.4.2	Coincident Doppler Broadening Spectroscopy - CDBS	54
4	The New CDB Spectrometer at NEPOMUC	57
4.1	Overview of the CDB Spectrometer Second Generation	57
4.2	Experimental Requirements of the New CDB Spectrometer	59
4.3	The CDBS <i>upgrade</i>	60
4.4	Components and Assembly of the CDBS <i>upgrade</i>	61
4.4.1	First Beam Monitor and Acceleration System	61
4.4.2	Brightness Enhancement System and Sample Chamber	62
4.5	Simulation of the Magnetic and Electrostatic Fields	66
4.6	Ni Foil Transmission Re-moderator	72
4.6.1	XPS Characterization of the Ni(100) Foil	72
4.6.2	Characterization by Temperature-Dependent DBS	72
4.6.3	DBS Measurement of the Implantation Energy	75
4.7	Performance of the CDBS <i>upgrade</i> Microbeam	76
4.7.1	Beam Profile Measurements	77
4.7.2	Count Rate Measurement at the CDBS <i>upgrade</i>	82
5	High Resolution Defect Spectroscopy	85
5.1	Modern Welding Techniques	85
5.1.1	Methods and Materials	86
5.1.2	Characterization of Friction Stir Welded AlCu6Mn	95
5.1.3	Characterization of Laser Beam Welded AlCu6Mn	105
5.1.4	Characterization of Laser Beam Welded Stainless Steel	113
5.1.5	Relation between S-Parameter and Vicker's Hardness in LBW-Samples	117
5.1.6	In-situ Tension Tests on LBW V2A	124
5.2	Annealed Pt Foil	128
6	Conclusion and Outlook	131
7	Danksagung	133
	List of Publications	137
	Bibliography	141
A	Appendix	151
A.1	Beam Monitor Assemblies	151

A.2	Accelerator	154
A.3	Magnetic Field Termination	155
A.4	Re-moderation Foil Preparation System	156
A.5	Values for the Magnetic and Electrostatic Fields of the CDBS <i>upgrade</i>	157
A.6	Data Sheets	159
A.7	Latex Code for Fitting the CDBS Ratio Curves	161

1

Chapter 1

Introduction

The investigation and tuning of mechanical properties such as brittleness, stiffness or tensile strength are of major interest for industrial applications and material science. Solid state physics links these properties to their atomic structure. In this regard, crystal defects such as dislocations, precipitates and different species of point defects highly influence the mechanical properties of a material. They can be deteriorated, e.g., due to the presence of structural vacancies, or considerably improved by deliberate introduction of defects. In order to probe these defects, various examination methods on microscopic length-scales from the nm- up to the μm -range have evolved. In figure 1.1, well-established techniques are compared according to their measurable defect size and depth-sensitivity. Among them, optical microscopy is probably the easiest and the earliest one. X-ray and neutron scattering are suitable for large bulk samples. Transmission electron microscopy (TEM) provides a high resolution but however requires a very demanding sample preparation. Moreover, scanning tunnelling microscopy (STM) and atomic force microscopy (AFM) provide a high surface sensitivity. Most prominent, positron annihilation spectroscopy (PAS) covers a large depth range with a sensitivity on an atomic scale. Thus, PAS is a highly suitable, non-destructive method with an unprecedented sensitivity for vacancy-like defects.

It was discovered early that the energy and momentum conservation during the annihilation process could be utilized to study properties of solids. In first experiments with positrons, the electronic structure such as the Fermi surface of metals and alloys was studied. This technique is also referred to as angular correlation of annihilation radiation (ACAR). In addition it was realized that the annihilation parameters such as the Doppler broadening of the annihilation line and the lifetime of the positron in matter are very sensitive to lattice imperfections. The positron is effectively trapped in vacancy-type defects and hence, can probe all kind of sample defects, the defect itself and its surrounding. The type of defect can be distinguished by positron lifetime spectroscopy and the presence of such defects and the chemical surrounding is determined by (coincident) Doppler broadening spectroscopy. Therefore, the investigation of crystal defects has become the dominant issue of positron annihilation studies.

The coincident Doppler broadening spectrometer (CDBS) using the high-intensity positron beam at the neutron induced positron source Munich (NEPOMUC) located

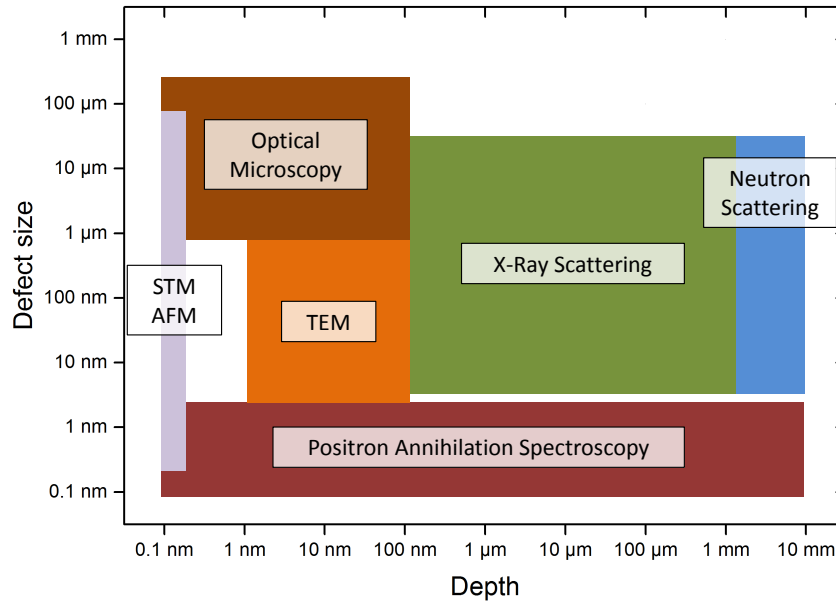


Figure 1.1: Examination techniques in solid state physics. Dependent on the examination technique different defect sizes in different depths of the sample can be investigated. With positrons virtual the entire range in depth from 0.1 nm up to 10 mm can be examined non-destructive. Moreover, with STM and AFM defect sizes in the sub-nm size can be reached but only in a small depth area.

at the research neutron source FRM II is designed for examining the crystal defects in 3D with high resolution. This is made possible by positioning a sample below a focused positron beam in 2D. The third dimension can be varied according to the implantation energy for depth-dependent measurements of up to a few μm depending on the density of the material. For spatially resolved measurements, the upgraded spectrometer routinely provides a beam $< 250 \mu\text{m}$. Moreover, in-situ experiments at low and elevated temperatures can be carried out.

The main focus of the present thesis was to introduce an additional brightness enhancement system comprising a 100 nm thin Ni(100) single crystal foil in order to reduce the beam diameter further by a factor of 5 (down into the μm range). Therefore, the entire set-up of the instrument was re-designed in order to meet the new requirements. Additionally, three new beam monitors were introduced and the entire sample chamber was rebuilt and equipped with a high-resolution sample positioning system. Beforehand, the design of the solenoidal coils and the electrostatic lens systems for beam transport and focusing was optimized by comprehensive simulations of the positron trajectories in the electrostatic and magnetic fields. Finally, it could be demonstrated that a high-brightness positron beam with a minimal beam diameter of $33 \mu\text{m}$ could be achieved.

In the second part of the present thesis, comprehensive material studies were carried out with a focus on two different welding techniques, namely friction stir welding (FSW) and laser beam welding (LBW) performed on an age hardening AlCu alloy and on stainless steel. AlCu alloys are well known age-hardenable alloys where the strength of the material can be significantly increased by various temper processes. Crucial for its strength is the formation of Cu precipitates during artificial ageing. As welding introduces heat into the work pieces, various dissolution and formation processes of precipitates can occur within the welded zones. As the CDBS is capable of detecting lattice defects and their chemical surroundings, it is highly suitable for the investigation of changes in defect distribution and chemical composition. Since LBWs can be produced on very small scales, the high-resolution beam of the CDBS *upgrade* is capable of resolving the relevant structures between 50-500 μm . Moreover, a newly developed in-situ tension testing machine was applied to a LBW stainless steel sample for the first time in order to image the defect distribution formed during putting load on the sample.

The new instrument comprises a great potential in fundamental research and material science. CDBS states a powerful tool to determine the distribution and concentration of vacancy-type defects as well as the chemical surrounding of the annihilation site, destruction-free and with unprecedented accuracy.

2

Theory of Positron Physics

Within this chapter the theoretical background of positron physics will be elucidated as this will be necessary to understand the later presented experimental results. In the first part, the generation of positrons as well as their behaviour in matter until their annihilation is described. The following part focusses on the moderation, transport and brightness enhancing of a positron beam. Lastly, the positron source NEPOMUC should be introduced as realization of the before mentioned theoretical considerations.

2.1 Positrons in Solid State Physics

2.1.1 Properties of the Positron

In 1930, the positron was postulated by Paul Dirac in his famous Dirac equation as the antiparticle of the electron [1]. Only two years later, in 1932, Carl D. Anderson detected the antiparticle of the electron in a cloud chamber while photographing cosmic ray tracks [2, 3]. Being the antiparticle of the electron, positron and electron possess identical physical properties such as rest mass and spin but opposite charge. As a result the positron exhibits a positive magnetic momentum. As the positively charged antiparticle of the electron (e^-) the positron is symbolized with an " e^+ ". Table 2.1 lists some of its fundamental properties.

In vacuum, the e^+ lifetime is longer than $2 \cdot 10^{21}$ s and it can therefore be regarded as a stable particle. Nevertheless, when implanted into matter, the presence of electrons leads to a drastically reduced positron lifetime. Hereby, it annihilates with an electron predominantly into two γ -quanta since each additional photon vertex gives an additional factor of $\alpha \approx 1/137$ to the annihilation rate. Hence, the three- γ -annihilation is suppressed by a factor of 370 due to an additional factor of $9/\pi$ occurring from quantum field theory. The annihilation into two γ -quanta exhibits a lifetime in the range of about hundred picoseconds up to nanoseconds, depending on defects or pores in the material. Nonetheless, under certain circumstances, a positron and an electron can form a bounded state called positronium (Ps) with a vacuum binding energy of -6.8 eV. Dependent on the spin orientation of the two particles, two different states

Property	Value	Unit
charge e	$1.602176487(40) \cdot 10^{19}$	C
rest mass m_0	$9.10938215(45) \cdot 10^{-31}$	kg
	$0.510998910(13)$	MeV/c^2
spin s	$1/2$	
magnetic moment $ \vec{\mu} $	$1.00115965218111(74)$	μ_B

Table 2.1: Fundamental properties of the positron [5].

can be formed, namely, a singlet state, called para-positronium (p-Ps) with a vacuum lifetime of 125 ps and a triplet state, so-called ortho-positronium (o-Ps) which exhibits a vacuum lifetime of 142 ns. The first state decays into two (four, six,...) γ -quanta (with decreasing probability) as the total spin of p-Ps is $S=0$ whereas the second possible state decays in one, three (five, seven,...) or more γ -quanta (with decreasing probability) according to its total spin $S=1$ [4].

2.1.2 Positron Sources

Whenever positrons are used in an experiment the source of the beam has to be taken into account. Dependent on considerations like costs and complexity of the production, three different sources are commonly used: emitting radioactive isotopes as well as research reactor and accelerator (linear accelerator (LINAC)) based sources producing positrons by pair production. The first two approaches will be explained in the following and examples of research establishments making use of these concepts will be given. In the end, the reactor based source used in this work will be introduced in more detail.

β^+ - Emitting Labsources

In small laboratory sources, positrons are usually produced via the β^+ decay of radioactive nuclides such as ^{22}Na , ^{58}Co and ^{64}Cu . Thereby, a proton within the atomic nucleus decays into a neutron, a positron e^+ and an electron neutrino ν_e . In general, this can be expressed by the following equation for an initial nuclide X, with Z protons and a mass number A:



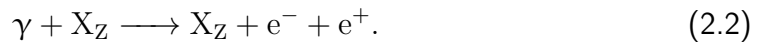
Nuclide	$\tau_{1/2}$	E_{mean} (keV)	E_{max} (keV)	I_{e^+}	E_γ (keV)	I_γ
^{18}F	110 min	249.8	633.2	0.967		
^{22}Na	2.60 a	215.5	545.4	0.898	1275	0.999
		835.0	1819.7	0.001		
^{58}Co	70.8 d	201.3	475.2	0.150	811	0.994
^{64}Cu	12.7 h	278.1	652.5	0.179	1346	0.005

Table 2.2: Positron emitting laboratory sources with specific half life $\tau_{1/2}$, average positron energy E_{mean} , endpoint energy E_{max} of the emitted positrons, positron yield I_{e^+} and the dominant γ -energy E_γ with its corresponding intensity I_γ [6].

Thus, the nuclide decays into three particles. Due to momentum conservation, the emitted positrons possess a continuous energy spectrum analogous to electrons produced in a β^- decay. In table 2.2 positron emitting isotopes used as lab sources are listed according to their mass number.

Pair Production

Positron sources of higher intensities, which are not limited by self absorption in the source, use the principle of pair production. The fundamental principle of this method is the conversion of energy into mass according to Einstein's equation $E = m \cdot c^2$. In order to create an electron-positron pair, a minimum photon energy of twice the electron's rest energy, i.e. $E_{\gamma,min} = 2 \cdot m_e \cdot c^2 = 2 \cdot 511 \text{ keV} = 1022 \text{ keV}$ is needed. Due to conservation of momentum, pair production only takes place in the Coulomb field of another charged particle like in the vicinity of a nucleus X with high atomic number Z . Thus, pair production can be described via the following reaction



If the incident γ -energy is higher than the minimum energy required for pair formation, the excess energy is transferred into kinetic energy of the products and the involved converter nucleus. For a positron-electron pair a minimal energy of 1022 keV is required.

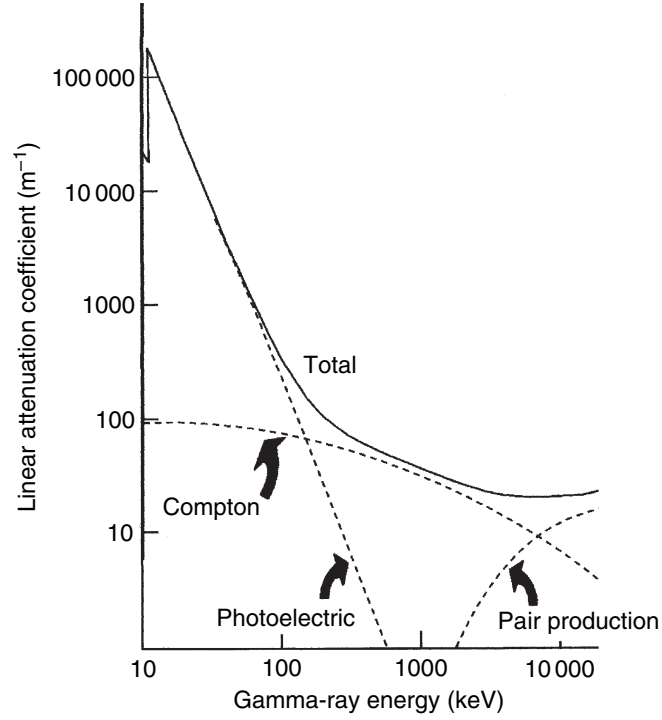


Figure 2.1: Example of linear attenuation coefficient and its component parts of Ge. Up to an energy of around 200 keV the photo effect dominates whereas at energies greater than 10 MeV pair production is the dominant mechanism. Image taken from [7].

Hereby, the pair production cross section σ_{pp} depends on the γ -energy E_γ and atomic number Z and can be expressed as

$$\sigma_{pp} \propto Z^2 f(E_\gamma, Z). \quad (2.3)$$

Hereby, σ_{pp} is dominated by the Z^2 term and therefore the atomic size. $f(E_\gamma, Z)$ changes only slightly with Z and increases continuously with energy from the threshold at 1022 keV. Comparing it to the photo- and Compton effect, at energies greater than 10 MeV pair production is the dominant mechanism of interaction [7]. An example for the attenuation coefficient is given in figure 2.1. Typical high- Z materials for positron-electron pair production are W and Pt [8, 9].

Today, there are three different concepts for the production of positrons that are based on the principle of pair production. The first one is realized at the Lawrence Livermore national laboratory (LLNL) located near San Francisco in California. Here, high-energy electrons produced in a LINAC are dumped in a target with high atomic number. As the electrons interact with the target material they lose their energy resulting in the emission of high-energy bremsstrahlung photons. These photons in turn interact with the high- Z

nuclei, which enable some of the high-energy photons to split into electron-positron pairs. As positron beams created from a LINAC are pulsed, they are beneficial for lifetime experiments [10, 11].

The second and third concept involve reactor based sources. At the research reactor at the Delft University of Technology in the Netherlands, the high flux of fission γ s produced in the core is directly used for pair production in an assembly of thin W foils [12].

Alternatively, at the research neutron source Heinz-Maier Leibnitz (FRM II) in Garching, Germany, the high flux of thermal neutrons is used to produce high energy γ -radiation via the nuclear reaction $^{113}\text{Cd}(n, \gamma) ^{114}\text{Cd}$ [13]. The strongest positron source of the world, NEPOMUC, uses this principle and a continuous primary positron beam with an intensity of $1.14 \cdot 10^9 \text{ e}^+/\text{s}$ is generated [14]. As this source is used for the experiments of the present thesis, it will be explained in more detail in the following section.

The Positron Source NEPOMUC *upgrade*

The positron production within the positron source NEPOMUC *upgrade* is based on pair production. Figure 2.2 shows a cross sectional view of the in-pile source. Here, a

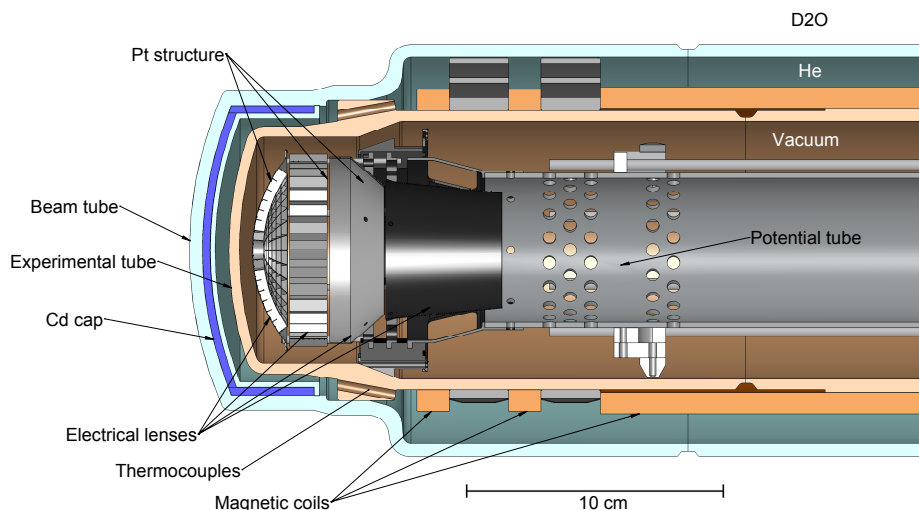


Figure 2.2: Cross sectional view of the in-pile positron source NEPOMUC *upgrade* housed at the FRM II. A layer of enriched ^{113}Cd , pressed into the tip of the beam tube, converts the thermal neutrons coming out of the reactor core of the FRM II into hard γ -radiation via (n, γ) reaction which is used for pair production in a Pt structure located at the tip of the potential tube. Different electrostatic lenses and magnetic fields separate the positrons from the electrons and accelerate and transport them to the experiments [15].

tube containing the beam tube itself, an evacuated experimental tube and a potential tube with the positron source is mounted close to the fuel element of the reactor FRM II inside of the moderator tank filled with heavy water. The principle is based on the emission of high-energy prompt γ -rays after thermal neutron capture in enriched ^{113}Cd which is pressed in a thin layer of a few mm into the tip of the beam tube. The high-energy γ -radiation is then converted into mono-energetic positrons produced by pair production in a structure of Pt foils. Using different electrostatic lenses and magnetic coils mounted on the experimental tube, a positron beam can be created and transported to the experiments inside an evacuated beamline as shown in figure 2.3 [15].

At NEPOMUC two different beam modes exist, the so-called primary and re-moderated beam, respectively. The former is produced in the set-up shown in the figures 2.2 and 2.3 already explained above. Its quality can be analysed at the first beam monitor. Here, the intensity, the shape and the size of the beam can be monitored inserting either a target or a micro channel plate (MCP) assembly with an additional camera imaging the scintillation image of the amplified beam on a phosphor screen [14]. Via two magnetic beam switches either the primary beam can be guided to the instruments or a re-moderation unit can be used for enhancing the brightness of the beam. A more comprehensive description of the beam switches and the re-moderation unit can be found in [17] and [18]. The re-moderated, brightness enhanced beam is also called NEPOMUC re-moderated beam.

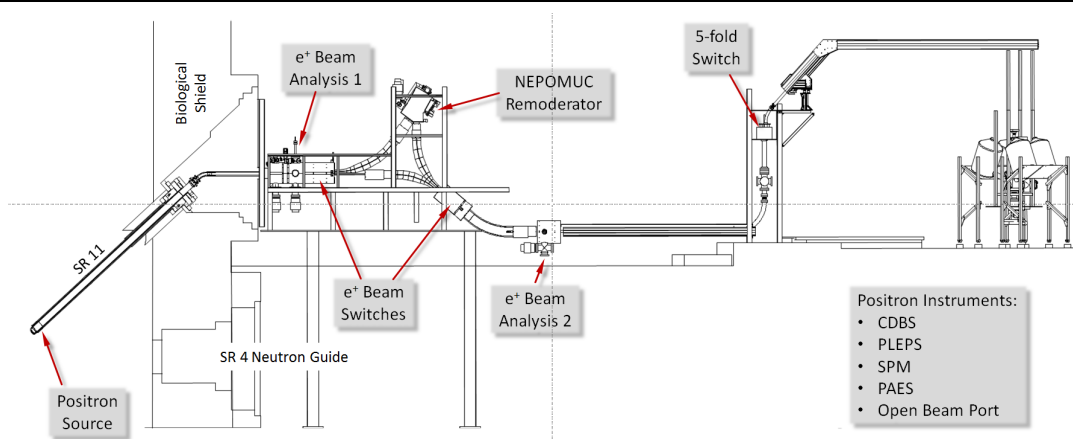


Figure 2.3: Schematic drawing of NEPOMUC and the positron facility at the FRM II. The produced positron beam is guided within magnetic fields to the experiments, within this drawing the coincident Doppler broadening (CDB) spectrometer. During this way it can be accessed at different beam monitors for analyzing the quality and intensity of the beam. NEPOMUC supplies a primary and a re-moderated beam to five instrument positions at different ports via a 5-fold switch [16].

In total five instruments can be supplied with positrons via a manually operated s-bend shown in figure 2.3. Four instruments, namely the CDBS [19], the positron annihilation induced Auger electron spectrometer (PAES) [20] operated by the Technische Universität München (TUM) and the pulsed low energy positron system (PLEPS) [21] and scanning positron microscope (SPM) [22, 23] operated by the UniBW in Neubiberg are permanently connected with NEPOMUC. One additional instrument can be moved to an open beam port for temporary experiments. The positrons are adiabatically guided in a magnetic transport field of about 6 mT. Most of the instruments use the re-moderated beam with a kinetic energy of 20 eV.

This work will focus on the CDB spectrometer which uses the re-moderated beam for PAS. Details on the measurement technique, the instrument and the upgrade of the instrument will be given in the chapters 3 and 4.

2.1.3 Positrons in Matter

In recent times positrons used as micro probe particles with outstanding sensitivity for crystal defects have evolved as a standard tool in material analysis [24]. After implantation in a material the positron thermalizes rapidly within ps, diffuses through the crystal lattice within its diffusion length in the order of 100 nm, and finally annihilates as a delocalized positron from the Bloch-state or from a localized state present in open volume defects. Hence, positron annihilation spectroscopy has become a well-established tool to investigate lattice defects in solids especially for the detection and investigation of vacancy-like defects [4, 25–27].

Implantation and Thermalization

As depicted in figure 2.4, when positrons enter a solid, several interactions can take place. First, the positrons have to pass the surface whereby a fraction of up to 40% dependent on the atomic number Z of the material and the implantation energy, are reflected [28]. Positrons impinging the material lose their kinetic energy mainly due to inelastic scattering with electrons until they are thermalized, i.e., positrons are in thermal equilibrium with the surrounding medium and subsequently only quasi-elastic scattering occurs. Thermalization is a very fast process and occurs typically within a few picoseconds depending on the implantation energy, the density and the elemental composition of the material [4]. At implantation energies between the Fermi energy and about 100 keV, inelastic scattering of the positrons, leading to their thermalization, is dominated by scattering at conduction electrons, in the case of metals, as well as

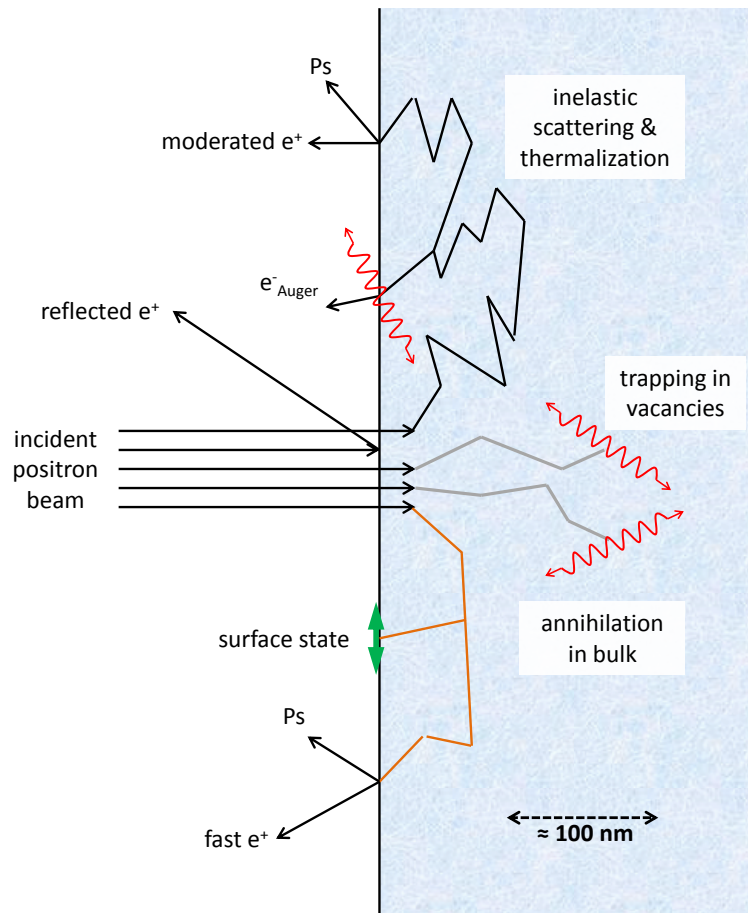


Figure 2.4: Positrons entering matter. At the surface a fraction of the positrons can be reflected or scattered inelastically. When they enter the material they can be scattered (in-) elastically back to the surface or get thermalized. After thermalization the positron can freely diffuse through the material and in case of a negative positron work function it can be re-emitted. The relevant process for Doppler broadening spectroscopy is the annihilation of positrons trapped in defects and in the defect free bulk.

as the excitation of cor- and valence electrons. At lower energies the main process of thermalization is phonon scattering [29–31].

Mathematically, the implantation profile $P(z)$ of a monoenergetic positron beam of energy E_{kin} can be described by the Makhovian profile [32]

$$P(z) = \frac{mz^{m-1}}{z_0^m} \exp \left[- \left(\frac{z}{z_0} \right)^m \right] \quad (2.4)$$

with z as the implantation depth. The parameter m is a dimensionless material constant determined by Monte Carlo simulations [33] and z_0 is expressed by the formula

$$z_0 = \frac{\bar{z}}{\Gamma\left(\frac{1}{m} + 1\right)} \quad (2.5)$$

with the gamma function Γ

$$\Gamma(x) = \int_0^\infty t^{x-1} e^{-t} dt. \quad (2.6)$$

The mean implantation depth \bar{z} is expressed by a power law and is a function of the density ρ

$$\bar{z} = \frac{A}{\rho} E^n. \quad (2.7)$$

A and n are material dependent parameters and have been empirically determined by simulations and experiments [26, 34, 35]. Exemplary, in figure 2.5, some implantation profiles and the positron mean implantation are calculated and shown for Ni. Note that with increasing implantation energy, the implantation profile becomes broader deteriorating the resolution in depth depending measurements.

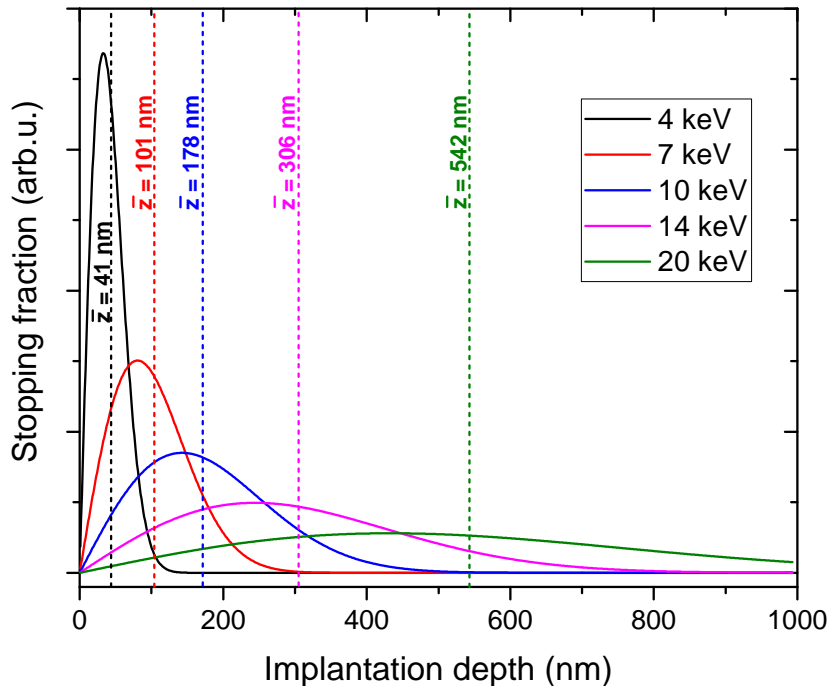


Figure 2.5: Makhovian profiles and mean implantation depths in Ni calculated for different implantation energies.

Diffusion and Trapping

After reaching thermal equilibrium within the solid, the positron can diffuse quasi-freely through the bulk. The total diffusion length L_{e^+} of a positron in a defect-free lattice depends on the lifetime τ_{e^+} and on the diffusion coefficient D_{e^+} [4] according to

$$L_+ = \sqrt{D_{e^+} \tau_{e^+}}. \quad (2.8)$$

Typical diffusion constants of $D_{e^+} = 0.1 - 1 \text{ cm}^2/\text{s}$ and average lifetimes $\tau_{e^+} = 0.1 - 0.4 \text{ ns}$ result in diffusion lengths of a few 100 nm [4]. During its diffusion through the solid, the positron may be trapped at vacancies, microcavities, dislocations and other kinds of defects. In figure 2.6, this situation is shown for a vacancy. The missing of the positively charged atomic core states an attractive potential for the positively charged positron as shown on the bottom of the figure. For mono-vacancies, the positron binding energy amounts to around 1 eV which makes it impossible for the

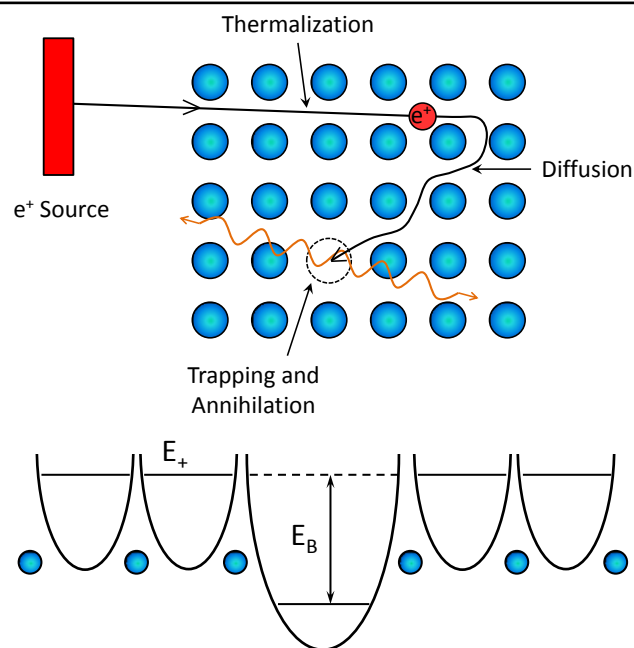


Figure 2.6: (top) Positrons emitted by a source entering a solid. At first the positrons are thermalized until they are in thermal equilibrium with the material. Then they can freely diffuse through the crystal lattice until they get trapped in the attractive potential of a crystal defect. The positron then annihilates with an electron from the crystal and two 511 keV γ -quanta are produced which can be detected. Traps for positrons possess a potential depth of typically $E_B = 1 \text{ eV}$. Due to this attractive potential thermalized positrons can not escape these traps (bottom) [4].

positron to escape within its lifetime. According to its diffusion length, the positron can diffuse over several lattice sites before being trapped at a defect site making it a convenient probe for defect spectroscopy. Alternatively in the presence of no vacancies, positrons can also diffuse back to the surface of the material and can annihilate on the surface or leave the solid [36, 37]. Besides the formation of bound states at the surface [38], a bound state of an electron and positron, called Ps, can be created. In addition, when materials with negative positron work functions are used, the re-emission of thermalized positrons, so-called moderated positrons, can take place. This process which is important for generating high-brightness mono-energetic positron beams, is explained in detail in section 2.2. The main measurement technique with positrons is based on the annihilation with electrons in the bulk material. Positron annihilation spectroscopy (PAS) comprises besides other techniques like ACAR [24] or total-reflection high-energy positron diffraction (TRHEPD) [39] lifetime measurements and (coincident) Doppler broadening spectroscopy ((C)DBS). The latter ones are based on the trapping of the positrons due to an attractive potential caused by the missing positive charge of the atom core which can localize the positron. In metals, for example, vacancies or grain boundaries reduce the repulsive positive potential for the positrons arising from the atomic cores. The resulting negative attractive potential works as efficient trapping center. Due to its delocalisation the positron can sample a large volume and is therefore suitable as extremely sensitive probe for vacancies. One single vacancy out of 10^6 atoms can be detected [40].

2.2 Positron Moderation and Beam Formation

Positrons being generated in radioactive sources possess a broad distribution in energy. Additionally, from sufficiently small sources in the mm range the positrons are emitted approximately isotropic. In order to carry out depth-dependent measurements, a mono-energetic positron beam is crucial. Within this section the principle of moderation, i.e., the cooling of the positrons with subsequent beam formation will be described in order to create high-brightness positron beams. Therefore, the focus is put on the interaction of positrons near the surface of a material and what is necessary in order to emit moderated positrons from moderation materials.

2.2.1 Purpose of Moderation

Positrons generated by pair production or by radioactive sources described in section 2.1.2 have a continuous kinetic energy spectrum. In the case of ^{22}Na a maximum kinetic energy of up to 545 keV is provided [41]. Higher energies of up to several MeV are

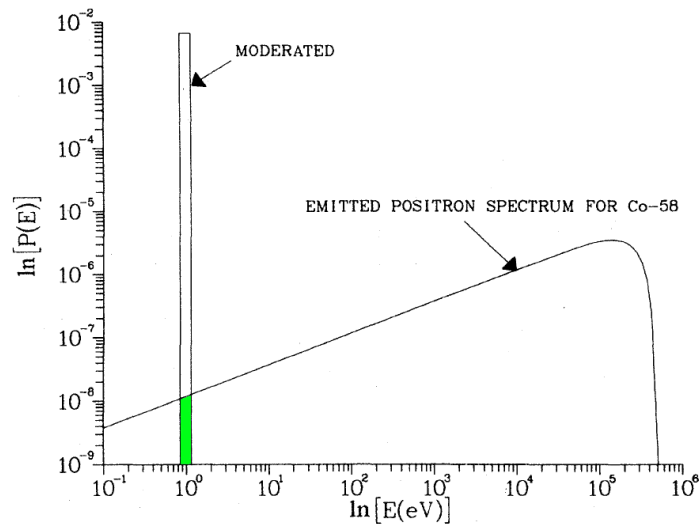


Figure 2.7: The consequences of moderation compared to the spectrum of positrons of a ^{58}Co source are shown. Due to moderation it is possible to increase the intensity of slow positrons by five to six orders of magnitude with a reduced beam divergence [4].

achieved by pair production [13]. When probing solids with positrons as highly sensitive micro-probes, it is often necessary to implant the positrons not only in the bulk, as it is done with lab-based sources, but also in certain depths or also parts of epitaxial grown layer systems. This is impossible by solely using a continuous kinetic energy spectrum because the implantation range reaches from the surface to the bulk limited by the maximum implantation depth. In the case of a ^{22}Na source, the energy spectrum peaks at 178 keV with an end point energy of 545 keV [24]. According to Brand et al. at the maximum energy corresponds to a maximum implantation depth of $\approx 28 \mu\text{m}$ calculated for Ni [42]. Here, the amount of implanted positrons drops to a value of $1/e$. Since the positrons are implanted in a range from the surface up to around twice the maximum mean implantation depth of $\approx 56 \mu\text{m}$, depth-dependent measurements are not possible. In order to probe different layers within the samples from the surface up to the bulk, mono-energetic positron beams have to be generated. By the use of the moderation technique the kinetic energy of the positron beam can be equalized. It can be explained by a cooling process of the positrons in the solid whereby they lose their kinetic energy through a number of inelastic interaction mechanisms, e.g. due to collisions, primarily with core and conduction electrons, until they reach thermal equilibrium. Within their diffusion length, a fraction of positrons dependent on the implantation energy is able to reach the surface of the material. Materials with a negative positron work function Φ^+ are able to re-emit thermalized positrons perpendicular to the surface. Such a re-emitted and moderated positron exhibits a distinct kinetic energy E_0 determined by

Material	Geometry	E (keV)	Thickness (nm)	Φ^+ (eV)	F_R (%)	Ref.
W(100)	t	5	100	-3.0	18	[46]
W(110)	r	2	3.2×10^7	-3.0	33	[47]
W(poly)	t	3	6000	-2.75	upto 31	[24, 48]
Ni(100)	t	5	150	-1.1	19	[49]

Table 2.3: Excerpt of typically used moderator materials with their work functions and re-emission fraction F_R of re-emitted positrons. The abbreviation "t" and "r" for the geometry stands for "transmission" and "reflexion", respectively. As the re-emission fractions are strongly influenced by temperature, surface treatment and geometry it is difficult to compare the values. Nevertheless, the order of magnitude can be estimated.

the work function of the material. The deviation of the positrons' kinetic energies from E_0 is in the order of thermal energies [24, 43, 44]. Typical values for E_0 are in the range of a few eV, e.g., $|\Phi_W^+|=3.0$ eV [24], $|\Phi_{Pt}^+|=1.95$ eV [45]. In figure 2.7 a comparison of the reachable intensities of slow positrons from a radioactive source, in this case ^{58}Co , versus moderation is shown. The gain in intensity of slow positrons in a narrow energy window in the eV-range after the moderation process from a ^{58}Co source is in the order of about six orders of magnitude. Although the moderation process has only an efficiency of typically 2×10^{-3} by using a W moderator crystal, it is much more efficient than only selecting the amount of positrons in a small energy window by e.g. a chopper (green area in figure 2.7) [24].

Since a large fraction of re-emitted positrons is desirable, moderator materials with high efficiency have to be used. However, different processes such as free annihilation or trapping and subsequent annihilation at defect sites within the bulk limit the number of re-emittable positrons. Moreover, positrons may escape the material before reaching thermal energies as so-called epithermal positrons, which do not possess the kinetic energy desired by the moderation process. Due to the annihilation and the escape of non-thermalized positrons from the moderation material the efficiency is reduced. By a first moderation process where a mono-energetic particle beam is produced and subsequent implantation in a moderator material higher efficiencies of up to 33 % as depicted in table 2.3 can be reached. Here, the implantation energy of a mono-energetic positron beam can be adjusted to the geometry of the moderation materials reaching efficiencies three orders of magnitude higher than at the first moderation process forming a mono-energetic beam.

2.2.2 Positrons at the Surface

If the implantation energy of the positron is low enough or the specimen is sufficiently thin, there is a given probability that the positron can reach the surface. Some materials, known as moderation materials, have the ability to emit thermalized positrons with a well-defined energy. This energy corresponds to the work function Φ^+ and is defined analogous to that of electrons. It can be calculated taking into account the potential barrier D due to the surface dipole layer and the chemical potential for positrons μ_+ [4, 50]

$$\Phi^+ = -D - \mu_+. \quad (2.9)$$

Hereby, the chemical potential is calculated by a superposition of two components. The first contribution arises from the positron-ion interaction. Here, the positron is rejected by the ion cores and in some cases the lowest single particle state lies several electron volts above the electrostatic potential in the interstitial region. This potential is named zero-point potential V_0 . The second component is the positron-electron correlation potential V_{corr} . It is defined as the difference between the ground-state energy of the metal and the positron [50]. All in all, the positron potential of a material with negative positron work function can be calculated and is shown in figure 2.8. For most materials

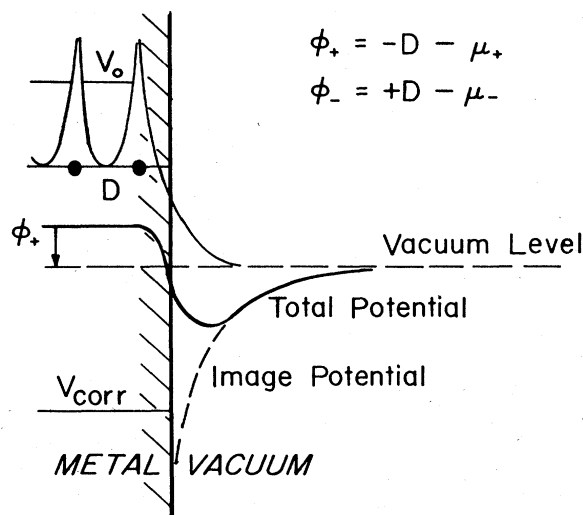


Figure 2.8: The particle potential for a thermalized positron in metals. The work function ϕ_+ can be calculated with the surface dipole layer D and the chemical potential μ_+ . If the work function is negative, thermalized positrons at the surface are emitted into the vacuum [4].

the positron work function is positive and leads at the surface to a force which is directed inwards into the solid. The surface dipole barrier gives a negative contribution to the positron work function which can in total result in a negative value. In this case, thermalized positrons diffusing to the surface can be emitted perpendicularly into the vacuum with a well-defined kinetic energy given by the amount of the negative positron work function [4].

Hence, with such materials, positron beams with a very sharp energy distribution, only smeared by the thermal energy of the moderation material, can be created. Additionally, such a material is used for re-moderation of a positron beam in order to enhance the beam brightness. This will be explained in detail in section 2.4.

2.3 Beam Guidance and Focusing of Charged Particles

Positrons are charged particles and as such they respond to electrostatic and magnetic fields. This fact can be exploited to guide the beam over large distances in vacuum tubes and focus it onto the probed sample. The principle of guiding a positron beam using electromagnetic fields is similar to light optics where light can be focused, reflected or refracted. In the following section, the most important fundamental mathematical equations and techniques necessary for describing and understanding the path of charged particles, such as the positron, in electromagnetic fields will be given. Most of the principles used in this work are based on references [51] and [52].

2.3.1 Movement of Charged Particles in Electromagnetic Fields

The most fundamental equation describing the path of a free charged particle in an electromagnetic field is the so-called Lorentz force

$$\vec{F} = q (\vec{E} + \vec{v} \times \vec{B}). \quad (2.10)$$

Here, a particle with charge q experiences a force \vec{F} when it is injected with a velocity \vec{v} in a region with an electric field \vec{E} and magnetic induction \vec{B} . This formula is valid both for static and time dependent fields as well as for relativistic energies of the particle. For relativistic particles the momentum \vec{p} is calculated according to

$$\vec{p} = \gamma m \vec{v}. \quad (2.11)$$

In this formula, m is the rest mass of the particle and $\gamma = (1 - \beta^2)^{-\frac{1}{2}}$, the Lorentz factor with the ratio of particle velocity to light speed $\beta = v/c$. The equation of motion is obtained from equation 2.11 by differentiating \vec{p} with respect to the time. Inserting the Lorentz force (equation 2.10) as deviation of the momentum leads to

$$\frac{d\vec{p}}{dt} = \dot{\gamma}m\dot{\vec{x}} + \gamma m\ddot{\vec{x}} = q(\vec{E} + \dot{\vec{x}} \times \vec{B}). \quad (2.12)$$

For most practical applications, rotational symmetry is valid as the charged particles are transported in beamline tubes wrapped with coils forming a solenoid-like magnetic field. Hence, a transformation of equation 2.12 into cylindrical coordinates with the components r , ϕ and z is convenient and results in

$$\frac{d}{dt}(\gamma m \dot{r}) - \gamma m r \dot{\phi}^2 = q(E_r + r\dot{\phi}B_z - \dot{z}B_\phi) \quad (2.13)$$

$$\frac{1}{r} \frac{d}{dt}(\gamma m r^2 \dot{\phi}) = q(E_\phi + \dot{z}B_r - \dot{r}B_z) \quad (2.14)$$

$$\frac{d}{dt}(\gamma m \dot{z}) = q(E_z + \dot{r}B_\phi - r\dot{\phi}B_r). \quad (2.15)$$

These equations, also known as the Newtonian form of the equation of motion, are applied to the simulation of charged particles trajectories in electrostatic and magnetic fields for example with the software package "COMSOL multiphysics" in their non-relativistic form. Even though they have their practical application, the equations are not valid for arbitrary systems as they depend on the choice of the coordinate system. Therefore, a more generalized version of the equation of the motion, the Lagrange equations with the generalized coordinates $q_i(t)$ and $\dot{q}_i(t)$ should be discussed in the following. For relativistic particles the Lagrangian \mathcal{L} is defined as

$$\mathcal{L} = -\frac{1}{\gamma}m_0c^2 + q(\vec{v} \cdot \vec{A} - \Phi). \quad (2.16)$$

In this equation \vec{A} defines the vector potential and Φ the electric scalar potential. The vector potential is defined from the magnetic field \vec{B} such that $\vec{B} = \nabla \times \vec{A}$ [53, 54]. The particle trajectories can then be determined from the Lagrangian by solving the Euler-Lagrange equation

$$\frac{d}{dt} \left(\frac{\partial \mathcal{L}}{\partial \dot{q}_i} \right) - \frac{\partial \mathcal{L}}{\partial q_i} = 0. \quad (2.17)$$

Hereby, the canonical momentum P_{q_i} is defined by the term $\partial\mathcal{L}/\partial\dot{q}_i$ and can be written as

$$P_{q_i} = \frac{\partial\mathcal{L}}{\partial\dot{q}_i} = p_{q_i} + qA_{q_i}(\vec{x}, t) \quad (2.18)$$

where p_{q_i} is the ordinary kinetic momentum. From the Lagrangian in cylindrical coordinates the canonical momentum p_i can be derived as

$$p_r = \frac{\partial\mathcal{L}}{\partial\dot{r}} = \gamma m\dot{r} + qA_r \quad (2.19)$$

$$p_\varphi = \frac{\partial\mathcal{L}}{\partial\dot{\varphi}} = \gamma mr^2\dot{\varphi} + qrA_\varphi \quad (2.20)$$

$$p_z = \frac{\partial\mathcal{L}}{\partial\dot{z}} = \gamma m\dot{z} + qA_z. \quad (2.21)$$

If the electromagnetic field and therefore Φ , \vec{A} and \mathcal{L} are time-independent, in conservative systems the canonical momentum is conserved. With q_i and P_{q_i} kept constant, equation 2.17 can be simplified as

$$\frac{d}{dt} \left(\frac{\partial\mathcal{L}}{\partial\dot{q}_i} \right) = \frac{d}{dt} P_{q_i} = 0. \quad (2.22)$$

When the parameters of the system are changed very slowly with respect to the period of the motion, these changes are called adiabatic changes and the behaviour of the system can be described by the derivative of the one dimensional action integral integrated over a full cycle of motion

$$J_i = \oint p_i dq_i. \quad (2.23)$$

Physical quantities which are unaffected under adiabatic changes are called adiabatic invariants [55]. This principle can be transferred to the system discussed within this thesis where positrons are guided in longitudinal magnetic fields with slight field variations due to the structure of the magnetic field within the beamline.

2.3.2 Magnetic Beam Guidance

The easiest way of transporting charged particles in evacuated beamlines is realized via magnetic solenoidal fields. In practice, this is realized by tubes made out of non-magnetic materials wrapped with isolated wire. Thus, slow charged particles can be

guided in a homogeneous magnetic field created by feeding a constant current through the wire loops. The magnetic flux density \vec{B} within the tube can be determined according to equation 2.24 valid for long magnetic coils.

$$|\vec{B}| = \mu_0 \frac{IN}{l} \quad (2.24)$$

Here, μ_0 is the magnetic field constant, I defines the current through the coil, N is the number of turns and the length of the coil is l . The force on particles with charge q can be calculated via equation 2.10 in section 2.3.1 using equation 2.24 for the magnetic field and setting the electric field to zero $E = 0$. Particles entering the magnetic field \vec{B} parallel to their velocity vector \vec{v} do not experience any deflecting force. If the direction of motion is inclined, then the velocity can be split into two components, one parallel to the magnetic field, v_{\parallel} , and one perpendicular, v_{\perp} . The latter leads to a gyration around the magnetic field lines with radius [56]

$$r = \frac{mv_{\perp}}{qB} \quad (2.25)$$

$$\omega_g = \frac{qB}{m}. \quad (2.26)$$

Additionally taking into account the parallel component of the particle velocity v_{\parallel} , the complete motion of the particle can be described by a spiral path in direction of the field lines. The length of this path within the period T is given by the gyration length

$$l_g = v_{\parallel}T = \frac{2\pi v_{\parallel}}{\omega_g}. \quad (2.27)$$

Whenever the adiabatic conditions are fulfilled, charged particles can be guided also in inhomogeneous fields. In this case the particles follow bended field lines which is convenient for guiding the particles around bends of the beam line consisting of a distorted solenoid producing a magnetic gradient towards the center of the bend as it is shown in figure 2.9.

This gradient and the inertness of the particles cause a small deflection perpendicular to the curvature plane on its path through the bend. The drift velocity leads to a deviation of the gyration as calculated by

$$\vec{v}_d = \frac{1}{\omega_g R} \left(\underbrace{v_{\parallel}^2}_{\text{curv.}} + \frac{1}{2} \underbrace{v_{\perp}^2}_{\text{grad.}} \right) \left(\frac{\vec{R} \times \vec{B}}{RB} \right). \quad (2.28)$$

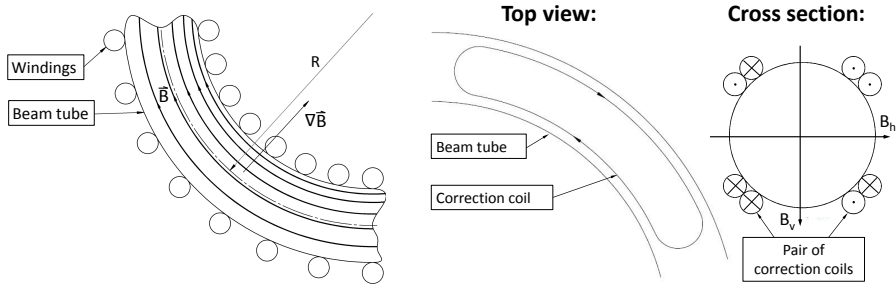


Figure 2.9: Magnetic field gradient produced due to the different winding density of the wire on the inner and outer side of the bent beam tube (left). This gradient, directed to the inner side of the bend leads to a so-called gradient drift whereas the curvature of the bend results in a centrifugal drift. Scheme of a mounted correction coil onto a curved beam tube. The coils produce a field perpendicular to the bend to compensate for deviations resulting from the curvature and gradient drift of the particles. By mounting a second correction coil perpendicular to the first one (not shown in the sketch), it is possible to correct the position in every direction by a superposition of the horizontal and vertical magnetic field (right).

Hereby, v_{\parallel} leads to a curvature drift and v_{\perp} to a gradient drift in the inhomogeneous magnetic field. \vec{R} defines the radius vector from the center of the bend to the corresponding field line and $R = |\vec{R}|$. When passing through a curvature of radius R and sector angle α , a particle experiences a certain deviation Δy from its original path. For small transverse velocities $v_{\perp} \ll v_{\parallel}$ and with $\omega = \frac{eB}{m}$ equation 2.28 can be rewritten as

$$\vec{v}_d = \frac{m}{e} v_{\parallel}^2 \cdot \frac{\vec{R} \times \vec{B}}{(RB)^2}. \quad (2.29)$$

For a bend with sector angle α and its corresponding arc length $s = (\pi/180^\circ) \cdot \alpha R$ the beam displacement Δy at the end of the bend is calculated with $\Delta y = v_d \cdot t$ and $t = s/v_{\parallel}$ to

$$\Delta y = \frac{m}{e} v_{\parallel} \frac{s}{RB} = \frac{\sqrt{2mE}}{e} \frac{\pi}{180^\circ} \alpha \frac{1}{B}. \quad (2.30)$$

Assuming a longitudinal beam energy $E = 20 \text{ eV}$, a magnetic guiding field $B = 7 \text{ mT}$ and an angle of the bend $\alpha = 90^\circ$ then a beam displacement perpendicular to the plane of the bend of $\Delta y = 3.3 \text{ mm}$ is calculated.

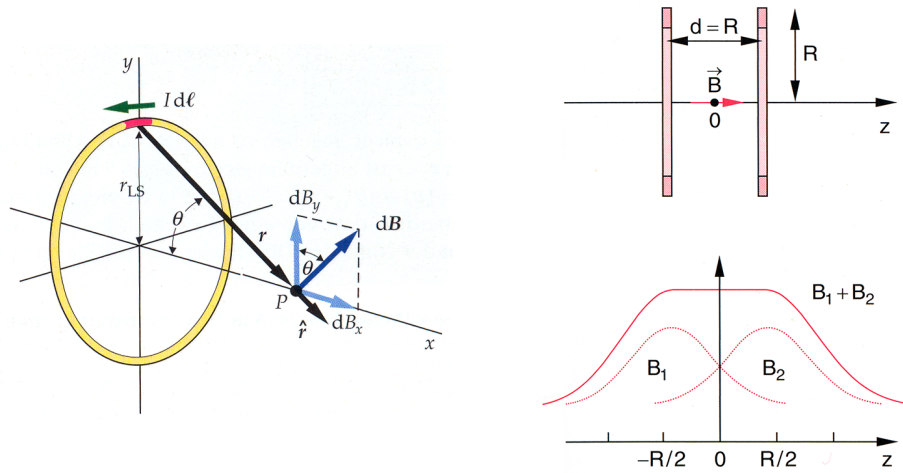


Figure 2.10: Geometry for the calculation of the magnetic field of a single round turn coil according to the Biot Savart law [57] (left). Helmholtz geometry of two coils and the produced homogeneous magnetic field by superposition of the two coils [58]. (right)

In order to keep the gyration center of the beam on the optical axis of the beam tube, this deviation has to be compensated by the use of so-called correction coils. They consist of two pairs of saddle coils mounted on the bend perpendicular to each other as shown in figure 2.9. Due to their geometry they produce in total two independent magnetic fields, each perpendicular to the solenoid. By superposition with the solenoidal field, the beam can be adjusted in any direction. Thus, it is possible to compensate the unwanted deviations of the curvature drift. A further problem is the earth's magnetic field of about $10 \mu\text{T}$. This can also be corrected by mounting the correction coils onto the straight parts of the beamline.

In some cases it is not always possible to directly mount a solenoid onto the experimental set-up due to various experimental restrictions. In this case a different approach is feasible namely so-called Helmholtz coils. Here, two short coils of radius R are positioned in distance R to each other. The principle is shown in figure 2.10.

The resulting magnetic field is homogeneous over a very large region and can be calculated according to Biot-Savart's law [57]

$$d\vec{B} = \frac{\mu_0}{4\pi} \frac{I d\vec{l} \times \hat{r}}{r^2}. \quad (2.31)$$

The magnetic field originating from a uniform motion of a charged particle with velocity \vec{v} can be expressed by the current element $I d\vec{l}$ as shown in figure 2.10 (left). In equation 2.31 the magnetic field is given in one point of the conductor loop. Integration

provides the total magnetic field along the z-axis of a single loop

$$B(z) = \frac{\mu_0 \cdot I \cdot R^2}{2(z^2 + R^2)^{\frac{3}{2}}}. \quad (2.32)$$

For the calculation of the magnetic field on the z-axis, the absolute zero is positioned exactly in the middle of the two coils. The resulting field produced by superposition of the magnetic fields B_1 and B_2 of the single coils is homogeneous over a very large region in between and is calculated as follows.

$$B_{\text{Helm}}(z) = B_1 \left(z + \frac{d}{2} \right) + B_2 \left(z - \frac{d}{2} \right) \quad (2.33)$$

Inserting equation 2.32, the total field results in

$$B_{\text{Helm}}(z) = \frac{\mu_0 I R^2}{2} \cdot \left[\frac{1}{\left(\left(z + \frac{d}{2} \right)^2 + R^2 \right)^{\frac{3}{2}}} + \frac{1}{\left(\left(z - \frac{d}{2} \right)^2 + R^2 \right)^{\frac{3}{2}}} \right]. \quad (2.34)$$

In a Taylor expansion of the magnetic field all odd terms can be set to zero due to symmetry reasons. The result can be written as

$$B_{\text{Helm}}(z) = \frac{\mu_0 I R^2}{\left(\left(\frac{d}{2} \right)^2 + R^2 \right)^{\frac{3}{2}}} \cdot \left[1 + \frac{3}{2} \frac{d^2 - R^2}{\left(\frac{d^2}{4} + R^2 \right)^2} z^2 + \mathcal{O}(z^3) \right]. \quad (2.35)$$

Inserting the Helmholtz condition $d = R$ also the second term vanishes and the field around $z = 0$ can be approximated as constant

$$B_{\text{Helm}}(z = 0) = \frac{8}{\sqrt{125}} \frac{\mu_0 I}{R}. \quad (2.36)$$

If homogeneous fields are needed over larger distances of the experimental set-up, the Helmholtz structure shown in figure 2.10 (right) also in combination with solenoids is suitable for guiding the positrons in fields with minor distortions influencing the motion of the beam.

2.3.3 Focusing of Charged Particles in Electromagnetic Fields

Generally spoken, the focusing of charged particles follows the same principles as light optics where a dispersive element of a suitable refractive index creates a focus. In the

case of charged particles, this task can be fulfilled by electrostatic and magnetic fields. Within this chapter the fundamental ideas of both electrostatic and magnetic lenses will be given. Hereby, the focus is laid on the former since it will be of greater importance in the experimental set-up. Detailed information can be found in [51–53, 59].

Electrostatic Beam Focusing

Dependent on the charge of the particles and the sign of the applied potentials, particle beams can be accelerated or decelerated. In addition to this velocity change, due to electrostatic gradients formed by the lens systems, the trajectory of the particles can be affected as well.

In figure 2.11(a) a simple geometry of an electrostatic lens is shown. It consists of two cylinder shaped electrodes of different electrostatic potentials Φ separated by a certain distance. Dependent on the applied potentials of the first and second electrodes and with respect to the energy and direction of the beam, the system acts as decelerate-

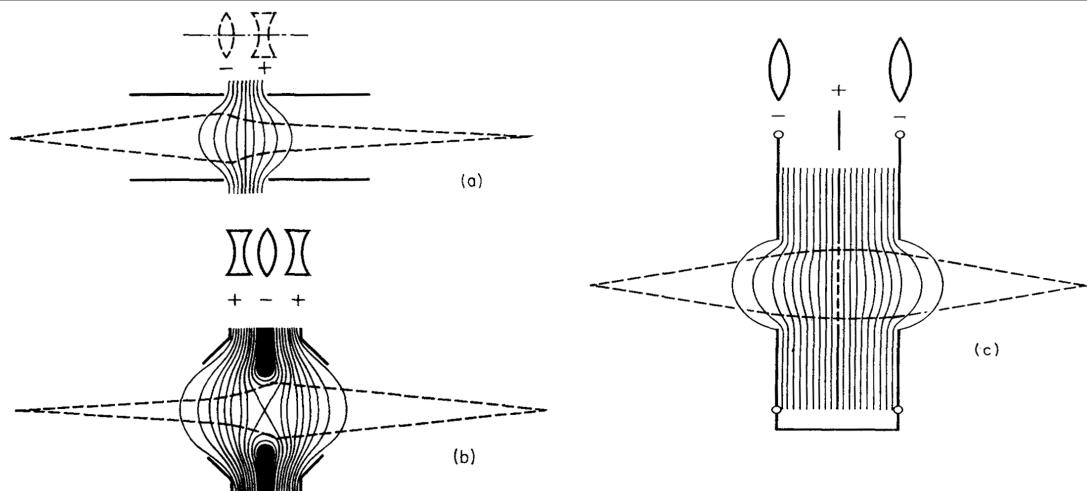


Figure 2.11: Excerpt of some electrostatic lens system designs taken from Grivet [52]. In (a), the easiest set-up of an electrostatic lens is shown. A particle beam passes through a gap of two tubes with different applied potentials creating an electrostatic gradient which alters the velocity and the trajectory of the particles. The analogue in light optics is shown above and consists of a doublet with one convex and one concave lens, creating a focus of the particle beam. In (b) and (c) two so-called einzel lenses, also called unipotential lenses, are shown with its optical counter part. They consist of three optical lens parts of which the first and the last one are put to the same potential whereas the middle one is altered resulting in a focusing unit.

accelerate system for electrons. Its optical analogue is sketched on top of figure 2.11(a) and consists of a focusing and a defocusing lens, respectively, building up a focusing system. Not shown is the case of an accelerate-decelerate system with an opposite sign of the potentials. In both cases the beam follows the tube axis z with the focal length f_i of the rotational symmetric system which can be calculated according to Hawkes and Caspers [51]

$$\frac{1}{f_i} = \frac{3}{16} \left| \frac{\Phi_a}{\Phi_b} \right|^{1/4} \int \left(\frac{\Phi'(z)}{\Phi(z)} \right)^2 dz. \quad (2.37)$$

Along the z -axis the electric potential Φ changes from the potential of the first lens Φ_a to that of the second lens Φ_b and thus creates an electrostatic potential gradient responsible for the focusing characteristics if $\Phi(z)$ and its derivative $\Phi'(z)$ is known.

In the case of equal potentials, the focal length f_i approaches infinity, meaning that the trajectories and energies of the particles is unaltered. The focal length on the object side can be obtained by an exchange of Φ_a and Φ_b . As the determination of the potential $\Phi(z)$ along the z -axis of such lens systems is not trivial in reality, the electric fields and the corresponding particle trajectories are mostly calculated numerically within special computer simulation software. Here, also the electrostatic fields of difficult electrode geometries and their combinations can be simulated to design complicated beam systems. However in the simple case of two similar rotational symmetric cylindrical electrodes separated by a distance S much smaller than their radii R , the potential $\Phi(z)$ results in [60, 61]

$$\Phi(z) = \frac{\Phi_a + \Phi_b}{2} \left(1 + \frac{1 - \gamma}{1 + \gamma} \tanh \left(\frac{\omega z}{R} \right) \right). \quad (2.38)$$

Within this formula, γ and ω is given by the following expressions with the zero-order Bessel function I_0

$$\gamma = \left| \frac{\Phi_a}{\Phi_b} \right| \quad \text{and} \quad \omega = \frac{1}{\pi} \int_{-\infty}^{+\infty} \frac{dt}{I_0(t)} = 1.318. \quad (2.39)$$

Unfortunately, in real lens systems small gaps between the tubes are unavoidable due to electrical isolation in between. Hence, these gaps, much smaller than the radius of the lenses, have to be taken into account. Assuming a gap distance S , the potential $\Phi(z)$ can be stated as [51]

$$\Phi(z) = \frac{\Phi_a + \Phi_b}{2} \left(1 + \frac{1 - \gamma}{1 + \gamma} \frac{R}{\omega S} \ln \frac{\cosh \left(\frac{\omega}{R} (z + S/2) \right)}{\cosh \left(\frac{\omega}{R} (z - S/2) \right)} \right). \quad (2.40)$$

However, for the configuration of an instrument the knowledge of the focus length of the lens systems alone is not sufficient, especially when adapting different instrument geometries to the lens systems or vice versa. Moreover, in some special cases, the distance of the last lens to the position of the minimal focus of a beam is fixed. Therefore, besides the focus length, the so-called mid-focal lengths z_{f_0} and z_{f_i} , measured from a reference plane z_0 , usually a plane of reflection symmetry, can be calculated according to

$$z_{f_0} = z_0 - \left(\frac{\Phi_b}{\Phi_a} \right)^{1/4} f_0 \quad (2.41)$$

$$z_{f_i} = z_0 - \left(\frac{\Phi_a}{\Phi_b} \right)^{1/4} f_i \quad (2.42)$$

with respect to z_0 , if f_0 and f_i are known [61].

Magnetic Lenses

An alternative to electrostatic lens systems is the use of magnetic fields to focus particle beams. Despite the existence of various lens system designs, this chapter will only deal with magnetic lenses chosen for the practical application in this thesis. In figure 2.12 the principle of such a magnetic lens system is depicted.

Similar to the electrostatic einzel lens, a field gradient with axial symmetry is needed to obtain a focusing effect. In most cases this is realized by feeding a direct current through a short coil resulting in a non-uniform magnetic field. A particle that passes this field will thus experience the Lorentz force which influences both velocity and direction of the particle. Thereby, the direction of the force is always perpendicular to the particle velocity \vec{v} and the magnetic field \vec{B} whereas in z-direction no force is acting on the particle implying that the speed of the particle is kept constant at all times. The magnetic force acting on the particles is calculated according to

$$F = e \vec{v} \cdot \vec{B} \sin(\varepsilon(x)) \quad (2.43)$$

with $\varepsilon(x)$ as the instantaneous angle between \vec{v} and \vec{B} at the location of the particle on its path. As $|\vec{v}|$ is constant throughout the coil and $|\vec{B}|$ is changing continuously, also $|\vec{F}|$ is changed along the trajectory resulting in the focusing characteristic [62].

However, for non-axial particle beams these assumptions are not valid any more. Instead, the trajectories of the particles have to be determined by the more general equation 2.10 for the Lorentz force and by introducing cylinder coordinates assuming a rotational

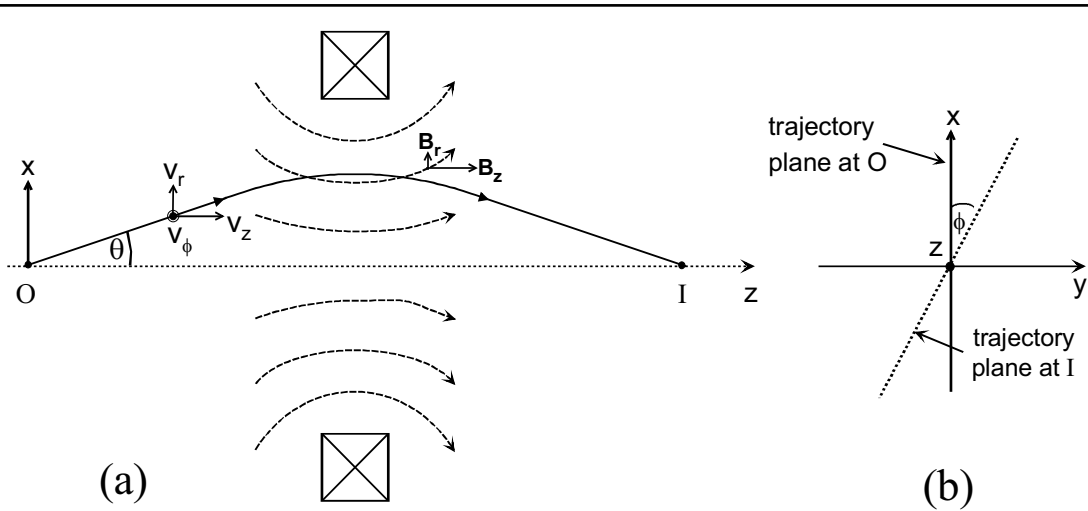


Figure 2.12: Principle of a simple magnetic lens. (a) A short radial symmetric coil produces the magnetic flux lines shown as dashed curves in the cross sectional view. In this case the trajectory of an electron starting from the axial object point 'O' is displayed when it is traveling through the coil geometry to its equivalent point 'I'. (b) According to a gyration motion along the z-axis the object and the imaging plane is tilted by an angle ϕ [62].

symmetric magnetic field generated by the coil. The force acting on the particle given in equation 2.43 can then be obtained in dependence on the tangential, radial and axial components of the magnetic field

$$F_\phi = -q(v_z B_r) + q(B_z v_r) \quad (2.44)$$

$$F_r = -q(v_\phi B_z) \quad (2.45)$$

$$F_z = q(v_\phi B_r) \quad (2.46)$$

with the radial distance r from the z-axis and the azimuthal angle ϕ representing the direction of the radial vector \vec{r} relative to the plane of the initial trajectory [62].

As a result of the above considerations, the uniform field produced by a long solenoidal lens can focus particles originating from a point source rather than a broad particle beam as only the fringing field at either end of the coil possess a focusing ability. Therefore, instead of using long coils it is advantageous to decrease the field as far as possible. This can be realized by the introduction of ferromagnetic pole pieces made of, e.g., soft iron partially housing the current carrying coil. The set-up is shown in figure 2.13.

The high permeability of the soft iron carries most of the flux lines to the gap of the

enclosure where they appear within the internal bore of the lens as shown in figure 2.13(a). The introduction of additional pole pieces leads to an increased concentration of the flux due to a reduced diameter of the lens to the optical axis. Moreover, it is possible to produce ultra high vacuum (UHV) systems by the application of flux carrying pole pieces. Hereby, the field generating coil is placed on the air-side of the instrument while the pole pieces transferring the magnetic field to the UHV side without breaking the vacuum. This enables an easier cooling of the current carrying coils.

By the use of ferromagnetic pole pieces, small focusing fields in the region of mm along the optical axis can be obtained. In this case, a thin lens approximation can be applied. Thus, the focusing power, the reciprocal of the focal length f_i , can be obtained as [62]

$$\frac{1}{f_i} = \frac{e^2}{8 m E_0} \int B_z^2 dz \quad (2.47)$$

where E_0 is the kinetic energy of the particle passing through the lens and B_z the z-component of the magnetic field. Due to its non-uniformity, the magnetic field is a function of z and is moreover, dependent on the current, the number of windings of the solenoid and the pole piece geometry. The focal point of the particles can thereby be adjusted by altering the current of the lens without influencing the particles' velocities. Note, however, that a stable lens current is required to avoid unwanted focusing shifts [62].

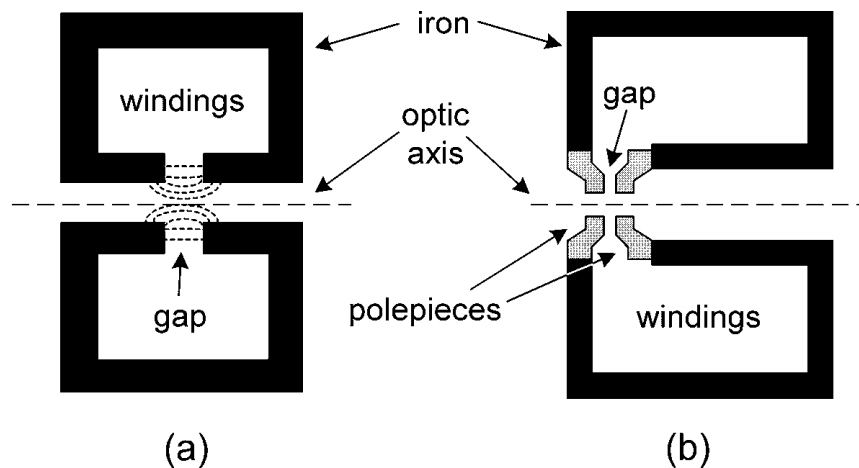


Figure 2.13: (a) Solenoidal coil enclosed with a ferromagnetic material such as soft iron concentrating the magnetic field within a small volume inbetween a gap of the housing. (b) Additional ferromagnetic polepieces further concentrate the field on the optical axis [62].

Aberrations of Electromagnetic Lenses

As in light optics also charged particle beams are influenced by aberration effects reducing the spatial resolution of the image under ideal conditions. Most common are chromatic aberrations due to velocity deviations of the particles and spherical aberrations stemming from particles at large distances from the optical axis. Both effects lead to a blurred image affecting even particles which trajectories lie on the optical axis.

The cardinal elements shown in figure 2.14 for ideal optical systems can be calculated according to Hawkes for ideal Gaussian beams [51].

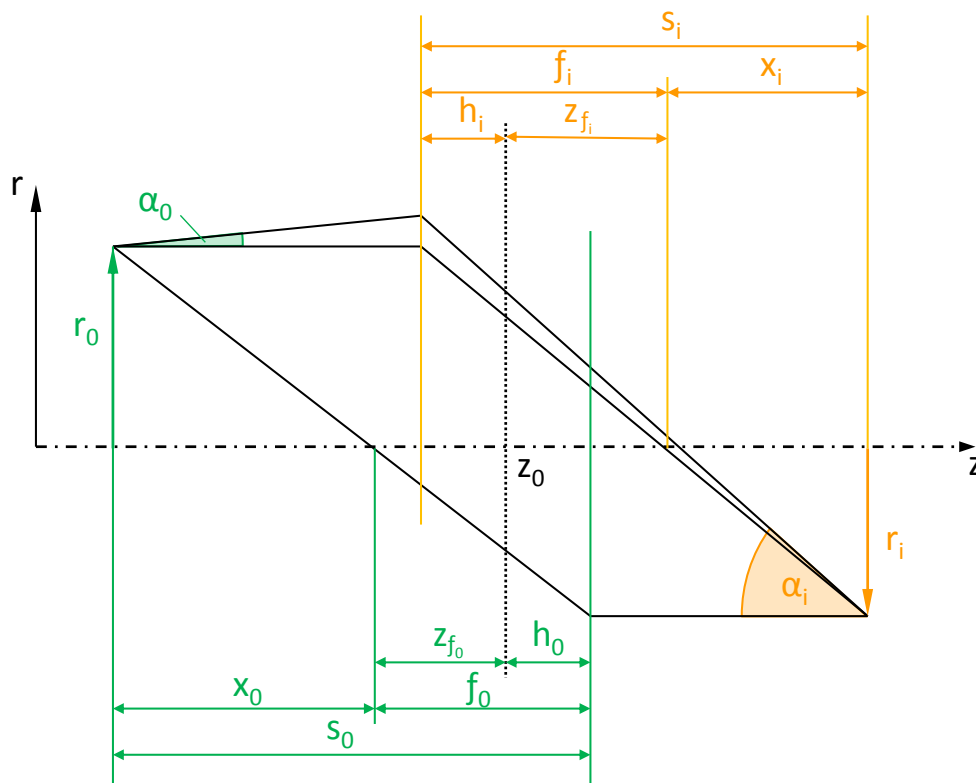


Figure 2.14: Cardinal elements describing focusing imaging lenses. An object of size r_0 is imaged by a lens system with reference plane z_0 to an image of size r_i . The two principal planes are in distances of h_0 and h_i of the reference plane. Object and image distance are defined as s_0 and s_i , respectively. For the object and imaging side the focal lengths given by f_0 and f_i as well as the aperture angles α_0 , α_i , and the mid focal lengths z_{f_0} and z_{f_i} .

$$\text{Lens equation:} \quad \frac{f_0}{s_0} + \frac{f_i}{s_i} = 1 \quad (2.48)$$

$$\text{Newton's lens equation:} \quad x_0 x_i = f_0 f_i \quad (2.49)$$

$$\text{Magnification:} \quad M = \frac{r_i}{r_0} = \frac{f_0}{f_i} \frac{s_i}{s_0} \quad (2.50)$$

$$\text{Angular magnification:} \quad M_\alpha = \frac{\alpha_i}{\alpha_0} = \frac{1}{M} \frac{f_i}{f_0} \quad (2.51)$$

Larger particle beams in which the single particles are further away from the optical axis are much stronger refracted than those close to the optical axis. This behaviour results in a blurring of the image due to a reduction in the focal length producing a different image spot for those particles. The blurred image spot is caused by higher order terms neglected in the paraxial approximation and the spot radius r_b can be calculated assuming a spot image of the object and a round rotational symmetric lens [51].

$$r_b = C_s \alpha_i^3 \quad (2.52)$$

where C_s is called spherical aberration coefficient and α_i the above introduced aperture angle at the image side. As shown in figure 2.15 (left), in the case of spherical aberrations there is another plane in front of the Gaussian image plane with smaller beam diameter than on all other planes. The plane with the smallest beam spot is called disk of least confusion. The radius of the disk of least confusion r_s can be calculated according to

$$r_s = \frac{1}{4} C_s \alpha_i^3. \quad (2.53)$$

The result is a disk with radius r_s four times smaller than r_b with its position between the focal plane and the Gaussian image plane. The distance of the least confusion plane is located at $0.75 \cdot f_i s_i$ from the principal plane h_i using the cardinal elements from figure 2.14 [51].

Chromatic aberrations stem from the fact that the focal length of a real lens system is dependent on the kinetic energy of the particles. Even a mono-energetic beam with finite bandwidth exhibits a velocity range sufficient to cause chromatic aberrations. As shown in figure 2.15 (right), a beam leaving the axis under the same angle gets diffracted differently at the lens system in dependence on the velocities of the particles. This leads, as in the case of spherical aberrations, to a blurring of the image which focal spot size with radius r_c can be calculated according to [51]

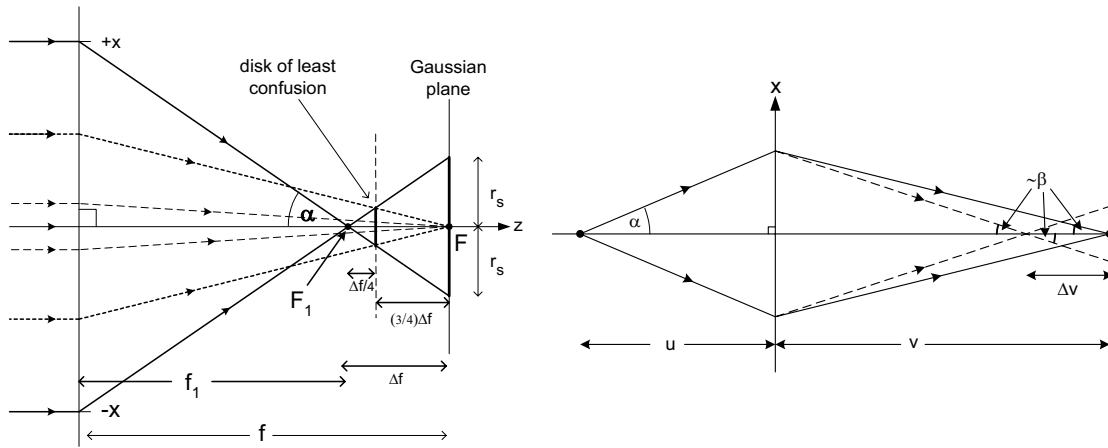


Figure 2.15: Influence on the minimal achievable particle focus due to spherical (left) and chromatic aberrations (right). Parallel particle trajectories with a larger distance from the optical axis experience a higher refraction due to larger field gradients at the outer borders of the lenses resulting in different focus points compared to trajectories near the optical axis result in spherical aberration. In contrast, chromatic aberration is caused when particles with different velocities pass the lens system resulting in different focusing points due to a velocity-dependent diffraction as shown on the right side [52].

$$r_c = C_c \frac{\Delta E}{E} \alpha_i. \quad (2.54)$$

Within this equation, ΔE defines the energy spread of a particle beam with kinetic energy E . The aberration coefficients C_c and C_s can be looked up in tables or are calculated numerically [63].

Minimum Achievable Beam Diameter

In most of all instruments using particle beams for imaging, it is advantageous to have a well-focused beam spot of minimal diameter for highest resolution. The minimum radius of the spot can be calculated by combining the equations for the magnification and angular magnification 2.50 and 2.51. The resulting spot size for an aberration free lens is calculated to

$$r_i = r_0 \cdot \frac{f_i}{f_0} \frac{\alpha_0}{\alpha_i}. \quad (2.55)$$

When using thin lenses, the object focus length f_0 and the image focus length f_i can

be assumed equal which simplifies the equation to

$$r_i = r_0 \cdot \frac{\alpha_0}{\alpha_i}. \quad (2.56)$$

In this formula, only the divergence angle α_0 is needed to solve the equation. It can be approximated with the longitudinal and transverse particle momentum p_{\parallel} and p_{\perp} , respectively. Using small-angle approximation one obtains

$$\tan(\alpha_0) = \frac{p_{\perp}}{p_{\parallel}} \approx \alpha_0. \quad (2.57)$$

Replacing the momentum with the longitudinal and transverse kinetic energy of the beam E_{\parallel} and E_{\perp} , respectively, and inserting it in formula 2.56, the minimum radius of the beam spot results in

$$r_i = r_0 \cdot \frac{1}{\alpha_i} \sqrt{\frac{E_{\perp}}{E_{\parallel}}}. \quad (2.58)$$

This result is the minimal achievable beam diameter for an aberration-free optical system. Taking into account the blurring by spherical and chromatic aberrations the final minimal beam spot r_{\min} can be calculated by summing up all forms for r_i since these contributions are independent of each other.

$$r_{\min}^2 = r_i^2 + r_s^2 + r_c^2 = \frac{E_{\perp}}{E} \left(\frac{r_0}{\alpha_i} \right)^2 + \frac{1}{16} C_s^2 \alpha_i^6 + C_c^2 \alpha_i^2 \left(\frac{\Delta E}{E} \right)^2 \quad (2.59)$$

As shown within this formula, the aberration coefficients are independent of the starting beam diameter and therefore for the same lens system different beam characteristics r_{\min} can be calculated when the coefficients C_s and C_c are known.

2.4 Brightness Enhancement of Positron Beams

In particle physics, a typical figure of merit for describing the quality of a beam is the so-called brightness. In general, the brightness of a beam is already defined by the particle emitting source and hence the minimal achievable diameter when introducing lens systems for beam focusing. Therefore, for a further reduction of the beam spot, techniques for enhancing the brightness have to be used. In positron physics this was first proposed by Mills in 1980 [64] and later discussed by Canter and Mills in 1982 [65]. In the following section the principle of brightness enhancement for achieving beam

spot diameters in the μm range will be explained as well as some useful quantities to characterize charged particle beams.

2.4.1 Definition of the Brightness

A common definition of the brightness B of an ensemble of particles can be found in literature. Proposed by A.P. Mills [64], for non-relativistic positron beams B is calculated according to

$$B = \frac{I}{\alpha^2 d^2 E} \quad (2.60)$$

with I standing for the beam intensity in number of particles per second, α the divergence angle of the particle beam, d the beam diameter and E the beam energy. Assuming a small divergence angle, small angle approximation can be employed and α can be written in dependence on the transverse and parallel components of the particle's momentum.

$$\alpha = \tan(p_{\perp}/p_{\parallel}) \approx p_{\perp}/p_{\parallel} \quad (2.61)$$

Thus, equation 2.60 can be re-written as

$$B = \frac{2m_e I}{d^2 p_{\perp}^2}. \quad (2.62)$$

2.4.2 Liouville's Theorem

For a full beam characterization not only its intensity I is needed but also its occupied phase space volume (PSV) Ω_{xyz} . The phase space density (PSD) obeys Liouville's theorem which states that the PSV of a beam occupied by an ensemble of non-interacting particles is constant under the influence of conservative forces [4]. This implies that the minimal achievable beam diameter is already determined by the properties of the source as it defines the inherent size of the occupied PSV.

In general, an n -dimensional PSV can be calculated using the general form of the volume of a n -dimensional ellipsoid [66]

$$V_n = \frac{2}{n} \frac{\pi^{n/2}}{\Gamma(n/2)} (a_1 \cdot a_2 \cdot a_3 \dots a_n) \quad (2.63)$$

where $a_1 \dots a_n$ represent the semi-axes and Γ denotes the gamma function.

For a given source, the PSV Ω_{xyz} can be split up into three components in Cartesian coordinates:

$$\text{Transverse phase space volume in x:} \quad \Omega_x = \pi \Delta x \cdot \Delta p_x \quad (2.64)$$

$$\text{Transverse phase space volume in y:} \quad \Omega_y = \pi \Delta y \cdot \Delta p_y \quad (2.65)$$

$$\text{Longitudinal phase space volume in z:} \quad \Omega_z = \pi \Delta z \cdot \Delta p_z \quad (2.66)$$

These three equations for the PSV represent areas of ellipses with lengths of the semi axes Δx , Δp_x , Δy , Δp_y and Δz , Δp_z , respectively. According to equation 2.63, Ω_{xyz} can be calculated as

$$\Omega_{xyz} = \frac{1}{6} \pi^3 \Delta x \cdot \Delta p_x \cdot \Delta y \cdot \Delta p_y \cdot \Delta z \cdot \Delta p_z = \frac{1}{6} \Omega_x \cdot \Omega_y \cdot \Omega_z. \quad (2.67)$$

Among them, especially the longitudinal component is of interest as constituent elements (z, p_z) are related to a time and energy spread, respectively, and are responsible for, e.g., chromatic aberrations.

Ω_{xyz} can be subdivided into two parts, the longitudinal PSV Ω_z and the transverse PSV Ω_{xy} . Hereby, the constituents (z, p_z) of the former are related to a time and energy spread, respectively, and are responsible for, e.g., chromatic aberrations. The latter can be calculated according to the volume of a four dimensional ellipsoid.

$$\Omega_{xy} = \frac{1}{4} \Omega_x \cdot \Omega_y = \frac{1}{4} \pi^2 \Delta x \cdot \Delta p_x \cdot \Delta y \cdot \Delta p_y \quad (2.68)$$

With the radius change of a certain beam $\Delta r = \sqrt{\Delta x^2 + \Delta y^2}$ and the transverse momentum expressed according to $\Delta p_{\perp} = \sqrt{\Delta p_x^2 + \Delta p_y^2}$ the above formula can be re-written as

$$\Omega_{xy} = \frac{1}{4} \pi^2 \Delta r^2 \cdot \Delta p_{\perp}^2 = \Omega_{\perp}. \quad (2.69)$$

By inserting the formula for the brightness (formula 2.60) the transverse PSV can be expressed as

$$\Omega_{\perp} = \frac{\pi^2 m_e I}{2 B}. \quad (2.70)$$

In summary, the transverse PSV is directly proportional to the intensity of a beam and inversely proportional to its brightness. According to Liouville, the occupied PSV stays

constant under the influence of conservative forces. Therefore, non-conservative forces are needed to reduce the transverse PSV and thus achieve small beam spot diameters. Arising from equation 2.70, the transverse PSV can be reduced by either reducing the beam intensity I or enhancing the brightness B . As the intensity of positron sources can not be increased as in the case of an electron gun, the brightness has to be enhanced. Two methods are used in particle physics. The first one uses multiple apertures, i.e., collimators which filter particles of high transverse momentum. Thus, the beam can be effectively focused due to a reduced transverse phase space. However, this method leads to an unwanted loss in intensity. Finally, a suitable alternative for the creation of positron microbeams is the so-called re-moderation taking the advantage of non-conservative forces. The method will be explained in full detail in the next section.

2.4.3 Re-moderation of Positrons

In electron microscopy, a very versatile tool for reducing the phase space and thus achieving small beam diameters are apertures and collimators. Due to high electron fluxes the disadvantage of an intensity loss can be neglected. Typical reflection high-energy electron diffraction (RHEED) systems can deliver beam currents of a few 100 μA equal to e^- -intensities of 10^{15} /s which are six orders of magnitude higher than the intensity of NEPOMUC (Data sheet by Createc [67]). The intensity of such electron guns can be increased by increasing the current through the filament. Unfortunately, positron sources provide less intensity than their electron counterpart. In the case of NEPOMUC the reactor power is limited. Hence, intensity losses due to apertures have to be avoided and their usage is not feasible. Instead, Liouville's theorem opens up a superior method to overcome this restriction: The re-moderation. With this method dissipative forces are used for enhancing the phase space density and as a consequence the brightness of a positron beam. The fundamental principle behind this technique was first proposed by Mills [64] and is shown in figure 2.16.

As a beam occupies a certain PSV propagating in real space, the shape of its PSV is altered due to its transverse momentum. Upon getting focused on a material of negative positron work function, a moderator, the beam spot is reduced in space which, according to Liouville, leads to an increase in transverse momentum. After being accelerated and implanted into the solid, the positrons thermalize (see section 2.1.3) and thus lose their energy by inelastic scattering until thermal equilibrium is reached. After re-emission from the moderator material, the beam can be regarded as a new positron source smaller in size and PSV. Even with an intensity loss due to the re-moderation efficiency of up to around 33 % (s. table 2.3) the brightness of a beam can be enhanced by multiple orders. For the NEPOMUC primary and re-moderated beam in addition to

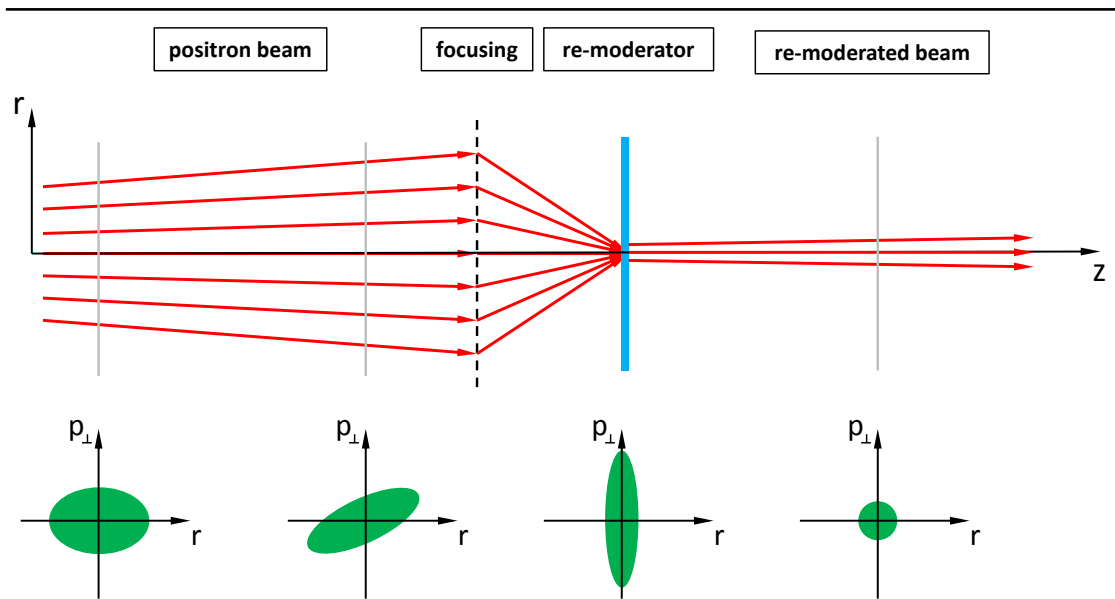


Figure 2.16: Fundamental principle of re-moderation of positron beams. The positron trajectories, the influence of the focusing and the re-moderation process on the phase space is shown. A positron beam can be defined by its radius and transverse momentum. The propagation of the unperturbed beam leads to a distortion. In this case an increase in the radius and rotation of the elliptical occupied phase space volume. Due to focusing onto the re-moderator, the transverse momentum is increased whereas the beam diameter reaches its minimum. After re-moderation, the re-emitted positrons have lost nearly all of their transverse momentum resulting in a reduced phase space.

the CDBS *upgrade* microbeam, the brightness for each enhancement step is calculated according to formula 2.62 and given in table 2.4.

Beam diameters in the μm range can be created by repeating this procedure. Although, depending on the efficiency of the moderation process of about 20 %, a loss in intensity and due to the implantation energy onto the re-moderator, a reduction in beam energy have to be noted.

This process of re-moderation can be performed in reflection and transmission geometry as depicted in figure 2.17 with each having benefits and disadvantages. In reflection geometry, thicker crystals can be used and their annealing and surface cleaning is easier as they can be mounted from the back side. The beam guidance, in contrast, is more challenging because the incident and outgoing positron beams have to be separated by different electrostatic and magnetic fields. Nevertheless, this principle is realized as a first re-moderation stage at NEPOMUC containing a W(100) single crystal [18]. An easier beam guidance can be realized in transmission geometry since the incident and

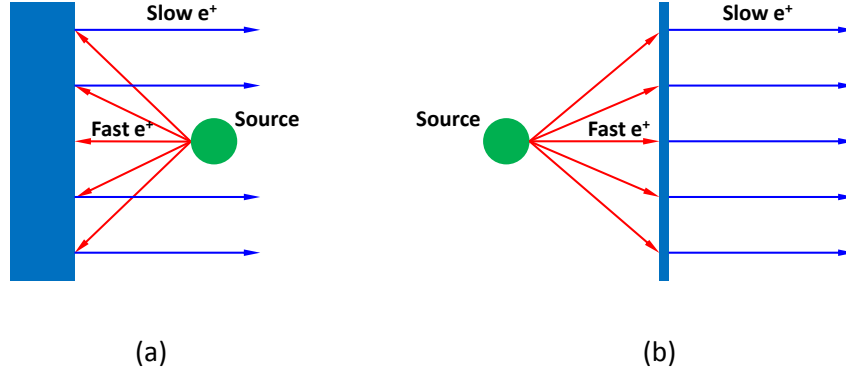


Figure 2.17: Principles of the two mostly used moderation geometries: (a) the moderation in reflection geometry and (b) in transmission geometry. In the first case positrons are emitted at the same side as they are implanted into the moderation material whereas with the second method, they are emitted at the opposite side. More moderation geometries can be found in [24].

outgoing beams are already separated. But very thin foils, in the range of 100 nm, have to be used to guarantee that the implanted positrons can reach, within their diffusion length, the opposite side of the moderation material and can be re-emitted.

	NEPOMUC		CDBS upgrade
	Primary	Re-moderated	Microbeam
Y_{mod}^+ (s ⁻¹)	9.0×10^8	4.5×10^7	4.3×10^6
$E_{\perp,FWHM}$ (eV)	50	1	0.025
d_{FWHM} (mm)	7	2	0.5
B ((mm ² eV s) ⁻¹)	3.7×10^5	1.1×10^7	6.9×10^9

Table 2.4: Brightness enhancement at NEPOMUC. For each beam provided by NEPOMUC and for the CDBS *upgrade*, the corresponding beam parameter, the intensity Y_{mod}^+ , the transverse energy $E_{\perp,FWHM}$, the diameter d_{FWHM} and the calculated brightness B is given. For the CDBS *upgrade* microbeam a transverse energy according to the thermal smearing of the re-emitted positrons is assumed. The NEPOMUC values are taken from [17]. When emitted by the Ni re-moderation foil, a high-brightness positron beam with a diameter of 0.5 mm could be achieved. Despite a reduced count rate due to the moderation efficiency of 19.1% as given in table 4.1, the brightness could be increased by about two orders of magnitude.

3

Doppler Broadening Spectroscopy of the Positron Annihilation Line

3.1 Positron as Probe for Open Volume Defects

Positrons can be used as highly mobile probe for the detection of missing atomic cores, i.e., vacancies and other kinds of open volume defects in crystals. In this regard, positron annihilation spectroscopy (PAS) is highly suitable for defect spectroscopy. Fundamentals of this process are content of various articles, reviews and textbooks, see e.g. [68, 69], and shall be outlined in this chapter.

After thermalization, positrons can diffuse through the solid (s. also section 2.1.3). During the diffusion, positrons can be trapped at defect sites such as vacancies, microcavities and other types of open volume defects. Since these defects form an attractive potential for the positively charged particle, positrons are likely to be trapped at the defect site within their diffusion length of a few 100 nm. Positrons can diffuse over multiple lattice sites before being trapped and are thus highly sensitive to vacancy concentrations in the range from 10^{-7} to 10^{-4} per atom [24]. At higher defect concentrations, all positrons are trapped in defects and no more variations are observed (saturation trapping). Despite the vividness of the classical model of a positron being trapped at a defect site, a quantum-mechanical trapping model is more suitable for a detailed explanation.

Within this model, the probability of trapping a positron in a mono-vacancy in Cu shall be discussed. In figure 3.1 (left), the 2D positron probability density $|\Psi_+(r)|^2$ is given for the case of an ideal Cu lattice (top) and in the presence of a Cu mono-vacancy (bottom). In a lattice without defects, a positron occupies a delocalized Bloch state and as shown in figure 3.1 (right) its corresponding probability function peaks between the atoms of the Cu lattice. If a mono-vacancy is generated by removing one atom of the lattice, the positron probability density $|\Psi_+(r)|^2$ is confined at the defect site. As the positron binding energy of a vacancy in metals of around 1 eV is orders of magnitudes

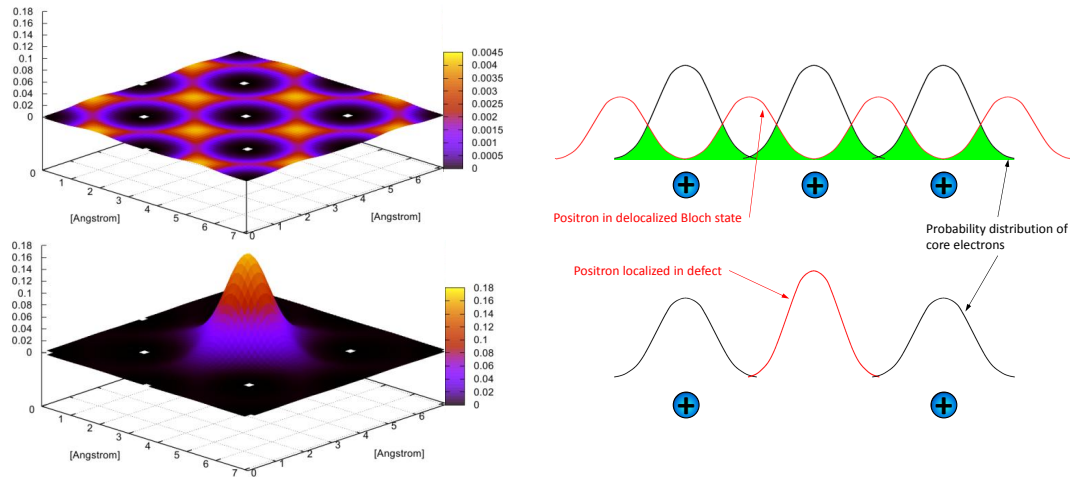


Figure 3.1: Left: Probability density of a positron simulated for a homogeneous Cu lattice (top) and for a vacancy in Cu (below). Image taken from [19]. Right: Sketch of a delocalized positron in a Bloch state and the probability distribution of the localized core electrons. The overlap between the wave functions of core electrons and positrons decreases if the positron is localized in a vacancy.

higher than the thermal energy of the positron in the bulk material, the positron cannot overcome this energy barrier and is efficiently trapped at the defect site.

Besides, the trapping model also describes positron trapping in any other kind of open volume defects and agglomerations of foreign atoms with higher affinities for positrons than the surrounding bulk material [70, 71].

Summarizing, positron trapping enables the investigation of different types of vacancy-like defects as well as their concentration and distribution using PAS. Within this work, the Doppler broadening of the annihilation radiation due to positron annihilation with surrounding electrons of different momenta is analyzed within the trapping model described e.g. in Hautojärvi et al. [72].

3.2 Principle of Doppler Broadening Spectroscopy

As introduced in section 2.1.3, positrons implanted in matter can get trapped and then annihilate with electrons under the emission of predominantly two γ -quanta [24]. In the center of mass system, shown in figure 3.2 (left), the two annihilating particles emit two γ -quanta in exactly opposite directions. In the case of an annihilating positron-electron pair, the released energy of this process equals twice the electron's rest mass

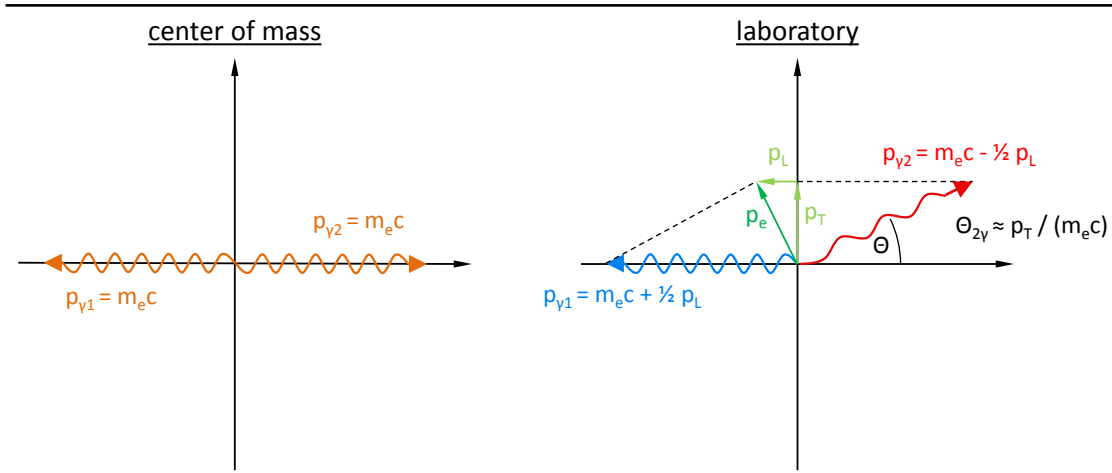


Figure 3.2: The Doppler effect at positron electron annihilation in the center of mass and laboratory system. Here, due to the momentum p of the annihilating pair, an angular deviation Θ and a Doppler shift of $\pm 1/2 p$ in the direction of emission can be observed.

of $E_{sum} = 2m_0c^2 = 1022 \text{ keV}$. This energy is equally distributed to both γ -quanta due to conservation of momentum and energy. As shown in figure 3.2 (right), this process can be transferred into the reference frame of the observer, in this case the laboratory system. Due to the conservation of momentum, the collinearity of the emitted γ -quanta is no longer valid. As the positron within the solid can be considered as thermalized, the total momentum is dominated by the momentum of the electron. Thus, the electron momentum p manifests itself in two observables: the deviation from the collinearity and the Doppler shift of the two emitted γ -quanta.

The transverse component can be measured within position sensitive (one or two dimensional) detectors in a so-called ACAR experiment [73, 74]. The direction of the γ -rays emission which differs from 180° by small angles of a few mrad directly enables the calculation of the electron momentum via $\theta \approx p_{\perp} / m_0c$. For high resolution experiments, rather large instruments have to be used for resolving the small angle deviations.

This work will focus on the observable longitudinal momentum component. As the positrons in the solid can be considered as thermalized and thus lead only to a small momentum contribution, the momentum of the annihilating pair is largely dominated by the electron. The longitudinal momentum p_{\parallel} is transferred to the two emitted γ -quanta causing a Doppler shift in direction of the annihilation radiation. This results in a positive and negative energy shift of $\Delta E = \frac{1}{2} p_{\parallel} c$ of the γ -quanta facing towards and away from the detector, respectively.

The fundamental principle behind Doppler broadening spectroscopy (DBS) with positrons, is the so-called Doppler effect, found in 1842 by Christian Doppler [75]. In general, a Doppler effect occurs if a source, emitting electromagnetic waves with a frequency of f_0 , has a certain velocity v_l either towards an observer (1) or away from him (2). These two cases can be calculated with the formulas for the relativistic longitudinal Doppler effect [76].

$$f_1 = f_0 \sqrt{\frac{1 + \beta}{1 - \beta}} \quad \text{and} \quad f_2 = f_0 \sqrt{\frac{1 - \beta}{1 + \beta}} \quad (3.1)$$

With $\beta = \frac{v}{c}$ these two equations can be rewritten as

$$f_1 = f_0 \sqrt{\frac{c + v_l}{c - v_l}} \quad \text{and} \quad f_2 = f_0 \sqrt{\frac{c - v_l}{c + v_l}}. \quad (3.2)$$

A source moving towards the observer with a longitudinal velocity of v_l results in a Doppler shift of the frequency which can be calculated as given in equation 3.2 (left), whereas the frequency of an escaping source can be calculated according to equation 3.2 (right). Furthermore, the transverse Doppler effect can be calculated for a transverse movement of the source with respect to the emission direction with a transverse velocity v_t .

$$f' = f_0 \cdot \sqrt{1 - \frac{v_t^2}{c^2}} \quad (3.3)$$

In case of observing the annihilation radiation of an electron positron pair, the frequency f_0 can be related to two unshifted 511 keV γ -quanta. As the positron is thermalized, only the longitudinal and transverse velocity component of the electron, v_l and v_t respectively, are responsible for transferring a momentum onto the two γ -quanta resulting in measurable shift of the 511 keV annihilation energy. For small longitudinal and transverse momenta of the electron and therefore small longitudinal and transverse velocity changes, the influence of the momentum can be determined by a first order Taylor approximation. In the longitudinal case one obtains

$$f_{1,2} = f_0 \pm \frac{f_0}{c} v_l + \mathcal{O}(v_l^2) \approx f_0 \left(1 \pm \frac{v_l}{c} \right). \quad (3.4)$$

The transverse contribution is calculated according to

$$f' = f_0 + \mathcal{O}(v_t^2) \approx f_0. \quad (3.5)$$

In the transverse case, the resulting frequency is approximately the unperturbed frequency as the second order term is $\frac{f_0 v_t^2}{2c^2}$. Due to $c^2 \gg v_t^2$, the transverse component can be neglected. In contrast, the longitudinal momentum case depends on a non-negligible transverse velocity in the approximation which results in a longitudinal Doppler shift. The longitudinal momentum can directly be expressed in terms of the energy difference of the emitted photons. The energy shift in the laboratory system can be calculated by multiplying the frequency with the Planck constant and by replacing the longitudinal velocity component by the corresponding momentum $p_l = 2m_0 v_l$.

$$E_{1,2} = \frac{1}{2} E_{sum} \left(1 \pm \frac{p_l}{2m_0 c} \right) \quad (3.6)$$

Here, E_{sum} stands for the rest energy $2m_0 c^2 - E_b$ with the binding energy E_b of the positron electron system which is usually negligible but can be of significance for strongly bound electrons in inner shells. By inserting $E_{sum} = 2m_0 c^2$ in equation 3.6 the energy of both γ -quanta can be calculated as

$$E_{1,2} = 511 \text{ keV} \pm \underbrace{\frac{c p_l}{2}}_{\Delta E} . \quad (3.7)$$

The second term is the longitudinal component of the energy shift ΔE and is added to or subtracted from the energy $E = 511 \text{ keV}$ of the two γ -quanta. This fraction can be calculated with the kinetic energy $E_{kin,e}$ of the electron which causes the longitudinal component of the Doppler effect. The non-relativistic ansatz for the kinetic energy can be made for the calculation as the velocity of the electrons is considered small.

$$E_{kin,e} = \frac{1}{2} m_0 v_l^2 \quad (3.8)$$

Multiplication with the rest mass m_0 reveals and inserting the longitudinal momentum $p_l = m_0 v_l$ gives

$$p_l = \sqrt{2m_0 E_{kin,e}} . \quad (3.9)$$

By multiplying with $\frac{c}{2}$, the longitudinal component of the energy shift ΔE is determined.

$$\Delta E \equiv \frac{p_l c}{2} = \sqrt{\frac{1}{2} m_0 c^2 E_{kin,e}} \quad (3.10)$$

With this formula the Doppler shift ΔE of the emitted γ -quanta is directly linked to the kinetic energy of the electron $E_{kin,e}$. For example an electron moving with a kinetic

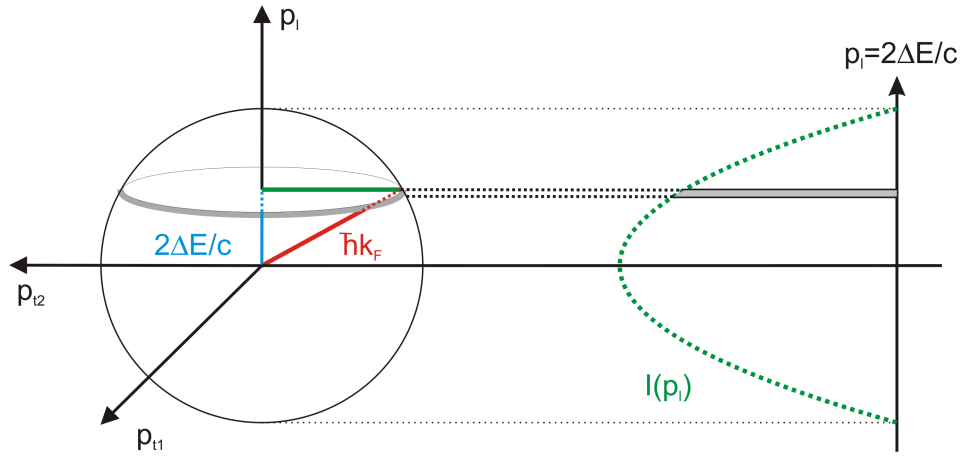


Figure 3.3: Momentum projection of the distribution of a free electron gas in the ground state at a temperature of 0 K onto the axis of the longitudinal momentum. The result of the projection is the intensity distribution $I(p_l)$. Image taken from [77]

energy of 10 eV causes a Doppler shift of 1.6 keV. This is in the measurement range of high purity germanium (HPGe) detectors which will be explained in section 3.3.

In figure 3.3, the relation between the Doppler shift ΔE of the γ -quanta and the electron momentum distribution is given for a free electron gas with the dispersion relation $E = \frac{\hbar^2 k^2}{2m}$ at $T = 0$ K. All states from $p = 0$ up to the Fermi momentum $p = \hbar k_F$ in the reciprocal space are occupied. The projection of the Fermi momentum onto the p_l -axis can then be obtained by calculating the volume of a disc perpendicular to the p_l -axis per each momentum interval Δp_l and thus results in a truncated inverted parabola of the form

$$I(p_l) \propto (\hbar k_F)^2 - p_l^2 \quad (3.11)$$

and is zero for $p_l > p_F$ [78].

The momentum distribution of a real material is then made up of two distributions: an inverted parabola up to $p_l = p_F$ which can be attributed to the valence electrons and a broader component at higher momenta attributed to the core electrons [72]. The shape of the latter can be calculated by a superposition of orbital electron wave functions [79].

3.3 High-Resolution γ -Detection

3.3.1 Working Principle of HPGe-Detectors

For measuring the broadening of the 511 keV annihilation line, which is in the range of a few keV, with sufficient accuracy, detectors with a suitable energy resolution are required. Moreover, a high efficiency is needed for detecting both emitted γ -quanta in coincidence with acceptable probability.

In general, a detector covers a certain volume which can be ionized by γ -quanta. Thus, the energy deposited in the detector material during the ionization process can be measured. This energy deposition can occur via the photo effect, the Compton effect and pair production. In CDB spectroscopy, the energy of the annihilation radiation which is to be detected is well below 1022 keV. Therefore, pair production can be neglected here. By contrast, energy deposition via the photo effect is of high interest as the full energy of the γ -quanta is deposited in the detector. Note that at a γ -energy of 511 keV, only 10% of the events can be ascribed to a pure photo effect while the rest occurs via combined Compton scattering and photo effect [80].

In total, a certain amount of charge carriers per γ -quanta is created in the detector which is directly linked to the energy resolution. Usually the resolution of the detector at a given energy E is defined as $\frac{\Delta E}{E}$ with ΔE as the full width at half maximum (FWHM). Assuming a Poisson statistic as it holds for independent ionization and excitation events, the variance is then given by

$$\sigma^2 = N \quad (3.12)$$

where N is the mean number of events produced at the given energy E . Indeed, the average energy w required for a single ionization event can be stated as being only dependent on the material. Thus, at fixed energy, the mean number of events N can be expressed as $N = \frac{E}{w}$. The resolution can then be calculated according to

$$R = \frac{\Delta E}{E} = \frac{w \Delta N}{w N} = \frac{\Delta N}{N} = 2.35 \frac{1}{\sqrt{N}}. \quad (3.13)$$

Hereby, the prefactor 2.35 stems from the relation between the FWHM and standard deviation of a distribution. Thus, the more charge carriers per γ -quanta are produced, the better the statistics resulting in a better energy resolution of the detector. [81].

Due to their high energy resolution, semiconductor detectors are mainly used for DBS. Among them, especially HPGe detectors are favoured due to their high Z and hence

high efficiency. Moreover, a small ionization energy of Ge of 2.96 eV guarantees a high number of created charge carriers per incoming γ -quanta. Hence, they provide the best energy resolution of $\approx 1.2 - 1.3$ keV at a γ -energy of 511 keV. [82, 83].

A semiconductor radiation detector is build up like a so-called PIN diode with an intrinsic (I) region between a positively (P) and negatively (N) doped contact. The intrinsic depletion zone is generated by applying a reverse bias voltage U to the N and P contact. Thereby, the width of the depletion zone is direct proportional to $\sqrt{U/n}$ with n as the impurity concentration of the crystal in the order of 10^9 atoms/cm³ [82]. For coaxial HPGe detectors as used in this work, bias voltages of up to 4.5 keV are supplied producing a depletion zone of several centimetres. However, one restriction has to be taken into account when using HPGe detectors. Since Ge has a small band gap of 0.7 eV, at room temperature thermal excitations are possible leading to a non-negligible leakage current if the high voltage bias is applied. To overcome this restriction, the Ge crystal has to be cooled with liquid nitrogen during operation.

3.3.2 Spectrum of Positron Annihilation Radiation

A spectrum of the positron annihilation radiation, acquired with a HPGe detector is shown in figure 3.4 (top). The entire energy spectrum depicts features typical for the detection of γ -radiation with a high energy resolution.

When working with positrons a pronounced Doppler broadened 511 keV photo peak is present which is evaluated in Doppler broadening spectroscopy. Taking into account the entire energy range, more features of the annihilation spectrum can be observed which are typical for the detection of γ -quanta. At small energies, the typical Compton continuum can be seen up to an energy of $E_{max,Comp} = 2/3m_0c^2$ of the energy of the photo peak, in this case 511 keV the annihilation radiation of positrons [81]. The upper limit of the Compton continuum is called Compton edge and can be found at 341 keV, the maximum energy a 511 keV γ -quantum can deposit by a single Compton scattering event in the detector. In the energy range between $E_{max,Comp}$ and m_0c^2 , the detection of γ -quanta stemming from multiple Compton scattering events in the detector and small angle scattering events in the is present additionally to the background. The so-called backscatter peak given at an energy of $m_0c^2 - E_{max,Comp} = 171$ keV is caused by γ -quanta that have Compton scattered in one of the surrounding materials before entering the detector. At around 90 keV the characteristic X-rays of the Pb shielding around of the detectors are visible. At energies larger than m_0c^2 , mostly pile up events arising from multiple simultaneously detected γ -quanta in the detector dominate the spectrum. In this regard, the pile up peak, occurring by the simultaneous detection of

two γ -quanta with an energy of m_0c^2 can be seen. Due to the channel limit of the acquiring hardware it is cropped at the right side.

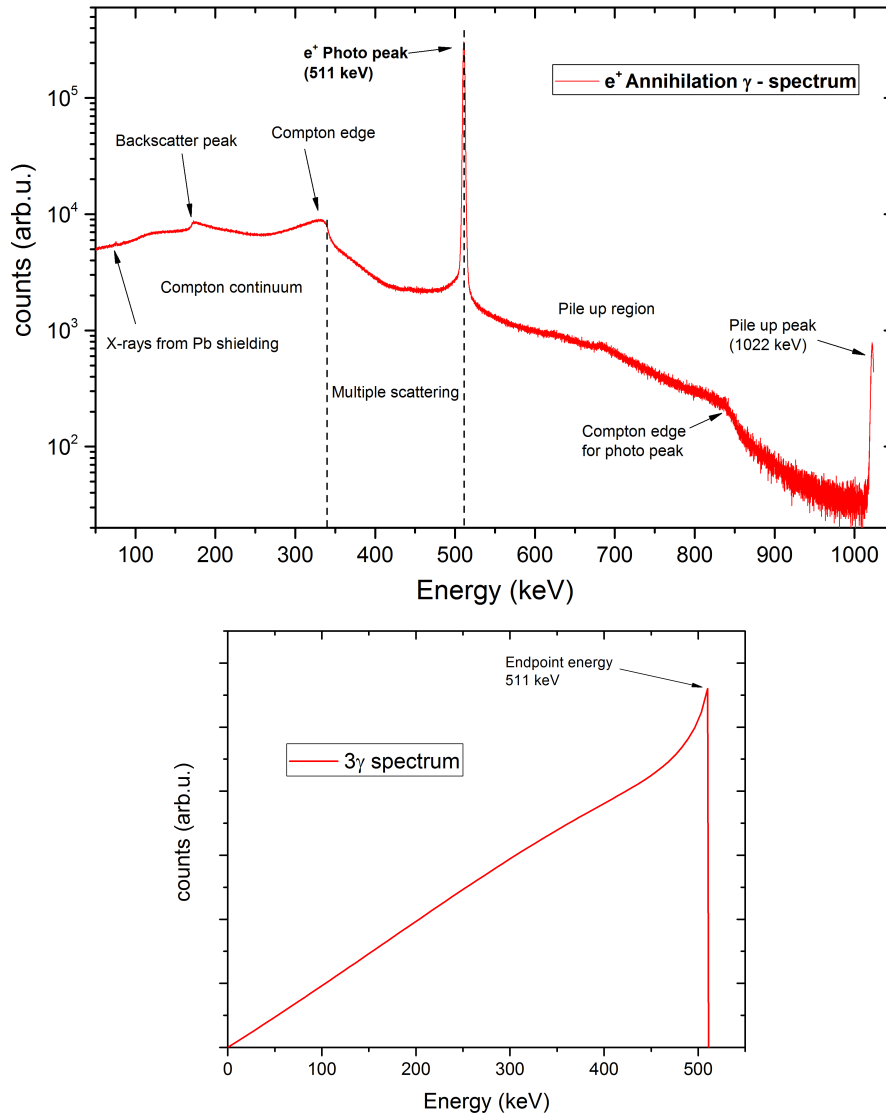


Figure 3.4: (top) Positron annihilation spectrum obtained from a Ni sample with typical features named. Of main interest in defect spectroscopy with positrons is the Doppler broadened photo peak at 511 keV. The left side of the spectrum is dominated by the Compton continuum up to a γ -energy of 341 keV. At the high energy side towards the right of the photo peak, so-called pile up events dominate which are caused by the simultaneous detection of multiple events. In this regard, the pile up peak at 1022 keV occurs from the simultaneous detection of two photo γ -quanta. (bottom) Scheme of the ortho-Ps annihilation spectrum. The spectrum was calculated according to Ore and Powell [84]. Typical for the three γ -decay is a continuous spectrum with the maximum endpoint energy of 511 keV in the case of positrons.

In addition to 2γ -annihilation events, 3γ -annihilation can occur either directly or via the decay of ortho-Ps. As shown in figure 3.4 (bottom), the corresponding spectrum is characterized by a continuum with the typical endpoint energy for positron annihilation of 511 keV. This three particle decay leads to a decrease of the 511 keV photo peak and a more pronounced shoulder at lower energies in the annihilation radiation spectrum in figure 3.4 (top).

3.4 Data Evaluation in PAS

Defect spectroscopy with positrons by using the technique of investigating the Doppler broadening of the annihilation radiation of the two emitted γ -quanta can be divided into two methods, DBS and CDBS. In the former, only one γ -quantum of the annihilation event is detected at a time by a detector. This mode is sensitive to the low energy Doppler shifted γ -quanta and thus, the concentration of defects in a material can be investigated. By comparison, the detection of both γ -quanta in coincidence significantly reduces the background and thus is sensitive to larger Doppler shifted events. Therefore, it is suitable to investigate the chemical surrounding of the annihilation site. Both methods, their observables and applications will be explained in detail in the following section.

3.4.1 Doppler Broadening Spectroscopy - DBS

In conventional DBS, the annihilation radiation of one of the two emitted γ -quanta is measured. Therefore, this measurement mode is also called "single mode". During annihilation, the momentum of involved electrons provokes an energy shift ΔE of the detected γ -quanta as discussed in detail in section 3.2. Thus, the photo peak at an energy of 511 keV is Doppler broadened.

Peak Profile and Defect Concentration The examination of the peak profile reveals the contribution of various positron states to the annihilation. In the presence of a defect, the probability of annihilating with valence electrons is enhanced (s. figure 3.1) and predominantly small Doppler shifts contribute to the profile. Normalized to the same counts in the spectrum, the height of the photo peak is increased whereas the width is narrowed as can be seen exemplarily in figure 3.5. Here, a polycrystalline Ni sample was measured as received (blue line) and after an annealing process (red line) which reduces the amount of defects in the material and therefore influences the peak as stated above.

S- and W Parameter For a quantitative analysis of the profile, two regions of the spectrum are of major interest: the low-momentum part in the center of the peak and the high-momentum part in the outer tails. The central part is dominated by positrons annihilating preferably with the low-momentum valence electrons in the interstitial region as they are repelled by the atomic nuclei. The lower intensity of the wings occurs due to the small overlap of the positron wavefunction with the core electron wavefunctions. Hence, in the absence of an atom with its core electrons, the high-momentum content is decreased resulting in a sharpening of the peak profile. Therefore, in order to characterize the profile of the peak, most commonly two lineshape parameters are evaluated from the DBS spectra: The S-parameter and the W-parameter [24].

As marked in figure 3.5, the S- and W-parameter are evaluated in a certain region of the annihilation peak. The S-parameter is defined as the ratio of the counts in the blue marked central region divided through the total counts of the spectrum. Hence, it is sensitive to the low momentum part of the spectrum attributed to the valence electrons. Additionally, the W-parameter is calculated in the outer region of the peak (yellow area) and thus sensitive to the higher momenta of the core electrons. In order

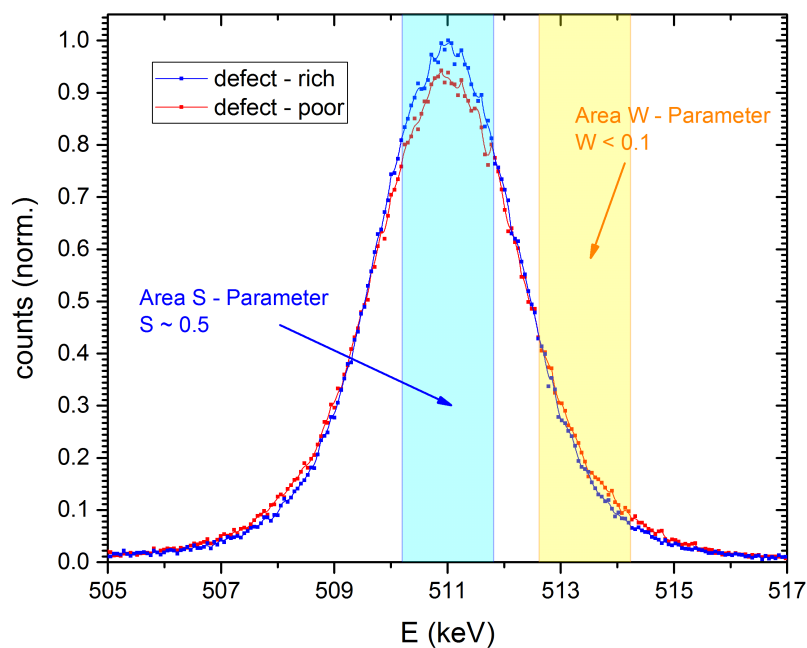


Figure 3.5: Doppler broadened profile of the 511 keV annihilation line of a polycrystalline Ni sample measured with a HPGe detector. A spectrum of the same sample was acquired before and after annealing. Clearly visible is the change in the height and broadness of the 511 keV peak. The lineshape parameters S and W are determined from the highlighted areas. During an annealing procedure, S decreases whereas W increases.

to compare different spectra to each other they first are normalized to equal counts. Additionally, a background reduction is carried out in the form of subtracting an error function fitted at the left and right background levels of the peak.

Within this work, the region of interest (ROI) for evaluating the S-parameter is defined as the energy interval of 511 ± 0.83 keV. This ROI is chosen to minimize the statistical error and results in a S-parameter of $S \approx 0.5$ [77]. The ROI of the W parameter is chosen for each investigated system individually in the outer region of the annihilation peak. If a high statistical precision is favoured, the ROI can be chosen such that the W-parameter is around a fourth of the S-parameter. Alternatively, a lower fraction of ≤ 0.1 is suitable to increase the sensitivity to defects [24].

When studying positron diffusion with a low-energy positron beam, the propagation of the positron reaching the surface with a certain probability has to be taken into account. As already described in section 2.1.3, the depth positrons are implanted into the sample depends on their implantation energy and subsequent positron motion after thermalization. Therefore, the positrons can annihilate in the bulk or diffuse back to the surface again. Hence, the annihilation characteristics varies with the probability of back diffusion and with the energy of the implanted positrons. By using a drift model, the positron transport can be described and, moreover, the positron diffusion constant can be determined. When electric field intensities are sufficiently small not to influence the positron motion, the probability of back diffusion to the surface prior to annihilation can be calculated as [85]

$$J(E) = \int_0^{\infty} \exp[-z/L_+]P(z, E)dz. \quad (3.14)$$

With this knowledge, so-called $S(E)$ depth profiles can be obtained. By varying the incident positron energy and taking into account the probability $J(E)$ of positrons reaching the surface before annihilation, the line shape parameters S and W are a superposition of a characteristic value for annihilating at the surface and a value for the annihilation within the bulk. Thus, the S-parameter can be calculated according to [85]

$$S(E) = S_{surf}J(E) + (1 - J(E))S_{bulk}. \quad (3.15)$$

An analogous equation is found for the W-parameter. Exemplary, two $S(E)$ profiles are shown in figure 3.6 (right). Here, the difference between two $S(E)$ scans of an untreated Si reference sample (open white symbols) and an irradiated Si sample (black symbols) is shown. The S-parameter is normalized to its corresponding bulk value. In the reference sample, the S-parameter starts at a value of 0.96 which is attributed to its surface value, increases with increasing implantation energy and finally converges to its bulk

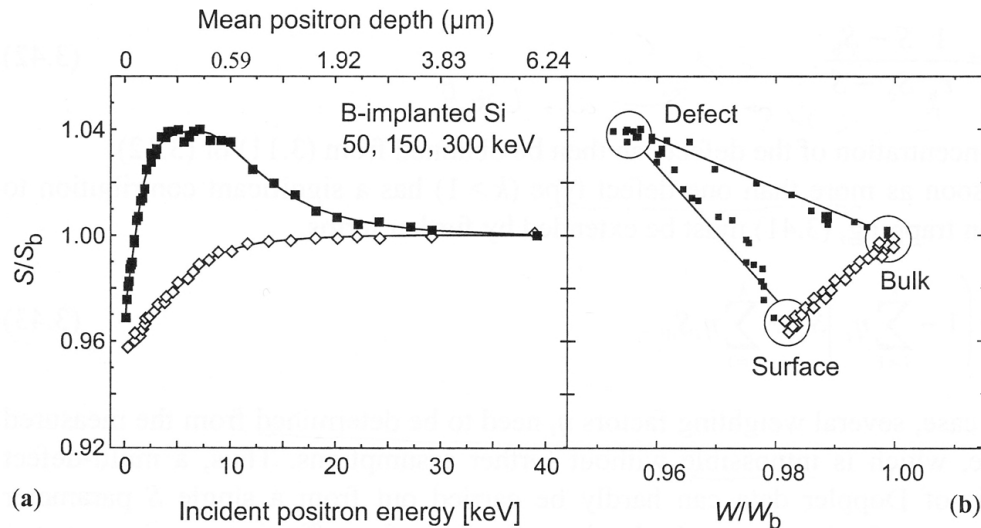


Figure 3.6: Example of a S - W diagram taken from Krause-Rehberg et al. [86]. In (a) two depth profiles are depicted. The S-parameter is plotted versus the incident positron implantation energy. Defect-free Si (open symbols) is compared to Si irradiated with B atoms (filled symbols). The open symbols depict a measurement on defect-free Si whereas in black the influence onto the depth profile due to implanted B atoms is shown. In (b) the corresponding S versus W plot is shown for the two measurements. For the defect free sample the (S,W) pairs lie on a straight line connecting the surface and the bulk state. During the penetration process with B atoms a new defect state is generated in a certain depth. Therefore, the curve of the implanted sample runs with increasing positron energy from the surface state through its characteristic point of the defect into the bulk value. The lineshape parameters are normalized to their corresponding bulk values.

value at energies of around 12 keV onwards. In comparison, the irradiated sample starts from a similar surface value and then steeply increases up to a normalized S-parameter of 1.04 before approaching the bulk value at higher incident positron energies. This change in S-parameter arises from generated defects during the irradiation process.

In a S/W-plot shown in figure 3.6 (right), the different annihilation states are visualized. For the non-irradiated sample, the annihilation of the positrons changes from a surface state to a bulk state with increasing implantation energy as no positron traps are present. The characteristic (W,S) pairs lie on the connection line between the surface and bulk state. Thus, both S- and W-parameter can be expressed as superposition of the surface and bulk parameters as already explained above. By contrast, in the case of the irradiated sample the appearance of a third annihilation site can be assigned to the presence of defects. This causes a deviation from the straight line connecting surface and bulk annihilation sites such that S-W curve runs clockwise through different

annihilation states with increasing energy. For annihilation at the surface and the bulk the same values are obtained as for the non-irradiated sample. Additionally, the positrons implanted into a medium depth are trapped in the generated defects.

3.4.2 Coincident Doppler Broadening Spectroscopy - CDBS

In addition to the just described "single mode", a so-called "coincident" set-up of two collinear aligned HPGe detectors enables the investigation of both γ -quanta created in a single annihilation event. This method is also called CDB spectroscopy [87, 88]. During the measurement, a 2D map with the coordinate axes E_1 and E_2 , represented by the measured energies of the two in coincidence aligned detectors, is acquired. An example of such a 2D spectrum is shown in figure 3.7. Here, each pixel of the figure represents the energy of the measured events detected by both detectors within a certain coincidence time in the range of typically 100 ns. The color code corresponds to the amount of counts within the spectrum.

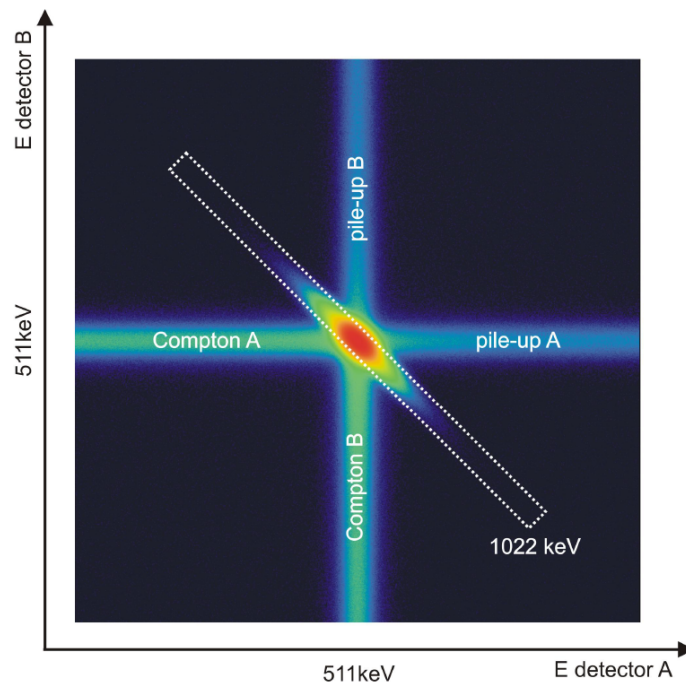


Figure 3.7: Typical CDB spectrum. The horizontal and vertical energy axes represent the two detectors in coincidence. For each detector, the Compton and pile up region is marked. The ROI contains the events with a total energy of $E_1 + E_2 = 1022$ keV representing the coincident measurement of both annihilation quanta in both detectors. The events on the diagonal ROI are nearly free of background since Compton and pile up events are excluded. [77].

In this type of map, the annihilation peak is defined by the marked ROI which is equal to a sum energy $E_{sum} = E_1 + E_2 = 1022$ keV. All events within this ROI stem from fully absorbed photons which are detected within the above mentioned coincidence time and therefore produce a valid event contributing to the spectrum. The photo peak is surrounded by a cross like structure mainly originating from detected Compton and pile up events in the correspondent detector. The ROI can be projected onto a common energy axis and produces a background free annihilation spectrum for the evaluation of high Doppler shifts which would not be possible in the single mode described before [77]. A special data evaluation software developed in the NEPOMUC group within a PhD thesis [89] was used for the present studies. In comparison to the acquisition of a spectrum by using the DBS method, the coincident detection of both γ -quanta produces an increased peak to background ratio of about $10^5 : 1$ [72]. Compared to a spectrum acquired in single mode, the background can be successfully reduced by about three orders of magnitude [86]. Moreover, the effective energy resolution can be enhanced by a factor of about $\sqrt{2}$ [24].

In figure 3.8 an example of evaluated CDB spectra of Al and Cu are shown. In the left image the two normalized projections of the evaluated diagonal ROI are displayed. In comparison to conventional DBS measurement, here also the high momentum region can be investigated due to the background free measurement. A standard technique is the evaluation of the so-called CDB ratio curves as shown in figure 3.8 (right). This profile is obtained by dividing a normalized CDB spectrum by a reference spectrum

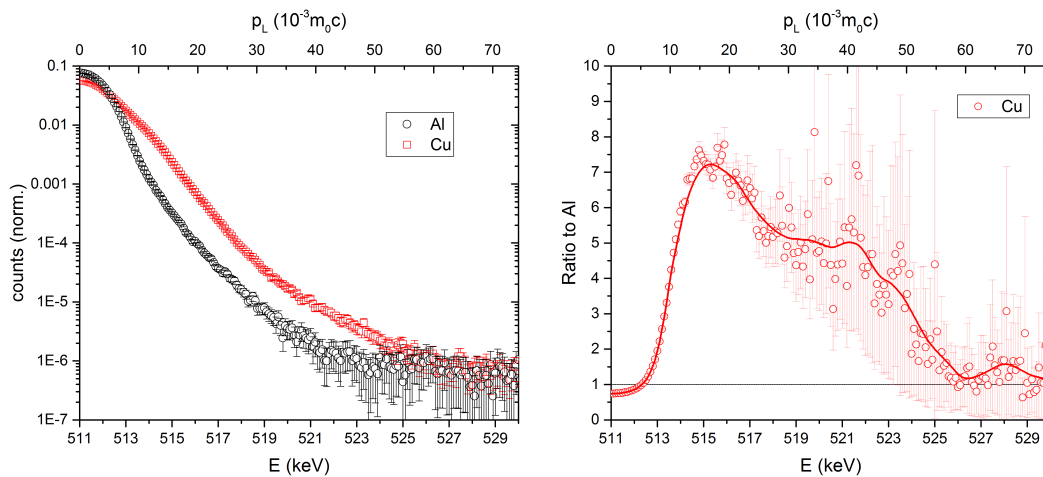


Figure 3.8: Coincident spectra of an Al and Cu sample as function of the energy E i.e. the longitudinal momentum p_L (left). By dividing the two spectra the element specific ratio curve, in this case the ratio of the Cu sample to an Al reference sample, can be obtained (right). Image taken from [19].

chosen individually for each study. In this case the reference spectrum was Al and the CDB signature of a Cu reference sample can be clearly visualized. This CDB signature is characteristic for each element, a so-called elemental finger print, and can therefore be used for the characterization of the elemental surrounding of the annihilation site. Also the identification of defect types such as precipitates or vacancies is possible with CDB spectroscopy.

4 The New CDB Spectrometer at NEPOMUC

4.1 Overview of the CDB Spectrometer Second Generation

The scope of this work was the design and installation of a new CDB spectrometer at NEPOMUC. In this section, the former version of the instrument is presented. After the first CDBS-set-up [90], the second version of the CDB spectrometer at NEPOMUC was designed and built by Stadlbauer [77]. With this set-up it was possible to perform depth-dependent coincident DBS measurements with a lateral resolution of about $300 \mu\text{m}$ (FWHM) and short measurement times of around 1 min for conventional DBS and 4 h for coincident measurements. In figure 4.1 a cross-sectional view of the main parts of the second CDB spectrometer version is given. The positrons leave the magnetic guiding field of the NEPOMUC beamline by passing through a magnetic field termination in front of the instrument. Via a subsequent aperture wheel, the beam intensity and the diameter can be adjusted. Afterwards, an electrostatic lens system consisting of four electrodes is used to focus the positron beam onto the sample which can be biased to a voltage of up to -30 kV . This allows the adjustment of the positron implantation energy in the range from 0.25 keV up to 30 keV . Depending on the chosen implantation energy the focus of the positron beam can be adjusted by a variation of the voltages U_3 and U_4 of the lenses "lens 3" and "lens 4" in figure 4.1 which are nearest to the sample. Below the electrostatic lens system, an additional component for optimizing the field geometry at the sample position was introduced: A potential ring consisting of a circular Al plate with a hole in the middle which is biased to the same voltage as the sample. An additional Al plate (not shown) with a hole in the middle was placed a few mm above the sample for further optimizing the beam focus and position. In this configuration, the sample is placed between two potential plates creating a potential-free area between them, allowing the measurement of non-conducting samples with high beam quality. For positioning the sample, a cross stage of two mounted stepper motors mounted on the outside of the UHV sample chamber via a flexible bellow was used.

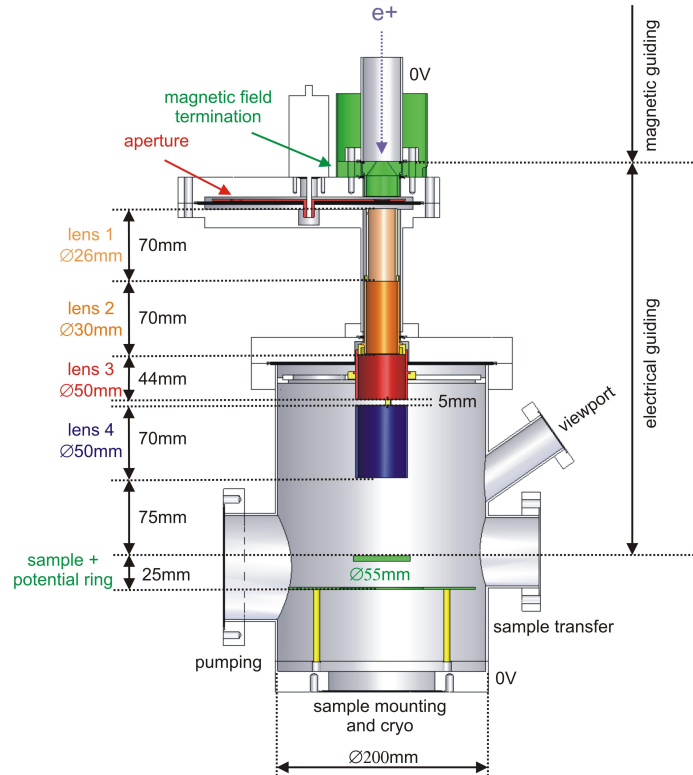


Figure 4.1: Cross-sectional sketch of the second version of the CDB spectrometer designed and built by Stadlbauer [77]. The positrons enter from the top, pass a magnetic field termination and an aperture before being electrostatically focused and accelerated onto the sample.

With this set-up the imaging of samples up to a size of 20×20 mm was possible. With this x-y-positioning unit also an implantation energy dependent beam shift due to electronic and magnetic stray fields at the instrument could be corrected. From the minimum implantation energy of 0.25 keV up to 15 keV, the position of the beam was distorted up to 10 mm in x- and y-direction with respect to the positioning axes. This was caused due to the slow velocity of the positrons and therefore higher influence on the path due to stray fields. During the measurements of depth depending profiles this influence was corrected in order to guarantee a stable position on the sample during the measurements. At higher implantation energies, the beam position was constant. Details of the lens system, as well as its influence onto the beam position can be found in [19].

For detecting the Doppler-broadened annihilation radiation, a set of two pairs of HPGe detectors are arranged in a collinear set-up around the sample chamber. Here, coaxial detectors equipped with transistor reset preamplifiers designed for high count rates and a good energy resolution are used. Details on their use and problems occurring due to high

count rates, electronic noise from neighbouring and ground loops influencing the spectra are discussed in [19] and [89]. The solutions to these problems and the experiences with this version of the instrument were considered and adopted to guarantee a stable operation and data acquisition of the new instrument described later in this chapter.

4.2 Experimental Requirements of the New CDB Spectrometer

Within the new version of the CDB spectrometer, a new positron microbeam should be realized for considerably improving the spatial resolution for imaging defect distributions with DBS and for performing defect spectroscopy with CDBS. In order to reach the goal of a positron microbeam, the entire spectrometer of "version 2" had to be redesigned, improved and expanded with different new components. The instrument should be capable of performing high spatial resolved measurements from the surface to the bulk of the materials. Additionally, as the former version, also temperature-dependent experiments at low temperatures as well as at elevated temperatures should be feasible, e.g. for the investigation of cold positronium formation and emission or for in-situ observation of annealing processes. In the following a summary of the requirements is given which the new spectrometer has to fulfil in order to increase its overall performance:

- Provision of a beam spot diameter of $< 100 \mu\text{m}$ at the sample position
- Ability of implanting the positrons with an energy of up to 30 keV
- High spacial resolution 2D-scanning of samples of $15 \times 15 \text{ mm}$ size within acceptable measurement times
- Capability of the optics of using both, the primary ($E_{kin} = 1 \text{ keV}$) as well as the re-moderated beam ($E_{kin} = 20 \text{ eV}$) provided by NEPOMUC
- Monitoring of the beam parameters such as shape and radial position at various key positions within the new instrument for optimizing the guidance and focusing parameters
- Possibility of performing temperature-dependent measurements in the range between 50 and 1000 K

In order to fulfil these requirements, the new CDBS *upgrade* was designed, simulated and constructed with respect to the experiences made with "version 2" of the spectrometer. The upgrade of the spectrometer will be described in the following sections pushing the capabilities to a new level.

4.3 The CDBS *upgrade*

The new instrument, the CDBS *upgrade*, was completely redesigned. The magnetic and electrostatic beam guidance as well as the brightness enhancement system were designed for an easy adoption to the beamline of NEPOMUC and the use of both, the primary and the re-moderated beam. For fulfilling the requirements mentioned in the last section, new beam monitors, an electrostatic accelerator, a brightness enhancement

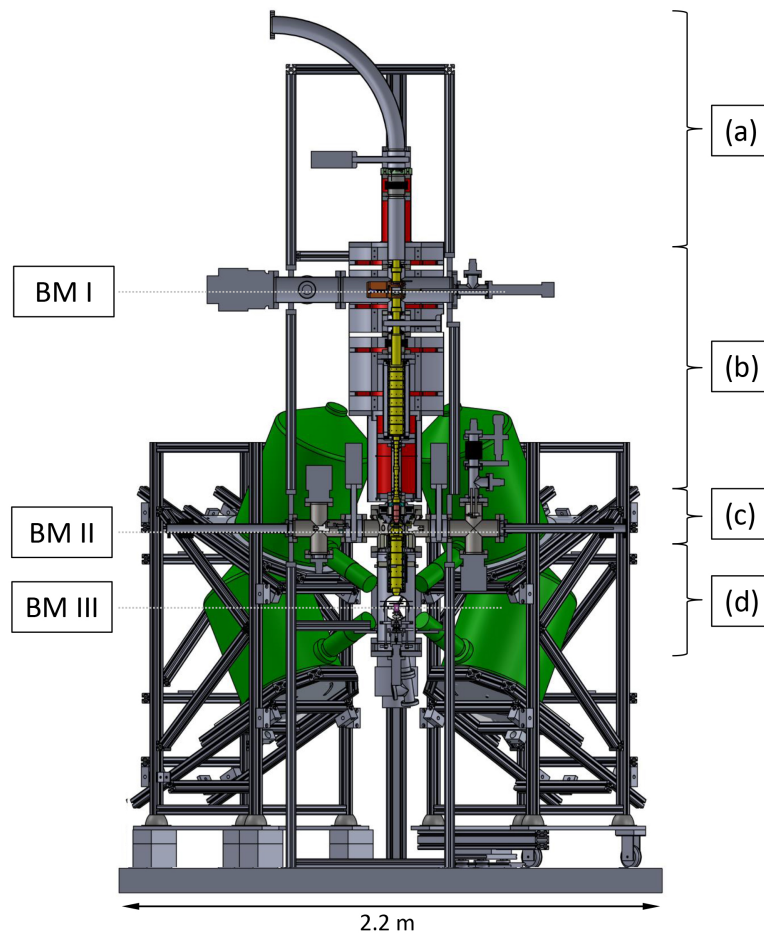


Figure 4.2: Cross-sectional sketch of the CDBS *upgrade* with the positions of the three new beam monitors (BM I - III) (dashed white lines). The different parts are: (a) section of the beamline of NEPOMUC, (b) the first beam monitor system with optional apertures and acceleration system, (c) brightness enhancement system with a second beam monitor and first electrostatic lens system for beam focusing onto the re-moderation foil and (d) the new sample chamber with the second electrostatic lens system for focusing the beam onto the sample, an optional third beam monitor and piezo positioning system for sample scanning. In green the HPGe detectors are displayed within their supports for positioning around the sample chamber.

system as well as a new sample chamber with improved sample positioning unit were designed, simulated and assembled. The final assembly of the instrument as it is set up in the experimental hall of the FRM II is displayed in figure 4.2. In the following section the different new components will be presented.

4.4 Components and Assembly of the CDBS *upgrade*

4.4.1 First Beam Monitor and Acceleration System

The positron beam enters the CDBS *upgrade* from the top via a large bend as shown in figure 4.2. For analysing the shape of the beam a first beam monitor system (BM I) consisting of a stack of MCP and a phosphor screen is installed.

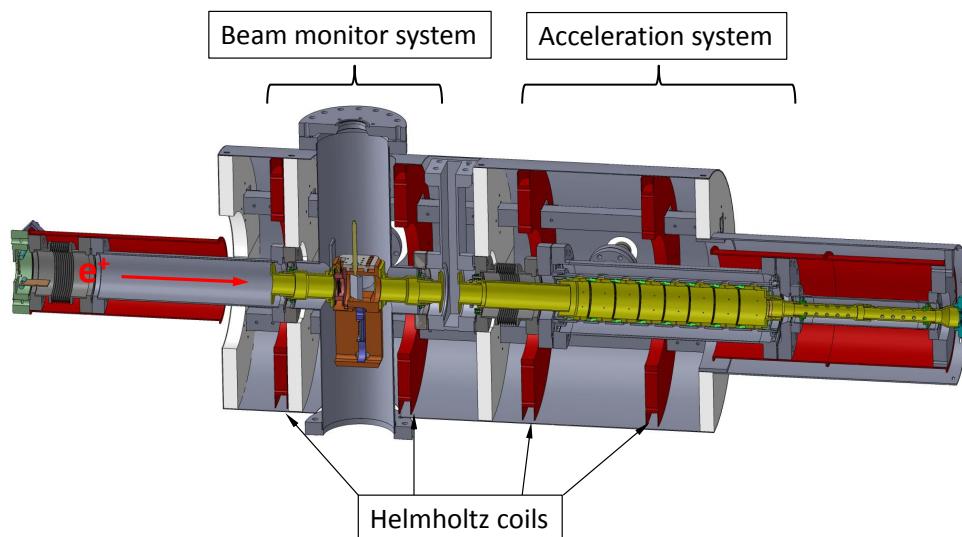


Figure 4.3: First beam monitor, BM I, and acceleration system of the CDBS *upgrade* (section (a) & (b) in figure 4.2). Before entering the instrument, the shape and the lateral position of the positron beam within the beamline can be inspected and tuned with magnetic correction coils by monitoring the beam with a MCP module (BM I in figure 4.2). Optional apertures can be inserted for adjusting the intensity of the beam. Dependent on operating the brightness enhancement system or not, an additional accelerator can be used. Due to the size of the modules, a Helmholtz like geometry was chosen for producing the magnetic guiding field. For avoiding magnetic stray fields influencing the positron beam, a μ -metal shielding was installed around the field coils.

Here the shape of the beam and its concentricity can be adjusted by tuning various transverse magnetic correction fields mounted on the beamline in front of the instrument. Optionally, apertures can be inserted into the path of the beam for adjusting the intensity. Dependent on the use of the brightness enhancement system, the kinetic energy of the beam can be varied by an acceleration system consisting of eight electrodes enabling an acceleration energy range of the beam from 20 eV up to 5 keV. Due to the size of the modules, the coils for the longitudinal magnetic guiding field are mounted in a Helmholtz-like geometry. In order to avoid any influences due to external magnetic stray fields, an additional μ -metal shielding was mounted over the entire module. In order to tune the radial position of the beam within the system, saddle coils are installed, producing a transverse magnetic field for correcting an off-axis beam position. The overall assembly is depicted in figure 4.3. Details concerning the construction of the beam monitor system and the accelerator as well as the applied potentials for accelerating the beam can be found in the Appendix.

4.4.2 Brightness Enhancement System and Sample Chamber

For brightness enhancement of the positron beam an additional chamber was implemented in front of the sample chamber. It is connected to the beam monitor and acceleration module, described in section 4.4.1, via a potential tube ((B) in figure 4.4) for keeping the potential of the positrons provided by the last electrode of the accelerator constant and for avoiding any field disruption which might lead to a beam distortion. Before entering the first electrostatic lens system ((D) in figure 4.4) and being focused onto the re-moderation foil, the positrons have to be released from the longitudinal magnetic guiding field. Therefore, a magnetic field termination at the end of the potential tube is installed ((C) in figure 4.4). Multiple metallic glass stripes are mounted in a Venetian blind geometry in a supporting ring of μ -metal, guiding the magnetic flux lines away from the optical axis without disturbing the path of the positrons. A detailed sketch can be found in the Appendix (Fig. A.5).

An optional insertable MCP module (BM II, (I) in figure 4.4) enables the monitoring of the beam at the position of the re-moderation foil allowing a quick tuning of an off axis beam position and adjustment of the potentials of the electrodes of the lens system for a minimal beam diameter at the re-moderator position. A detailed sketch of BM II is given in the Appendix in figure A.2.

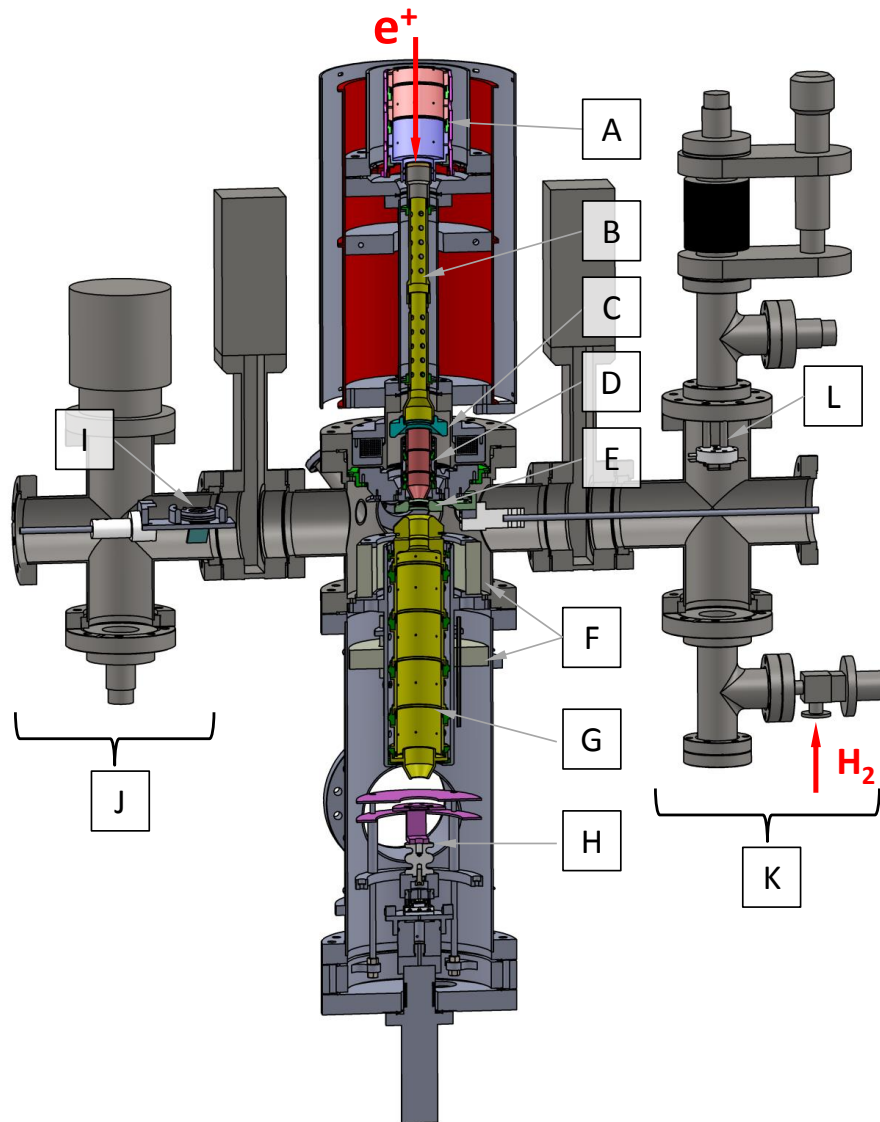


Figure 4.4: After passing the acceleration unit (A), the positron beam is transported via a potential tube (B) to a magnetic field termination (C). A Venetian blind geometry of multiple metallic glass stripes terminate the magnetic guiding field. By the use of a first electrostatic lens system (D) after the field termination, the positrons can be focused onto the re-moderator (E) consisting of a 100 nm thick Ni(100) foil. A second electrostatic lens system (G) forms the re-emitted positrons to a beam again and focuses them onto the sample which can be biased up to a potential of -30 kV. High resolution sample positioning is realized by a stack of two piezoelectric positioners (H). On the left indicated by (J), the housing of BM II (I) is shown. Prior to its use, the re-moderation foil can be retracted into a separate environment on the right (K) and annealed by a heating device (L) and treated with H_2 via a needle vent for surface cleaning. Both can be separated from the re-moderation chamber by a vacuum gate valve. (F) In order to shield the detectors from radiation created at the re-moderation foil, two tungsten rings are installed covering the solid angle of the detectors (shown in figure 4.2 (green)).

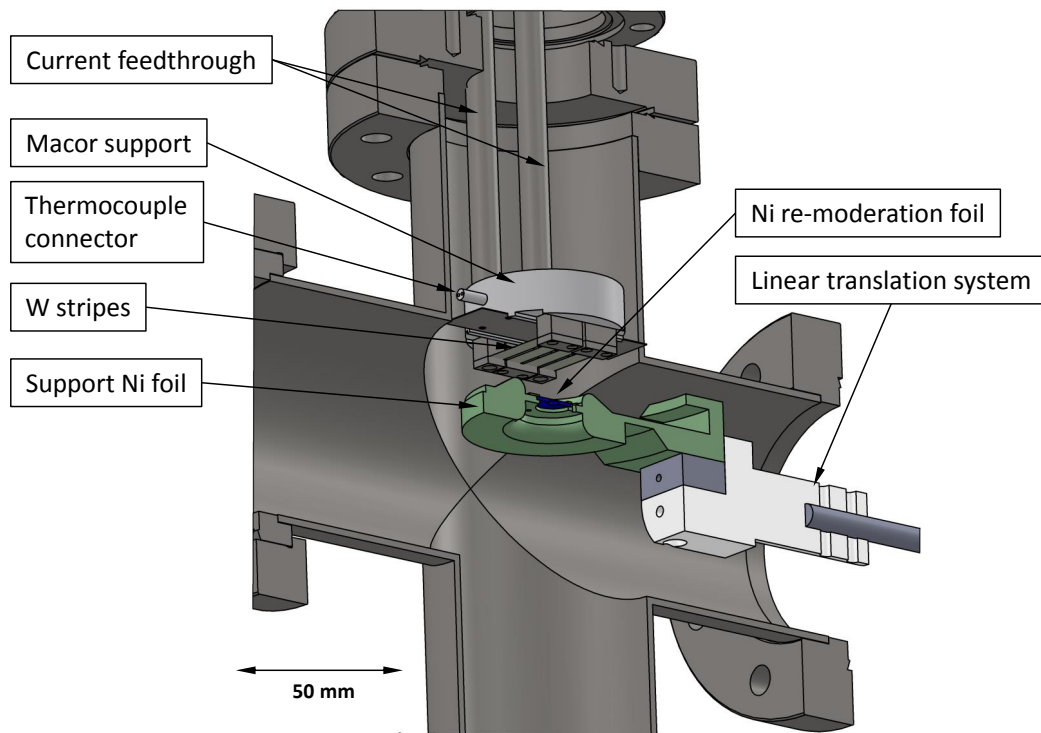


Figure 4.5: Set-up for preparing the re-moderation foil before its insertion in the re-moderation chamber in the path of the positron beam. Via a linear translator the re-moderation foil mounted within its support is positioned below the heating device. The heater can be lowered via a z-translation up to 15 mm above the Ni foil. By feeding a current of up to 20 A through the W stripes a temperature of up to 800 °C can be reached at the position of the Ni foil.

Dependent on the operation of the brightness enhancement system, a second electrostatic lens system, consisting of six electrodes is used to extract the re-emitted positrons from the re-moderation foil and to focus the re-moderated beam onto the sample in the analysis chamber. Without the brightness enhancement system, the positron beam is simply guided and focused onto the sample. As will be explained in more detail in section 4.6, the Ni re-moderation foil has to be prepared for improving the re-moderation process by a heat and H₂ treatment. For this, a separate environment next to the re-moderation chamber with a needle valve for H₂ and a special designed heating device was designed ((K) in figure 4.4). A more detailed sketch can be found in the Appendix A.6. Separated by a vacuum gate valve, the re-moderation foil can be retracted from its position within the sample chamber into a position below the heating device without exposing the re-moderator to air. After the preparation procedure the re-moderation foil is put back into its operating position. In figure 4.5 the preparation position of the support of the Ni foil under the special designed heating device is shown.

The heat is generated by feeding a current of up to 20 A to four W stripes mounted on a Macor support. With an additional thermocouple the temperature can be measured in-situ at a calibrated reference point. The Ni re-moderation foil can be heated up to 800 °C for removing any surface impurities via annealing. For surface treatment at elevated temperatures, H₂ can be fed into the preparation chamber via a needle valve.

For depth-dependent measurements, the sample can be biased up to -30 kV enabling a positron implantation depth of a few μm . By the use of a stack of two piezoelectric positioners with optical encoders, 2D scans of samples with a maximum size of up to $19 \times 19 \text{ mm}^2$ with high accuracy and repeatability in the nm-range can be performed. Hereby, the positioners can handle a sample weight of up to 3 kg according to the data sheet and have a blocking force in x- and y-direction of 3.5 N. The sample is sandwiched between two potential plates creating a potential free space at the sample's positron. This allows the investigation of conducting as well as insulation samples without beam distortion. Unfortunately, these potential plates and the sample holder geometry limits the maximum height of the samples to 10 mm. A detailed sketch of the positioning system and the sample holder is given in figure 4.6.

As already mentioned in section 4.2, the geometry of the sample chamber was designed for a quick set-up change between measurements at high and low temperatures. Instead of the piezoelectric positioning system an insert of a heatable sample holder can be mounted. It consists of an ellipsoidal Cu reflector where the light of a 250 W halogen lamp, located in one focus of the reflector, is concentrated on the back side of the sample located in the other focus point. Therefore, in-situ (C)DBS measurements in a temperature range from room temperature up to 1100 K can be performed. Details of the heatable sample holder can be found in [19] and [91].

Low temperature experiments down to 40 K can be performed by an insert of a Cu sample holder mounted on the cold head of a closed-cycle He cryostat via a sapphire insulator. Due to the size of the sample holder, the scanning range of $19 \times 19 \text{ mm}$ is reduced to $5 \times 5 \text{ mm}^2$. The geometry of the sample holder and details of the sample mounting can be found in [77].

Since the process of re-moderation at the position of the Ni(100) foil produces a significant amount of γ -radiation, the inclined detectors surrounding the sample chamber as shown in figure 4.4 (F), have to be shielded in order to reduce the background. Therefore, two systems of radiation shields are applied. Inside the re-moderation chamber and the sample chamber, two W ring assemblies are mounted, covering the solid angle of the HPGe detectors. On top of the detectors an additional Pb shielding with a thickness of 4 cm is mounted which is not shown in figure 4.2.

As an add-on, an in-situ tension test machine was developed. Hereby, specially shaped

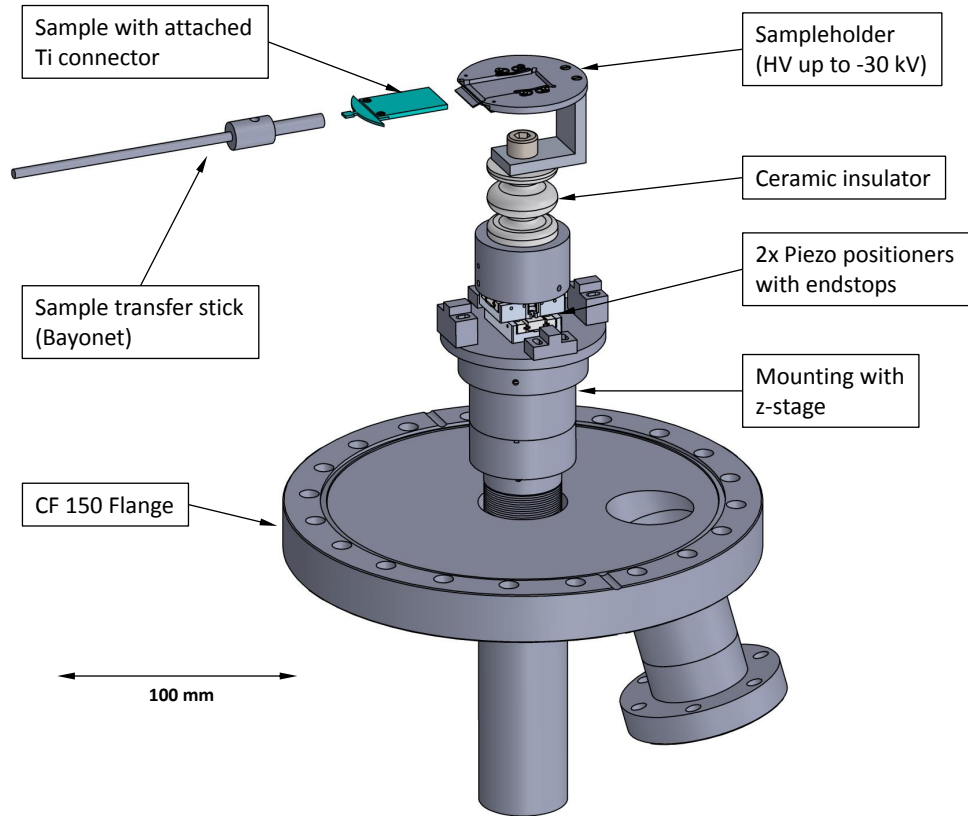


Figure 4.6: Sample holder and positioning system of the CDBS *upgrade*. The sample is positioned by two high resolution piezo positioners mounted on top of a z-translator in order to vary the height according to the sample thickness. The head can be biased up to a voltage of -30 keV and is insulated via a ceramic insulator. The sample mounted on a sample holder can be transferred via a bayonet coupling.

samples can be scanned in 2D while performing tension measurements. This enables the in-situ recording of 3D defect profile maps and CDBS measurements on tensile testing samples. Details are given in [92].

4.5 Simulation of the Magnetic and Electrostatic Fields

Prior to the fabrication of all components for the CDBS *upgrade*, comprehensive simulations of the magnetic longitudinal field created by various magnetic coil geometries and especially for the electrostatic lens systems were carried out with the COMSOL multiphysics package within an iterative process between CAD designing of the com-

ponents and their simulation. The goal was to find optimal values for the currents producing the magnetic longitudinal guiding fields and for the potentials of the two electrostatic lens systems. Finally, a minimum of the positron beam diameter at the position of the sample should be reached.

Due to the poor optimization performance of COMSOL, a JAVA software was developed, enabling the computation of the electrostatic and magnetic fields with COMSOL and simulating the positron trajectories on and close to the optical axis of the instrument of a more realistic positron beam. In order to avoid any correlations between the starting point of the positrons within the simulation and their endpoint at the sample position, different independent positron trajectories with different starting values such as different transverse momentum and the starting point along the optical axis were simulated. With this realistic beam, the real conditions of the positron beam could be imitated.

The combination of COMSOL with JAVA enabled a simultaneous usage of multiple workstations and therefore dramatically reduced the time per simulation and hence more simulations could be carried out. In the following sections, the results of the simulations for the different parts such as the acceleration system, the first electrostatic lens system for focusing the positrons onto the re-moderation foil as well as the second electrostatic lens system for focussing the positrons onto the sample will be shown.

Simulation of the Acceleration System

For simulating the beam passing through the acceleration system of the CDBS *upgrade*, it was required that the kinetic energy of the beam can be increased upon its implantation energy for the following brightness enhancement system without introducing a deterioration in diameter. In order to simulate the worst case of a realistic positron beam, the simulations were performed by starting the beam with a diameter of 2 mm (FWHM) [14] and its maximum transverse energy component of around 1 eV [17].

Positron particle trajectories were simulated starting from different distances in z -direction from the acceleration system. Independent of their starting point, all trajectories showed the same trend. Exemplary and for a better overview, in figure 4.7 the simulation of one of these positron particle trajectories (orange) is shown. The beam was split into ten single trajectories equally spaced over the beam diameter. Injected with a kinetic energy of 20 eV, the positrons' energy is increased to 5 keV when passing the acceleration unit with its eight electrodes. Within a magnetic field of 7 mT created by a surrounding solenoid (not shown in figure 4.7), the positrons are gyrating around the field lines with a gyration length of 1.9 cm, in agreement with calculation (formula 2.27). As the positrons are accelerated due to the potential gradient applied to the different electrodes, it can be shown that the gyration length increases with increasing velocity.

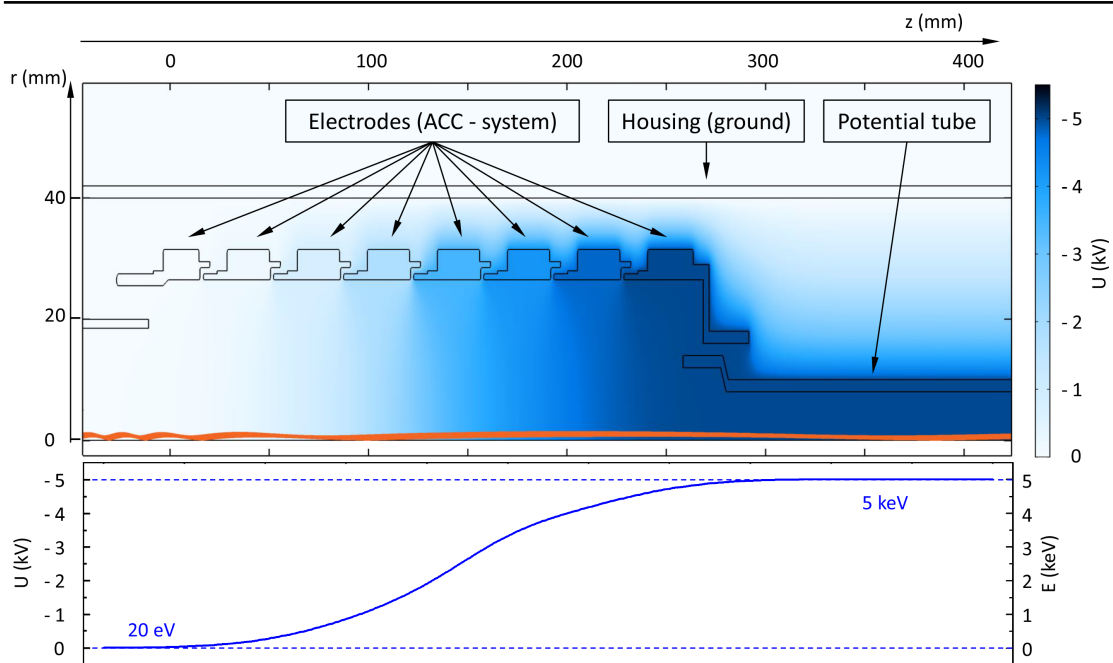


Figure 4.7: Simulation of the acceleration system shown in figure 4.3 performed with COMSOL multiphysics. The kinetic energy of the 20 eV positron beam provided by NEPOMUC is boosted over a length of about 300 mm to the implantation energy for the re-moderator foil of 5 keV. Beneficial for the beam acceleration is a slight increase of the potential at the beginning, reaching its maximum gradient in the middle and ending up with a shallow increase to its endpoint energy of 5 keV as shown in the graph below. The complete acceleration system is located within the magnetic guiding field of 7 mT. Therefore, the gyration of the particle trajectories, shown in orange, and the influence of the acceleration on the gyration length can be observed. The beam diameter of 2 mm is not influenced by the acceleration system.

Within the simulation it could be shown, that the diameter of the beam is not influenced in a negative way throughout its acceleration range. The gyration length at 5 keV ends up with about 30 cm. According to the simulations, this acceleration system is suitable for using it in front of the brightness enhancement system. Beneficial for the simulation was a steeper potential gradient in the middle of the accelerator and a smooth transition for reducing the disturbances at the beginning of the acceleration line onto the particles.

First Electrostatic Lens System

According to the principle of brightness enhancement explained in section 2.4 the positron beam has to be focused onto the re-moderator. To do so, the first electrostatic lens system was simulated with COMSOL and the result is shown in figure 4.8. The magnetic guiding field is terminated by a magnetic field termination (MF termination in figure 4.8). Afterwards, the positron beam is focused via a modified einzel lens onto the re-moderation foil. As shown, the first lens with a potential of 7 kV extracts the positrons out of the potential tube, and the third lens produces the required electrostatic field gradient for achieving a focus at the position of the Ni(100) re-moderation foil. According to the simulations a minimal diameter of 0.5 mm could be achieved.

Assuming a triple element lens which voltage of the first ($V1$) and last element ($V3$) is equal and only the voltage of the center electrode ($V2$) is altered, the minimal achievable beam diameter found by the simulation should be tested. This lens system with $V1 = V3$ is also called "unipotential" or "einzel" lens. The fundamental properties can be calculated numerically and can be looked up in Harting et al. [63]. Here, for several lens systems and voltage ratios the focal lengths are calculated. For the

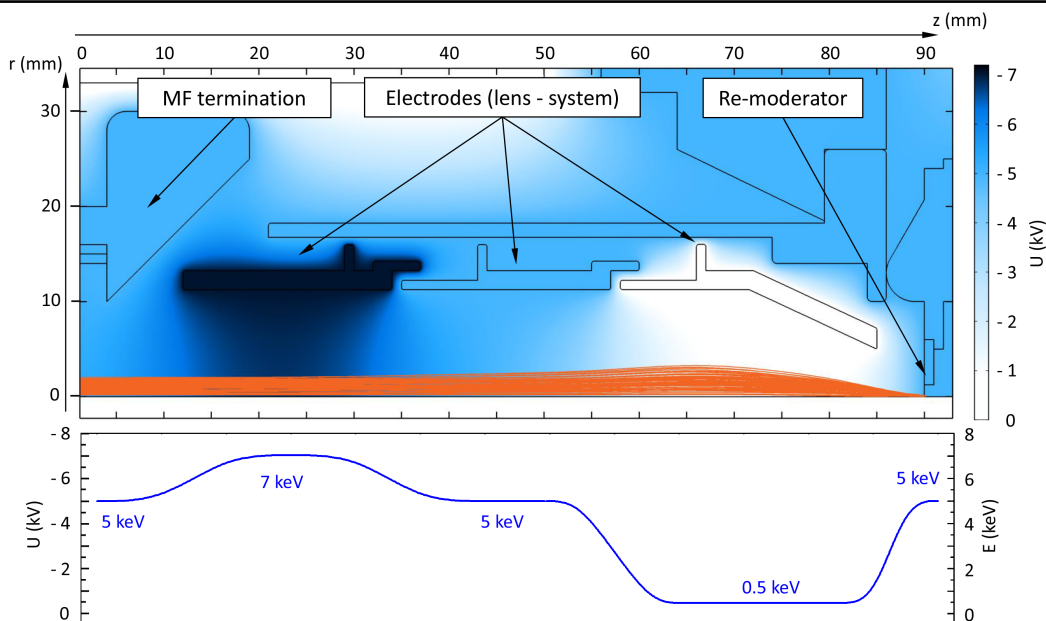


Figure 4.8: Positron particle traces (orange) through the first electrostatic lens system. The positron beam enters from the left and, after passing a magnetic field termination (MF termination), is focused by electrostatic lenses consisting of three electrodes. Here a "real" beam was simulated with different transverse momenta of the positrons and different starting points. At the position of the re-moderation foil a focused beam spot of 0.5 mm could be achieved.

model system following values are taken: A constant diameter of the electrodes of $D = 10$ mm, an aperture to diameter ratio of 1 and a gap to diameter ratio of 0.1. With a voltage ratio of V_2/V_1 of 0.1 and $V_1 = V_3$ a focal length of $1.36 \times D = 13.6$ mm is given [63]. With an initial beam diameter of $d = 2.5$ mm and beam energy of $E_{\parallel} = 5$ keV, the minimal achievable spot size $d_i = 2r_i$ can be calculated according to equation 2.58 taking into account a transverse beam energy of the re-moderated beam of $E_{\perp} = 1$ eV [15, 17, 93]. The resulting diameter amounts to $d_i = 0.38$ mm. The diameter obtained by the simulation is a factor of 1.3 larger which can be explained by a deviation of the lens geometry and aberrations not taken into account in the estimate.

Second Electrostatic Lens System

The optimized simulation of the second electrostatic lens system is shown in figure 4.9 and results in a simulated minimal beam diameter of $40 \mu\text{m}$ when starting with a diameter of 0.5 mm at the position of the re-moderation foil determined by the simulation of the first electrostatic lens system of figure 4.8.

The result of the simulation can be confirmed by estimating the beam diameter according to Harting et al. Assuming an einzel lens with three electrodes with voltage ratios of $V_3/V_1 = 16.7$ and $V_2/V_1 = 0.33$ the values for the focal length is given as $1.6 \times D = 24$ mm [63]. Since the re-moderation foil can be considered as a new positron source with a starting diameter of 0.5 mm and a maximal transverse energy of $E_{\perp} = 25$ meV due to the thermal smearing of the re-emitted positrons, a minimal beam diameter of $44 \mu\text{m}$ is calculated according to formula 2.58 for a beam energy of $E_{\parallel} = 30$ keV.

Within the path of the beam, two cross-overs can be seen in figure 4.9 at positions 10 mm and 230 mm. The first arises from the potential which accelerates the slow re-emitted re-moderated positrons and forms them to a beam. Since electrostatic lens systems primarily focus a particle beam, cross-over are necessary to collimate the beam. For this, a focusing lens was placed behind the cross-over where the beam diverges. The second cross-over was used in order to enhance the depth of sharpness at the sample position. Since a cross-over defines a virtual beam source, the divergence can be re-defined. By a focus produced at the cross-over at position $z = 230$ mm, a small divergence angle within the new virtual source can be generated. Since the distance from the last lens to the sample is short compared to the entire lens system, a short focal length with high divergence angle would be required. This would result in a narrow depth of sharpness in which the sample has to be positioned. To overcome this restriction, the virtual source at the cross over minimizes the divergence and therefore, the region in which the sample can be positioned gets larger. Otherwise, the divergence

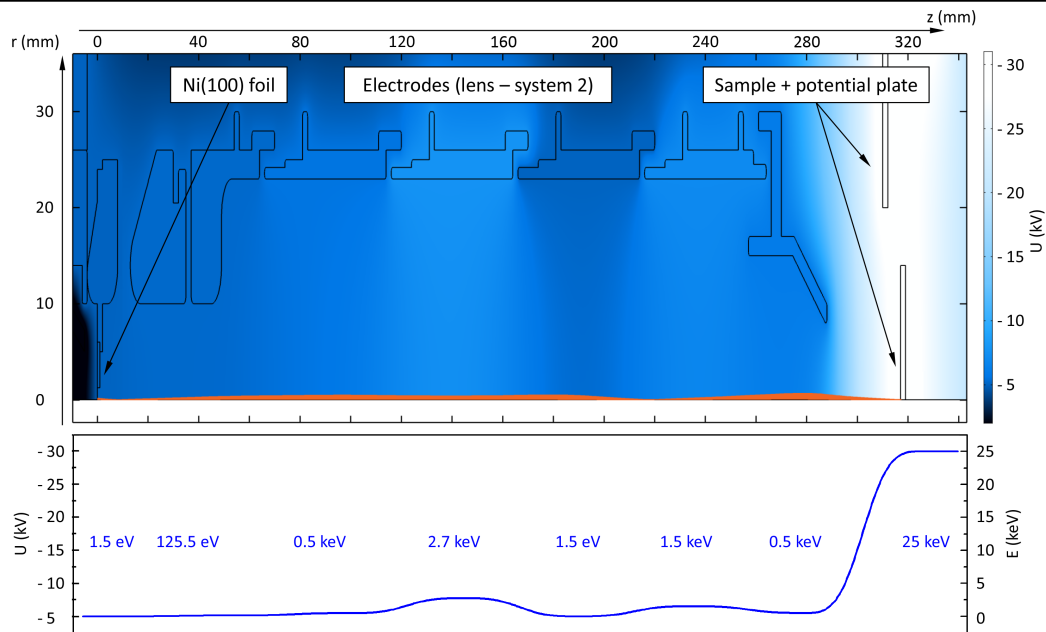


Figure 4.9: Within the second electrostatic lens system, the re-emitted positrons from the Ni(100) foil are formed to a beam by the first electrode of the lens system. Before focused onto the sample position, a cross over of the positron beam at position $z = 10$ mm enables a collimation of the beam trajectories. Since the divergence of a beam can be defined by a virtual source, with the second cross over at position $z = 230$ mm the depth of sharpness at the sample position can be enlarged. Within the gap between the last electrode and the sample, the positrons are focused and accelerated to their implantation energy of up to 30 keV. When using the brightness enhancement system, an offset of -5 kV due to the acceleration onto the Ni(100) foil limits the implantation energy at the sample to 25 keV.

defined by the first virtual source (first cross over) restricts the depth of sharpness.

In the gap between the sample and the last electrode, besides the focusing, the positrons are also accelerated onto their final implantation energy of up to 30 keV. Therefore, the potentials of the last two electrodes have to be adjusted depending on the sample potential, for guaranteeing a minimal beam spot at every implantation energy. The simulation above only shows the case where the brightness enhancement system is used. Here an offset of the potential of -5 kV has to be taken into account due to the required implantation energy of the Ni(100) foil. This limits the maximum energy at the sample to 25 keV.

All in all, the simulations enabled the tuning of the design of the electrodes of the lens systems and they showed a functioning system resulting in a beam diameter of nearly one magnitude smaller than that of the CDBS "version 2".

4.6 Ni Foil Transmission Re-moderator

Conditioning of the Ni(100) re-moderation foil drastically increases the yield of re-emitted positrons [94, 95]. Therefore, prior to its integration in the brightness enhancement system, a pre-treatment of the re-moderation foil comprising an annealing process under UHV conditions, as well as an additional oxygen and hydrogen treatment for removing any surface impurities deteriorating the re-moderation yield of the foil has to be carried out.

Prior to its final installation in the CDBS *upgrade*, a comprehensive study on the conditioning of the Ni foil was carried out via XPS and temperature-dependent DBS measurements [91]. Moreover, the optimum positron implantation energy was determined using the former CDBS "version 2". Within this section, the results leading to a maximum amount of re-emitted moderated positrons will be shown.

4.6.1 XPS Characterization of the Ni(100) Foil

The removal of surface impurities is a key factor in maximizing the re-emittance of (re-)moderated positrons using materials with negative positron work functions. Especially C and O impurities contaminating the surface reduce the positron yield and therefore have to be removed before operation.

In order to get detailed information on the amount of impurities and on the conditioning process, temperature depending in-situ XPS was carried out on the 100 nm thick Ni foil for observing the removal of the surface impurities of C and O. As shown in figure 4.10, a simple heating process of the foil up to a temperature of 400 °C increases the signal of the Ni peaks in the XPS spectrum by a factor of six whereas the C and O peaks decrease by a factor of two and four, respectively. Hence, just by heating the foil, the C and O contaminations can be significantly reduced resulting in a higher re-moderation yield. Moreover, a further reduction of the surface impurities can be achieved by an additional treatment of the foil in an O and H atmosphere at elevated temperatures as shown by Fujinami et al. [94].

4.6.2 Characterization by Temperature-Dependent DBS

Besides the removal of the surface impurities, also the defects within the material itself affect the re-moderation efficiency. This issue can be accessed by DBS measurements carried out at the former spectrometer, the CDBS "version 2". Here the annealing behaviour was examined by using a polycrystalline Ni sample. In figure 4.11 (top),

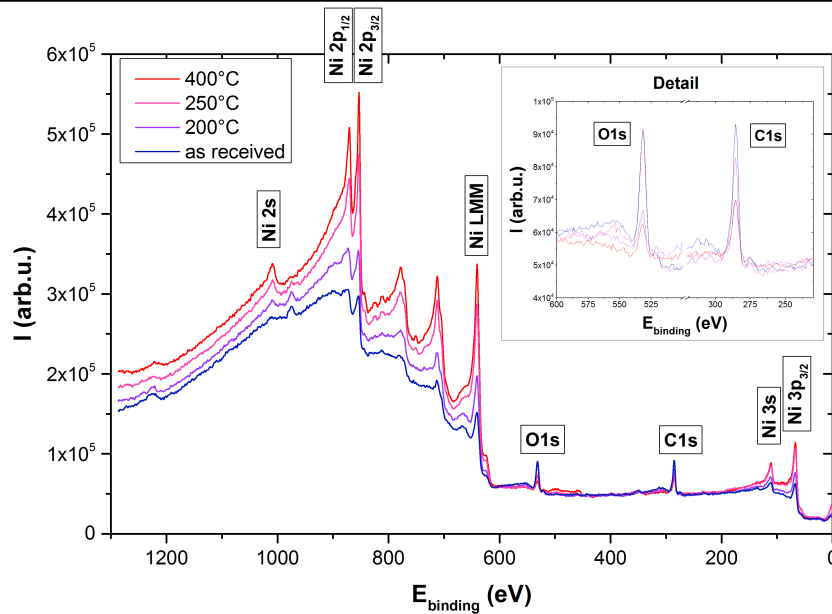


Figure 4.10: Temperature-dependent characterisation of the Ni(100) re-moderation foil by x-ray induced photo electron spectroscopy (XPS). By heating the re-moderation foil to about 400 °C the surface impurities such as C and O can be successfully reduced (insert) whereas the Ni signal is increased by a factor of six leading to a significant increase in the yield of re-moderated positrons.

the bulk S -parameter which is related to the open volume defects in the sample, is shown as a function of temperature. The high S -parameter at the beginning of the heating process is determined by the production process of the raw material. The Ni sample was cut off a rod produced by rolling which introduces a lot of defects in the as-received state because of the absence of a subsequent annealing process. Between a temperature of 150 °C and 550 °C the curve shows a shallow decrease in the beginning and a significant drop from 300 °C on, indicating the annealing of the Ni crystal due to the diffusion of vacancies. At 540 °C the minimum value of the S -parameter is observed meaning a complete annealing of the sample. The trend in S -parameter with respect to temperature is in good agreement with the literature. Within an isochronal annealing curve a value of around 800 K \cong 527 °C is given by literature for full annealing of the material [97]. When exceeding temperatures of 820 °C, the S -parameter increases again due to the thermal expansion of the crystal lattice and the thermal creation of vacancies.

Additionally to the quality improvement of the Ni crystal during annealing, it has to be taken into account that for re-moderation the thermalized positrons have to reach the back side of the Ni foil within their diffusion length. In order to do so, the

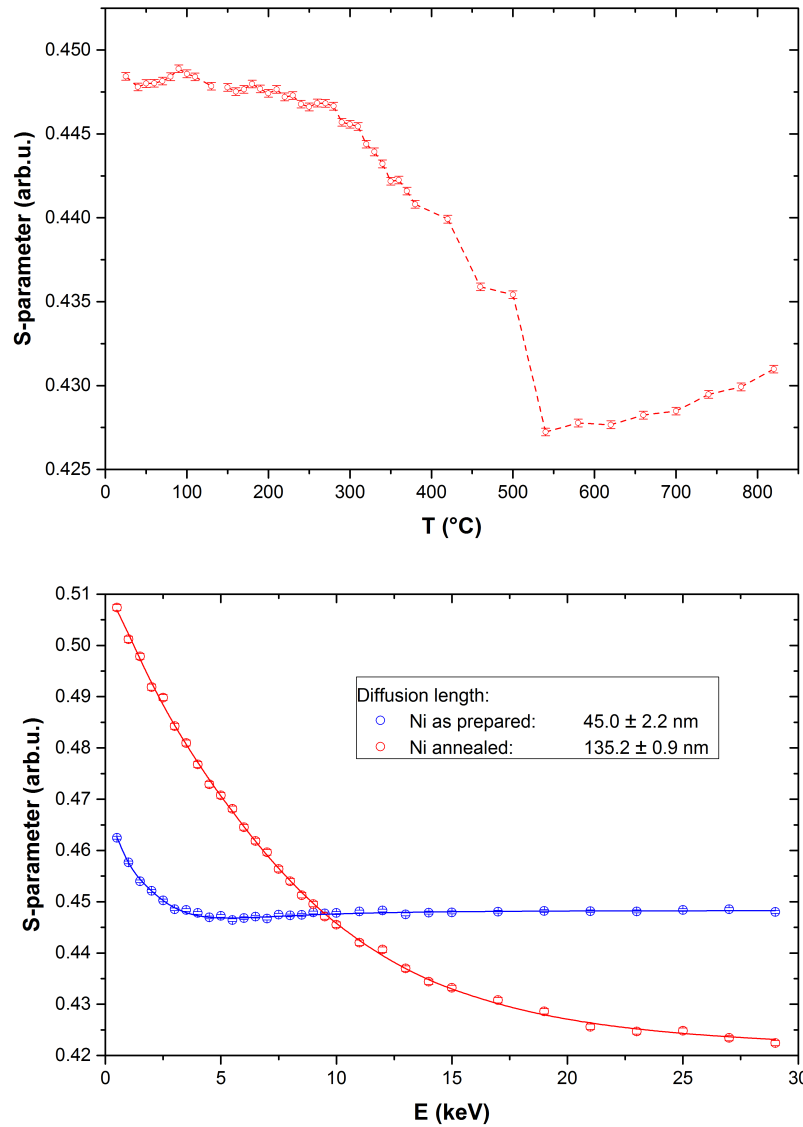


Figure 4.11: Temperature-dependent measurements carried out on a polycrystalline Ni sample at the CDBS "version 2". In the top figure, an in-situ temperature-dependent measurement of the S-parameter was performed clearly showing the annealing process of the as-received sample. The minimum S-parameter at 540 ° indicates full annealing of the sample. Due to the thermal expansion and to thermally created vacancies, the S-parameter rises again at higher temperatures. Bottom figure: Two depth-dependent $S(E)$ scans of the Ni sample taken before and after the annealing process are shown. In both cases the positron diffusion length was obtained by fitting the data with VEPFIT [96] (solid lines). By annealing the sample, the diffusion length could be increased by a factor of three to 135.2 nm

positron trapping in defects has to be avoided. The positron diffusion length can be determined by so-called "S-over-E"-scans $S(E)$. Figure 4.11 shows the $S(E)$ profiles corresponding to the sample before and after the heat treatment, respectively. As shown, the S-parameter for the as-received sample reaches its bulk value already at 5 keV. By the tempering process the bulk value is increased to about 25 keV. As expected, the S-parameter is significantly reduced after the heat treatment compared to the initial state due to its lower defect concentration. The diffusion length in both cases was fitted with VEPFIT [96]. After the annealing process the diffusion length could be increased by a factor of three to 135.2 nm compared to 45.0 nm of the initial state. Hence, an annealed Ni foil re-moderator with a thickness of 100 nm is well suitable for the brightness enhancement since the diffusion length is in the order of the foil thickness and even larger.

4.6.3 DBS Measurement of the Implantation Energy

When using a brightness enhancement system in transmission geometry in order to obtain the maximum re-moderation efficiency, it has to be ensured that the thermalized positrons reach the opposite surface of the material with high probability. Besides the losses due to positron trapping in lattice defects within the material, also the thickness of the re-moderation material is a critical issue. The re-moderators have to be produced thin enough in order to guarantee that the positrons reach the opposite side of the material within their diffusion length. Within this work, a free-standing 100 nm thick Ni foil is used for re-moderating the positrons.

In a next step, the positron implantation energy shall be chosen such that it is sufficiently high to ensure that a maximal fraction of the moderated positrons reaches the back side of the foil but low enough for them to be fully thermalized. In order to do so, the energy-dependent annihilation rate in the re-moderator foil was determined with the CDBS "version 2". In figure 4.12 the result of the measurement is shown. Here, the measured counts in the 511 keV photo peak divided by the total counts of the spectrum is plotted over the implantation energy. This serves as an indicator for the fraction of positrons annihilating inside the re-moderation foil. With increasing implantation energy, the fraction of positrons annihilating inside the foil increases until a maximum is reached at around 4.3 keV. At higher energies the positrons pass the foil without being fully moderated resulting in a decrease of the annihilation rate. According to the Makhovian profiles, a positron energy of 4.3 keV is equal to an implantation depth of 45 nm. Even if 2.2 % of the positrons are shot through the foil as calculated, it is ensured that within the diffusion length of 135 nm a maximum amount of positrons can reach the opposite side of the Ni(100) foil.

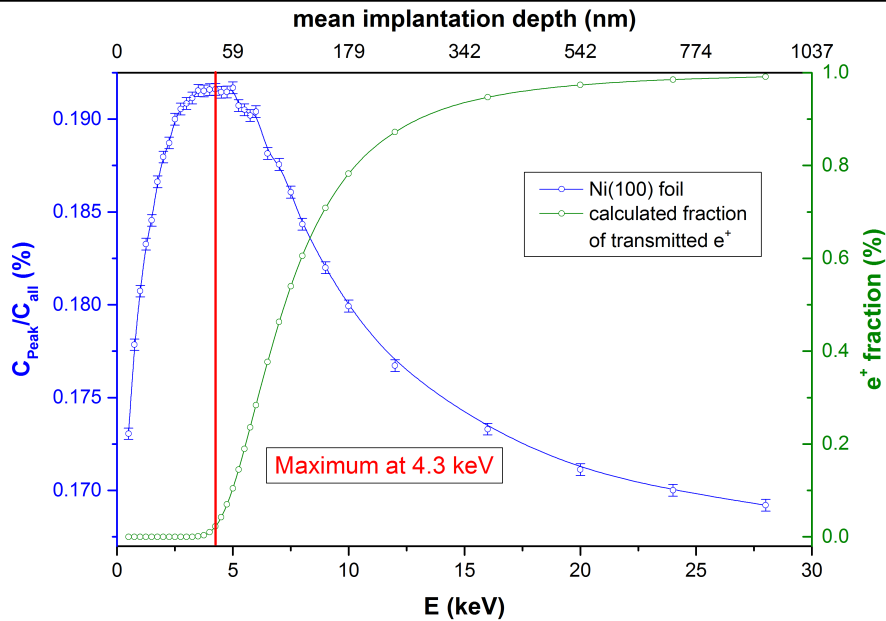


Figure 4.12: Intensity measurement performed on the 100 nm thick Ni(100) foil. For different implantation energies the fraction of positrons annihilating within the 100 nm thick foil is calculated and measured with the CDBS "version 2". The amount of positrons annihilating within the re-moderation foil is calculated by dividing the amount of counts in the 511 keV photo peak C_{Peak} through the total counts in the spectrum C_{all} . At an implantation energy of 4.3 keV which is equal to an implantation depth of 45 nm, most of the positrons are implanted in the re-moderation foil. According to the calculation of the Makhovian implantation profile, only a fraction of 2.2 % is passing through the foil without getting thermalized (right axis).

4.7 Performance of the CDBS *upgrade* Microbeam

The goal of the CDBS *upgrade* was to achieve a reduction in the diameter of the positron beam down to the micrometer range in comparison to the former instrument CDBS "version 2" for high resolution experiments. The simulations presented in section 4.5 suggest that the beam diameter should be successfully reduced with the help of the new components. In the following section, the measurement results showing the capabilities of the upgraded spectrometer will be shown. In the final state a three fold moderation is used to create the positron microbeam. In the following, the 20 eV re-moderated beam provided by NEPOMUC is called "NEPOMUC re-moderated beam" and the three-fold moderated beam using the new brightness enhancement system of the CDBS *upgrade* is called "positron microbeam".

4.7.1 Beam Profile Measurements

Profiles at the Beam Monitors

The performance of the various magnetic guiding and correction fields as well as the electrostatic acceleration and focusing systems of the spectrometer can be examined by the use of three beam monitor (BM) systems located at key positions of the spectrometer as shown in figure 4.2. The detected beam profiles at these positions can be seen in figure 4.13. Since no apertures have been used for avoiding any transport losses within the electrostatic guiding system, the intensity profiles are normalized to the same value. The NEPOMUC re-moderated beam with an energy of 20 eV enters the spectrometer with a diameter of about 2.5 mm as determined at BM 1. Noteworthy is the good quality in shape which is important for the proper operation of the electrostatic acceleration and focusing systems. After passing the accelerator and the first lens system, a beam spot diameter of 0.5 mm at the position of the Ni(100) foil is achieved (middle image in figure 4.13) with a beam energy set to 5 keV as it is necessary for the brightness enhancement. As shown in the right profile of figure 4.13, the NEPOMUC re-moderated beam can be focused to a spot size of 0.25 mm by the use of the new second electrostatic lens system at the maximum beam energy of 30 keV, even without the brightness enhancement system. Comparing this value to the CDBS "version 2", the beam spot size could be reduced by 16 % at the maximum implantation energy

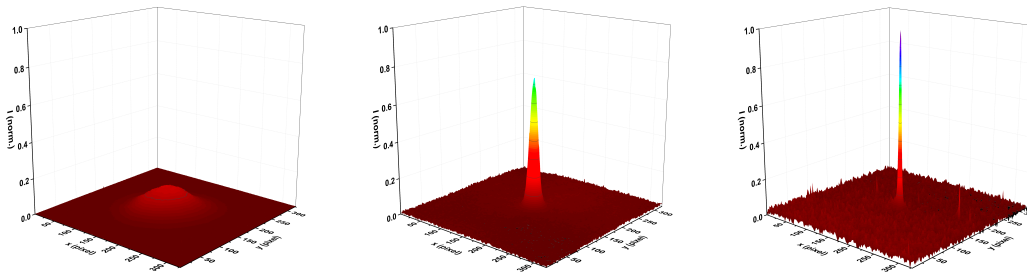


Figure 4.13: Measured 2D intensity plots with the beam monitors BM 1-3 of the CDBS *upgrade* without the use of the brightness enhancement system. (left) 20 eV re-moderated beam as provided by the NEPOMUC source with a diameter of 2.5 mm (FWHM) measured at BM 1. (middle) beam profile after accelerating and focusing onto BM 2 at the position of the re-moderation foil. A diameter of 0.5 mm (FWHM) is obtained with the first electrostatic lens system. By focusing with the second electrostatic lens system and acceleration of the positrons onto the sample position, a beam diameter of 0.25 mm (FWHM) at an energy of 30 keV could be achieved (right). The peaks are normalized to the same integrated counts.

which is mainly attributed to the more homogeneous magnetic beam guidance, an additional μ -metal shielding, the use of non-magnetic materials for all instrument parts and the new designed and simulated lens systems for beam focusing.

Noteworthy is the use of a new beam monitor (BM 3) at the sample position. A simple phosphor screen without the use of MCPs enables a quick direct visual feedback, monitored by a Basler scout camera (Basler scout scA1300 - 32gm), for adjustment of the magnetic and electrostatic fields before each beamtime. This makes it possible to reduce the beam adjustment time to about one hour before the first measurement. The blank phosphor screen in combination with the Basler CCD (pixel size: $4.65 \mu\text{m} \times 4.65 \mu\text{m}$) and an optics of 35 mm focal length results in minimal resolvable structures in the range of $23.3 \mu\text{m}$ per pixel.

Beam Diameter Measurement with the Knife Edge Method

Smaller beam spot sizes such as in the range of a few μm can no longer be resolved with the above mentioned system. For this purpose, a more accurate method is feasible, the so-called knife edge method. This technique, already used in light optics, enables a precise measurement of the beam diameter [98]. It is not circumscribed by the resolution of the camera and phosphor screen any more. The only restriction is the minimal

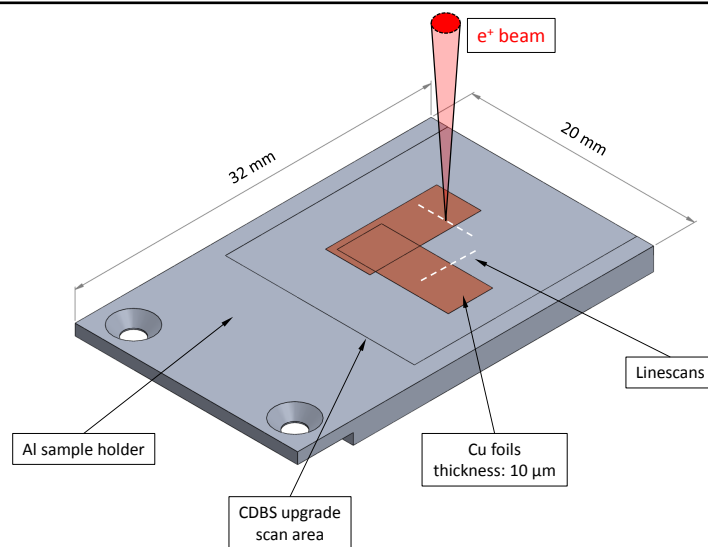


Figure 4.14: Specially prepared sample holder of the CDBS *upgrade* for determining the beam spot diameter in x- and y-direction (dotted white lines). By scanning over an Al/Cu edge, a profile which can be fitted by an error function according to the knife-edge method is obtained as these two materials provide a distinct contrast of the measured S-parameter.

positionable distance of the knife edge with the piezo positioners. Here, the accuracy is in the range of nm and therefore enables a sufficient accuracy.

For the CDBS *upgrade*, a specially prepared sample holder consisting of an Al base material with two stripes of 10 μm thick Cu foils stucked on it was prepared (figure 4.14). Due to a distinct contrast in the S-parameter between these two materials, a typical profile of an error function can be obtained by scanning over the sharp edge. Hence, the $S(x)$ profiles were fitted by the following formula [19].

$$S(x) = \frac{S_{Al} + S_{Cu}}{2} + \frac{S_{Al} - S_{Cu}}{2} \cdot \text{erf} \left(\frac{x - x_0}{\Delta x} \right) \quad (4.1)$$

Here, x_0 is the coordinate of the Al/Cu edge on the sample holder. With Δx , the spot diameter of the beam can be determined according to

$$d_{\text{FWHM}} = \Delta x \cdot 2\sqrt{\ln 2}. \quad (4.2)$$

The results of the linescans for the focused NEPOMUC re-moderated beam as well as for the positron microbeam are given in figure 4.15.

As expected a clear transition from low to high S-parameter at the position of the Cu/Al edge can be observed. An error function (dotted lines in figure 4.15) was

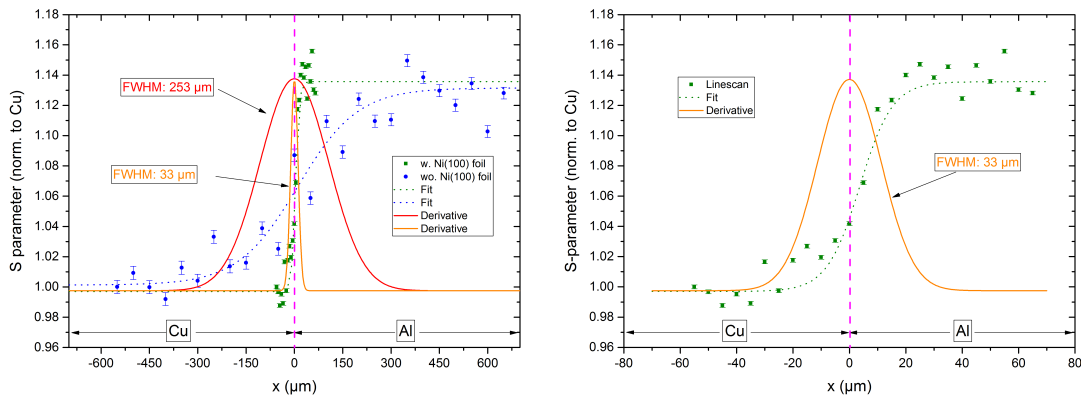


Figure 4.15: Linescans over the Al/Cu edge performed with the CDBS *upgrade* on the sample holder shown in figure 4.14 at the maximum beam energy. By fitting an error function to the obtained S-parameter profile (dotted lines) a beam diameter of 33(7) μm is obtained for the positron microbeam and 253(40) μm for the NEPOMUC re-moderated beam. The derivatives are plotted as solid lines. The right figure shows a zoom-in of the left figure with its evaluation of the positron microbeam.

fitted to the data in order to obtain the beam diameter from its derivative (solid lines). At the maximum beam energy, 30 keV for the re-moderated NEPOMUC beam and 25 keV for the positron microbeam, the FWHM values for the diameter are determined to $253 \pm 40 \mu\text{m}$, which is in good agreement with the beam profile shown in figure 4.13(right), and to $51 \pm 11 \mu\text{m}$ respectively by using the brightness enhancement system. This value could be further reduced to $33 \pm 7 \mu\text{m}$ by the use of an aperture in front of the Ni(100) foil as shown in figure 4.15(right).

Using the movable sample holder also larger samples of a size of up to $20 \times 20 \text{ mm}^2$ can be positioned below the positron beam. Throughout the measurements the position of the beam remains unchanged whereas the sample is moved by the sample holder. Therefore, since the entire movable head of the sample holder including the potential plates are put on high voltage, a possible distortion of the electrostatic field at the sample position can influence the quality of the beam. Hence, it is necessary to verify if the performance for both beam settings keeps constant over the full scanning range.

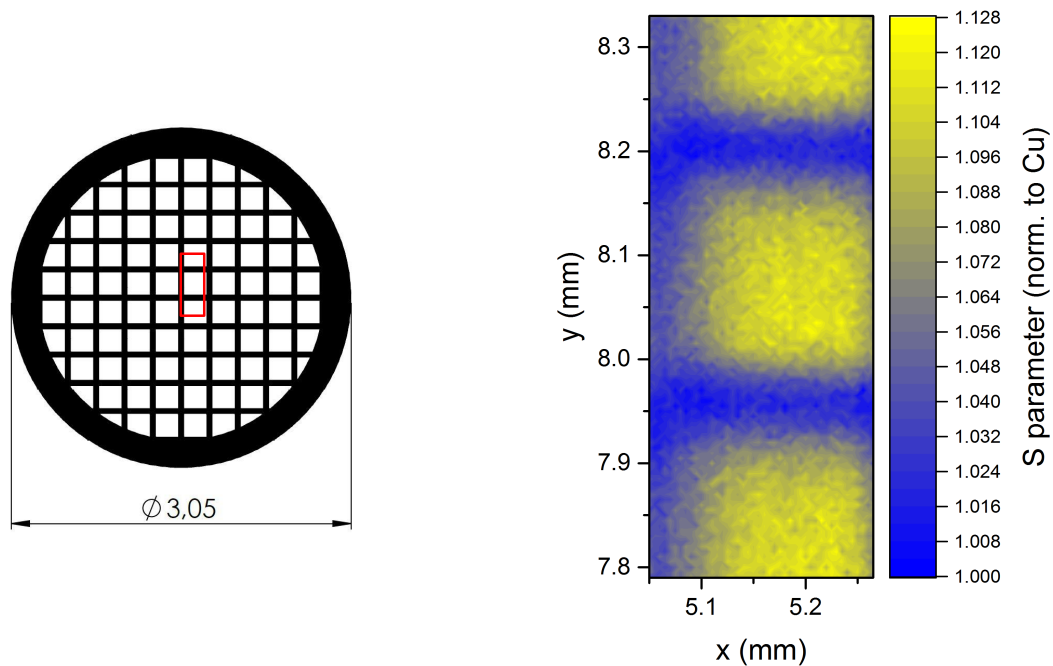


Figure 4.16: 2D S-parameter map performed on a Cu mesh glued onto an Al sample holder. (left) Cu mesh with a thickness of the bars of $50 \mu\text{m}$ with $204 \mu\text{m}$ spacing in between. The scan area is marked by the red rectangle. (right) Recorded S-parameter map with the positron microbeam of the CDBS *upgrade* at an implantation energy of 25 keV. The step width in x- and y-direction was $5 \mu\text{m}$ each with an acquisition time of 7 s per measurement point. Notice the distortion free imaging of the mesh.

This was tested on two specially patterned samples by performing 2D scans with various step widths (Δ_x, Δ_y) and measurement times (t_m).

First, a 2D S-parameter map on a suitable sample consisting of a thin Cu grid with $50 \mu\text{m}$ thick bars spaced by $204 \mu\text{m}$ produced by Plano GmbH for testing the resolution of secondary electron microscopes (SEMs) was measured. The sample was scanned in x- and y-direction with a step width of $5 \mu\text{m}$, respectively, and a measurement time $t_m = 7 \text{ s}$ yielding a 2D S-parameter map shown in figure 4.16 (right). Despite the short measurement time per point of only 7 s, the Cu bars can be easily resolved due to the high contrast in S-parameter between the Cu and Al. Moreover, the 2D S-parameter map shows no distortions, meaning that the beam quality is maintained throughout the scanning range.

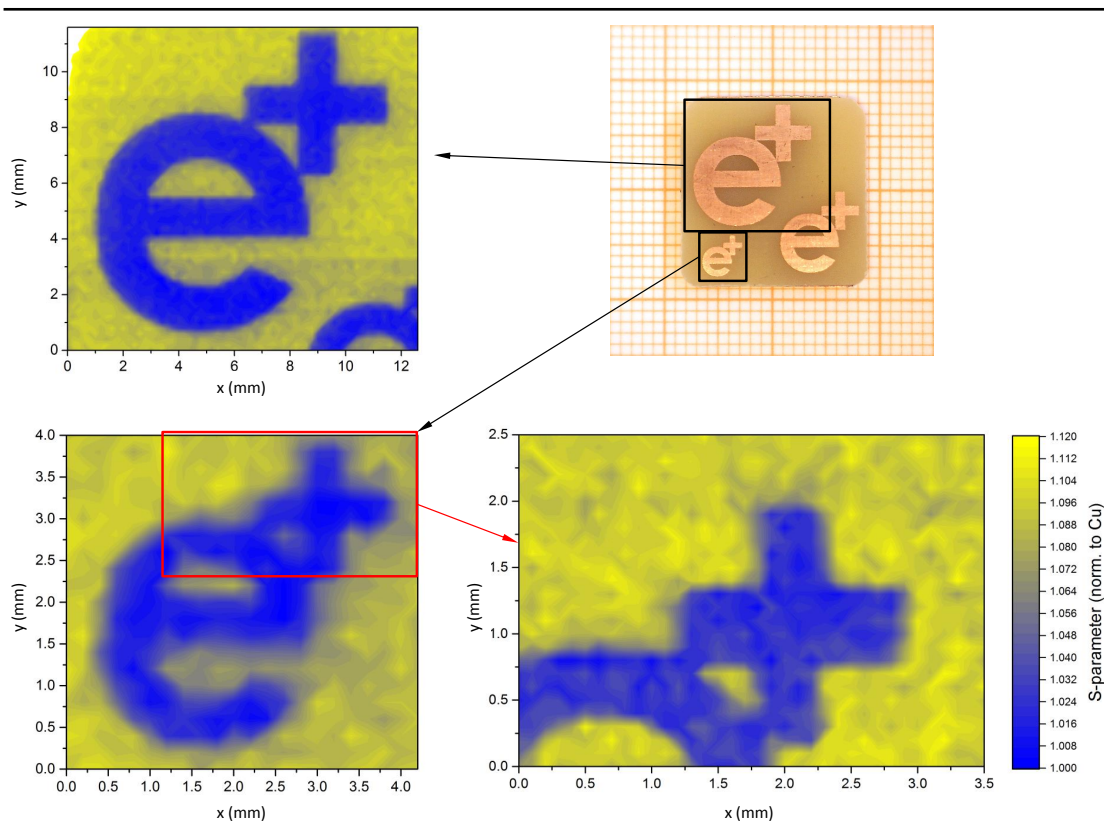


Figure 4.17: Sample holder with etched Cu "e+" patterns in a circuit board (optical image upper right). 2D S-parameter maps were performed of the largest and smallest e^+ pattern marked by the black rectangles with the NEPOMUC re-moderated beam and a step width of $\Delta_{x,y} = 200 \mu\text{m}$ and measurement time of $t_m = 13 \text{ s}$. Both patterns could be resolved without any distortions. A smaller part of the smallest "e+" (red rectangle) was mapped with the positron microbeam providing the best resolution (step width of $\Delta_{x,y} = 100 \mu\text{m}$, $t_m = 25 \text{ s}$).

For investigating larger samples up to the size of the full scanning range of 20×20 mm, a 2D S-parameter map on a second sample consisting of three patterns of "e⁺" with different sizes etched in a circuit board are shown in figure 4.17 upper right. The S-parameter was obtained by averaging the data of all four HPGe detectors at an implantation energy of 30 keV for the NEPOMUC re-moderated beam and 25 keV for the positron microbeam. The step size for the NEPOMUC re-moderated beam was set to $200 \mu\text{m}$ and despite some blurring at the smallest e⁺, it is possible to resolve the structure with the $250 \mu\text{m}$ beam diameter without distortions over the entire scanning area. Nevertheless, with a resolution of $50 \mu\text{m}$ (FWHM) of the positron microbeam the pattern easily can be resolved without blurring and distortions also for larger scanning areas up to the maximum range (step width of $\Delta_{x,y} = 100 \mu\text{m}$, $t_m = 25$ s). Note that the fast measurement times for acquiring complete 2D S-parameter maps of roughly 160 min/mm^2 with the positron microbeam and $< 2 \text{ min/mm}^2$ with the NEPOMUC re-moderated beam and a step width and measurement time of $\Delta_{x,y} = 50 \mu\text{m}$, $t_m = 25$ s per point and $\Delta_{x,y} = 250 \mu\text{m}$, $t_m = 7$ s per point, respectively. Hence, the upgrade of the spectrometer provides an outstanding performance in routine operation enabling high resolution defect imaging over a scanning range of $17 \times 20 \text{ mm}^2$ with short measurement times.

4.7.2 Count Rate Measurement at the CDBS *upgrade*

Short measurement times can only be realized by the high intensity of the NEPOMUC source and the in situ preparation of the Ni(100) foil for maximizing the re-moderation yield. Before each operation of the brightness enhancement system, the Ni(100) foil has to be prepared by a combined heat and H treatment. For this, the foil can be placed inside a special chamber by a rotatable push/pull translator with an installed resistive heating device which is explained in detail in the appendix A.4. First the foil is slowly heated to 500°C in UHV conditions within one hour to prevent any rippling caused by the heat expansion. Then the temperature is held constant for an additional hour in a H atmosphere of 10^{-3} mbar. After slowly cooling down to avoid cracking of the free-standing foil, it can be transferred into its position in the brightness enhancement system. The influence of this procedure on the count rate can be found in table 4.1.

The NEPOMUC re-moderated beam provides an intensity of typically 3.0×10^7 moderated positrons per second [14]. This leads to a count rate of 60000 cps displayed by one of the four DSPs of the CDBS by taking into account the solid angle and the detection efficiency of the detectors. However, it has to be emphasized that the count rate displayed by the DSPs is not proportional to the counts recorded in the spectrum. At low count rates (< 45 kcps) this number is underestimated by the DSPs and, vice versa, overes-

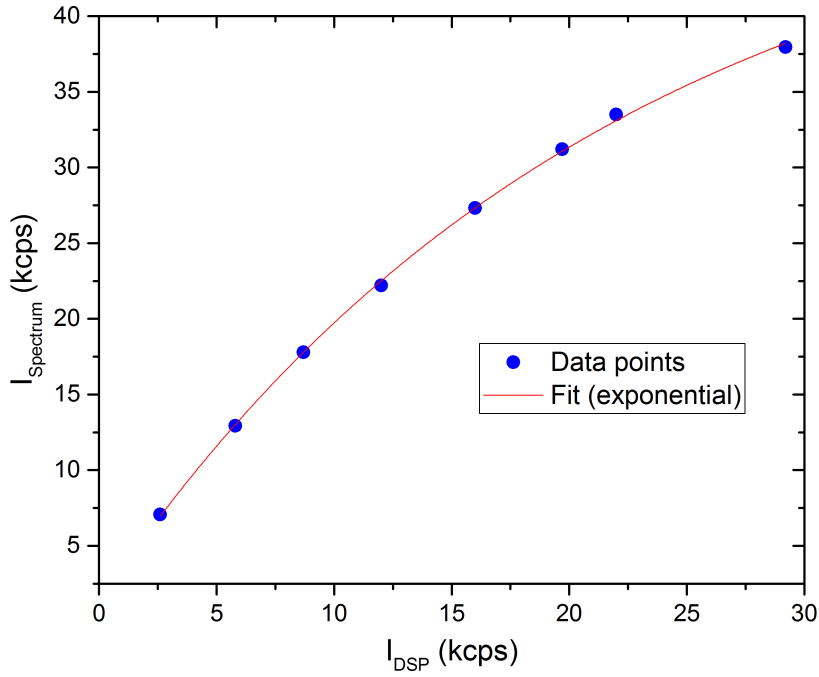


Figure 4.18: Calibration curves for the count rate measurement with the digital signal processor (DSP) of the CDBS. For the calibration a radioactive ^{152}Eu source with an activity of 2.42×10^5 Bq, was positioned at different distances in front of the detector. As a result, an exponential correlation between the count rate I_{Spectrum} determined from the recorded spectra and the displayed DSP count rate I_{DSP} was found.

timated at high count rates (> 45 kcps). In order to determine the efficiency of the brightness enhancement system this displayed rate has to be corrected for background and dead time. Afterwards, the total count rate in the 511 keV photo peak could be determined with the help of the peak to total ratio determined from two spectra with and without the use of the brightness enhancement system. For the determination of the dead time corrected count rate a calibration curve was recorded as shown in figure 4.18. For this, a radioactive ^{152}Eu source with an activity of 2.42×10^5 Bq was positioned at different distances in front of the HPGe detector. The count rate displayed by the DSP was plotted versus the dead time corrected count rate determined from the spectrum. With an exponential fit a model function of the dead time corrected count rate could be obtained. After subtracting the typical background of 0.12 kcps in the experimental hall during reactor operation the corrected DSP count rate could be obtained (I_{Spec} in table 4.1). With the peak to total values of 0.179 and 0.139 for the NEPOMUC re-moderated and the CDBS *upgrade* micro beam, respectively, the total count rate in the photo peak was obtained and is given in column I_{PH} in table 4.1.

By inserting the Ni(100) foil in the as-received state the count rate in the photo peak drops to 0.12 kcps equivalent to an efficiency of 1.4 %. Already by heating the foil, the count rate could be increased to 0.6 kcps, attributed to the desorption of the surface impurities to some extent as measured with XPS presented in figure 4.10. With the additional H treatment, a final efficiency of 19.1 % equivalent to a count rate of 1.59 kcps in the photo peak could be achieved.

Condition of Ni(100) foil	I_{DSP} (kcps)	I_{Spectrum} (kcps)	I_{PH} (kcps)	Efficiency (%)
Not inserted	60.0	46.5	8.32	—
As received	0.51	0.88	0.12	1.4
Heated to 500 °C in UHV	2.10	4.32	0.60	7.2
Heated to 500 °C + H ₂	5.80	11.4	1.59	19.1

Table 4.1: Measured dead time corrected count rates and efficiencies of the brightness enhancement system of the CDBS *upgrade*. Given are the total counts I_{DSP} delivered by the DSP for the entire spectral range. Additionally, after dead time and background correction (I_{Spectrum}) subsequent to determination of the counts in the photo peak (I_{PH}), the efficiency of the brightness enhancement system could be calculated.

5 High Resolution Defect Spectroscopy

Within this chapter, measurements performed with the CDBS *upgrade* are presented in order to show its outstanding performance for 3D defect spectroscopy with highest spatial resolution. The first sections are dedicated to the comparison of two commercially available welding techniques, FSW and LBW. CDBS is chosen to elucidate the microscopic distribution of the welding process in terms of the formation of precipitates and vacancies. The obtained information is then compared to material properties such as strength and hardness. In the last section, the capability of the CDBS *upgrade* microbeam will be presented to analyse the texture and hence, visualize different oriented grains in polycrystalline Pt.

5.1 Modern Welding Techniques

Most of today's industrial processes comprise the joining of different parts of produced items, especially in the automotive sector and the aircraft construction industry. In this regard, various joining techniques such as screwing, riveting, welding and, more recently, gluing have been developed. In this thesis, the focus lies on FSW and LBW. The investigated materials are an AlCu6Mn alloy and stainless steel.

During a welding process, materials are exposed to high temperature and deformation. Therefore, in the zone of welded joints, the local mechanical properties are influenced due to the strong spatial dependent structural changes and production of various defects. Detailed knowledge on the atomic disorder and the defect structure is necessary to understand the local materials properties. Positron spectroscopy is a powerful tool to gain insight on these micro-structural effects.

In order to do so, defect measurements with positrons are combined with optical microscopy to determine the grain structure of the materials and Vickers hardness measurements to investigate their influence on the strength of the joints. Finally, differences and similarities of the different measurement techniques will be discussed.

Demonstrated on the case of the stainless steel alloy weld, a newly invented in-situ tension testing machine enables the investigation of the defect depending strength of the material during putting load on the sample.

5.1.1 Methods and Materials

In this section, the general procedure of the welding techniques employed on the investigated samples will be explained first. In section 5.1.1.2, the principle of age hardening is introduced taken the example of an AlCu alloy. Age hardening is largely applied in industrial processes to influence a material's hardness. The investigated materials, AlCu6Mn and stainless steel, will be content of section 5.1.1.3. Their physical properties will be given as well as the parameters used during preparation. In section 5.1.1.4, theoretical considerations will be given needed for the examination of AlCu alloys with positrons.

5.1.1.1 Welding Techniques

When metallic parts have to be joined together, mostly welding techniques, such as arc welding or spot welding are applied. In comparison to the techniques mentioned above, welding can lead to a significant reduction in weight as additional components, such as screws or rivets, are not necessary. Moreover, an overlap of the construction parts can be avoided.

Traditional arc welding techniques, such as stick welding, use an electrical arc in order to create enough heat to melt the metal resulting in a binding of the parts after cooling. However, in order to create larger welds, filler materials are needed. In contrast, with friction stir welding (FSW) and laser beam welding (LBW), two parts can be joined together without any filling material. Therefore, light-weight constructions can be created that are crucial for, e.g., the aircraft industry.

Friction Stir Welding (FSW) Historically, FSW was invented as a solid-state joining technique by the welding institute (TWI) in the United Kingdom. It was patented in 1991 by Thomas et al. and initially applied to Al alloys [99]. With this technique, two components are joint together by a rotating tool consisting of a specially designed pin and shoulder that can withstand the welding temperatures. For joining Al alloys the pin material of choice is mostly steel [100]. This tool is inserted into the abutting edges of two sheets or plates that should be joined as shown in figure 5.1. As a result of the interaction between the inserted tool and the two parts, frictional heat is generated and due to the softening of the material the joint is produced by plastic deformation

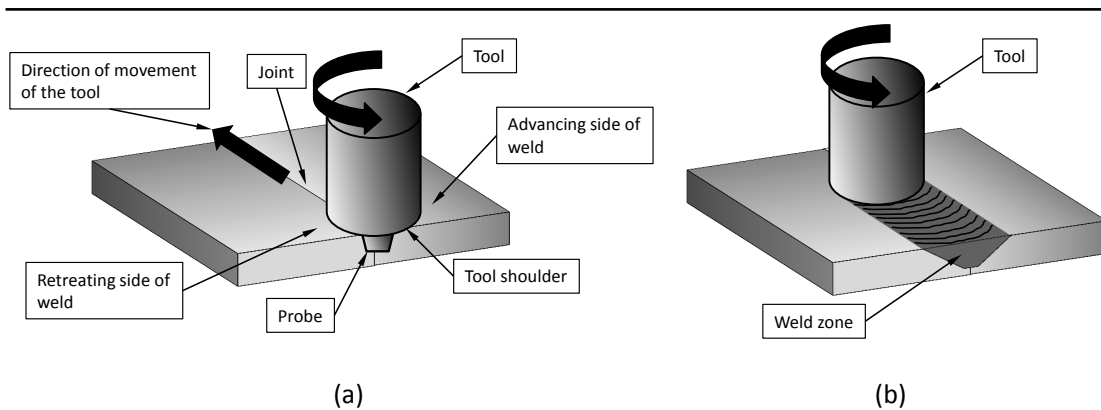


Figure 5.1: Principle of friction stir welding (FSW). (a) A rotating tool consisting of a small pin surrounded by a flat shoulder is plunged into the abutting edges of two parts which should be welded together. (b) The frictional heat of the pin and its translation through the work pieces causes a plastic deformation at elevated temperature below the melting point. Hence, the two parts are "stirred" together and the shoulder of the tool flattens out the surface of the produced weld.

of the work pieces. Thus, due to the rotation of the pin and the translation through the work pieces, a movement from the material from the front of the pin to the back caused. The shoulder of the tool then flattens out the produced joint.

FSW is a solid state, hot-shear joining process that causes severe plastic deformation of the work material at elevated temperature. As a result, fine and equiaxed recrystallized grains are induced within the material [101–104]. This fine micro-structure is of major advantage as it improves the mechanical properties of the working material. Further advantages are the consummation of less energy during the welding process. Besides this, the weld is highly stable against oxidation and, thus, no protective gas or fluxing agent have to be used for protection. This technique is capable of joining different materials together, such as copper and aluminum [105, 106]. Because of these benefits, FSW is considered as a most significant development in metal joining.

Laser Beam Welding (LBW) LBW uses a focused laser beam in order to melt the junction of the work pieces. After subsequent cooling, the materials are effectively joined together. A sketch of the process is shown in figure 5.2.

LBW is an excellent technique that frequently outperforms traditional welding techniques due to various advantages [107]. The laser beam can be focused to create a weld spot diameter in the micrometer range. Consequently, a high weld accuracy, also in complicated joint geometries, can be achieved with high reproducibility. A well focused

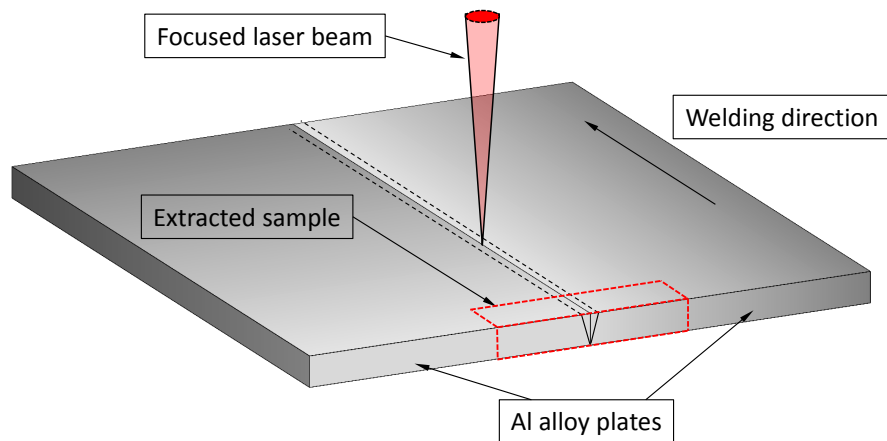


Figure 5.2: Principle of laser beam welding. A laser beam melts the junction of two materials which are jointed after subsequent cooling. In this work, two Al sheets of 4 mm thickness were welded together. For the investigation, a 20 mm broad and 5 mm long block was cut out symmetrically around the weld indicated by the red region.

laser beam bears the advantage of a low heat input causing only minor changes of the micro structure of the material and low thermal distortion of the construction parts. In this regard, the heat affected zone (HAZ) described by the area near the weld which is not melted during the process but which micro structure and properties are still influenced throughout the process. LBW is able to reduce the HAZ to the millimetre range while with FSW it is in the range of centimetres due to the larger welding tools. All in all, cavity-free welds can be realized with high reliability enhancing the mechanical strength of the joint [107].

Especially the welding of high strength Al alloys, containing Cu or Li, is a key technology in modern manufacturing engineering since lightweight constructions more and more replace heavier steel and riveted joint constructions [108, 109]. Therefore, in order to avoid deterioration of the mechanical properties it is of particular interest to produce high strength welds with low defect concentration.

5.1.1.2 Age-Hardening of Al-Cu Alloys

Age hardening is of technological importance as a means of strengthening many alloys. Alloy systems in which the solid solubility of one or more of the alloying elements increases with increasing temperature are amenable to the technique of age hardening [110]. In this context, solid solubility refers to the magnitude of material that is able to be dissolved in the base material without phase-separation. During solution treatment,

the alloy is exposed to high temperatures where the alloying elements mix according to the phase diagram shown in figure 5.3. This process increases the solid solubility of the alloy and a higher amount of alloying elements is homogeneously distributed within the material. Subsequent quenching, usually carried out in cold water, leads to the formation of a so-called supersaturated solid solution (SSSS) which can dissolve more material than under normal conditions. Over time the SSSS decomposes to form finely dispersed precipitates of an impurity phase hardening the material. This phenomenon is called age or precipitation hardening. It is a naturally and spontaneously occurring process that can, however, be accelerated by so-called artificial age hardening. Hereby, the SSSS is tempered at intermediate temperatures for convenient ageing times.

Historically, the phenomenon of age hardening was discovered in an AlCuMg alloy by the German metallurgist Alfred Wilm in 1911 [111]. His work led to the development of the alloy duraluminium which is extensively used in the aircraft industry. Since then many other age hardenable aluminum alloys have been developed. Among them, especially AlCu alloys are well-known high-strength and low-weight materials with a wide range of applications. In AlCu alloys, the Cu can be dissolved completely at a temperature of 548 °C. Due to the same lattice structures of Cu and Al which is fcc, the solubility of Cu is enhanced [109]. At lower temperatures, coherent and semi-coherent precipitates are formed.

The AlCu alloy investigated within this work, EN AW-2219-T87 or AlCu6Mn, is a typical representative of a heat treatable age hardening Al alloy with mechanical properties which strongly depend on the presence of Cu precipitates [109, 112]. Figure 5.3 shows its corresponding phase diagram. The entire process of solution annealing and artificial ageing and therefore the formation of Cu precipitates is described by Hatch and Ostermann [109, 112]. Its phases correspond to the following sequence:

1. supersaturated solid solution α -phase
2. coherent plate-like Guinier-Preston (GP) zones
3. coherent plate-like θ'' -phase
4. semi-coherent plate-like θ' -phase
5. non-coherent plate-like θ -phase

Since the technique of age hardening is highly dependent on the nature of precipitation processes, the latter continues to stimulate the converging interest of metallurgists, chemists, and solid state physicists.

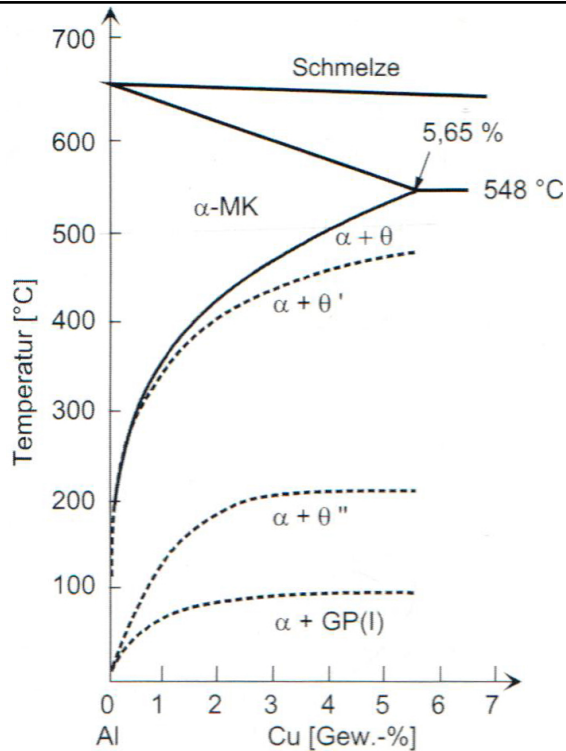


Figure 5.3: Phase diagram of the binary alloy system AlCu. Image taken from [109].

5.1.1.3 Preparation and Physical Properties of the Examined Materials AlCu6Mn and V2A

The two materials investigated within this work are the age-hardening Al-based alloy AlCu6Mn (DIN number: EN AW-2219 T87) and the state-of-the-art material for many industrial applications stainless steel or also called "V2A" (X5CrNi18-10, material number: 1.4301). Table 5.1 comprises their most important physical properties. Additional information is given in the appendix A.6.

The AlCu alloy EN AW-2219 T87 with a Cu content of 6.3% is a typical example of a precipitation hardening material (s. section 5.1.1.2). Its strength is significantly enhanced by the formation of Cu precipitates in the material matrix during a first heat treatment [109, 112]. In this context, the suffix "T87" in the DIN number refers to the artificial aging process. During this process, a solution heat treatment followed by quenching with cold water is carried out. Afterwards, the material is 7% cold worked and aged at a temperature of 170 °C for several hours [115]. The formation of Cu precipitates depends on the phase diagram of the alloy and influences the strength of the material [109, 116].

Property	AlCu alloy (EN AW-2219 T87)	Steel V2A (1.4301)	Unit
Density	2.84	8.00	g/cm^3
Melting point	643	1450	$^{\circ}C$
Modulus of elasticity	73.1	193	GPa
Tensile strength, yield	393	215	MPa
Tensile strength, ultimate	476	505	MPa
Thermal conductivity	121	16.2	W/mK

Table 5.1: Important properties of the age hardening AlCu alloy and the stainless steel 1.4301 taken from data sheets of the ASM Aerospace Specification Metals Inc. [113, 114].

Complementary to LBW and FSW of this age hardening AlCu alloy, a LBW produced out of stainless steel (X5CrNi18-10, WNr. 1.4301), also known as V2A, will be presented. As V2A is mostly employed in the automotive sector where weight-reduction is crucial, welding as joining technique is of high interest. Similar to the Al alloy, the influence on the strength of the material due to the defect distribution produced during the welding process will be shown.

5.1.1.4 Theoretical Framework for the Examination of Al and AlCu Complexes with Positrons

Crystal defects such as dislocations, precipitates and different species of point defects highly influence or even significantly determine the macroscopic physical properties of all kind of materials. Therefore, the investigation of the nature and concentration of lattice defects plays a major role for an improved understanding of the material properties, which can be deteriorated, e.g., due to the presence of structural vacancies, or considerably improved by deliberate introduction of defects. It may be recalled that the basis of defect spectroscopy using positrons is based on their trapping in open volumes, vacancies and vacancy clusters. Moreover, also agglomerations of a certain material in a different host material can be detected. Hereby, it must be considered that different elements possess different positron affinities. Comparing the elements of interest in this study, Al ($A_{Al}^+ = -4.41$ eV) and Cu ($A_{Cu}^+ = -4.81$ eV), Cu has a higher positron affinity [71]. Applying a quantum-well model, the minimal radius of a

Cu cluster r_c embedded in Al for confining the positron wave function can be estimated by

$$r_c \cong 5.8 \cdot a_0 / \sqrt{|A_{Cu}^+ - A_{Al}^+| / (\text{eV})} \quad (5.1)$$

with Bohr radius a_0 . Inserting the above mentioned affinities for Al and Cu yields to $r_c = 0.49$ nm. Since the van der Waals radius of Cu is $r_{Cu} = 0.2$ nm [117] and thus smaller than r_c , a single Cu atom in an Al matrix cannot be detected. Instead, positrons are only sensitive to clusters of a few Cu atoms.

With (C)DBS, the occurrence of these defects can be monitored as changes in the momentum distribution by detection of the annihilation radiation. In figure 5.4 (left), the momentum density distribution is shown for Al vacancies for two different instrument resolutions. Hereby, the distribution is normalized to a defect-free bulk according to $\frac{I(E)}{I_{ref}(E)} - 1$ and is therefore also called ratio curve (see also section 3.4.2).

As can be clearly seen, the presence of vacancies causes a peak just beyond the bulk Fermi momentum (marked by an arrow). Trapped in such a vacancy, the positron is no longer free to move but is spacially confined. In this confinement, the contribution of the positron momentum to the total momentum of electron and positron can no longer be neglected and thus, results in the so-called confinement peak. More specific, the elemental fingerprints can be determined within the high-momentum region of the annihilation radiation. In this regard, a low background is needed which is accessible in CDBS [118]. Note that the theories referred to in this thesis are based on the work of Folegati et al. [119, 120] and Calloni et al. [118].

Defect Type Calloni et al. demonstrate that along with the chemical information around the annihilation site of the positron, further information about the type of defect can be obtained from the CDBS data. In this regard, a case study was carried out by differently defected Al samples, namely, thermally generated vacancies referred to as "quenched Al" and defects introduced by compression deformation referred to as "deformed Al". In figure 5.4 (right), the momentum density curves of the annihilation radiation in presence of the two defect types are shown. Concerning their shape, three distinct features can be discussed: a broad maximum at $p = 0$, the already mentioned confinement peak at around $8 - 9 \times 10^{-3} m_0c$ and negative values at high momenta.

In their work, Calloni et al. relate these features to the magnitude of linear relaxation of the lattice within a theoretical framework. In Al, the expected relaxation for an empty vacancy in the bulk is inwards whereas in the presence of a positron it is outwards. The first feature is explained by a narrowed valence electron momentum distribution

associated with the reduction of electron density at the defect. Dependent on the relaxation mechanism of the lattice at the defect site, the electron density may be in- or decreased and subsequently the broad maximum at zero momentum may be de- or increased. Besides this, the height of the confinement peak increases with increasing degree of relaxation. Lastly, negative values at high momenta result from the reduction of the annihilation with core electrons.

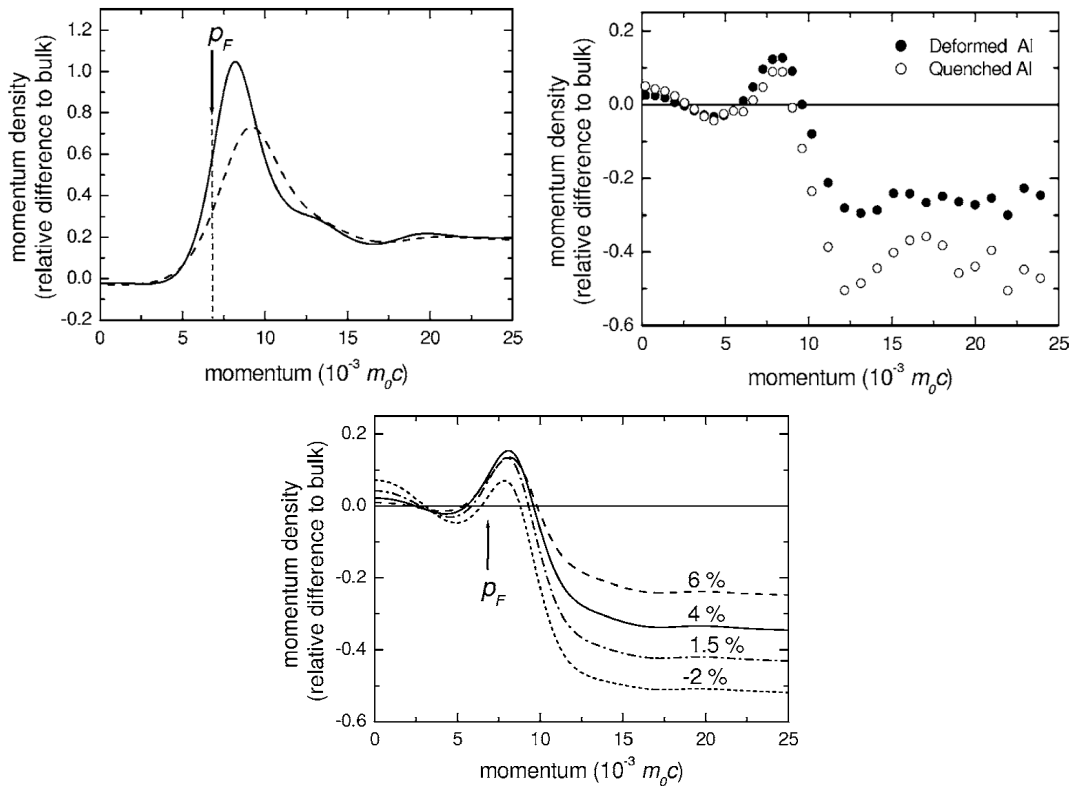


Figure 5.4: Positron confinement in an Al vacancy. A non-negligible momentum causes a so-called confinement peak in the Doppler broadened spectrum at a momentum of around $8 - 9 \times 10^{-3} m_0 c$. Upper left: Simulation of confinement peaks for two different instrument resolutions (solid line: $2 \times 10^{-3} m_0 c$, dashed line: $4 \times 10^{-3} m_0 c$). With higher resolution the confinement peak is narrowed, higher in intensity and shifted towards lower momenta. Upper right: Comparison of the confinement peaks for deformed and quenched Al. The shape of the confinement peak differs dependent on the type of defects. The confinement peak in deformed Al is higher compared to quenched Al. Lower middle: Computed momentum densities with respect to bulk Al for positron trapped at a vacancy. The in- and outward relaxation of the nearest neighbour atoms (negative value for outward relaxation) is influencing the confinement peak as well as the intensity of the ratio curve at higher momenta. Plots taken from [118].

As a conclusion, the difference in the ratio curves in figure 5.4 (right) was then assigned to the local geometry of the defect site and interpreted by a difference between the defect types with regard to the magnitude of their open volume as seen by the positron. In this regard, mono-vacancies rather evolve in "quenched" materials whereas a high density of dislocations and vacancy point defects preferentially form in a "deformed" material [121].

Chemical Composition Additionally, Folegati et al. proof that CDBS is a powerful tool to investigate the chemical surrounding of the defect sites on the example of an Al vacancy. In their work, they show the possibility to determine the number of nearest neighbors of copper atoms that surround an Al vacancy by a linear combination of the ratio curves of an Al vacancy in pure Al (dash dotted line in figure 5.5) and pure Cu. Within their model they assume the crystal structure of their system to be the same as for their constituents, pure Al and pure Cu, namely, face centered cubic (fcc). Within this crystal structure a maximum of 12 nearest neighbors is possible that can be occupied by Cu atoms surrounding an Al vacancy [109, 122]. In figure 5.5, the

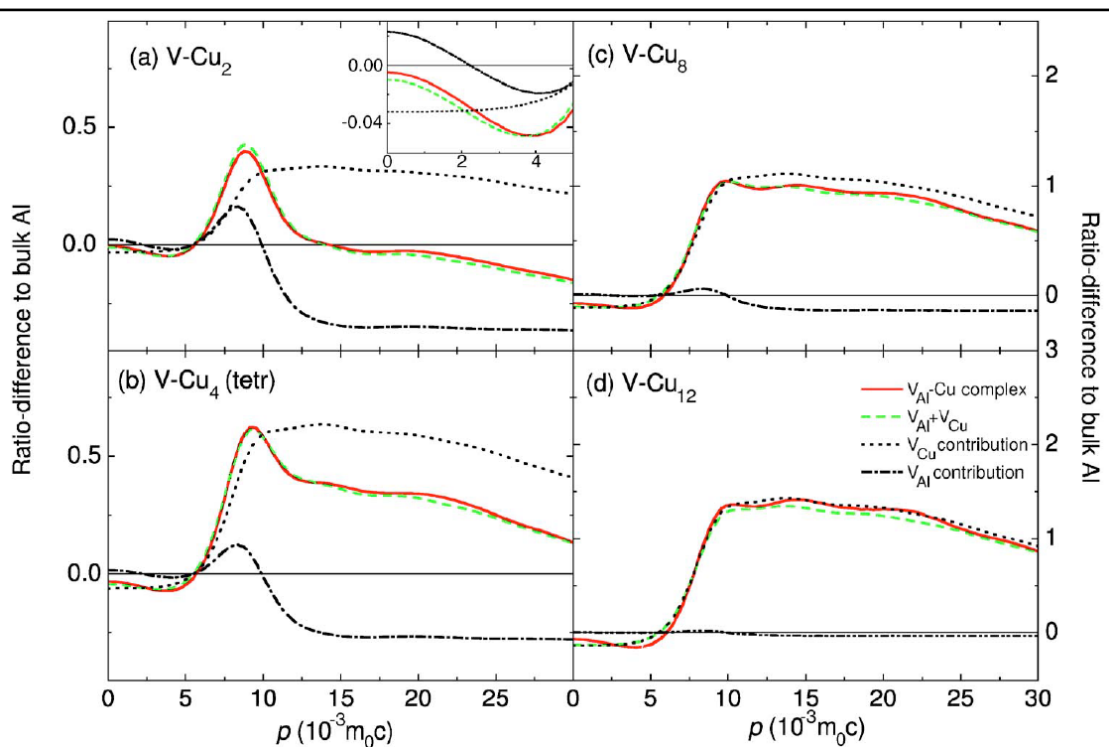


Figure 5.5: Calculated ratio curves for different Al vacancy Cu complexes $V-Cu_n$ in AlCu alloys for (a) $n=2$, (b) 4, (c) 8 and (d) 12 nearest neighbours Cu atoms around the vacancy in an fcc crystal structure of Al and Cu [109, 122]. Image taken from [119].

calculated curves for an Al vacancy with 2, 4, 8 and 12 Cu atoms as nearest neighbours, respectively, are shown. In this approach, a fraction of the theoretical curve for an Al vacancy in pure Al is added to different fractions of the Cu signature is examined in the framework of this thesis.

For the analysis of the CDB-spectra in this thesis the theoretical curve for an Al vacancy in pure Al combined with an experimentally determined spectrum of a Cu reference will be the basis for estimating the mean number of Cu atoms around a vacancy.

5.1.2 Characterization of Friction Stir Welded AlCu6Mn

Within this section, FSW welds performed on EN AW-2219 T87 are examined. General features of the welding process and the material can be found in chapter 5.1.1. According to Bachmann et al. [123] the ultimate tensile strength (UTS) of friction stir welds is predominantly determined by the welding temperature and the welding speed. Therefore, two samples welded with different rotational and welding speed of the tool resulting in different ultimate tensile strength will be compared with the help of optical microscopy. In order to investigate open volume defects and the spatially distributed formation of Cu precipitates, CDBS measurements were carried out.

5.1.2.1 Sample Preparation

FSW samples were manufactured by the institute for machine tools and industrial management (IWB) at TUM. The 4 mm thick Al alloy sheets were welded together with the industrial robot *KUKA KR500-MT* equipped with a FSW spindle and a sensor to control the axial force and temperature during the welding process. The welding tool consisted of a concave shoulder with a diameter of $d_{\text{shoulder}} = 20$ mm and a conical pin

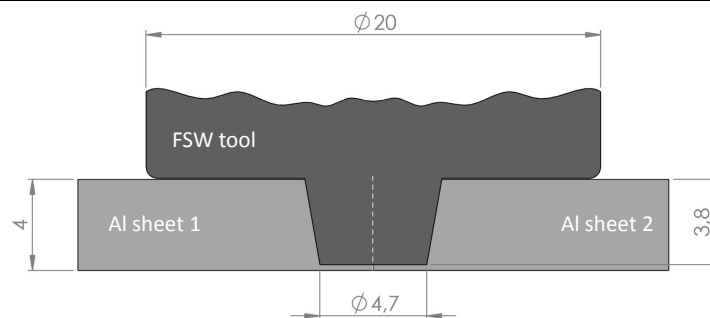


Figure 5.6: Dimensions of the welding tool plunged into the abutting faces of the two Al sheets.

(cone angle $\alpha_{cone} = 10^\circ$) with a tip diameter of $d_{pin} = 4.7$ mm and a pin length of $l_{pin} = 3.8$ mm. An overview of the tool plunged into the abutting faces of the two Al sheets is given in figure 5.6. More details on the entire welding set-up can be found in Bachmann et al. [124].

For the visualization of the depth structure and for 3D defect spectroscopy, a 20 mm broad and 5 mm thick sample was cut out symmetrically around the weld. The abutting surface was polished for the measurements by the IWB. Details to the polishing process can be found in [125].

Exemplarily, the samples of lowest ($R_{m,min}$) and highest ($R_{m,max}$) UTS were chosen from [123] for further investigation, referred to as experiment no. 13 and 6, respectively. The welding parameter for the two samples are given in table 5.2.

exp. no.	welding temperature (°C)	welding speed (mm/min)	mean RPM (min ⁻¹)	mean UTS R_m (MPa)
6	540	320	1510	349.67
13	415	50	260	271.67

Table 5.2: FSW welding parameters of the investigated Al-Cu samples [123].

5.1.2.2 Optical Analysis

In order to gain a first insight on the grain structure and the dimensions of the weld, optical light microscopy was carried out with a Nikon SMZ1500 microscope. In a preparation processes, the polished samples were treated chemically for 2 min with a solution of 60 ml H₂O/10 g NaOH/5 g C₆N₆FeK₃ and observed with different magnifications. In order to avoid an influence of the chemical treatment on the CDBS measurements, optical microscopy and the corresponding treatment were performed afterwards. In figure 5.7 the optical images of the samples of maximal and minimal UTS are shown on the left and right, respectively.

Both samples clearly show the structure of the weld within the base material. Moreover, the typical contour shape of the welding tool as well as a clear distinction between the advancing side and the retreating side of the welds located at the right and left, respectively is visible. The differences in the preparation of the two samples concerning welding speed and rotational speed (RPM) during FSW(see table 5.2)is reflected in structural differences. Consequently, higher friction between the welding tool and the

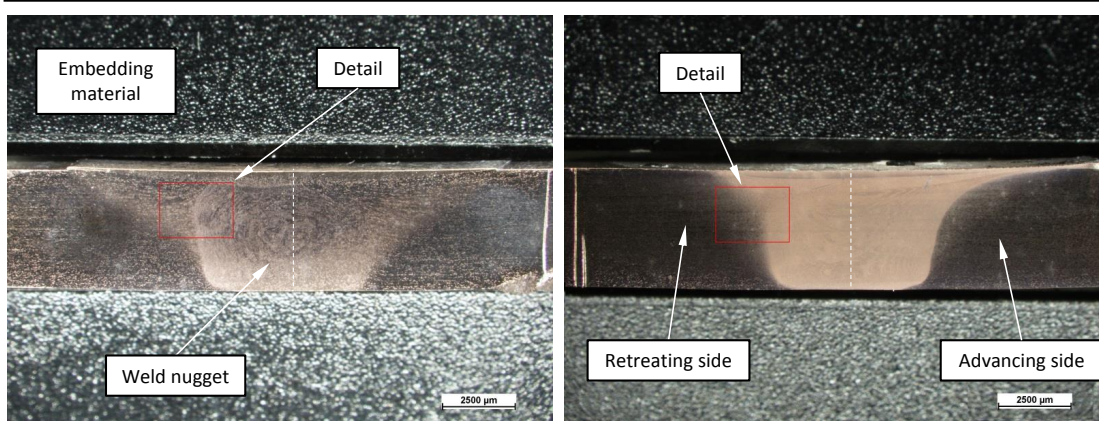


Figure 5.7: Light microscopy images of FSW samples of higher tensile strength $R_{m,max}$ (no. 6, left) and lower tensile strength $R_{m,min}$ (no. 13, right). For details of sample preparation see table 5.2. In comparison, the transition between base material and welding nugget of sample no. 6 (left) is more diffuse and less sharp than of sample no. 13 (right). As the left sample was produced at higher welding speed and rotation, more heat was generated during the welding process. This resulted in more friction between welding tool and base material and, thus, in a blurred-out border between the weld nugget and base material. The red rectangles mark the position of a zoom-in given in figure 5.8.

All sheets is generated which causes a broader zone of the sample due to the resulting higher temperatures being influenced by the welding process. Therefore, the sample with the higher welding speed and RPM, sample no. 6 (left image in figure 5.7), shows diffuse wings towards both sides of the weld nugget when compared to the sample no. 13 of low welding speed and RPM (right image) containing a sharper border between the welding nugget and base material.

A more detailed view resolving the grain structure at the transition of the weld nugget to the base material was obtained by optical imaging with increased magnification. Figure 5.8 presents a zoom-in of the red rectangles shown in figure 5.7. For both samples, the grain structure of the base material (B) outside of the weld nugget (A) can be resolved. During the FSW process, the matrix inside the weld is destroyed and new structures are formed. For sample no. 6 (left image of figure 5.8) the typical onion shaped structure can be observed in region A. For sample no. 13 (right image) a homogeneous area within the welding zone is observed. The onion shaped structure is betoken only at the very right bottom. Comparing the region within and outside of the weld of sample no. 6 (image on the left), a very steep transition from the undistorted structure of the base material and the onion shaped structure of the weld can be seen.

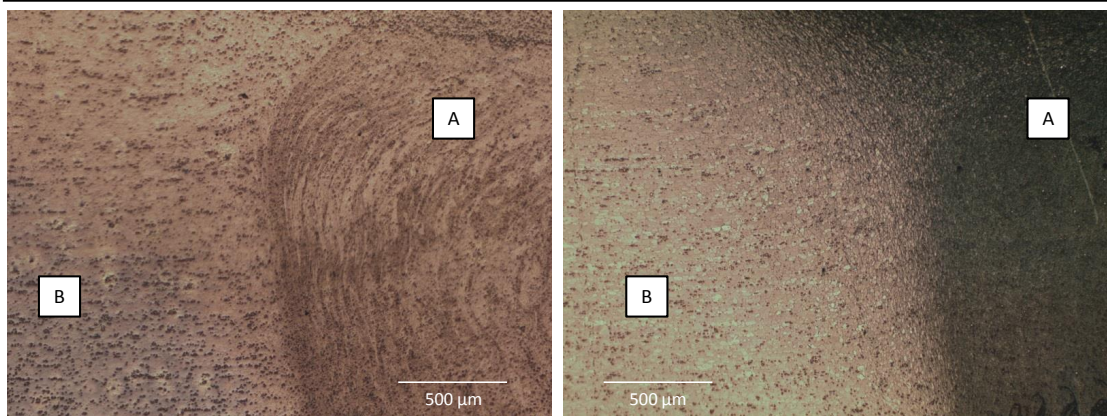


Figure 5.8: Four fold magnification of the light microscopy images in figure 5.7 of FSW samples of higher (sample no. 6, left) and lower (sample no. 13, right) tensile strength. The grain structure of the weld nugget (A) and the base material (B) is resolved. The typical onion like structures obtained during FSW can be seen in region A of ample no. 6 whereas in sample no. 13 a homogeneous area is observed. Only at the far right corner of sample no. 13 the structure is betoken. Whereas the transition from region B to A of sample no. 6 is steep (left image), the grain structure smooths for sample no. 13 (right image). In the latter case, the grains get more and more distorted in vertical direction until the optical resolution limit is reached.

By contrast, for sample no. 13 (right image), the transition is much more smooth. Here, the grains get more and more distorted in vertical direction until the optical resolution limit is reached.

5.1.2.3 CDBS Measurements

The measurements with the CDBS *upgrade* can be divided into two parts. First, a bulk defect map of both samples was acquired with the NEPOMUC re-moderated beam and a beam diameter of $250\ \mu\text{m}$. Therefore, the positrons were implanted with an energy of 30 keV resulting in a mean implantation depth of about $3.3\ \mu\text{m}$ calculated with the density of the material of $2.85\ \text{g}/\text{cm}^3$. In order to determine the chemical composition of the samples and their differences, according to the defect maps, coincident measurements were performed at selected positions.

The acquired 2D bulk defect maps of both samples, $R_{m,min}$ and $R_{m,max}$, sample no. 13 and no. 6 are shown in figure 5.9 top and bottom, respectively. For comparing both sample to each other, the S-parameter is normalized to the non-influenced Al bulk S-value outside of the weld nugget. The features obtained in the defect map are highly consistent with the optical images in figure 5.7. In the top figure, a high S-parameter

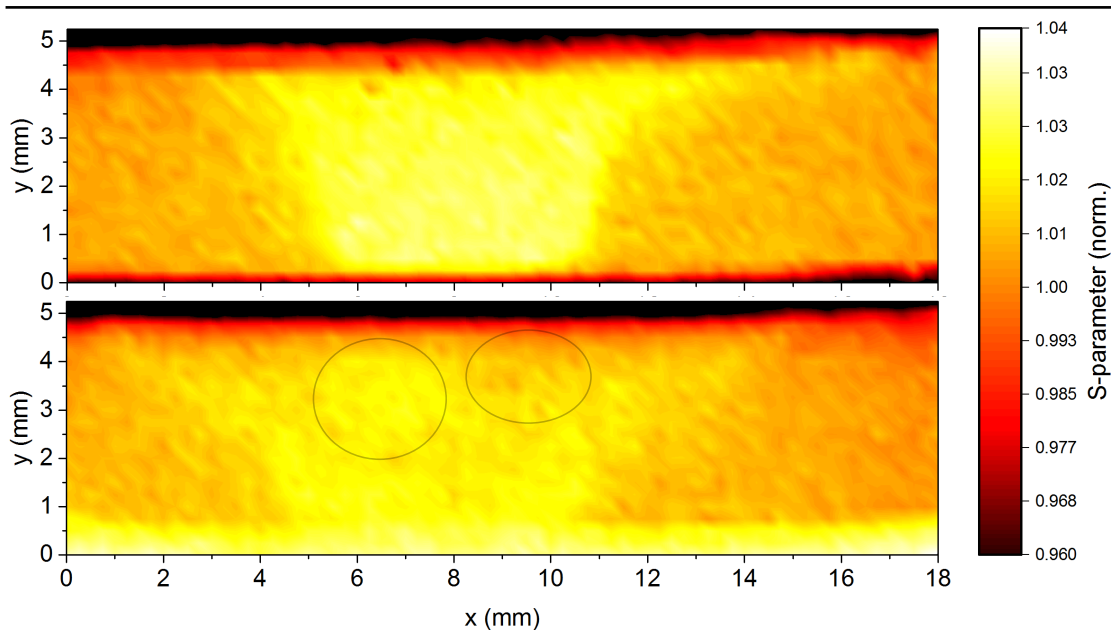


Figure 5.9: 2D bulk defect maps performed with a resolution of $250 \mu\text{m}$ using the NEPOMUC re-moderated beam. The implantation energy was set to its maximum of 30 keV. A step width of $250 \mu\text{m}$ in x- and y-direction was chosen, respectively. In both samples (sample no. 13, $R_{m,min}$ top, sample no. 6, $R_{m,max}$ bottom), the weld nugget and the influences of the movement of the tool creating an advancing and retreating side can be observed by the higher S-parameter. The defect structures in these two maps match very well to the optical images given in figure 5.7. Two inhomogeneities in the S-parameter, which can not be detected in the optical image, are observed (Marked by the two circles in the lower image).

is observed in the region of the weld nugget. The advancing side on the right of the weld is separated from the weld nugget by a sharp transition in the S-parameter. By comparison, the transition towards the retreating side is smoother. Within the nugget, a small gradient in the S-parameter decreasing from the bottom to the top of the sample is observed. The 2D defect map of the sample no. 6 (figure 5.9(bottom)) also exhibits the structures of the optical image in figure 5.7 (left). However, in the defect map, inhomogeneities in the S-parameter, marked by two circles in the image, are measured that can not be seen in the optical image. Moreover, compared to the first sample, the average S-parameter is lower which can be related to a possible annealing effect of the material due to the higher heat input during the welding process. All in all, a significant difference in the defect distribution between the two samples due to their different welding parameters can be observed affecting the strength of the weld.

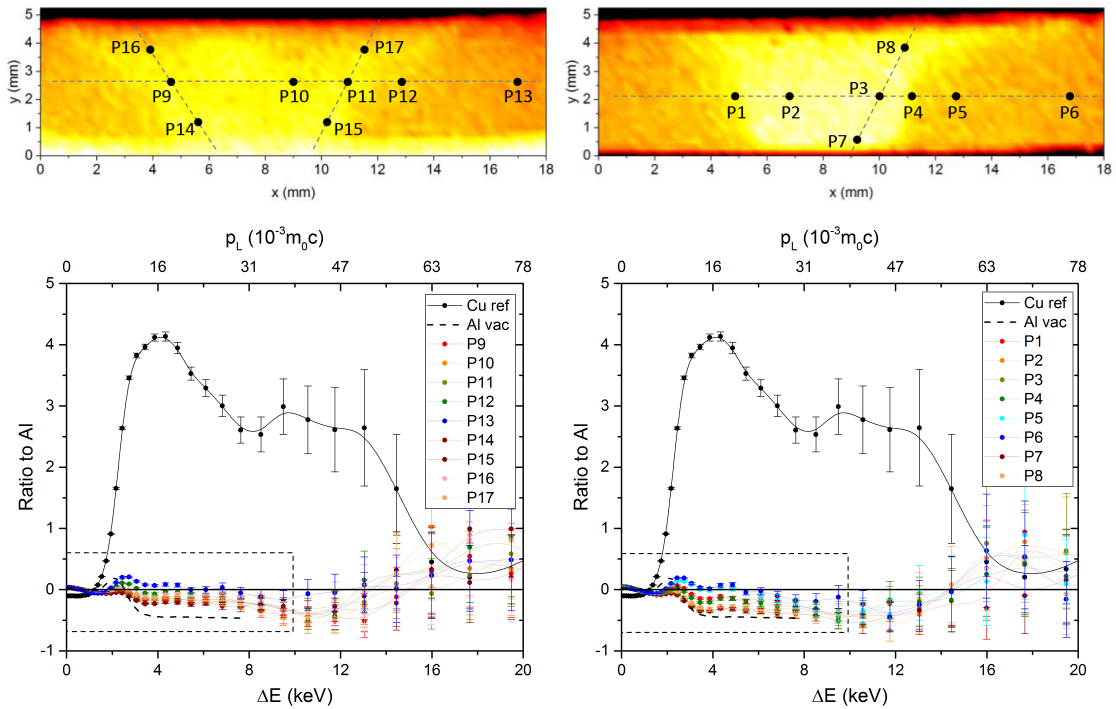
Sample no. 6 ($R_{m,max}$)**Sample no. 13 ($R_{m,min}$)**

Figure 5.10: CDBS ratio curves normalized to pure Al of all measurement points carried out on the FSW samples no. 6 (left) and no. 13 (right). The dashed black rectangles mark the regions of the enlarged views given in figure 5.11 to visualize the differences between the measurement points of the two samples. The signature of pure Cu (black) and the theoretical curve of an Al vacancy (dashed black line) normalized to pure Al calculated by Folegati et al. [119] are shown as well.

Aside from the introduction of defects, also the formation of Cu precipitates is known to have an impact on the strength of the alloy. Thus, bulk CDBS measurements were carried out at selected positions in order to gain information on the type of defects and the chemical distribution of Cu formed during the welding process. CDB spectra were recorded at 17 selected positions, marked from P1 to P17 in figure 5.10 (top) on both samples no. 6 ($R_{m,max}$) and no. 13 ($R_{m,min}$). The investigated positions were chosen in the middle of the weld nugget, at the transition of the nugget to the base material and in the base material. This first set of measurement points was aligned in a horizontal line indicated by the dashed horizontal line in figure 5.10 (top). A second set of measurements was carried out at positions where the sample is likely to fail during tensile tests, marked by the points on the tilted dashed line in figure 5.10 (top). For the sample of lower UTS, two of these "failure lines" were tested.

Sample no. 6 ($R_{m,max}$)

Sample no. 13 ($R_{m,min}$)

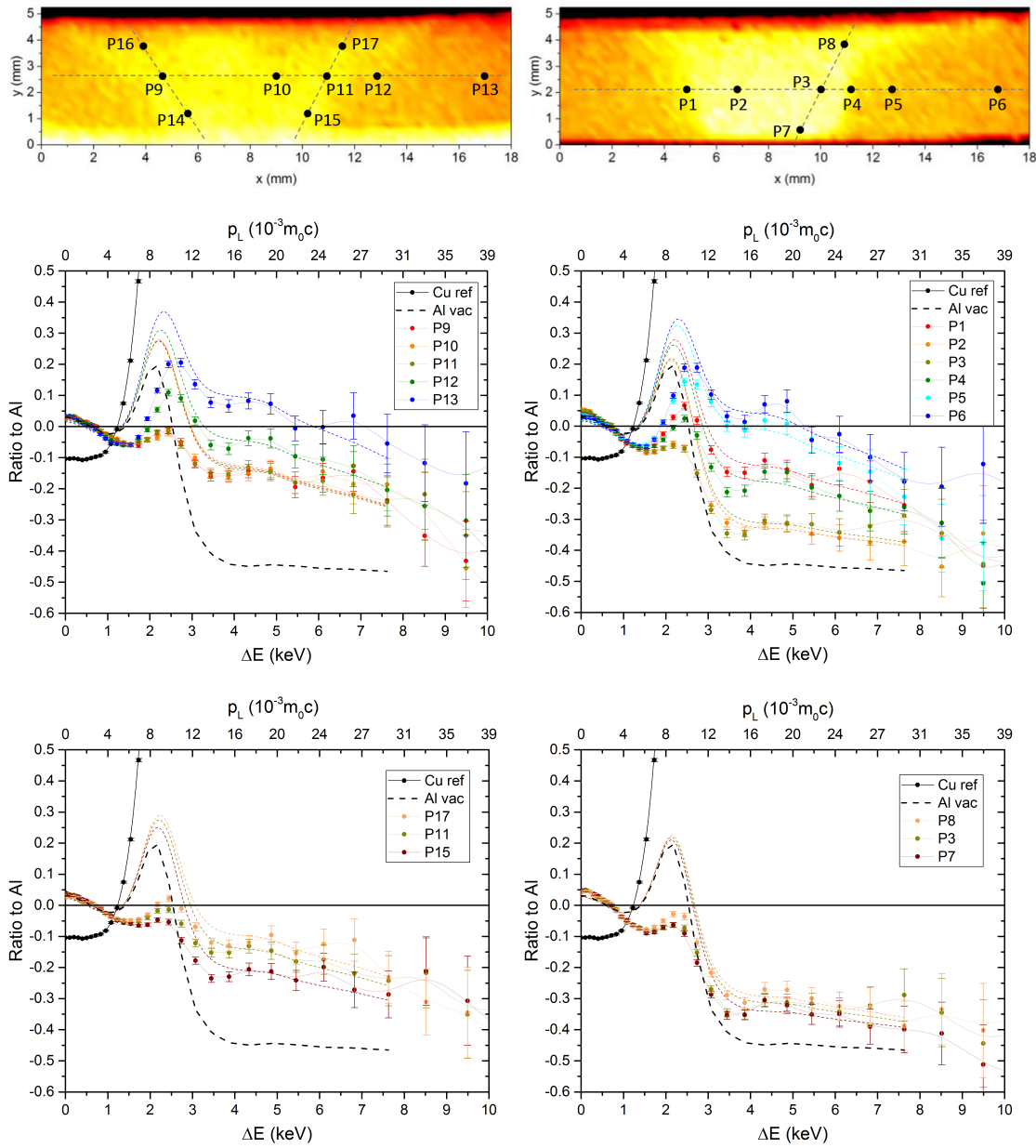


Figure 5.11: Enlarged view of the ratio curves for the samples $R_{m,max}$ (left) and $R_{m,min}$ (right) respectively. The positions where CDBS measurements were carried out are marked in the S-parameter maps above. The calculated curve for an Al vacancy (taken from Folegati et al. [119]) is indicated by a black dashed line. For all ratio curves, a linear superposition of the Cu signature with the Al vacancy signature was fitted to the data points by a least squares fit in order to obtain the amount of Cu (coloured dashed lines). Additionally, the shape and height of the confinement peak enables the distinction between deformation or quenching of the material within the weld.

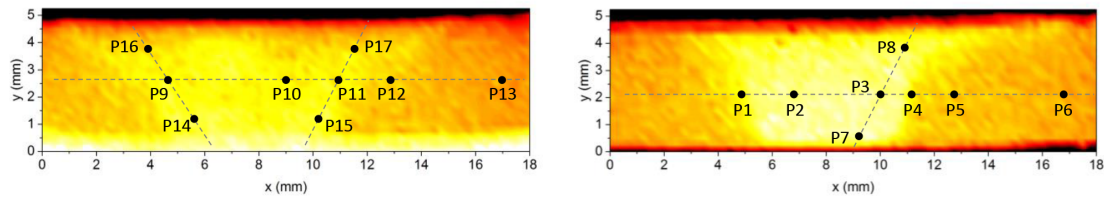
The results of the CDB measurements as ratio curves normalized to pure Al are given in figure 5.10 (bottom) for the two samples no. 6 ($R_{m,max}$) and no. 13 ($R_{m,min}$), and a Cu reference. For better comparison of the single measurements, an enlarged view of the sample ratio curves (marked by the black dashed rectangles in the ratio curves in figure 5.10 (bottom)) is given in figure 5.11. It is recommendable to divide the confinement peak referring to defects from the high-energy range of the spectrum related to the chemical composition (see section 5.1.1.4). At first glance, a confinement peak can be detected in both samples with different intensities dependent on the measurement position. In the tails of all ratio curves, i.e., at $\Delta E > 4$ keV, the intensity is significantly higher than the theory curve for an Al vacancy in pure Al.

Evaluation Details For a more detailed evaluation, each ratio curve was normalized to pure Al and fitted using a linear superposition of the Cu reference signature (I_{Cu}) and the signal of an Al vacancy in pure Al ($I_{Al,vac}$). The former was determined in the here presented experiment and the latter was extracted from Folegati et al. [119] (see section 5.1.1.4). Measurement and theory curve exhibit comparable instrument resolutions and can therefore be related. The fit was carried out with a least square approximation according to the fit function given in equation 5.2 with c as the Cu content.

$$I_{fit}(E) = cI_{Cu}(E) + (1 - c)I_{Al,vac}(E) \quad (5.2)$$

In order to avoid the influence of the confinement peak and focus on the plateau of the Al vacancy theory curve, the measured ratio curves were fitted from an energy of approximately 4 keV to the maximum of the theory curve slightly below 8 keV. The fit was carried out using a Python script (see appendix A.7). The fit employed a step width of 0.1 % and resulted in the highest possible agreement. An example of such a χ^2 -test is shown in figure 5.16.

Cu Content From the fits, the Cu content c of all measurement points for both samples were extracted and are listed in table 5.3. The Cu content varies in the range from 2.3 % measured in the weld nugget center of sample no. 13 up to 10.8 % and 11.9 % in the base material of samples $R_{m,min}$ and $R_{m,max}$, respectively. Within both samples, the Cu content of the weld nugget is lower compared to the rest of the sample. Due to the mechanical stirring process and the corresponding high heat input, the Cu precipitates formed during age-hardening are re-dissolved in the material. Outside of the weld nugget, the Cu precipitates remain unaffected. Moreover, Cu clusters of only a few atoms cannot be resolved in the CDBS measurements (see section 5.1.1.4). Therefore, a part of the Cu atoms that are assumed to be finely dispersed during the welding process, do not contribute to the measured Cu content.



Sample no.6 ($R_{m,max}$)		Sample no. 13 ($R_{m,min}$)	
Position	Cu fraction (%)	Position	Cu fraction (%)
P9	6.8	P1	7.0
P10	7.0	P2	2.6
P11	6.7	P3	3.0
P12	8.8	P4	5.9
P13	11.9	P5	9.6
P14	5.9	P6	10.7
P15	5.2	P7	2.3
P16	7.8	P8	3.4
P17	7.7		

Table 5.3: Cu content determined by least squares fits of the superposition of the Al vacancy theory curve by Folegati et al. [119] and the Cu reference curve.

Accordingly, finely dispersed Cu may also not contribute to the measurement of the S-parameter already presented in figure 5.9. This leads also to the enhanced S-parameter in the weld nugget of $R_{m,min}$ since the S-parameter of pure Al is generally higher than for pure Cu.

Comparing the Cu content of both samples, the absolute values in the weld nugget of sample $R_{m,max}$ are higher than of sample $R_{m,min}$. This is explained by the following effects. After welding, a re-formation of Cu precipitates takes place, most likely during cooling down to room temperature. Since sample $R_{m,max}$ was exposed to a higher welding temperature, the formation of precipitates was accelerated and more precipitates were formed in the time interval between the welding process and the subsequent cool-down. By comparison, the outside of the weld nugget was less heat-affected during the welding process. Therefore, the difference in Cu content at positions P13 and P6 were comparable for both samples $R_{m,max}$ and $R_{m,min}$, respectively.

In summary, the higher the amount of Cu precipitates in the weld nugget, the higher the UTS of the sample. For example, when comparing the corresponding positions

P2 and P10 as well as P8 and P17, their Cu contents differ by a factor of two. This high discrepancy in Cu content, may explain the difference in UTS of 78 MPa. As the formation of Cu precipitates is known to enhance a material's strength, this observation is in good accordance with theory [109, 112].

Confinement Peak Bear in mind that the chosen fitting range excludes the region of the confinement peak in order to determine the Cu content c . Still, the fitted intensity of an energy range up to approximately 4 keV was plotted using c and equation 5.2. Notably, the intensity of the fitted confinement peak overestimates the measurement. This may be attributed to the fact that only Cu-Al vacancy complexes are included in the Al vacancy theory curve used for the fit whereas precipitates, dislocations and other defect types are not taken into account. Therefore, in order to discuss the defect type, only the measured confinement peak will be examined.

The ratio curves measured in the base material are in good accordance between different measurement points and the two samples. In contrast, when comparing measurement point recorded in the weld nugget, significant differences can be observed. These shall be explained taking the example of P10 in sample no. 6 ($R_{m,max}$) and P2 in sample no. 13 ($R_{m,min}$). The maxima of the two confinement peaks are of similar intensities. However, P10 in sample no. 6 ($R_{m,max}$) possesses a smaller height of the confinement peak relative to its tail in comparison to P2 in sample no. 13 ($R_{m,min}$). This head-to-tail elevation shall now be referred to as "peak height". In numbers, peak heights of 0.12 and 0.28 can be extracted for P10 and P2, respectively. According to Calloni [118] (see section 5.1.1.4), defects can be assigned to deformed or quenched-in with respect to the peak height of the confinement peak (see figure 5.4 (upper right)). Thus, defects in sample no. 6 ($R_{m,max}$) and no. 13 ($R_{m,min}$) can be assigned to be deformed and quenched-in, i.e, vacancy-like, respectively.

In this regard, deformations, especially dislocations, are known to increase the strength of a material [109, 121]. This is in accordance with the fact that $R_{m,max}$ is the sample of higher UTS. Besides, dislocations are also believed to induce the formation of Cu precipitates [121] which again increases the strength of a material [109].

5.1.3 Characterization of Laser Beam Welded AlCu6Mn

LBW samples out of the AlCu6Mn alloy were produced and investigated by optical microscopy and CDBS to investigate the structure and chemical composition of the weld. Since the dimensions of the fusion zones in LBW are on the order of millimetres they are about one order of magnitude smaller compared to the centimetre range of FSW. In order to resolve the small structures of LBWs, a high resolution positron beam is needed. The new positron microbeam at the CDBS *upgrade* is predestined for this work and therefore used to image the concentration of open volume defects and to investigate the locally dependent formation of Cu precipitates.

5.1.3.1 Sample Preparation

A weld of two Al alloy sheets (EN AW-2219 T87) with a thickness of 4 mm was produced by the IWB at TUM. The two sheets were welded together using a single-mode laser (IPG YLR-3000) with a spot size of 50 μm and a welding speed of 45 mm/s. The laser power was set to 2.6 kW and the beam spot was oscillated with 200 Hz at an amplitude of 0.2 mm. As indicated by the red lines in figure 5.2, a suitable sample around 20 mm broad and 5 mm thick for the CDBS *upgrade* was cut out symmetrically around the weld. For examining the profile of the LBW, the cross sectional cut was polished by the IWB in the same manner as for the FSW samples presented in section 5.1.2.1.

5.1.3.2 Optical Analysis

Light microscopy imaging was performed by the IWB to visualize the grain structure and dimensions of the weld. In order to resolve the structures of the alloy matrix and the weld, the polished sample was electrolytically etched with Barker's solution (5 vol.% fluoroboric acid in water). To exclude effects of this pre-treatment on the CDBS measurements, which are very sensitive to defects at the surface, optical spectroscopy was carried out afterwards.

Figure 5.12 shows the Al LBW sample embedded in a polymer matrix used for chucking during polishing. The lighter region of the welding nugget can be clearly distinguished from the darker parts of the base material. Apparently, the two Al sheets were not completely welded together as can be seen in a small region below the weld nugget.

For better resolution of the grain structure in the weld, figure 5.13 shows a higher magnified image of the weld nugget. A clear structural difference can be observed when comparing the base material (region C) to the weld nugget (region A). During the welding process, the microstructure of the base material is completely destroyed via a

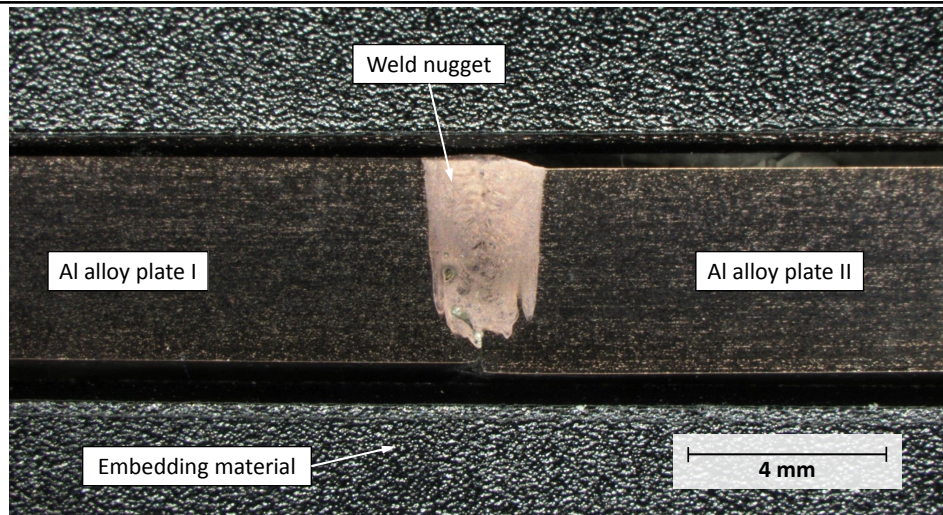


Figure 5.12: Cross-sectional microscopy image of the Al alloy LBW sample. For polishing the sample was embedded in a polymer material which can be seen on top and bottom. After an etching process according to Barker, the grain structure of the base material, as well as the structure within the weld nugget and the nugget itself become visible.

complete melting of the alloy within the fusion process. After cooling down, this fusion zone is forming the weld nugget. During this cooling process a recrystallization of the fusion materials takes place and a mixed crystal is formed. In the case discussed here, a dendrital crystal structure of supersaturated dissolved alloying elements is formed. This crystal consists of a composition of the alloying and impurity elements of the Al alloy and is formed via a mixture of an α mix-crystal and different other intermetallic phases [109]. At the lower left of the weld nugget, three dark bubble-shaped formations can be seen. These pores are formed mainly due to the presence of hydrogen since the solubility of hydrogen is 20:1 for liquid and solid Al, respectively. Moreover, pores can either be produced by the vaporisation of the alloying elements or due to an imperfect collapse of the keyhole during the welding process [126, 127]. In region B, a very sharp transition between the weld nugget and the surrounding base material is observed whereas in region C the original grain structure of the base material seems to be uninfluenced.

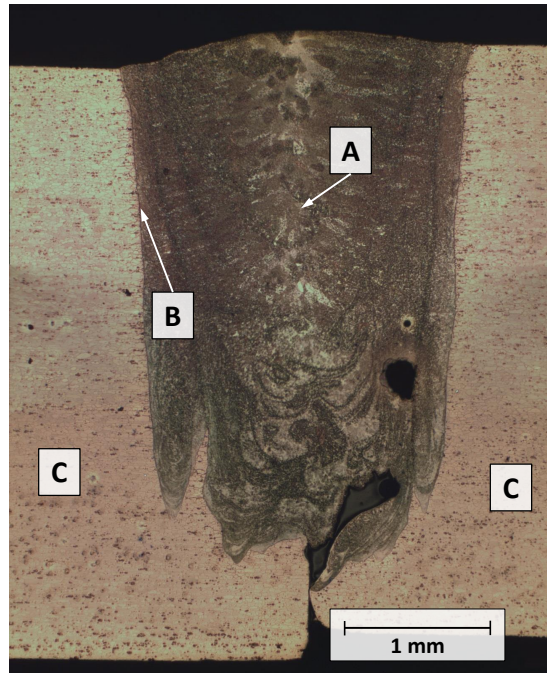


Figure 5.13: Close-up of the weld nugget and the transition to the base material of the LBW Al alloy. Three different regions can be distinguished. (A) Fusion region which was completely melted during the fusion process. During the cooling process a dendritival crystal growth structure is formed dominating the weld nugget. (B) A very sharp transition between the fusing zone and the surrounding base material is observed. (C) In this region the grain structure of the base material with grain sizes in the range of $15\ \mu\text{m}$ is dominant. Additionally, three bubble-like geometries at the lower left of the weld nugget can be observed, most likely stemming from gas inclusion.

5.1.3.3 CDBS Measurements

For a first overview, CDBS measurements were performed using the NEPOMUC re-moderated beam with a diameter of $250\ \mu\text{m}$ recording a bulk defect map over the entire LBW sample. For a detailed evaluation of the defect distribution within the weld, and for visualizing the transition to the base material with high resolution, the CDBS microbeam with a diameter of $50\ \mu\text{m}$ was chosen. From these high-resolution measurements, it was possible to extract the Cu amount at three different positions of the sample.

Overview 2D-scan with DBS The overview 2D S-parameter map shown in figure 5.14 was recorded with the NEPOMUC re-moderated beam with a positron energy of 30 keV and a step width of $200\ \mu\text{m}$ in x- and y-direction, respectively. The weld nugget

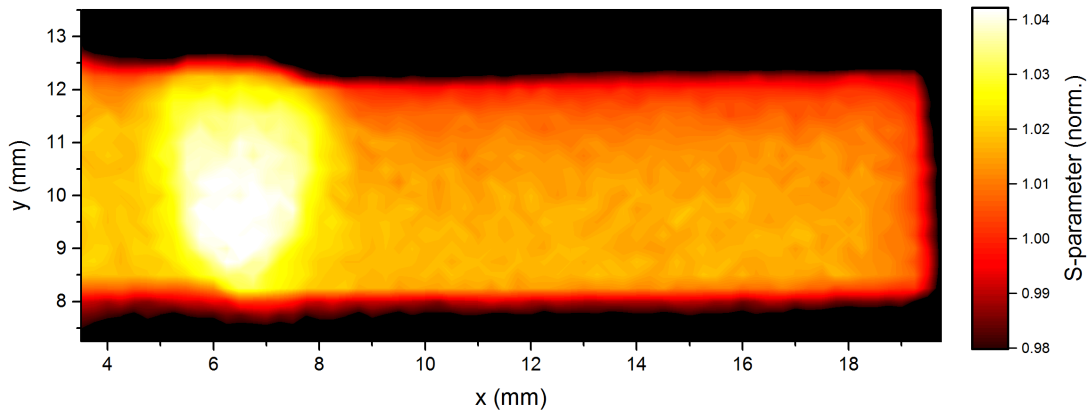


Figure 5.14: 2D S-parameter map acquired with a beam diameter of $250\ \mu\text{m}$ at an implantation energy of 30 keV. The step width was chosen to be $200\ \mu\text{m}$ in x- and y-direction, respectively. With an S-parameter around 4% higher than the base material, the weld nugget can be clearly seen. Due to cold rolling during fabrication of the alloy, an S-parameter gradient in y-direction can be observed in the base material [128].

can be clearly distinguished from the base material due to a significantly increased S-parameter. During the welding process, a large amount of vacancy-like defects is induced by the high heat input of the laser beam. Due to the high thermal conductivity of the material, the heat input of the laser is efficiently dissipated. Therefore, the defects created in the welding process cannot be annealed during the short cooling time from high temperatures and hence are effectively "quenched in". Outside of the welded zone above an x-coordinate of 10 mm, a gradient in the S-parameter can be observed in y-direction. This effect is most likely due to the creation of defects at the lower side of the sample generated during cold-rolling of the metal sheets.

High Resolution DBS In a second step, the region of the weld nugget was recorded with the positron microbeam. Thereby, the position of the weld nugget was determined using the overview map in figure 5.14 and additional linescans. The high resolution 2D S-parameter map is presented in figure 5.15. The weld nugget with high S-parameter can be clearly distinguished from the base material of low S-parameter. In order to gain more information on the HAZ and on a larger region of the sample being possibly influenced by the welding process, a high resolution linescan up to the maximum x-coordinate of 18 mm was performed. The scan was carried out at a y-coordinate of 10 mm and with a step size of $50\ \mu\text{m}$ in x-direction as shown in figure 5.15 (bottom). Here, a steep change of the S-parameter can be observed at positions $x = 5$ and 7.5 mm. The border between base material and weld nugget expands over a range of less than

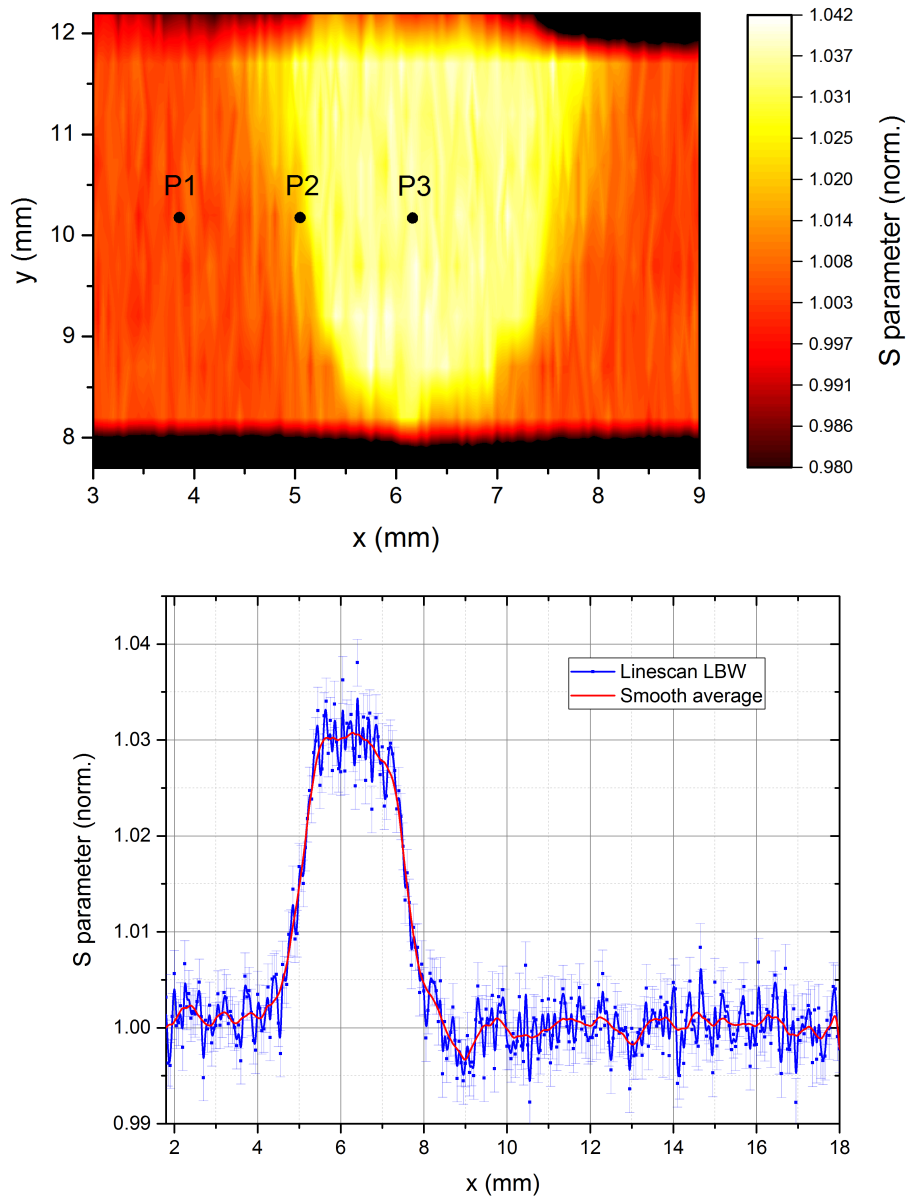


Figure 5.15: (top) 2D S-parameter map recorded with the positron microbeam at the CDBS *upgrade* at an implantation energy of 25 keV. The sample was scanned with a step with of $50\ \mu\text{m}$ in x- and $500\ \mu\text{m}$ in y-direction. Weld nugget, HAZ and base material can be clearly distinguished by a decreasing S-parameter. Three points are marked where additional coincident measurements were carried out presented in figure 5.16 (bottom) High resolution linescan at $y = 10\ \text{mm}$. The region of the weld nugget differs from the base material by a higher S-parameter. At $x = 9\ \text{mm}$ a decrease in S-parameter is visible which may attribute to an annealing of defects [128].

1 mm and indicates a well localized and small HAZ. At $x = 9$ mm, a small dip of the S-parameter is visible. This might be attributed to the annealing of point defects here. The S-parameter in the base material from an x coordinate of 10 mm on seems to be constant throughout the scanning range. This implies that the base material further away from the fusion zone is not influenced by the welding process.

Detection of Cu Precipitates Bulk CDBS measurements were carried out at three selected positions of the sample. The positions were chosen in the weld nugget, in the HAZ and in the base material, marked by P1-P3 in figure 5.15. In figure 5.16 the ratio curves with respect to pure Al are shown and compared to a Cu reference sample. Additionally, the theory curve for an Al vacancy in pure Al [119] is given (dashed gray line in figure 5.16).

Note that the examined material is an AlCu6Mn alloy meaning it contains 6 wt% of Cu (see data sheet in appendix A.8). Since the formation of Cu precipitates is known to enhance the strength of the material, the distribution of Cu in the sample is of major interest and examined in the here presented study. In this regard, the signature of the Cu reference can be clearly seen in the spectra of the LBW sample, most prominently at positions P1 and P2. Additionally, a confinement peak at approximately $9 \times 10^{-3} m_0 c$ indicates the presence of vacancies (see section 5.1.1.4). Considering these two features, the measurement will be discussed concerning the presence of Al vacancies as they occur in pure Al, Al vacancies decorated by Cu atoms and Cu precipitates in Al. The second species is also called Al vacancy-Cu complex.

For evaluation, the measured signal is therefore normalized to the main constituent Al and fitted by a superposition of the theory curve for Al vacancies in pure Al and the pure Cu reference. The procedure is the same as for the FSW sample and is explained in more detail in section 5.1.2.3. From the fit, the Cu content resulted in the highest amount of 30.4 % for P1 in the base material, 22.7 % for P2 in the HAZ and in the lowest amount of 12.0 % for P3 in the weld nugget.

The material shows the highest Cu content at P1 which is in the as-received state of the sample. This can be explained by the industrial artificial age hardening of the AlCu alloy where a certain amount of Cu precipitates in the θ phase forms (see section 5.1.1.2). Taking into account the least distinct confinement peak in P1, Al vacancies are most likely not present but precipitates formed in the θ phase.

By contrast, the HAZ and weld nugget show a more pronounced confinement peak and a lesser detected Cu content, and thus a different behaviour. During the welding process, the fusion zone is exposed to high temperatures exceeding the melting point of the alloy. The phenomena occurring at high temperatures can be divided in the

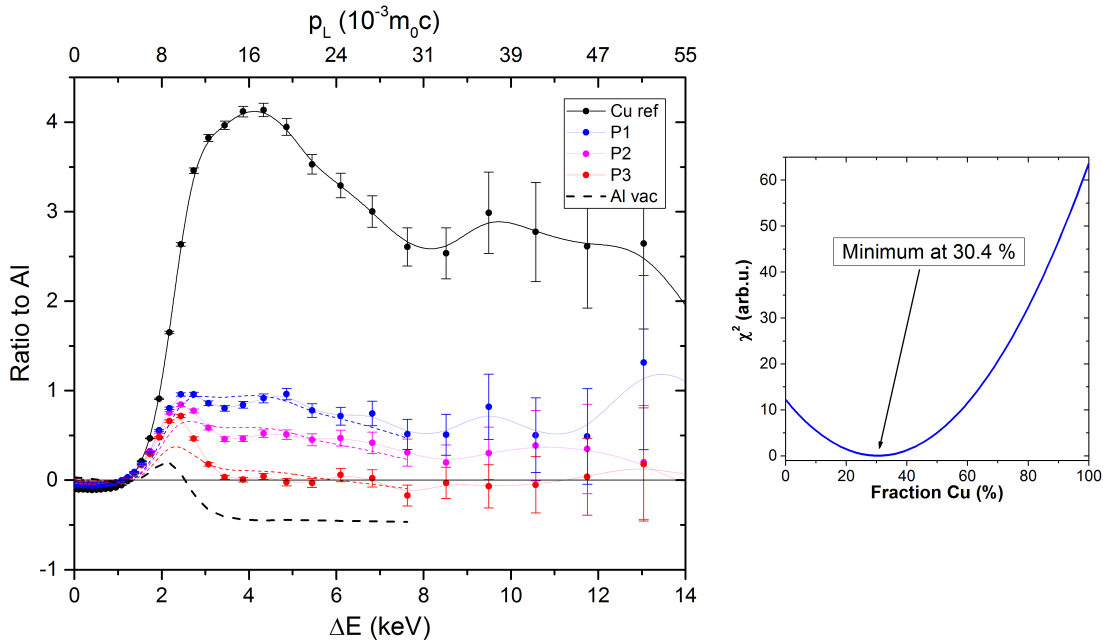


Figure 5.16: (left) CDB ratio curves, normalized to pure Al, measured with the positron microbeam at three positions P1-P3 as marked in figure 5.15. The data is fitted (colored dashed lines) by a linear combination of the Al vacancy theory curve (black dashed line) [119] and the Cu reference signature (black line). In P2 and P3 the confinement peak at a momentum of around $9 \times 10^{-3} m_0 c^2$ indicates the presence of vacancies. The Cu signature, caused by Cu-rich precipitates is observed in the HAZ (P2) and in the base material (P1). (right) Example of the χ^2 -test for the fraction of Cu in point P1.

enhanced solubility of the Cu precipitates and in the formation of additional Al vacancies which will be discussed in the following.

Firstly, at high temperatures the Cu precipitates formed in the age-hardening process prior to welding re-dissolve. Note that agglomerations with a radius of less than 0.49 nm do not trap positrons (see calculation section 5.1.3). Thus, finely dispersed Cu does not contribute to the Cu content determined here. However, since the Cu content in the weld nugget (P3) is not zero, a sufficient amount of Cu complexes of detectable size is still present. More insight in the nature of these Cu complexes can be found when taking the confinement peak into account. As a second effect, an increasing number of vacancies is introduced in the material with increasing temperature [109]. The time frame where the material is exposed to the high temperatures induced by the laser is very short due to the high welding speed and a highly localized laser spot. Additionally, because of the high thermal conductivity of $120 \text{ W}/(\text{m}\cdot\text{K})$ of the AlCu

alloy, the heat is efficiently transported away from the fusion zone. Both leads to a rapid cooling and introduced vacancies are quenched in. Since it is suggested that Cu preferably agglomerates at vacancies [109], it can be concluded that Al vacancy-Cu complexes form in the weld nugget during the welding process. These considerations hold also for the HAZ but due to a lower temperature and a higher Cu content, the formation of these Al vacancy-Cu complexes can be considered as less distinct and a part of the initial Cu precipitates may still be present.

5.1.3.4 Comparison of Welding Techniques

In this section, the results obtained from FSW-samples (section 5.1.2.1) will be compared to LBW-samples (section 5.1.3.1). A main difference is the Cu content determined for both welding methods in the assumed base material. It is a factor of 2.6 higher for LBW than for FSW. The reason for this may be attributed to the underestimation of the HAZ in FSW. It is realistic that the actual HAZ may exceed the measurement range. During FSW not only the pin of the welding tool with diameter of 4.7 mm but also its shoulder of 20 mm is assumed to produce a heat input on the material. Since the measurement range was in the order of the size of the shoulder, this is assumed to explain the lower Cu content in the "base material". In general, the HAZ in LBW is much smaller which can be attributed to the nine times higher welding speed and the very localized up-melting of the material.

Furthermore, the weld nugget in LBW is intrinsically smaller than in FSW. This is related to the difference in technique. The laser beam is focused to a single spot of the material whereas in FSW the material is in direct contact to a stirring tool of much larger dimensions.

In both cases, the relative Cu content of the weld nugget is lower due to an enhanced solubility of the Cu in the material at high temperatures. Since the Cu content is non-zero, still a certain amount of Cu precipitates might be present in the weld nuggets of both welding techniques. But more likely, the interaction between the vacancy like defects and the mobile Cu atoms forming vacancy-Cu-complexes. In LBW, the defects are believed to be thermally induced, quenched-in and vacancy-like. This is in agreement with the welding process, where heat is locally induced by the laser beam and, subsequently, transported away from the fusion zone very efficiently due to a high thermal conductivity of the material. By contrast, in FSW, deformations and hence a large concentration of dislocations are assumed to be introduced by the stirring process during welding.

5.1.4 Characterization of Laser Beam Welded Stainless Steel

LBW of stainless steel (1.4301, X5CrNi18-10) was chosen since it is a widely used material in all kinds of industrial processes. As in the last section, this material was investigated by optical microscopy, bulk DBS and CDBS at predefined points to investigate the defect distribution and the chemical composition after the welding process.

5.1.4.1 Sample Preparation

Material properties of V2A can be found in chapter 5.1.1, table 5.1. The sample was prepared similar to the AlCu LBW shown in figure 5.21 according to the LBW principle of figure 5.2 but with different welding parameters. The laser power was set to 2.7 kW with a welding speed of 100 mm/s and a circular oscillation of 0.2 mm. The sample was polished and etched for the CDB and microscopy experiments.

5.1.4.2 Optical Analysis

In order to depict and distinguish the structures of the weld nugget and the base material, optical microscopy of the cross-section was performed. As preparation for the microscope, the sample was polished and etched with V2A etchant (100 ml water, 100 ml hydrochloric acid, 10 ml nitric acid). For stability, the sample was embedded

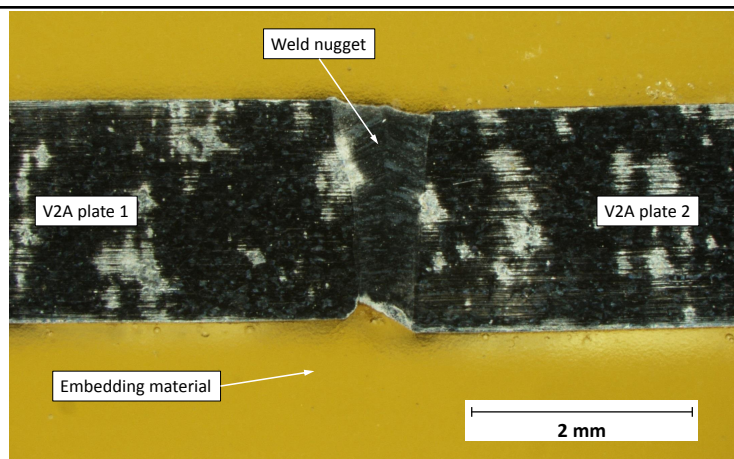


Figure 5.17: Optical microscopy image with fourfold magnification of the LBW performed on stainless steel, V2A. For polishing, the sample was embedded in a polymer (yellow). After etching, the structures within the base material as well as in the fusion zone of the weld become visible.

in a polymeric material during polishing. In order to avoid an influence of the etching process on the CDBS measurements which are sensitive to surface defects, optical microscopy was carried out afterwards. Preparation and optical microscopy was done by IWB at TUM.

In figure 5.17 an optical image in 4-fold magnification of the sample is shown. The weld nugget is separated from the welding material by a sharp line to both sides. The yellow-colored zones on top and bottom of the sample are the embedding material used for the polishing process. Since the contrast in color between the weld nugget and base material is rather low, figure 5.18 contains an optical image of higher (25×) magnification in black and white colors.

In the high-resolution image, three zones can be differentiated. The fusion zone with its typical dendrite structure can be observed in (A). This structure crystallizes during the cooling-process subsequent to welding in a process similar to the case of AlCu LBW discussed in section 5.1.3.2. In the base material (C), common crystallites in the as-received state are present. Analogue to the AlCu LBW, a sharp transition zone (B) between fusion zone and base material can be observed. The regularly ordered black dots across the material stem from hardness tests carried out after the CDBS measurements and have no structural meaning.

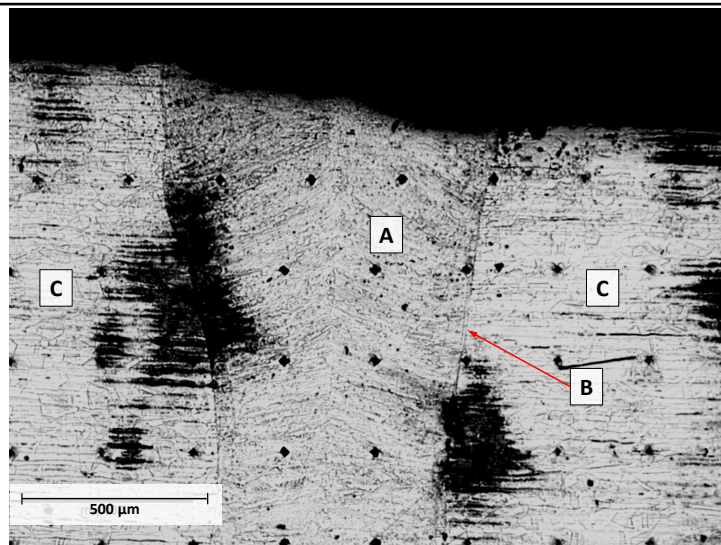


Figure 5.18: Optical microscopy image with 25-fold magnification of the LBW performed on stainless steel, V2A. (A) Fusion zone of the weld with dendrite structures formed during the welding process. (B) transition zone between weld nugget and base material. (C) Base material with unaltered grain structure. The regularly ordered black dots across the material stem from hardness tests and have no structural meaning.

5.1.4.3 CDBS Measurements

High resolution DBS Throughout the measurements on stainless steel, the high resolution CDBS microbeam was used due to the sample thickness of 2 mm and expected small effects. Figure 5.19 shows the 2D-DBS defect map. Three regions can be distinguished. The weld nugget ranges from an x-coordinate of 1.5 mm up to 2.2 mm and the base material from an x coordinate of 3.5 mm onward. Both regions show a similar S-parameter. By contrast, two regions around an x-coordinate of 0.75 mm and

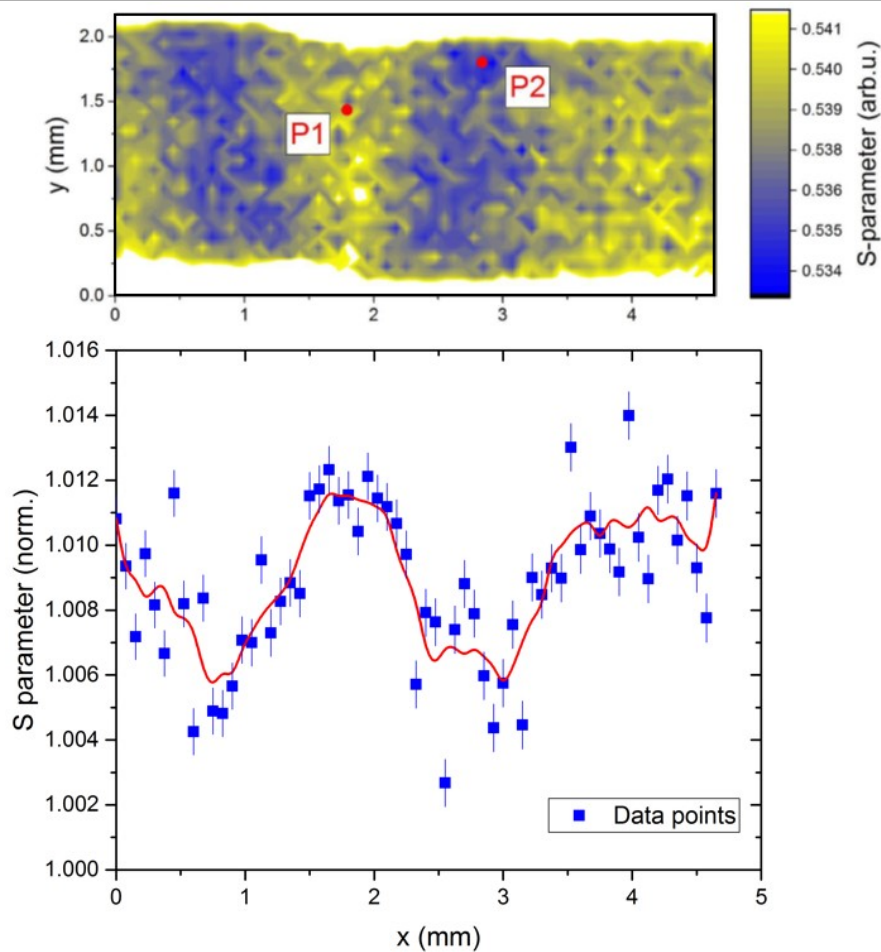


Figure 5.19: DBS on V2A LBW: (top) 2D defect map recorded with the CDBS microbeam. (bottom) Corresponding linescan at $y = 1.25$ mm with an averaged curve as a guide to the eye. The weld nugget located between $x = 1.5$ mm and 2.2 mm shows a similar S-parameter like the base material located from $x = 3.5$ mm onward. On the right and left side of the weld nugget, the HAZ with lower S-parameter is observed. The decreased S-parameter is attributed to a local annealing of the material. At position P1 and P2, further chemical analysis with CDBS was carried out.

2.75 mm, respectively, exhibit a significantly lower S-parameter indicated by the blue color. These two regions can be attributed to the HAZ. The division of these different regions within the material can be confirmed in the high resolution line scan of the sample in figure 5.19 (bottom). As a guide to the eye, an averaging curve (red line) was drawn to the data.

The reason for the low S-parameter of the HAZ compared to the rest of the sample, may be given by the heat conduction process during and after welding. Due to the low thermal conductivity of the material (see table 5.1), the heat introduced during the fusion process cannot be transported away from the fusion zone effectively. Therefore, within these regions a partial annealing process of the material takes place which results in a lower S-parameter.

CDBS Measurements In addition to the 2D bulk S-parameter map, CDBS measurements were performed at two defined points P1 and P2 located in the middle of the weld nugget and in the HAZ, respectively, as marked in figure 5.19. The results of the two measurements are given in figure 5.20.

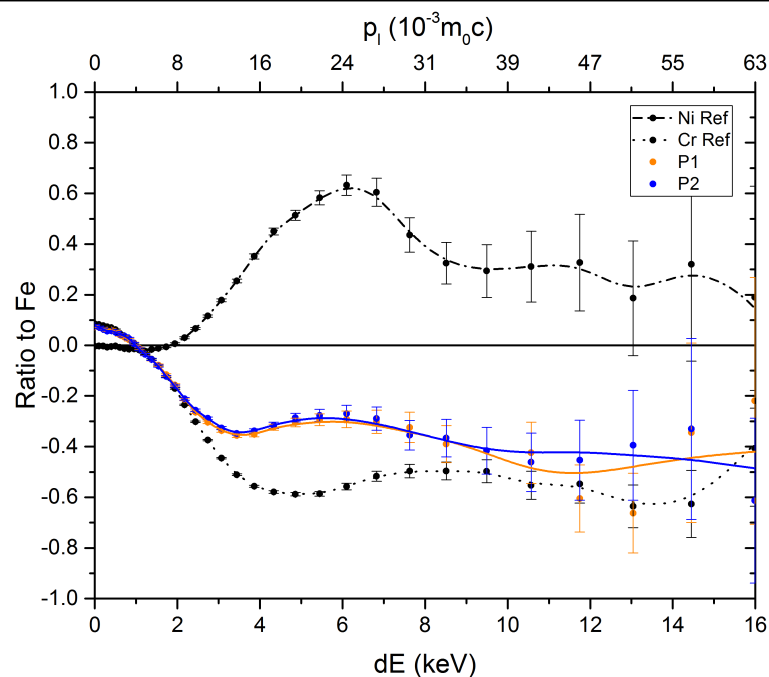


Figure 5.20: CDBS ratio curves of the V2A LBW within the weld nugget (P1) and the HAZ (P2). The ratio curves are shown with respect to Fe as main constituent of V2A and compared to Cr and Ni. Both curves overlap within their error bars. Therefore, no significant difference in chemical composition between the weld nugget and the HAZ is observed.

A CDB analysis was performed concerning the constituent elements of the V2A alloy, namely, Fe, Ni and Cr. The measured ratio curves as well as the references are shown with respect to the main constituent Fe. Both curves obtained for P1 and P2 overlap within their respective error bars from which can be deduced that the chemical composition of both, the weld nugget and HAZ, are indistinguishable. At around 5.5 keV, a small increase can be observed which might be due to the presence of Ni. However, since the overall Ni content is almost half of Cr (see data sheet in appendix A.6), this signature may be attributed to the higher positron affinity towards Ni than Cr [71].

In summary, (C)DBS gives structural and chemical insights in LBW V2A. In optical imaging, the boarder of the weld nugget and HAZ can be resolved as a sharp line. Additionally, DBS reveals details on the HAZ which S-parameter is lowered with respect weld nugget and base material which possess comparable S-parameters. This discrepancy in the S-parameter of the HAZ can be ascribed to an annealing effect during welding. CDBS shows similar chemical composition of HAZ and weld nugget.

5.1.5 Relation between S-Parameter and Vicker's Hardness in LBW-Samples

It is widely believed that vacancies, and in the case of AlCu alloys also Cu precipitates, have an impact on the hardness of a material [109]. Therefore, Vicker's hardness measurements were performed by the IWB according to the norms "DIN EN ISO 6507-1:2005" - "DIN EN ISO 6507-4:2005". Here, a pyramidal diamond indenter is pressed in a material with a certain force F . Using the diagonal d of the square-shaped imprint of the indenter in the material, the materials Vicker's hardness HV can then be determined according to

$$HV = \frac{1}{g} \frac{2F \sin \frac{\alpha}{2}}{d^2} \approx 0.1892 \frac{F}{d^2} \quad (5.3)$$

where g is the gravitational acceleration and $\alpha = 135^\circ$ is the opening angle of the pyramidal indenter [129].

In the following, the hardness maps of both LBW samples, the AlCu6Mn alloy and stainless steel V2A, are compared to their respective S-parameter maps. The latter ones were given and discussed in the sections 5.1.3.3 and 5.1.4.3.

AlCu6Mn The polished Al LBW sample was mapped with a step with of $250 \mu\text{m}$ in x- and y-direction, respectively. During the measurement, a pyramid shaped tip

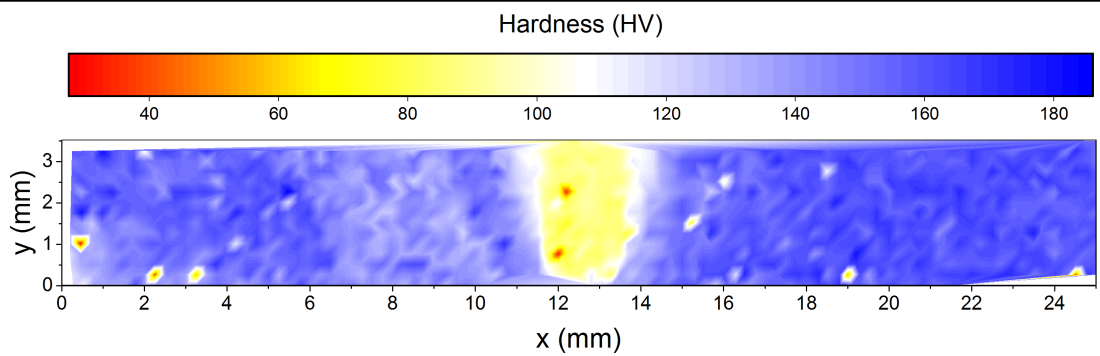


Figure 5.21: Vickers hardness map of the Al alloy LBW sample. The step width was $250\ \mu\text{m}$ in x- and y-direction, respectively. The weld nugget at position $x = 12.5\ \text{mm}$ possesses a hardness of approximately 80 HV. It can thus be distinguished from the base material of higher hardness.

is pressed with a certain force into the material. This causes the material to deform within a certain radius beyond the actual measurement point. As measurements within these deformed regions are to be avoided, the step width can thus not be minimized further. A graphical software then examines the shape of the produced imprint and calculates the hardness [129].

The resulting Vicker's hardness map is shown in figure 5.21. The base material shows a hardness of 160 HV whereas the hardness in the weld nugget is a factor of two lower. A sharp transition between base material and weld nugget can be detected which is in good accordance with the optical images presented in figure 5.13.

In figure 5.22, the hardness values determined at certain positions are related to their corresponding S-parameter obtained from the 2D defect map (see figure 5.14). The distribution of the data points can be approximated by the sigmoidal function (green line in figure 5.22)

$$y = y_1 + (y_0 - y_1)/(1 + \exp((x - x_0)/dx)). \quad (5.4)$$

The values determined with the software package Origin for the variables including their uncertainties are given in table 5.4.

In the plot, different regions within the sample (shown in figure 5.22 (bottom)) can be assigned to different "clouds" of data points. Each region is marked by a pattern of the same color as the corresponding data cloud in the hardness vs S-parameter map above. Approaching the weld nugget from the left (regions I to IV), the hardness decreases whereas the S-parameter increases indicating a higher amount of defects. Towards the right edge of the weld nugget, in regions V and VI, this trend is reversed. Here, the

hardness increases whereas the S-parameter decreases until the values for hardness and S-parameter are reached as in region I.

In the base material, i.e., from $x = 7$ mm onwards, a gradient of the S-parameter in y-direction is present. In order to relate this gradient to the hardness, the base material is divided into different regions in y-direction, marked in figure 5.22 (bottom). Each region is assigned to a different shade of gray. As can be seen in 5.22 (top), the S-parameter decreases with increasing y-coordinate whereas the hardness remains

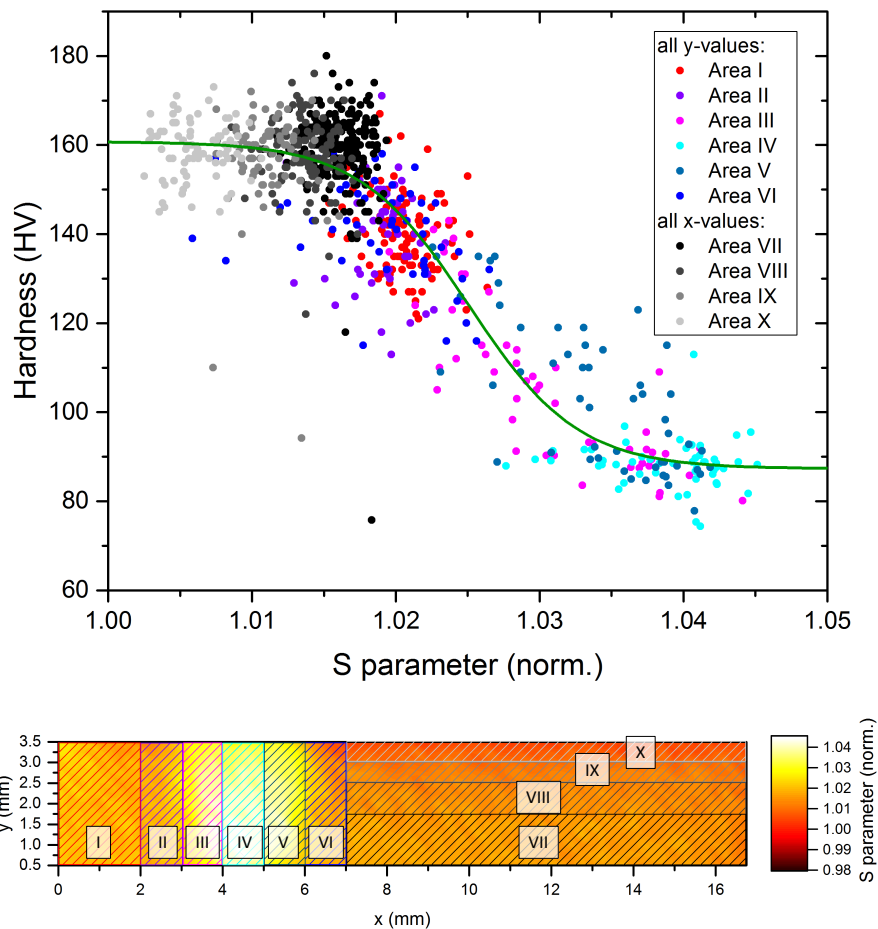


Figure 5.22: Relation between the Vickers hardness measurement and the S-parameter of the Al LBW sample. The distribution of the data points was fitted by an error function (green line). Within different regions of the sample (bottom), similar hardness and S-parameter values are observed. Thus, the data points coloured according to the regions I-X "accumulate" in the hardness vs S-parameter plot. The weld nugget possesses the highest S-parameter and lowest hardness. In the base material, a gradient in S-parameter in y-direction at constant hardness is attributed to the fabrication process of the raw material.

Variable	Value
y_0	87.31 ± 1.57
y_1	160.77 ± 0.98
x_0	$1.03 \pm 3.44 \cdot 10^{-4}$
dx	$3.81 \cdot 10^{-3} \pm 2.90 \cdot 10^{-4}$

Table 5.4: Values for the Variables determined via a fit according to equation 5.4 with Origin.

constant at 160 HV. S-parameter indicates an increase of open volume defects that apparently does not affect the hardness. Moreover, the Vickers hardness shows a large scattering, which is attributed to the accuracy of its determination. The graphical analysis provides an accuracy of about ± 2 HV.

In order to present an additional view of the correlation between S-parameter and Vicker's hardness, linescans were performed horizontally across the weld. As can be seen in figure 5.23, the trends in S-parameter and hardness are inverse.

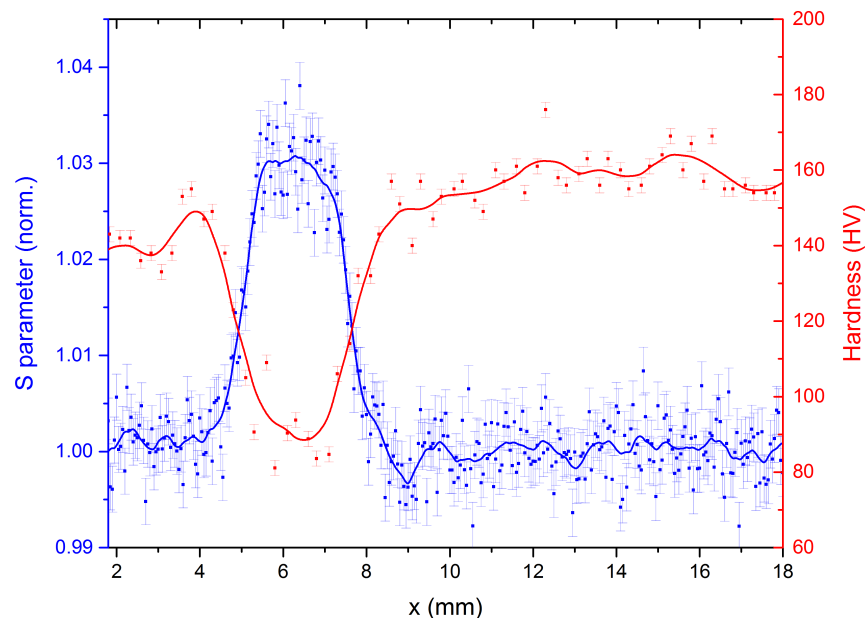


Figure 5.23: High resolution linescan of S-parameter and measured Vickers hardness in x-direction across the weld. Both properties are inverse to each other.

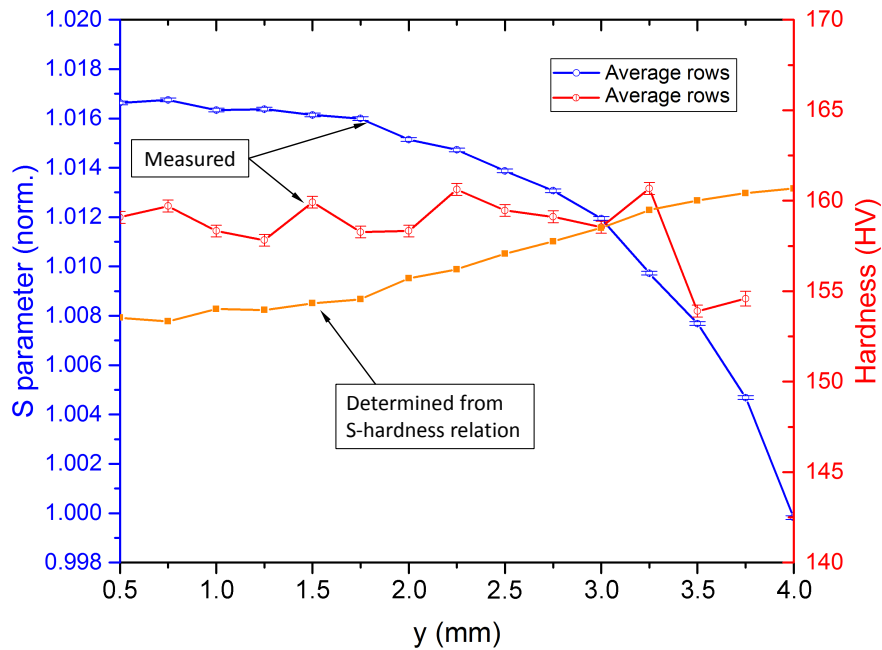


Figure 5.24: High resolution linescan S-parameter and hardness in y-direction. The hardness values were determined (orange) using the sigmoidal function (equation 5.4 with values for the variables given in table 5.4) fitted in the hardness vs S-parameter map (green line in figure 5.22).

Additional linescans in y-direction were performed in the base material, from $x = 10$ mm onwards. For an increased statistics, the region of $x = 10$ mm up to 18 mm was averaged for each y-coordinate. Figure 5.24 shows the resulting linescans for both the S-parameter and hardness. Again the gradient of the S-parameter can be observed whereas the hardness stays constant. In contrast to the smooth S-parameter trend a larger scattering is observed within the hardness measurement. This can be explained by the limited resolution of the hardness measurement since the measurement points have to be spaced in order not to influence the measurement. Additionally the local hardness can vary due to the grain distribution of the material itself. Here, the measurement is dependent on the position if a grain or rather a grain boundary is positioned below the hardness measurement tool deteriorating the local hardness value.

For this reason, the potential to determine the local hardness using the found relation between Vicker's hardness and the S-parameter shall be exploited. To do so, the relation of the S-parameter to the hardness was approximated by an error function as fitted in figure 5.22 (top). This model function was applied to the measured S-parameters (blue line) in figure 5.24 in order to calculate the hardness values shown in orange. In conclusion, the found S-HV-relation can be employed as first approximation to resolve hardness with higher accuracy than conventional hardness.

All in all, the results show a first attempt to combine DBS measurements in this special case the S-parameter with Vickers hardness. Due to the sensitivity of the positrons for defects in materials, it could be shown that probable inhomogeneities due to the manufacturing process of the Al sheets can be resolved in the DBS measurements. According to the fit presented in figure 5.22 it was tried to predict the hardness value of the material according to the measured S-parameter (yellow in figure 5.23). As can be seen, at the top and bottom of the Al sheet a 4% higher and lower hardness value, respectively, is expected than is measured (red curve in figure 5.23). In this regard, uncertainties in the hardness measurement such as probing different grains or grain boundaries of the material as well as destroying the sample that way that measurement points can not be repeated also by a small displacement of the tool are limiting conventional hardness measurement.

V2A The hardness measurements were carried out with a step width of 200 μm in both x- and y-direction in the same manner as described above. In the hardness map in figure 5.25, the weld nugget can be easily distinguished as its hardness is by factor of 1.4 lower than in the base material. The weld nugget and base material show a hardness of 220 HV and 310 HV, respectively. In the hardness map, the transition between the base material and the weld nugget is less distinct compared to the defect map 5.19. This can be attributed to the higher resolution of DBS using the positron beam.

In figure 5.26, S-parameter and Vickers hardness are plotted with respect to each other. Two centers of accumulation can be distinguished stemming from the weld

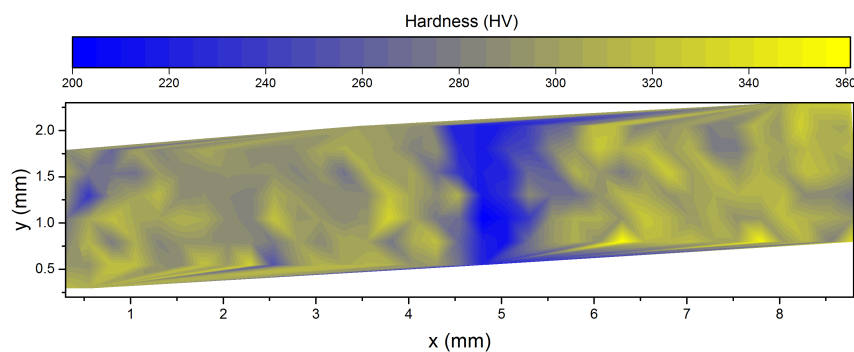


Figure 5.25: Vickers hardness map performed on the V2A LBW. Due to a small misalignment in the measurement apparatus, the 2D map is slightly inclined. The step width was set to 200 μm in x- and y-direction respectively. The middle of the weld nugget is attributed to the reduced hardness at an x coordinate of 4.8 mm. Within the base material the hardness values are nearly constant.

nugget and the unaffected bulk material. The weld nugget differs in a smaller hardness. Besides this, a difference between the HAZ and base material can not be observed in the hardness but as a slightly decreased S-parameter, i.e. lower S-values in areas II and IV.

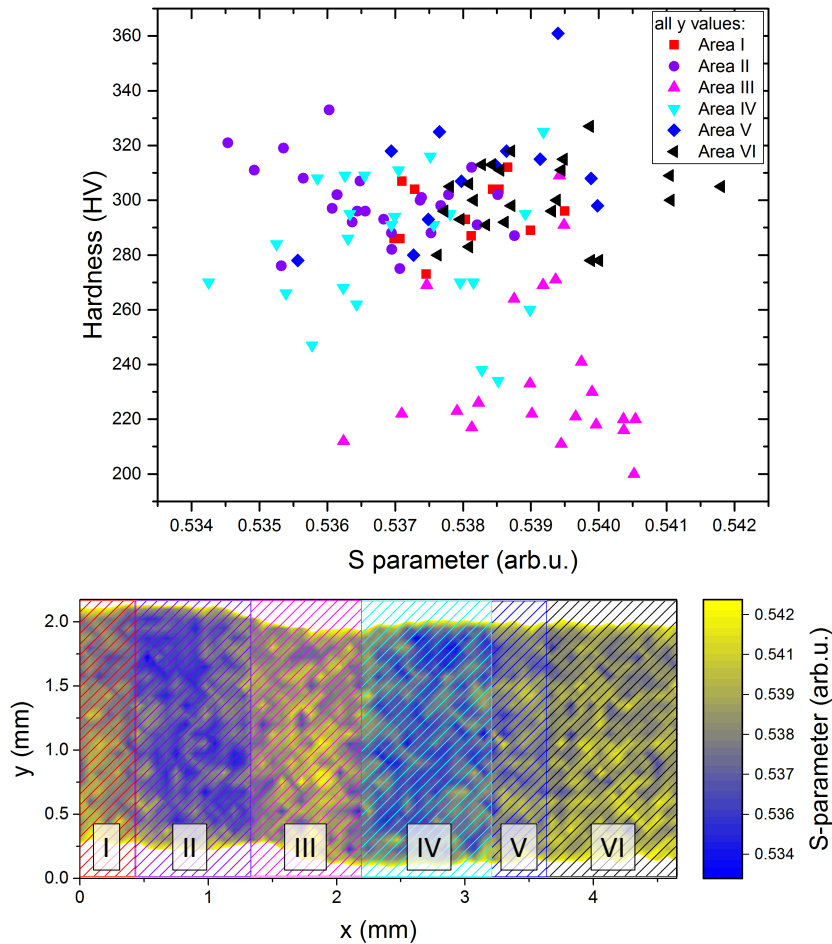


Figure 5.26: Relation between the Vickers hardness and S-parameter measurements around the V2A LBW. Similar to the Al LBW shown in figure 5.22 Different regions of the sample (bottom) can be assigned to different hardness and S-parameter values. The measurement area was divided into six different regions with their corresponding colored data points in the hardness vs S-parameter plot. The weld nugget with the lowest hardness is clearly distinguished from the rest of the sample. Here, the data points accumulate within a hardness around 300 HV. The two areas around the HAZs are shifted to lower S-parameter. In the hardness measurement, as well as in the S-parameter measurements a larger scattering of the data points is observed caused due to the small differences i.e. in the S-parameter of $< 2\%$ between the zones of the HAZs and the base material and weld nugget.

5.1.6 In-situ Tension Tests on LBW V2A

The LBW V2A was investigated optically and via CDBS measurements as reported in section 5.1.4. Hardness maps were presented and compared to the S-parameter in section 5.1.5. Additionally to these previous investigations, in-situ tension tests were performed. The corresponding set-up is introduced in section 4.4.2. In figure 5.27 an optical image of the sample mounted on a standard sample holder of the CDBS *upgrade* is presented. For the pre-investigation of the weld prior to the performed tension test, the position of the weld nugget was marked by a copper stripe. The corresponding S-parameter map is presented in the last section in figure 5.26 (bottom).

For the DBS measurement during applied stress, the sample was mounted within the tension test sample support. During the DBS measurements with a positron energy of 21 keV, stress was applied to the sample. In order to guarantee that the breaking point of the sample is within the measurement area, the width of the sample bar was reduced from 10 mm to 2 mm within this region (see figure 5.27). The reduced width

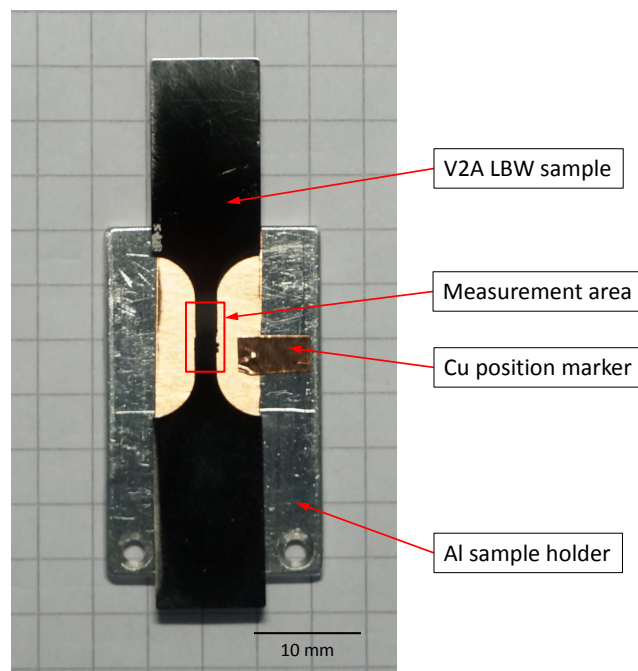


Figure 5.27: Image of the polished V2A LBW tension test sample prepared on a standard CDBS *upgrade* Al sample holder. In order to fix the measurement area a Cu position marker was positioned beside the middle of the LBW weld. The geometry of the sample was chosen in a way, that the sample would fail in the middle of the weld nugget during a performed tensile test. Therefore, the width of the bar in the middle was reduced from 10 mm to 2 mm. The overall sample thickness was 1 mm.

was chosen to be sufficient to break the sample below the maximum force applicable by the tension testing machine of 2 kN. Equation 5.5 relates the maximum tension strength R_m of the material (see data sheet in appendix A.6) to the force F and the cross-sectional area A of the sample.

$$F = R_m \cdot A \quad (5.5)$$

With a width of 2 mm, a sample thickness of 1 mm and a R_m of 700 MPa, the maximum force at which the sample fails is calculated to 1.4 kN which is well below the maximum force applicable by the set-up.

The tension test was then conducted in the following way. A certain force was applied to the sample and meanwhile a 2D bulk S-parameter map was acquired each consisting of 250 measurement points. Figure 5.28 shows the force applied to the sample during the measurements.

Within the elastic range, the applied force was maintained during each measurement sequence. By contrast, in the plastic range, a decrease in force especially at the beginning of each map is visible due to plastic relaxation. At a force of approximately

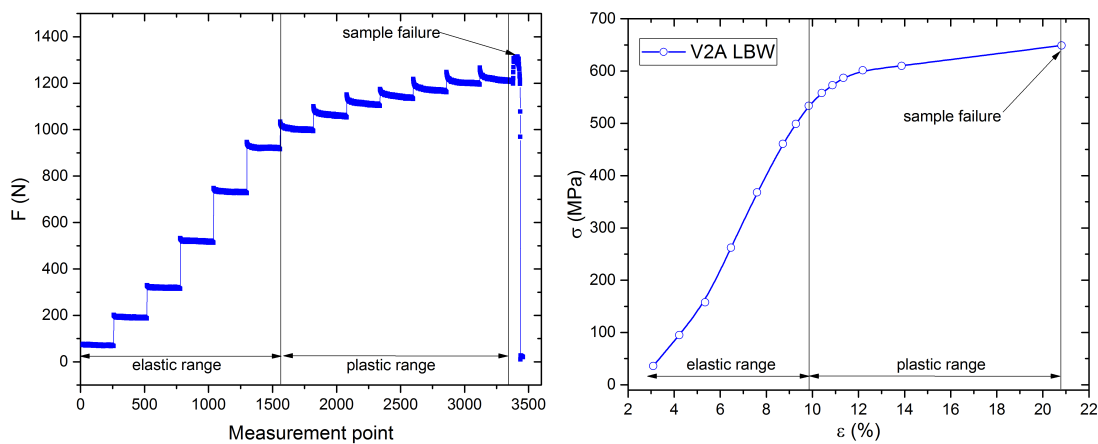


Figure 5.28: (left) Intervals of the performed tension force onto the sample. In every interval a 2D S-parameter map was acquired. Within the elastic range of the sample the force is nearly constant, whereas in the plastic range, a relaxing effect to the end of the measurement is observed according to a decrease of the measured force. The sample broke at around 1.3 kN which is slightly below the calculated maximum force. (right) Corresponding stress-strain-curve of the V2A LBW. The plastic range starts at around 10 % of strain indicated by a decreasing slope of the curve.

1.3 kN, the sample failed which is slightly below the calculated breaking force. This is most likely attributed to the weakening of the sample due to the welding process. Additionally depicted in figure 5.28 is its corresponding stress-strain curve. Here, again the linear elastic range up to a strain of around 10 % can be seen whereas from 10 % on the plastic deformation region is depicted due to a difference in the slope of the curve up to its maximum of around 650 MPa. Due to the mounting procedure of the sample the first measured S-parameter map was already acquired at a strain of around 1 %.

In figure 5.29, the CCD images acquired through a view port at the instrument and the corresponding 2D bulk S-parameter maps are given. The results are exemplary shown for an applied force of 0 N, 1000 N, 1100 N and 1200 N. Since the sample holder is fixed, beam positioning was carried out with a movable magnet located below the sample.

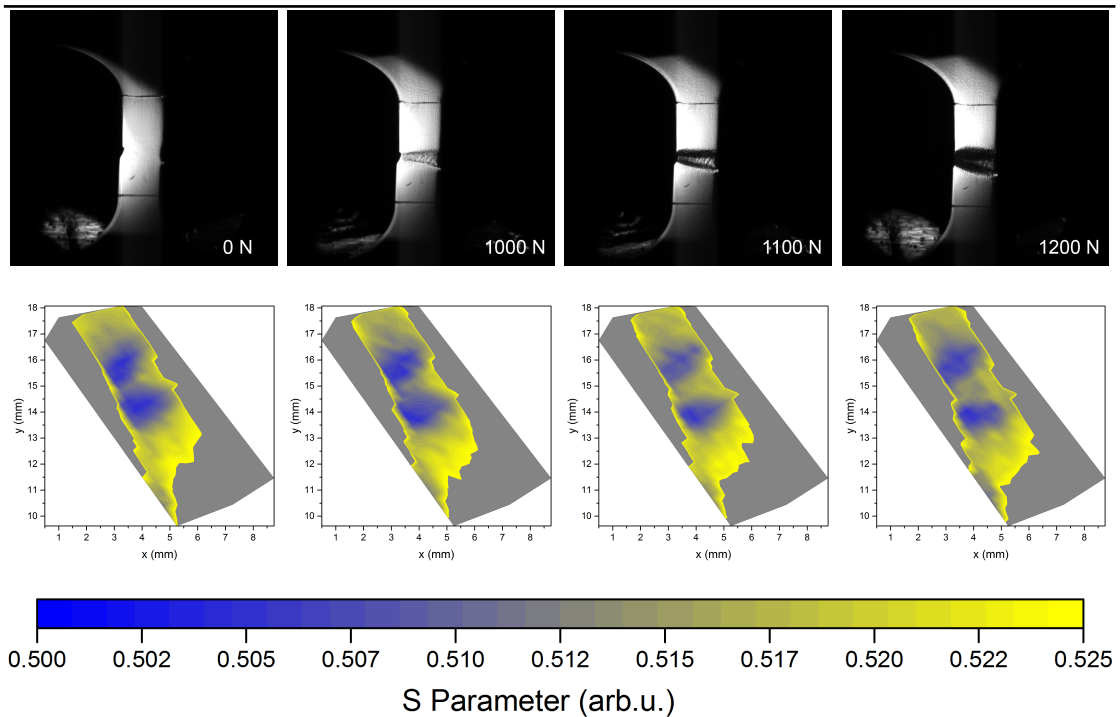


Figure 5.29: V2A LBW tension test measurements during DBS with the positron beam. In the first row, at four different force steps an image of the V2A sample is displayed during applied stress onto the samples. Within the plastic region the necking of the material at the weld nugget position can be seen. In the second row, the corresponding 2D bulk S-parameter maps are depicted. The maps are inclined due to the beam positioning with a magnet below the sample. The region of the weld nugget is stretched that can be also seen in the S-parameter. Here the region of a high S-parameter is growing whereas the widths of the HAZ are unaffected but the regions of the HAZs are moving apart.

This resulted in an inclination of the 2D S-parameter maps. In each 2D S-parameter map, the weld nugget is surrounded by two HAZs of lower S-parameter (blue areas). As can be seen in the optical images in the upper row, the applied stress mainly leads to a strained weld nugget. More details can be gained from the 2D S-parameter maps in the lower row. Remarkably, the form and width of the HAZs stay constant during the tension test. However, their distance is significantly increasing with increasing applied stress. Between the HAZs, a region of higher S-parameter evolves which can be attributed to the introduction of defects due to the deformation of the material.

Altogether, the integration of an in-situ tensile testing machine into the CDBS *upgrade* opens up the possibility of recording a spatially resolved, depth-dependent S-parameter map in-situ during applied external stress.

5.2 Annealed Pt Foil

The microbeam of the CDBS *upgrade* is well-suited for the investigation of grains and grain boundaries as these structures are in the size of micrometers. In the following, this capability of the CDBS *upgrade* is demonstrated on Pt.

The sample was a Pt foil with a size of 2.5 mm \times 3 mm and a thickness of 250 μ m. In order to decrease the number of defects and increase the grain size, the foil was annealed at a temperature of 1100 $^{\circ}$ C for 6 hours. As Pt is inert to oxidation, the annealing was performed in air.

The optical microscopy image is shown in figure 5.30 (left). Grains with a maximum size of 750 μ m were formed during the annealing process. With the CDBS microbeam of 50 μ m diameter, a 2D defect map was acquired at an implantation energy of 25 keV resulting in a mean implantation depth of 322 nm. The defect map is shown in figure 5.30

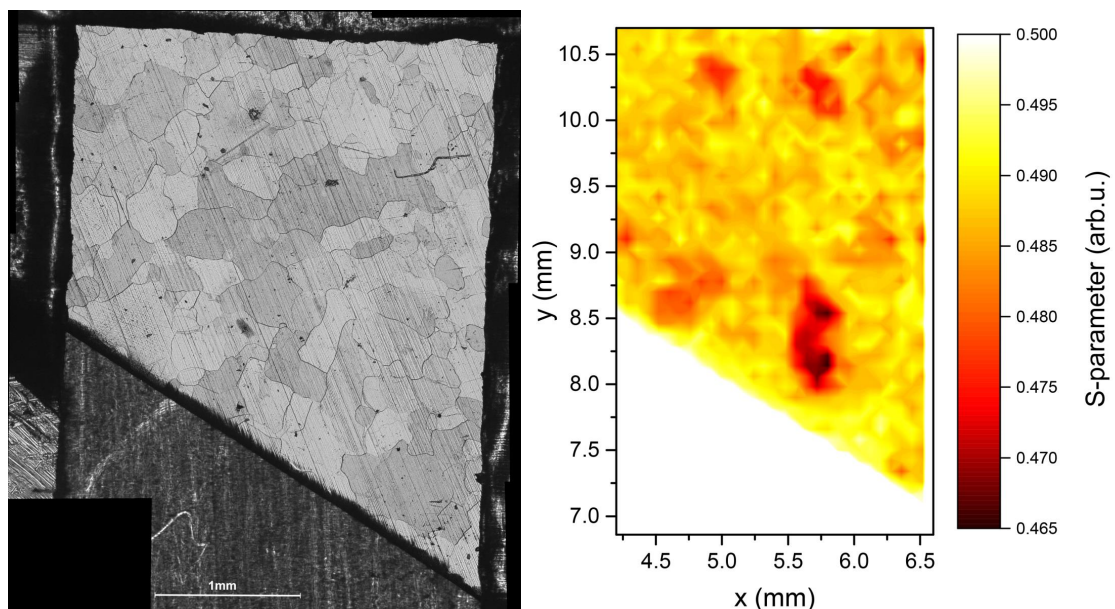


Figure 5.30: (left) Optical image of an annealed Pt foil prepared for CDBS measurements. Within the foil grains of a size of up to 750 μ m were formed during an annealing procedure. (right) 2D S-parameter map acquired at a positron energy of 25 keV with the CDBS microbeam (step size of 50 μ m in x- and y-direction respectively). According to the optical image different grains show different S-parameters. Especially one elongated grain at position (5.75 mm|8.25 mm) shows a significantly reduced S-parameter compared to the rest of the map. An overlay of the two figures results in a perfect match of the 2D S-parameter map with the grains in the optical image.

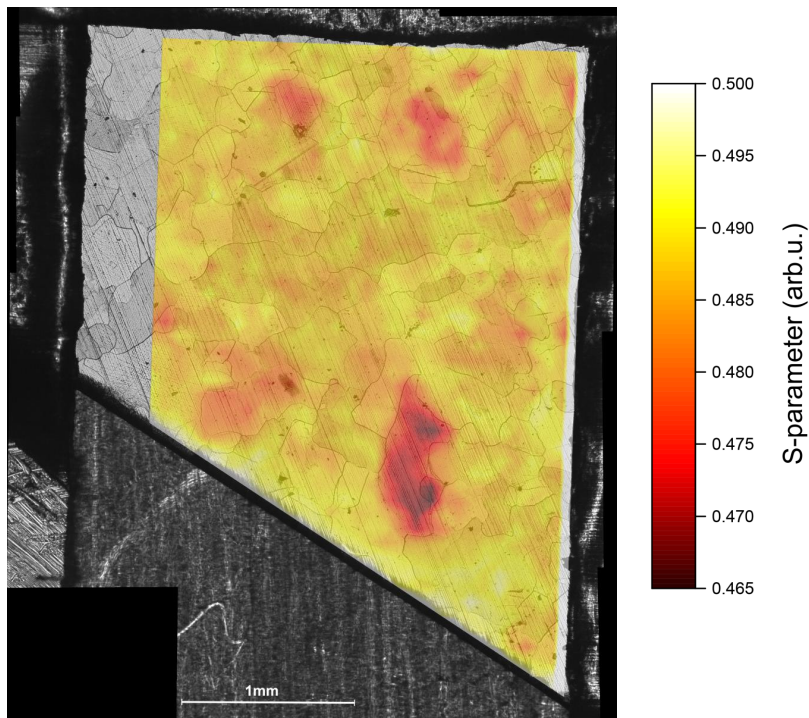


Figure 5.31: Overlay of the 2D S-parameter map with the optical image of the Pt foil. The areas of the lower S-parameter matches perfectly with the Pt grain structure.

(right). Within certain regions, the S-parameter is significantly decreased with respect to the rest of the sample. When comparing the DBS map to the optical image in figure 5.30, it becomes clear that the regions of decreased S-parameter correspond to the grain structure.

For a more detailed view, figure 5.31 shows an overlay of the optical image with the 2D S-parameter map. Especially the elongated grain at position (5.75 mm | 8.25 mm) showing a decreased S-parameter matches perfectly to the grain observed in the optical image. The decreased S-parameter of the grain may be due to a decreased defect concentration within the grain or a different crystal orientation compared to the other grains in the foil formed during the annealing procedure.

In this DBS study on polycrystalline Pt, it was possible to connect for the first time a significant variation in S-parameter to the grain structure of the material with outstanding spatial resolution. Hereby, the variation in S-parameter matches the grain structure of the material perfectly. These promising results pioneer future investigations including electron diffraction and micro-XRD.

6 Chapter 6

Conclusion and Outlook

Within the scope of this thesis, a new CDB spectrometer, the CDBS *upgrade*, was successfully set into operation at the positron source NEPOMUC. The instrument possesses a positron microbeam for the investigation and 2D imaging of defects on the atomic scale with a resolution in the micrometer range. The here presented work includes the design, simulation and implementation of various new components.

These novelties comprise three beam monitor systems, two MCP assemblies and an additional single phosphor screen at the sample position for convenient beam adjustment prior to each beamtime. Besides, a new sample chamber was developed for high-resolution sample positioning using piezo positioners. The key component is a brightness enhancement system comprising a 100 nm thin Ni(100) foil in transmission geometry. The usage of this system and subsequent focusing enables a further reduction of the beam diameter from 250 μm to 33 μm . Prior to the usage of the Ni single crystal re-moderation foil, comprehensive studies were carried out in order to maximize the re-moderation yield which can be considerably deteriorated by surface contaminations such as C and O. In order to remove these surface contaminations, a standard preparation method of the foil has been developed. Hereby, the foil is heat treated in a vacuum chamber designed exclusively for this purpose. Since the chamber is connected to the CDB spectrometer and separated from the brightness enhancement system with a shutter, the pre-treated foil can be inserted into its re-moderation position without being exposed to air and without breaking the UHV of the system.

The CDB *upgrade* can routinely be operated on samples up to a size of $19 \times 19 \text{ mm}^2$ with high lateral resolution and without any distortion. Both features have been proven in this work. Additionally, short measurement times of about 160 min/ mm^2 with the positron micrometer beam ($\Delta_{x,y} = 50 \mu\text{m}$, $t_m = 25 \text{ s}$) and around 2 min/ mm^2 ($\Delta_{x,y} = 250 \mu\text{m}$, $t_m = 7 \text{ s}$) with the NEPOMUC re-moderated beam are now feasible. Depth-dependent measurements can be carried out via adjusting the sample potential in a range from -0.2 to -30 kV enabling an implantation depth from the surface to the bulk of the material. Besides, in-situ temperature-dependent measurement can be carried out ranging from 50 K up to 1000 K. Low temperatures are realized with a closed cycle He-cryostat whereas the high temperature range can be accessed with a heatable sample holder operated via a specially designed ellipsoidal Cu reflector oven

with the sample and a halogen lamp located in its two foci. For supplementary in-situ tension tests, a special sample holder was developed capable of applying an external force to the sample. Therefore, the simultaneous recording of stress-strain curves and DBS was realized for the first time.

The outstanding capabilities of the CDBS *upgrade* for the detection of defects and precipitates were demonstrated in this work. In this regard, two welding techniques, FSW and LBW, were carried out on the age-hardening AlCu alloy EN AW-2219 T87 as well as LBW on stainless steel V2A. Suitable welding techniques are of major interest for today's industry, especially in the aircraft and automotive sector as a means of weight reduction. By scanning the sample in 2D, the S-parameter variation visualizes the lateral defect distribution across a material. According to this map, the differences between the base material and the weld nugget could be detected and confirmed by optical imaging for all samples. In addition to defect detection, the chemical information at the positron annihilation site at different sample positions was determined focusing on Cu precipitates in the AlCu alloy. As a general trend, the base material showed a higher Cu signal compared to the weld nugget. This discrepancy is assumed to originate from the dissolution of Cu during the welding process. Moreover, taking into account the confinement peak in the ratio curves, the type of defects can be assigned to quenched-in or deformed. Since the formation of defects is known to influence the strength of a material, the hardness of both LBWs were related to their corresponding S-parameters. Therefore, complementary Vickers hardness measurements were carried out. In the case of the AlCu alloy a sigmoidal relation between the S-parameter and its corresponding hardness was found. By contrast, for the stainless steel only the weld nugget could be differentiated from the base material in the S-parameter versus hardness plot.

Additionally with the newly developed in-situ tension testing machine (Master thesis [92]), it was possible to record stress-strain curves while performing DBS measurements on LBW stainless steel. Thereby, the rupture zone was located between the two HAZs being separated by a region of higher S-parameter increasing with higher stress.

Moreover, the grain structure of a material, in this case of an annealed and polished Pt sample was investigated with the microbeam. In this experiment, the grains could be clearly distinguished from each other by a significant difference in the S-parameter. Additional light microscopy confirmed the grain structure observed in DBS with outstanding resolution.

The CDBS *upgrade* opens the pathway to directly relate the defect distribution to the mechanical properties of a material. Together with complementary techniques such as hardness measurements and optical imaging, it can be used as a powerful tool for a wide field of research for fundamental physics and material science.

7

Chapter 7

Danksagung

An dieser Stelle möchte ich mich bei allen bedanken, die mich in den letzten fünfzehn Jahren unterstützt haben und ohne die meine Arbeit in dieser Form nicht möglich gewesen wäre. Ich bedanke mich herzlich bei...

... meinem Betreuer Herrn PD Dr. Christoph Hugenschmidt. Von meiner Zeit als Diplomand an bis zum Ende meiner Doktorarbeit stand mir seine Tür immer offen. Er stand mir mit Rat und Tat zur Seite und half mir beim Lösen von Problemen theoretischer und praktischer Natur. Er brachte mir das Vertrauen entgegen und eröffnete mir damit die einmalige Möglichkeit ein neues Instrument an der Positronenquelle aufbauen zu können.

... Dr. Christian Piochacz, von dessen Erfahrung und Fachwissen bezüglich der Instrumententwicklung sowie der Konstruktion der Linsensysteme ich profitieren konnte. Er war besonders in meiner Anfangszeit bei NEPOMUC eine große Hilfe.

... Dr. Markus Reiner als ehemaligen Kollegen am CDBS. Er gab seine praktischen Erfahrungen am Spektrometer und bei der Datenauswertung an mich weiter und erleichterte mir damit die Konstruktion und Verwirklichung des neuen Instruments ungemein. Außerdem bedanke ich mich für produktive und unterhaltsame gemeinsame Strahlzeiten.

... Dr. Marcel Dickmann für ausführliche Diskussionen hinsichtlich der elektrostatischen Strahlführung, -fokussierung und Remoderation von Positronen. Außerdem für seine Hilfe bei der Inbetriebnahme des Linsensystems und des ganzen Instruments und fürs Strahlfädeln von den ersten Versuchen bis zur letzten Strahlzeit. Nicht zuletzt bedanke ich mich für einen sehr schönen und Pinacolada-lastigen Cuba-Urlaub.

... Dr. Hubert Ceeh für seinen Einsatz als wandelndes Lexikon und die Beantwortung sämtlicher Fragen, ob Theorie oder Praxis. Die Bergtour auf den Krottenkopf sowie diverse Skiausflüge werden mir in schöner Erinnerung bleiben.

... Benjamin Rienäcker und Niklas Grill für die Programmierung der Ansteuer- und Auslegesoftware des Instruments.

... unserem Techniker Sebastian Vohburger für seine tatkräftige Unterstützung beim Aufbau und der Instandhaltung des Instruments, für seine verlässliche und oft kurzfristige

Hilfe, für seine herzliche Art und dafür, dass "nein" und "unmöglich" nicht in seinem Wortschatz vorkommen.

... allen Bachelor- und Masterstudenten. Diese haben maßgeblich zum erfolgreichen Aufbau des Instruments, zur Simulation der elektrischen und magnetischen Felder sowie zur Inbetriebnahme des Instruments beigetragen. Des Weiteren waren sie eine große Hilfe bei den diversen Strahlzeiten.

... Lukas Beddrich für die Mithilfe bei der ersten Inbetriebnahme des Positronen-Mikrostrahls und die Übernahme einiger Messzeiten und deren Auswertung.

... Leon Chryssos für die Mithilfe bei einigen Strahlzeiten und Auswertungen.

... Lucian Mathes für seine Hilfe beim Vorbereiten des Instruments und Probenwechseln während einiger Strahlzeiten.

... Matthias Hackenberg für die Hilfe beim Simulieren der elektrostatischen und magnetischen Felder des CDBs.

... Eicke Hecht für seine Mithilfe bei den Strahlzeiten.

... Matthias Thalmayr für seine tatkräftige Unterstützung beim Aufbauen des neuen Instruments und den diversen Strahlzeiten.

... David Vogl für seine Unterstützung bei den Auswertungen der Messungen.

... dem Team der Werkstatt des FRM II und der Zentralwerkstatt des Physik-Departments für die Fertigung zahlreicher Komponenten des Instruments.

... Dr. Michael Leitner, Dr. Josef Weber, Dr. Pascal Neibecker, Josef Schmidtbauer, Johannes Mitteneder, Markus Singer, Matthias Dodenhöft, Bernhard Kalis, Thomas Schmidt, Matthias Tischler und allen anderen Kollegen der Positronengruppe für Ihre Unterstützung und für die angenehme Arbeitsatmosphäre, die durch zahlreiche Eiszeiten, grillen und Laborbesprechungen noch angenehmer wurden.

... Regina Kluge, die in den letzten Jahren aufgrund der diversen Strahlzeiten auch mal am Wochenende auf mich verzichten musste, für das Korrekturlesen meiner Doktorarbeit und für aufmunternde Worte. Dankeschön, dass du da warst, wenn ich dich brauchte.

... meinen Eltern Anita und Gerhard Gigl, dass sie mich auf meinem Lebensweg begleiten. Sie haben mir mein Physik-Studium ermöglicht und mich auch während meiner Doktorarbeit unterstützt. Ich habe Ihnen viel mehr zu verdanken als "nur" diese Doktorarbeit.

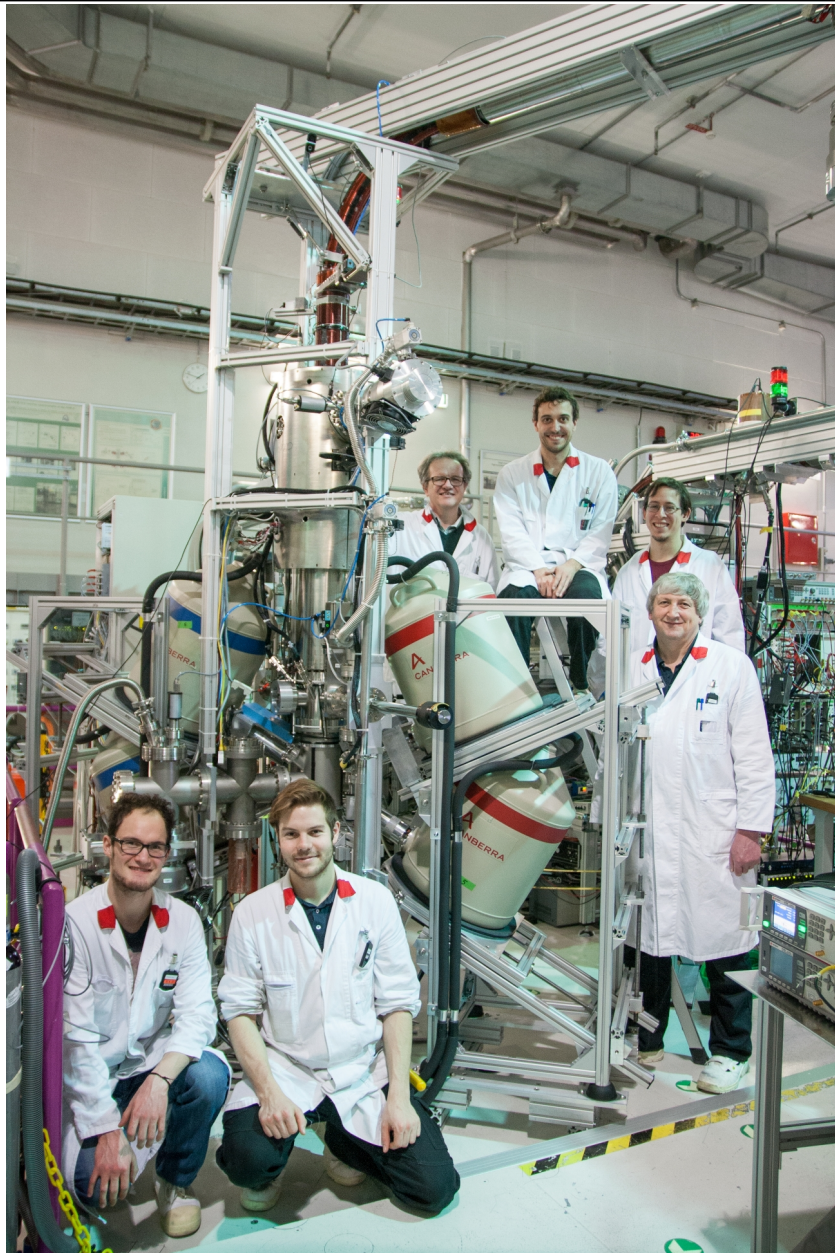


Figure 7.1: Gruppenfoto der Helfer und des Instrumentverantwortlichen von NEPOMUC vor dem CDBS *upgrade*. Von links nach rechts: Lukas Beddrich, Matthias Thalmayr, Dr. Christoph Hugenschmidt, Thomas Gigl, Benjamin Rienäcker, Sebastian Vohburger.

List of Publications

1. CHARACTERIZATION OF THE MICROSTRUCTURE IN FRICTION STIR WELDS OF EN AW-2219 USING COINCIDENT DOPPLER-BROADENING SPECTROSCOPY
A. Bachmann, **T. Gigl**, C. Hugenschmidt, M.F. Zaeh
to be published (2018)
2. INTERRELATION BETWEEN MECHANICAL RESPONSE, STRAIN FIELD, AND LOCAL FREE VOLUME EVOLUTION IN GLASSY POLYMERS: SEEKING THE ATOMISTIC ORIGIN OF POST-YIELD SOFTENING
H. G. Hosseinabadi, R. Bagheri, **T. Gigl**, C. Hugenschmidt, D. Raps, V. Altstaedt
Express Polymer Letters **12** (2018) 2-12
3. IMPACT OF OXYGEN DIFFUSION ON SUPERCONDUCTIVITY IN $\text{YBa}_2\text{Cu}_3\text{O}_{7-\delta}$ THIN FILMS STUDIED BY POSITRON ANNIHILATION SPECTROSCOPY
M. Reiner, **T. Gigl**, R. Jany, G. Hammerl, C. Hugenschmidt
Physical Review B **97** (2018) 144503
4. IONIC LIQUID LOADED SILICA GEL PARTICLES STUDIED BY SPATIALLY RESOLVED DBS USING A SCANNING POSITRON BEAM
M. Reiner, H. Ceeh, **T. Gigl**, M. Haumann, A. Schönweiz, C. Hugenschmidt
Defect and Diffusion Forum **373** (2017) 80-83
5. DEFECT IMAGING AND DETECTION OF PRECIPITATES USING A NEW SCANNING POSITRON MICROBEAM
T. Gigl, L. Beddrich, M. Dickmann, B. Rienäcker, M. Thalmayr, S. Vohburger, C. Hugenschmidt
New Journal of Physics **19** (2017) 123007
6. POSITRON SPECTROSCOPY OF POINT DEFECTS IN THE SKYRMION-LATTICE COMPOUND MnSi
M. Reiner, A. Bauer, M. Leitner, **T. Gigl**, W. Anwand, M. Butterling, A. Wagner, P. Kudejova, C. Pfleiderer, C. Hugenschmidt
Scientific Reports **6** (2016) 29109

7. DEFECTS AND CHARGING PROCESSES IN LI-ION BATTERY CATHODES STUDIED BY OPERANDO MAGNETOMETRY AND POSITRON ANNIHILATION
R. Würschum, S. Topolovec, G. Klinser, W. Sprengel, H. Kren, S. Koller, H. Krenn, C. Hugenschmidt, M. Reiner, **T. Gigl**, F. Berkemeier, M. Fiedler
Materials Science Forum **879** (2016) 2125-2130
8. FIRST-CYCLE DEFECT EVOLUTION OF $\text{Li}_{1-x}\text{Ni}_{1/3}\text{Mn}_{1/3}\text{Co}_{1/3}\text{O}_2$ LITHIUM ION BATTERY ELECTRODES INVESTIGATED BY POSITRON ANNIHILATION SPECTROSCOPY
S. Seidlmayer, I. Buchberger, M. Reiner, **T. Gigl**, R. Gilles, H.A. Gasteiger, C. Hugenschmidt
Journal of Power Sources **336** (2016) 224-230
9. QUALITY OF HEUSLER SINGLE CRYSTALS EXAMINED BY DEPTH-DEPENDENT POSITRON ANNIHILATION TECHNIQUES
C. Hugenschmidt, A. Bauer, P. Böni, H. Ceeh, S.W.H. Eijt, **T. Gigl**, C. Pfeleiderer, C. Piochacz, A. Neubauer, M. Reiner, H. Schut, J. Weber
Applied Physics A **119** (2015) 997-1002
10. DETECTION AND IMAGING OF THE OXYGEN DEFICIENCY IN SINGLE CRYSTALLINE $\text{YBa}_2\text{Cu}_3\text{O}_{7-\delta}$ THIN FILMS USING A SCANNING POSITRON BEAM
M. Reiner, **T. Gigl**, R. Jany, G. Hammerl, C. Hugenschmidt
Applied Physics Letters **106** (2015) 111910
11. CHARACTERIZATION OF ION-IRRADIATED ODS Fe–Cr ALLOYS BY DOPPLER BROADENING SPECTROSCOPY USING A POSITRON BEAM
P. Parente, T. Leguey, V. de Castro, **T. Gigl**, M. Reiner, C. Hugenschmidt, R. Pareja
Journal of Nuclear Materials **464** (2015) 140-146
12. NANOMETER SIZE PORES IN IONIC LIQUID LOADED SILICA GEL CHARACTERIZED BY POSITRON LIFETIME SPECTROSCOPY
C. Herold, H. Ceeh, **T. Gigl**, M. Reiner, M. Haumann, A. Schönweiz, C. Hugenschmidt
Physica Status Solidi (A) **213** (2015) 165-169
13. POSITRON BEAM FOR μm RESOLVED COINCIDENT DOPPLER BROADENING SPECTROSCOPY AT NEPOMUC
T. Gigl, C. Piochacz, M. Reiner, C. Hugenschmidt
Journal of Physics: Conference Series **505** (2014) 012032

14. ENHANCEMENT AND TRANSFORMATION OF THE PHASE SPACE DENSITY OF THE NEPOMUC POSITRON BEAM
C. Piochacz, E. Erdnüß, **T. Gigl** N. Grill, C. Hugenschmidt
Journal of Physics: Conference Series **505** (2014) 012027
15. AB-INITIO CALCULATION OF CDB SPECTRA - A CASE STUDY ON TRANSITION METALS
M. Reiner, **T. Gigl** C. Hugenschmidt
Journal of Physics: Conference Series **505** (2014) 012025
16. POSITRON BEAM CHARACTERISTICS AT NEPOMUC UPGRADE
C. Hugenschmidt, H. Ceeh, **T. Gigl**, F. Lippert, C. Piochacz, M. Reiner, K. Schreckenbach, S. Vohburger, J. Weber, S. Zimnik
Journal of Physics: Conference Series **505** (2014) 012029
17. THE UPGRADE OF THE NEUTRON INDUCED POSITRON SOURCE NEPOMUC
C. Hugenschmidt, H. Ceeh, **T. Gigl**, F. Lippert, C. Piochacz, P. Pikart, M. Reiner, J. Weber, S. Zimnik
Journal of Physics: Conference Series **443** (2013) 012079

Bibliography

- [1] P.A.M. Dirac. A Theory of Electrons and Protons. *Proc. Roy. Soc. A*, 126:360–365, 1930.
- [2] Carl D. Anderson. The Positive Electron. *Phys. Rev.*, 43(6):491–494, Mar 1933.
- [3] Carl D. Anderson. Energies of Cosmic-Ray Particles. *Phys. Rev.*, 41(4):405–421, Aug 1932.
- [4] P.J. Schultz and K.G. Lynn. Interaction of positron beams with surfaces, thin films and interfaces. *Rev. Mod. Phys.*, 60(3):701–779, Jul 1988.
- [5] Peter J. Mohr, Barry N. Taylor, and David B. Newell. CODATA recommended values of the fundamental physical constants: 2006. *Reviews of Modern Physics*, 80(2):633, 2008.
- [6] C. Hugenschmidt. *Positron sources and positron beams*, volume 174. Proceedings of the International School of Physics "Enrico Fermi", 2010.
- [7] Groden R. Gilmore. *Practical gamma-ray spectrometry*. Hoboken, N.J. : Wiley ; Chichester : John Wiley [distributor], 2nd edition, 2008.
- [8] C. Hugenschmidt, G. Kögel, R. Repper, K. Schreckenbach, P. Sperr, B. Straßer, and W. Triftshäuser. The neutron induced positron source at Munich - NEPOMUC. *Nucl. Instr. Meth. B*, 221:160 – 164, 2004.
- [9] A. van Veen, H. Schut, J. de Roode, F. Labohm, C.V. Falub, S.W.H. Eijt, and P.E. Mijnders. Intense Positron Sources and their Applications. *Mat. Sci. For.*, 363-365:415–419, 2001.
- [10] R. H. Howell, R. A. Alvarez, and M. Stanek. Production of slow positrons with a 100-MeV electron linac. *Appl. Phys. Lett.*, 40(8):751–752, 1982.
- [11] T. Akahane, T. Chiba, N. Shiotani, S. Tanigawa, T. Mikado, R. Suzuki, M. Chikawa, T. Yamazaki, and T. Tomimasu. Stretching of slow positron pulses generated with an electron linac. *Appl. Phys. A*, 51(2):146–150, August 1990.
- [12] H. Schut, A. van Veen, C.V. Falub, J. de Roode, and F. Labohm. Performance of an Intense Nuclear-Reactor Based Positron Beam. *Mat. Sci. For.*, 363-365:430–432, 2001.

- [13] B. Krusche and K. Schreckenbach. Intense positron sources by pair creation with neutron capture γ -rays. *Nucl. Instr. Meth. A*, 295(1-2):155 – 171, 1990.
- [14] C. Hugenschmidt, H. Ceeh, T. Gigl, F. Lippert, C. Piochacz, M. Reiner, K. Schreckenbach, S. Vohburger, J. Weber, and S. Zimnik. Positron Beam Characteristics at NEPOMUC Upgrade. *Journal of Physics: Conference Series*, 505(1):012029, 2014.
- [15] C. Hugenschmidt, H. Ceeh, T. Gigl, F. Lippert, C. Piochacz, M. Reiner, J. Weber, and S. Zimnik. The Upgrade of the Neutron Induced Positron Source NEPOMUC. *Journal of Physics: Conference Series*, 443(1):012079, 2013.
- [16] C. Hugenschmidt and C. Piochacz. NEPOMUC: Neutron induced positron source Munich. *Journal of large-scale research facilities*, 1:A22, 2015.
- [17] C. Hugenschmidt, C. Piochacz, M. Reiner, and K. Schreckenbach. The NEPOMUC upgrade and advanced positron beam experiments. *New Journal of Physics*, 14(5):055027, may 2012.
- [18] C. Piochacz, G. Kögel, W. Egger, C. Hugenschmidt, J. Mayer, K. Schreckenbach, P. Sperr, M. Stadlbauer, and G. Dollinger. A positron remoderator for the high intensity positron source NEPOMUC. *Appl. Surf. Sci.*, 255(1):98 – 100, 2008.
- [19] Markus Reiner. *Point Defects in MnSi and YBCO Studied by Doppler Broadening Spectroscopy Using a Positron Beam*. PhD thesis, Physik Department Technische Universität München, 2015.
- [20] Jakob Mayer. *High energy resolution and first time-dependent positron annihilation induced Auger electron spectroscopy*. Phd thesis, Lehrstuhl für Experimentalphysik E21, Technische Universität München, 2010.
- [21] W. Egger, P. Sperr, G. Kögel, and G. Dollinger. Pulsed low energy positron system (PLEPS) at the Munich research reactor FRM II. *phys. stat. sol. (c)*, 4(10):3969–3972, 2007.
- [22] C. Piochacz, W. Egger, C. Hugenschmidt, G. Kögel, K. Schreckenbach, P. Sperr, and G. Dollinger. Implementation of the Munich scanning positron microscope at the positron source NEPOMUC. *phys. stat. sol. (c)*, 4(10):4028–4031, 2007.
- [23] M. Dickmann and C. Piochacz. SPM: Scanning positron microscope. *Journal of large-scale research facilities*, 1(A26), 2015.
- [24] P. Coleman. *Positron beams and their applications*. World Scientific, 2000.
- [25] R. N. West. Positron studies of condensed matter. *Adv. Phys.*, 22(3):263–383, 1973.

- [26] M.J. Puska and R.M. Nieminen. Theory of positrons in solids and on solid surfaces. *Rev. Mod. Phys.*, 66(3):841–897, Jul 1994.
- [27] A. Dupasquier and A. P. Mills. *Positron Spectroscopy of Solids*. IOS Press, Amsterdam, 1995.
- [28] J Mäkinen, S Palko, J Martikainen, and P Hautojarvi. Positron backscattering probabilities from solid surfaces at 2 – 30 keV. *J. Phys.: Condens. Matter*, 4(36):L503–L508, 1992.
- [29] A. Perkins and J. P. Carbotte. Effect of the Positron-Phonon Interaction on Positron Motion. *Phys. Rev. B*, 1(1):101–107, Jan 1970.
- [30] J. Oliva. Inelastic positron scattering in an electron gas. *Phys. Rev. B*, 21(11):4909–4917, Jun 1980.
- [31] K. A. Ritley, K. G. Lynn, V. J. Ghosh, D. O. Welch, and M. McKeown. Low-energy contributions to positron implantation. *Journal of Applied Physics*, 74(5):3479–3496, 1993.
- [32] A. F. Makhov. The penetration of electrons into solids. 2. The Distribution of electrons in depth. *Sov. Phys. Solid State* 2, 2:1942 – 1944, 1961.
- [33] S. Valkealahti and R. M. Nieminen. Monte Carlo Calculations of keV Electron and Positron Slowing Down in Solids. *Appl. Phys. A*, 35:51, 1984.
- [34] J. Algers, P. Sperr, W. Egger, G. Kögel, and Frans H. J. Maurer. Median implantation depth and implantation profile of 3–18 keV positrons in amorphous polymers. *Phys. Rev. B*, 67(12):125404, 2003.
- [35] J. Keinonen, M. Hautala, V. Rauhala, E. and Karttunen, A. Kuronen, J. Räisänen, J. Lahtinen, A. Vehanen, E. Punkka, and P. Hautojärvi. Defect formation in H implantation of crystalline Si. *Phys. Rev. B*, 37(14):8269 – 8277, 1987.
- [36] H. Huomo, A. Vehanen, M. D. Bentzon, and P. Hautojärvi. Positron diffusion in Mo: The role of epithermal positrons. *Phys. Rev. B*, 35:8252 – 8255, 1987.
- [37] D. T. Britton, P. C. Rice-Evans, and J. H. Evans. Epithermal effects in positron depth profiling measurements. *Philosophical magazine letters*, 57(3):165–169, 1988.
- [38] Allen P. Mills. Thermal activation measurement of positron binding energies at surfaces. *Solid State Communications*, 31(9):623–626, 1979.
- [39] T. Hyodo, Y. Fukaya, M. Maekawa, I. Mochizuki, K. Wada, T. Shidara, A. Ichimiya, and A. Kawasuso. Total reflection high-energy positron diffraction (TRHEPD). *Journal of Physics: Conference Series*, 505:012001, 2014.

- [40] P. Hautojärvi and C. Corbel. Positron spectroscopy of defects in metals and semiconductors. *Positron spectroscopy of solids. IOP*, 125:491–532, 1995.
- [41] B.T. Wright. Spectrometer measurement on the high energy positrons of Sodium 22. *Physical Review*, 90(1):159, 1953.
- [42] Werner Brandt and Robert Paulin. Positron implantation-profile effects in solids. *Phys. Rev. B*, 15(5):2511–2518, Mar 1977.
- [43] E. M. Gullikson, A. P. Mills, W. S. Crane, and B. L. Brown. Absence of energy loss in positron emission from metal surfaces. *Phys. Rev. B*, 32(8):5484–5486, Oct 1985.
- [44] D. A. Fischer, K. G. Lynn, and D. W. Gidley. High-resolution angle-resolved positron reemission spectra from metal surfaces. *Phys. Rev. B*, 33(7):4479–4492, Apr 1986.
- [45] C. Hugenschmidt, G. Kögel, R. Repper, K. Schreckenbach, P. Sperr, and W. Triftshäuser. First platinum moderated positron beam based on neutron capture. *Nucl. Instr. Meth. B*, 198:220–229, 2002.
- [46] D. M. Chen, K. G. Lynn, R. Pareja, and B. Nielsen. Measurement of positron reemission from thin single-crystal W (100) films. *Phys. Rev. B*, 31(7):4123, 1985.
- [47] A. Vehanen, K. G. Lynn, Peter J. Schultz, and M. Eldrup. Improved slow-positron yield using a single crystal tungsten moderator. *Appl. Phys. A*, 32(3):163–167, November 1983.
- [48] R. Suzuki, T. Ohdaira, A. Uedono, Y.-K. Cho, S. Yoshida, Y. Ishida, T. Ohshima, Y. Itoh, M. Chiwaki, T. Mikado, T. Yamazaki, and S. Tanigawa. Investigation of positron moderator materials for electron-linac-based slow positron beamlines. *Japanese journal of applied physics*, 37(8R):4636, 1998.
- [49] P. J. Schultz, E. M. Gullikson, and A. P. Mills. Transmitted positron reemission from a thin single-crystal Ni(100) foil. *Phys. Rev. B*, 34(1):442–444, Jul 1986.
- [50] C. H. Hodges and M. J. Stott. Work Functions for Positrons in Metals*. *Phys. Rev. B*, 7(1):73–79, 1973.
- [51] P.W. Hawkes and E. Kasper. *Principles of Electron Optics*. Academic, London, 1989.
- [52] P. Grivet. *Electron Optics*. Pergamon Press, Oxford and New York, 1972.
- [53] Martin Reiser. *Theory and design of charged particle beams*. Wiley, Weinheim-VCH Verlag GmbH & Co. KGaA, 2008.

- [54] John David Jackson. *Classical Electrodynamics*. John. Wiley & Sons, 3rd ed., 1998.
- [55] F.S. Crawford. Elementary examples of adiabatic invariance. *American Journal of Physics*, 58(4):337 – 344, 1990.
- [56] Helmut Vogel. *Gerthsen Physik*. Springer-Verlag, 1999.
- [57] Gene Mosca Paul A. Tipler. *Physik für Wissenschaftler und Ingenieure*. Spektrum Akademischer Verlag, 2007.
- [58] W. Demtröder. *Experimentalphysik 2; Elektrizität und Optik*. Springer, 2009.
- [59] Joachim Großer. *Einführung in die Teilchenoptik*. Springer Verlag, 2013.
- [60] F. Gray. Electrostatic Electron-Optics. *The Bell System Technical Journal*, 18(1):1–31, 1939.
- [61] Franz Ollendorf. *Elektronik des Einzelelektrons*. Springer, 1955.
- [62] R.F. Egerton. *Physical Principles of Electron Microscopy An Introduction to TEM, SEM, and AEM*. Springer, 2005.
- [63] E. Harting and F.H. Read. *Electrostatic Lenses*. Elsevier, Amsterdam and Oxford and New York, 1976.
- [64] A. P. Mills. Brightness enhancement of slow positron beams. *Appl. Phys.*, 23:189–191, October 1980.
- [65] K. F. Canter and A. P. Mills, Jr. Slow positron beam design notes. *Can. J. Phys.*, 60:551–+, 1982.
- [66] A.J. Wilson. Volume of n-dimensional ellipsoid. *Scientia Acta Xaveriana*, 1(1):101–106, 2009.
- [67] CreaTec Fischer & Co. GmbH
https://createc.de/media/resources/Data%20Sheet/Equipment/data_sheet_RHEED_system_101.pdf (accessed on 03.08.2018).
- [68] O. Brümmer and G. Dlubek. Positron studies of defects in metals and semiconductors. *Mikrochimica Acta*, 11:187–204, 1985.
- [69] G. Dlubek and N. Meyendorf. *Positron Annihilation Spectroscopy (PAS)*. In: *Meyendorf N.G.H., Nagy P.B., Rokhlin S.I. (eds) Nondestructive Materials Characterization*, volume 67. Springer Series in Materials Science, 2004.
- [70] G. Dlubek. Positron studies of decomposition phenomena in Al alloys. *Mat. Sci. For*, 13:11–32, 1987.
- [71] M. J. Puska, P. Lanki, and R. M. Nieminen. Positron affinities for elemental metals. *J. Phys.: Condens. Matter*, 1:6081–6094, 1989.

- [72] P. Hautojärvi. *Positrons in Solids (Topics in Current Physics)*. Springer, 2011.
- [73] S. Berko and J.S. Plaskett. Correlation of Annihilation Radiation in Oriented Single Metal Crystals*. *Phys. Rev.*, 112(6):1877–1887, 1958.
- [74] S. Berko, M. Haghgoie, and J. J. Mader. Momentum density measurements with a new multicounter two-dimensional angular correlation of annihilation radiation apparatus. *Phys. Lett. A*, 63:335–338, 1977.
- [75] C. Doppler. *Ueber das farbige Licht der Doppelsterne und einiger anderer Gestirne des Himmels: Versuch einer das Bradley'sche Aberrations - Theorem as integrierenden Teil in sich schliessenden allgemeinen Theorie*, volume 2 of 5. Verlag der Königlichen Böhmischen Gesellschaft der Wissenschaften, 1842.
- [76] Hammer/Hammer. *Physikalische Formeln und Tabellen*. J. Lindauer Verlag (Schaefer), 8. edition, 2002.
- [77] Martin Stadlbauer. *Investigation of the chemical vicinity of defects in Mg and AZ31 with positron coincident Doppler broadening spectroscopy*. PhD thesis, Lehrstuhl für Experimentalphysik E21, Technische Universität München, 2008.
- [78] A. I. Gusev and A. A. Rempel. *Nanocrystalline Materials*. Cambridge International Science Publishing Ltd, 2003.
- [79] M. Reiner, T. Gigl, and C. Hugenschmidt. Ab-initio calculation of CDB spectra - a case study on transition metals. *Journal of Physics: Conference Series*, 505:012025, apr 2014.
- [80] J. Eberth and J. Simpson. From Ge(Li) detectors to gamma-ray tracking arrays - 50 years of gamma spectroscopy with germanium detectors. *Progress in Particle and Nuclear Physics*, 60(2):283–337, apr 2008.
- [81] W. R. Leo. *Techniques for Nuclear and Particle Physics Experiments*. Springer, New York, 1993.
- [82] G. F. Knoll. *Radiation Detection and Measurement*. John Wiley & Sons, Inc., 2000.
- [83] M. Haaks, T.E.M. Staab, and K. Maier. Analyzing the high-momentum part of positron annihilation Doppler spectra with a single germanium detector. *Nucl. Instr. Meth. A*, 569:829–836, 2006.
- [84] A. Ore and J. L. Powell. Three-photon annihilation of an electron-positron pair. *Phys. Rev.*, 75(11):1696–1699, Jun 1949.
- [85] E. Soininen, J. Mäkinen, D. Beyer, and P. Hautojärvi. High-temperature positron diffusion in Si, GaAs, and Ge. *Phys. Rev. B*, 46(20):13104–13118, Nov 1992.

- [86] R. Krause-Rehberg and H. S. Leipner. *Positron Annihilation in Semiconductors*. Springer, Berlin, Heidelberg, New York, 1999.
- [87] P. Asoka-Kumar, M. Alatalo, V. J. Ghosh, A. C. Kruseman, B. Nielsen, and K. G. Lynn. Increased elemental specificity of positron annihilation spectra. *Phys. Rev. Lett.*, 77(10):2097–2100, Sep 1996.
- [88] P. E. Mijnaerends, A. C. Kruseman, A. van Veen, H. Schut, and A. Bansil. Two-detector Doppler broadening study of enhancement in Al. *J. Phys.: Condens. Matter*, 10:10383–10390, 1998.
- [89] Philip Pikart. *Advances in Coincident Doppler Broadening Spectroscopy: Element Selective Studies on Metallic Nanolayers with Monoenergetic Positrons*. Dissertation, Technische Universität München, Lichtenberstr. 1 85747 Garching Germany, June 2012.
- [90] Martin Stadlbauer. Aufbau eines ortsauflösenden Doppler-Koinzidenzspektrometers zur Untersuchung der Positronenzerstrahlung. Diploma thesis, Lehrstuhl für Experimentalphysik E21, Technische Universität München, 2004.
- [91] Markus Reiner, Philip Pikart, and Christoph Hugenschmidt. In-situ (C)DBS at high temperatures at the NEPOMUC positron beam line. *Journal of Physics: Conference Series*, 443(1):012071, 2013.
- [92] M. Thalmayr. Spatially resolved in-situ defect spectroscopy with positrons during tensile tests. Master's thesis, Technische Universität München, Fakultät für Physik, 2017.
- [93] C. Piochacz, E. Erdnüß, T. Gigl, N. Grill, and C. Hugenschmidt. Enhancement and transformation of the phase space density of the NEPOMUC positron beam. *Journal of Physics: Conference Series*, 505:012027, apr 2014.
- [94] M. Fujinami, S. Jinno, M. Fukuzumi, T. Kawaguchi, K. Oguma, and T. Akahane. Production of a positron microprobe using a transmission remoderator. *Anal. Sci.*, 24(1):73–79, 2008.
- [95] N. Oshima, R. Suzuki, T. Ohdaira, A. Kinomura, T. Narumi, A. Uedono, and M. Fujinami. Brightness enhancement method for a high-intensity positron beam produced by an electron accelerator. *J. Appl. Phys.*, 103(9):094916, 2008.
- [96] A. van Veen, H. Schut, J. de Vries, R. A. Hakvoort, and M. R. Ijpma. Analysis of positron profiling data by means of "VEPFIT". *4th International workshop on: Slowpositron beam techniques for solids and surfaces*, 218(1):171–198, 1991.
- [97] P. Ehrhart. *Atomic defects in metals*, volume 25 of 1615-1925. 1991.

- [98] M. González-Cardel, P. Arguijo, and R. Díaz-Urbe. Gaussian beam radius measurement with a knife-edge: A polynomial approximation to the inverse error function. *OSA Publishing*, 52(16):3849–3855, 2013.
- [99] W.M. Thomas, E.D. Nicholas, J.C. Needham, M.G. Murch, P. Templesmith, and Dawes C.J. G.B. Patent Application No. 9125978.8, Dezember 1991.
- [100] R. Rai, A. De, H. K. D. H. Bhadeshia, and T. DebRoy. Review: Friction stir welding tools. *Science and Technology of Welding and Joining*, 16(4):325–342, may 2011.
- [101] C.G. Rhodes, M.W. Mahoney, W.H. Bingel, R.A. Spurling, and C.C. Bampton. Effects of friction stir welding on microstructure of 7075 aluminium. *Scripta Materialia*, 36(1):69–75, 1997.
- [102] G. Liu, L.E. Murr, C-S. Niou, J.C. McClure, and F.R. Vega. Microstructural aspects of the friction-stir welding of 6061-T6 aluminum. *Scripta Materialia*, 37(3):355–361, 1997.
- [103] K.V. Jata and S.L. Semiatin. Continuous dynamic recrystallization during friction stir welding of high strength aluminum alloys. *Scripta Materialia*, 43:743–749, 2000.
- [104] S. Benavides, Y. Li, L.E. Murr, D. Brown, and J.C. McClure. Low-temperature friction-stir welding of 2024 aluminum. *Scripta Materialia*, 41(8):809–815, 1999.
- [105] P. Xue, B.L. Xiao, Z.Y. Ni, and Z.Y. Ma. Enhanced mechanical properties of friction stir welded dissimilar Al-Cu joint by intermetallic compounds. *Materials Science and Engineering A*, 527:5723–5727, 2010.
- [106] P. Liu, Q. Shi, W. Wang, X. Wang, and Z. Zhang. Microstructure and XRD analysis of FSW joints for copper T2/aluminium 5A06 dissimilar materials. *Materials Letters*, 62(25):4106–4108, 2008.
- [107] Seiji Katayama. *Handbook of Laser Welding Technologies*. Woodhead publishing, 1st edition edition, 2013.
- [108] Dirk Dittrich, Jens Standfuss, Jens Liebscher, Berndt Brenner, and Eckhard Beyer. Laser Beam Welding of Hard to Weld Al Alloys for a Regional Aircraft Fuselage Design First Results. *Physics Procedia*, 12:113–122, 2011.
- [109] Friedrich Ostermann. *Anwendungstechnologie Aluminium*. Springer, 2. neu bearbeitete und aktualisierte auflage edition, 2007.
- [110] L.F. (Lucio F.) Mondolfo. *Aluminum alloys: structure and properties*. London; Boston: Butterworths, 1976.

- [111] A. Wilm. Physikalisch-metallurgische Untersuchungen über Magnesiumhaltige Aluminiumlegierungen. *Metallurgie: Zeitschrift für die gesamte Hüttenkunde*, 8(8):225–227, 1911.
- [112] J.E. Hatch. *Aluminum: Properties and physical metallurgy*. American Society for Metals, Materials Park, 1984.
- [113] *Data sheet EN-AW 2219 T87, ASM Aerospace Specifications Metals Inc.*, 2018.
- [114] *Data sheet AISI Type 304 Stainless Steel, ASM Aerospace Specifications Metals Inc.*
- [115] R.K. Gupta, R. Panda, A.K. Mukhopadhyay, V. Anil Kumar, P. Sankarave-layutham, and K.M. George. Study of Aluminum Alloy AA2219 After Heat Treatment. *Material Science and Heat Treatment*, 57:5–6, 2015.
- [116] Sindo Kou. *Welding Metallurgy*. John Wiley & Sons, Inc., second edition edition, 2003.
- [117] S. S. Batsanov. Van der waals radii of elements. *Inorganic Materials*, 37(9):871–885, 2001.
- [118] A. Calloni, A. Dupasquier, R. Ferragut, P. Folegati, M. M. Iglesias, I. Makkonen, and M. J. Puska. Positron localization effects on the Doppler broadening of the annihilation line: Aluminum as a case study. *Phys. Rev. B*, 72(5):054112, Aug 2005.
- [119] P. Folegati, I. Makkonen, R. Ferragut, and M. J. Puska. Analysis of electron-positron momentum spectra of metallic alloys as supported by first-principles calculations. *Phys. Rev. B*, 75:054201–1, 2007.
- [120] R. Ferragut M. M. Iglesias I. Makkonen M. J. Puska P. Folegati, A. Dupasquier. Quantitative chemical analysis of vacancy-solute complexes in metallic solid solutions by coincidence Doppler broadening spectroscopy. *phys. stat. sol. (c)*, 4:3493–3496, 2007.
- [121] Charles Kittel. *Einführung in die Festkörperphysik*. Gruyter, de Oldenbourg, 2013.
- [122] N.N. Greenwood and A. Earnshaw. *Chemistry of the Elements*, chapter 28 - Copper, Silver and Gold, pages 1173 – 1200. Butterworth-Heinemann, second edition edition, 1997.
- [123] A. Bachmann, M. Krutzlinger, and M. F. Zaeh. Influence of the welding temperature and the welding speed on the mechanical properites of friction stir welds in EN AW-2219-T87. *IOP Conference Series: Materials Science and Engineering*, 373:012016, 2018.

- [124] A. Bachmann, M. Roehler, Pieczona S.J., M. Kessler, and M.F. Zaeh. Torque-based adaptive temperature control in friction stir welding: A feasibility study. *Production Engineering*, 12(3):391–403, 2018.
- [125] A. Bachmann, T. Gigl, F. Beck, C. Hugenschmidt, and M. F. Zaeh. Characterization of the microstructure in friction stir welds of EN AW-2219 using coincident Doppler-broadening spectroscopy. *to be published*, (2018).
- [126] L. Quintino, R. Miranda, U. Dilthey, D. Iordachescu, M. Banasik, and S. Stano. Laser welding of structural aluminium. In *Structural Connections for Lightweight Metallic Structures*, pages 33–57. Springer Berlin Heidelberg, 2010.
- [127] H. Zhao, D.R. White, and T. DebRoy. Current issues and problems in laser welding of automotive aluminium alloys. *International Materials Reviews*, 44(6):238–266, jun 1999.
- [128] T. Gigl, L. Beddrich, M. Dickmann, B. Rienäcker, M. Thalmayr, S. Vohburger, and C. Hugenschmidt. Defect imaging and detection of precipitates using a new scanning positron microbeam. *New Journal of Physics*, 19:123007, 2017.
- [129] *International Standard, ISO 6507-1, Metallic materials - Vickers hardness test - Part 1: Test method*, 2005.
- [130] M. Thalmayr. Ausheilen eines Ni(100) Einkristalls zur Positronenremoderation mittels einer neuen Heizvorrichtung. Bachelor thesis, Technische Universität München, Fakultät für Physik, 2014.

A Appendix

Appendix A

A.1 Beam Monitor Assemblies

Beam Monitor I

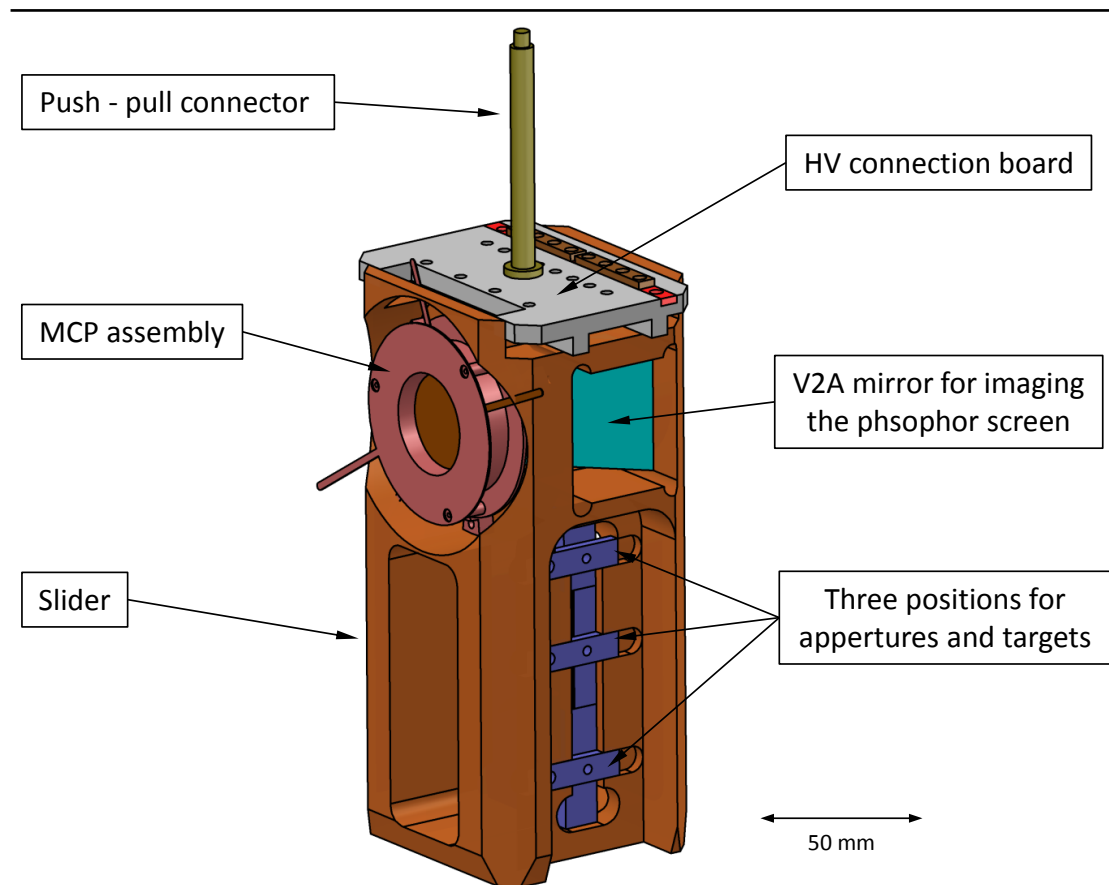


Figure A.1: Assembly of the first beam monitor with additional slots for apertures and targets.

The first beam monitor of the CDBS *upgrade* consists of a MCP module from ELMUL and various replaceable inserts such as different apertures and targets which can be

inserted into the path of the beam. Therefore, everything is mounted in a positionable slider fed by a stepper motor. A polished V2A mirror, mounted under 45° enables the imaging of the phosphor screen of the MCP system with a CCD camera attached to a viewport at the UHV chamber. At the current instrument three different apertures are mounted with diameters of 0.5 mm, 1.5 mm and 5 mm for adjusting the beam intensity. With an optional mountable target consisting of Al, the beam intensity can be measured at the entrance of the instrument.

Beam Monitor II

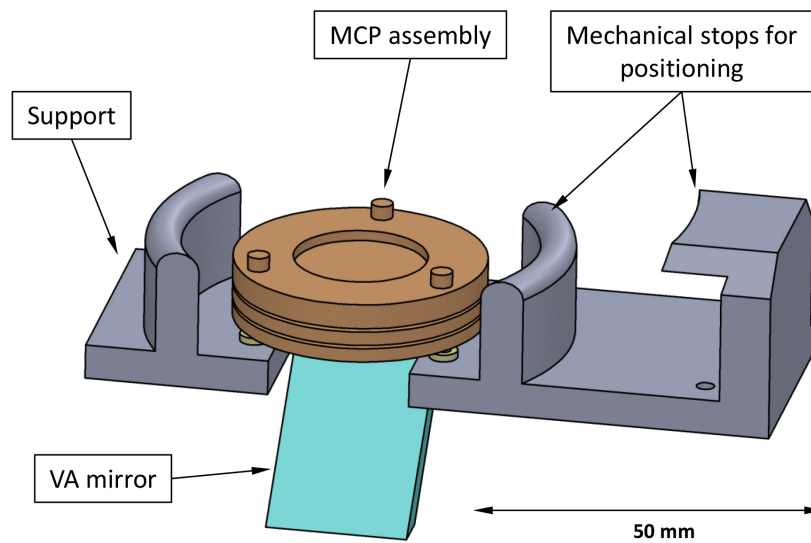


Figure A.2: Second beam monitor assembly which can be optionally positioned at the re-moderation foil position for tuning the beam focus of the first electrostatic lens system.

A second smaller MCP module is mounted on a V4A support which can be inserted at the position of the re-moderation foil in the brightness enhancement chamber by a linear and rotatable feed-through. Again the beam image on the phosphor screen is monitored via a tilted V4A mirror and a CCD camera at a view port. For guaranteeing the correct height position and the centricity to the first electrostatic lens system, two mechanical end stops are machined to the support. The complete system can be biased to an offset potential of up to 5 kV enabling the same potential of the first channel plate as the re-moderation foil.

Beam Monitor III

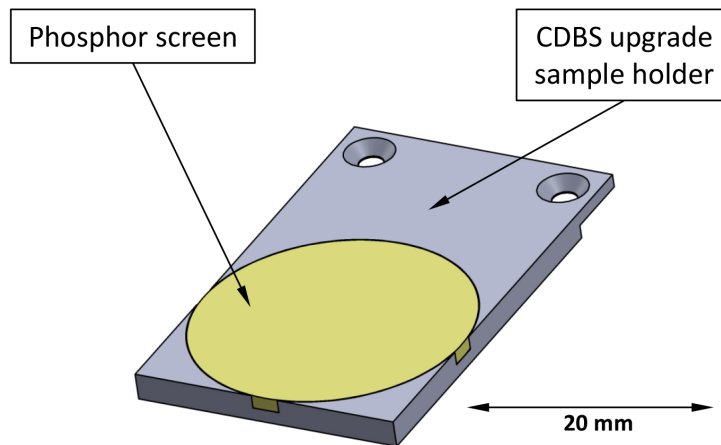


Figure A.3: New beam monitor III: Single phosphor screen mounted on a CDBS *upgrade* sample holder.

For visually monitoring the beam spot at the sample position a simple phosphor screen was mounted onto a sample holder of the CDBS *upgrade*. The scintillation image of the beam can be monitored down to an energy of about 3 keV with a CCD camera at a view port. At lower energies the light output of the phosphor screen is too low to be detected within exposure times of a few seconds. This beam monitoring system is used for the first time and drastically reduces the time for tuning the parameters of the lens system focusing the beam onto the sample position. Before the implementation of this BM into the routine operation, the position and the form of the beam had to be obtained by performing multiple linescans over a special prepared sample holder consisting of an Al/Cu edge. In addition, the energy dependent offset of the beam can be monitored. This offset is corrected routinely to guarantee that the beam spot remains stable throughout all implantation energies.

A.2 Accelerator

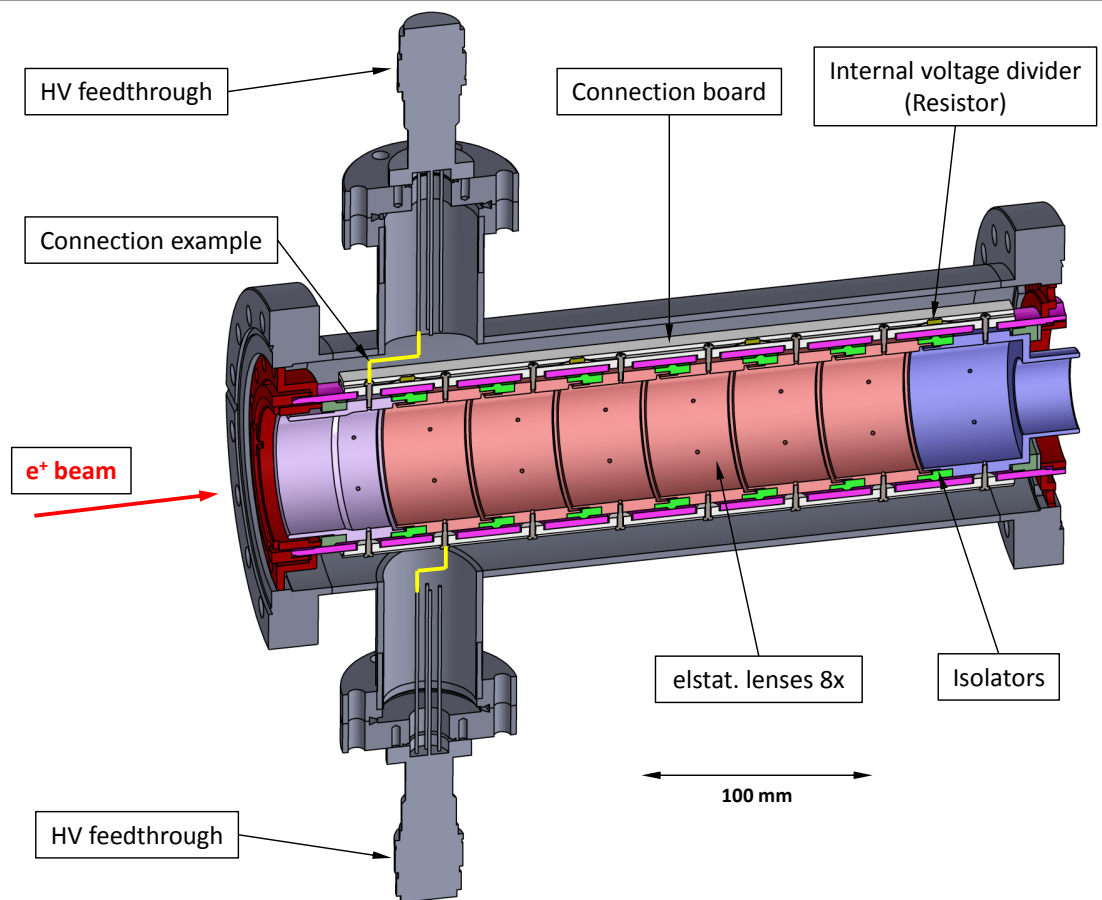


Figure A.4: Detailed cross sectional view of the acceleration system. As shown in the connection example, two of each electrodes are connected inside of the vacuum housing via a voltage divider. Therefore, only at each second electrode the high voltage (HV) has to be applied.

Within this detailed view of the acceleration system the high voltage connection of the lenses is shown in one example. Within one HV-connection two lenses are fed by an internal voltage divider consisting of a resistor mounted in-between two electrodes on top of the connection board. With a second resistor connected to the second electrode outside of the vacuum chamber (not shown in the figure), the voltage ratio between the electrodes can be adjusted.

A.3 Magnetic Field Termination

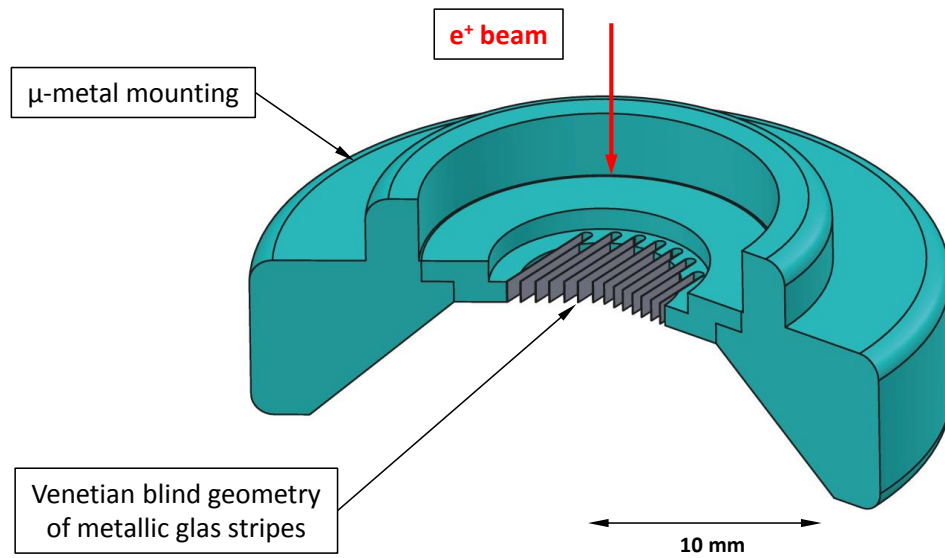


Figure A.5: Detailed view of the magnetic field termination in front of the first electrostatic lens system (section C in fig. 4.4).

Detailed view of the magnetic field termination mounted in front of the first electrostatic lens system focusing the positron beam onto the re-moderation foil. 14 metallic glass stripes with a thickness of 10 μm are mounted in a Venetian blind geometry to terminate the magnetic field generated by the solenoidal coils before. Afterwards the positrons are guided electrostatically to the re-moderation foil and the sample.

A.4 Re-moderation Foil Preparation System

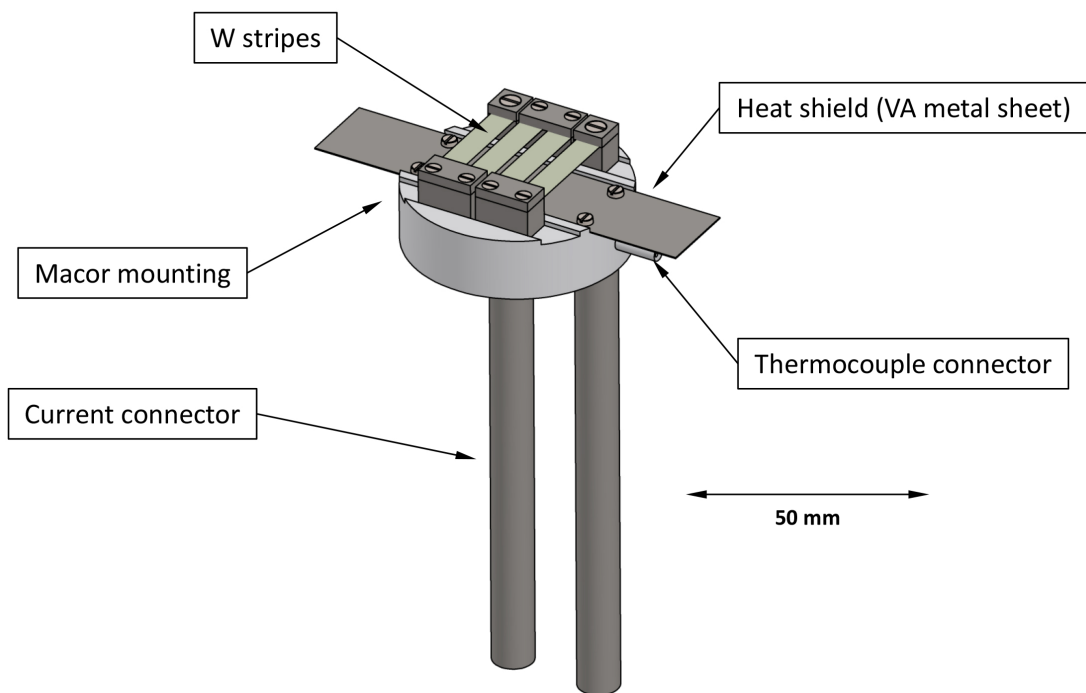


Figure A.6: Re-moderator heating device for surface preparation of the Ni(100) foil prior to its usage within the brightness enhancement system.

Heating device for preparing the re-moderation foil prior to its usage for maximizing the re-moderation yield as described in section 4.6. The heat is generated resistively via four W stripes mounted in series on a macor support for electric insulation. A current of up to 20 A can be fed through the W stripes generating a temperature of up to 800 °C. A heat shield produced out of a reflective stainless steel sheet protects the structures below the heating device. Via a mounted thermocouple type K the whole heating device can be calibrated. Therefore, the thermocouple is welded directly to the stainless steel sheet. Details to the device can be found in [130].

A.5 Values for the Magnetic and Electrostatic Fields of the CDBS *upgrade*

In figure A.7 a cross sectional view of the electrostatic components of the CDBS *upgrade* is given. The positrons enter the electrostatic system from the left at electrode "E1". Afterwards they pass the acceleration system with electrodes "ACC 1 - ACC 8" until they are focused via a first and second electrostatic lens system with lenses "LS1_1 - LS1_3" and "LS2_1 - LS2_6", respectively. The applied high voltages are given in table A.2. Additionally, the current values producing the magnetic guiding and correction fields are given in table A.1.

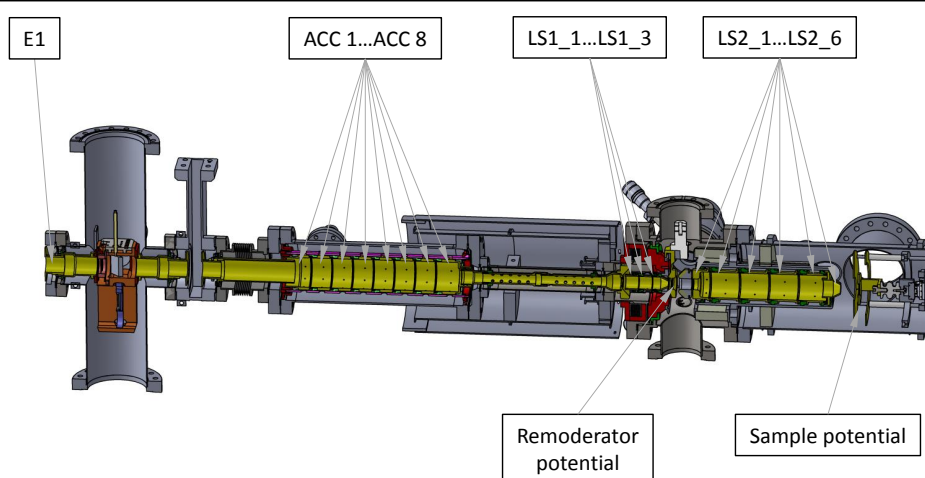


Figure A.7: Re-moderator heating device

Field	Current (A)	Voltage (V)	Field	Horizontal (mA)	Vertical (mA)
FF 61	10.11	4.92	KP 29	-120	170
FF 62	9.2	9.6	KP 30	30	-190
FF 63	8.41	6.75	KP 31	-2070	-1500
FF 64	12.02	12.75	KP 32	30	140
FF 66	8.4	9.5	KP 33	220	30
FF 67	0	0	KP 34	1	-

Table A.1: Current values for the longitudinal solenoidal magnetic guiding field (left) and for the horizontal and vertical magnetic correction fields (right).

Part	U w/o Rem (V)	U with Rem (V)	ISEG Module
BM I	-30	-30	i03
ACC 1	10 (a)	40 (a)	
ACC 2	15	70	i20
ACC 3	90 (a)	1700 (a)	
ACC 4	193	3800	i21
ACC 5	550 (a)	4100 (a)	
ACC 6	623	4600	i22
ACC 7	1600 (a)	4800 (a)	
ACC 8	1700	5000	i23
Remoderator	1100	5000	i25
LS1_1	900	7400	i13
LS1_2	15	4000	i26
LS1_3	150	300	i27
LS2_1	650	5124	i30
LS2_2	1050	5468	i31
LS2_3	1000	7734	i11
LS2_4	1506	5000	i32
LS2_5	1260	6756	i12
LS2_6	1780	6050	i10
Sample	30000	30000	

Table A.2: CDBS *upgrade* potentials of the electrostatic acceleration and focusing systems. For the potentials in the case of the acceleration system (ACC 1 - 8) only the even numbers are fed by an applied HV. The HV of the electrodes with odd numbers, indicated by an (a) in the table, is given by a voltage divider as shown in the connection example in figure A.4. Thus, the HV has to be applied only at each second electrode.

A.6 Data Sheets

Aluminum 2219-T87

Subcategory: 2000 Series Aluminum Alloy; Aluminum Alloy; Metal; Nonferrous Metal

Close Analogs:

Composition Notes:

This designation is considered the sole original alloy for this alloy family.

Aluminum content reported is calculated as remainder.

Composition information provided by the Aluminum Association and is not for design.

Key Words: UNS A92219; ISO AlCu6Mn; Aluminium 2219-T87; AA2219-T87

Component	Wt. %	Component	Wt. %	Component	Wt. %
Al	91.5 - 93.8	Mn	0.2 - 0.4	Ti	0.02 - 0.1
Cu	5.8 - 6.8	Other, each	Max 0.05	V	0.05 - 0.15
Fe	Max 0.3	Other, total	Max 0.15	Zn	Max 0.1
Mg	Max 0.02	Si	Max 0.2	Zr	0.1 - 0.25

Material Notes:

Data points with the AA note have been provided by the Aluminum Association, Inc. and are NOT FOR DESIGN.

Physical Properties	Metric	English	Comments
Density	2.84 g/cc	0.103 lb/in ³	AA; Typical

Mechanical Properties

Hardness, Brinell	130	130	500 kg load with 10 mm ball
Hardness, Knoop	163	163	Converted from Brinell Hardness Value
Hardness, Rockwell A	49.5	49.5	Converted from Brinell Hardness Value
Hardness, Rockwell B	80	80	Converted from Brinell Hardness Value
Hardness, Vickers	149	149	Converted from Brinell Hardness Value
Ultimate Tensile Strength	476 MPa	69000 psi	AA; Typical
Tensile Yield Strength	393 MPa	57000 psi	AA; Typical
Elongation at Break	10 %	10 %	AA; Typical; 1/16 in. (1.6 mm) Thickness
Modulus of Elasticity	73.1 GPa	10600 ksi	AA; Typical; Average of tension and compression. Compression modulus is about 2% greater than tensile modulus.
Notched Tensile Strength	379 MPa	55000 psi	2.5 cm width x 0.16 cm thick side-notched specimen, K _t = 17.
Poisson's Ratio	0.33	0.33	Estimated from trends in similar Al alloys.
Fatigue Strength	103 MPa	15000 psi	AA; 500,000,000 cycles completely reversed stress; RR Moore machine/specimen
Shear Modulus	27 GPa	3920 ksi	Estimated from similar Al alloys.
Shear Strength	280 MPa	40600 psi	

Electrical Properties

Electrical Resistivity	5.82e-006 ohm-cm	5.82e-006 ohm-cm	AA; Typical at 68°F
------------------------	------------------	------------------	---------------------

Thermal Properties

CTE, linear 68°F	22.3 μm/m-°C	12.4 μin/in-°F	AA; Typical; Average over 68-212°F range.
CTE, linear 250°C	24.1 μm/m-°C	13.4 μin/in-°F	Estimated from trends in similar Al alloys. 20-300°C.
Specific Heat Capacity	0.864 J/g-°C	0.207 BTU/lb-°F	
Thermal Conductivity	121 W/m-K	840 BTU-in/hr-ft ² -°F	AA; Typical at 77°F
Melting Point	543 - 643 °C	1010 - 1190 °F	AA; Typical range based on typical composition for wrought products 1/4 inch thickness or greater. Eutectic melting is not eliminated by homogenization.
Solidus	543 °C	1010 °F	AA; Typical
Liquidus	643 °C	1190 °F	AA; Typical

Figure A.8: Data sheet for the age hardening AlCu alloy EN AW-2219 T87. Source: [113]

AISI Type 304 Stainless Steel

Subcategory: Ferrous Metal; Heat Resisting; Metal; Stainless Steel; T 300 Series Stainless Steel

Close Analogs: UNS S30400; AMS 5501, 5513, 5560, 5565; ASME SA182, SA194 (8), SA213, SA240; ASTM A167, A182, A193, A194

Key Words: aisi304, aisi 304, T304, T 304, SUS304, SS304, 304SS, 304 SS, UNS S30400, AMS 5501, AMS 5513, AMS 5560, AMS 5565, AMS 5566, AMS 5567, AMS 5639, AMS 5697, ASME SA182, ASME SA194 (8), ASME SA213, ASME SA240, ASME SA249, ASME SA312, ASME SA320 (B8), ASME SA358, ASME SA376, ASME SA403, ASME SA409, ASME SA430, ASME SA479, ASME SA688, ASTM A167, ASTM A182, ASTM A193, ASTM A194, ASTM A666, FED QQ-S-763, MILSPEC MIL-S-5059, SAE 30304, DIN 1.4301, X5CrNi189, B.S. 304 S 15, EN 58E, PN 86020 (Poland), OH18N9, ISO 4954 X5CrNi189E, ISO 683/13 11, 18-8

Component	Wt. %
C	Max 0.08
Cr	18 - 20
Fe	66.345 - 74
Mn	Max 2
Ni	8 - 10.5
P	Max 0.045
S	Max 0.03
Si	Max 1

Material Notes:

Austenitic Cr-Ni stainless steel. Better corrosion resistance than Type 302. High ductility, excellent drawing, forming, and spinning properties. Essentially non-magnetic, becomes slightly magnetic when cold worked. Low carbon content means less carbide precipitation in the heat-affected zone during welding and a lower susceptibility to intergranular corrosion.

Applications: beer kegs, bellows, chemical equipment, coal hopper linings, cooking equipment, cooling coils, cryogenic vessels, dairy equipment, evaporators, flatware utensils, feedwater tubing, flexible metal hose, food processing equipment, hospital surgical equipment, hypodermic needles, kitchen sinks, marine equipment and fasteners, nuclear vessels, oil well filter screens, refrigeration equipment, paper industry, pots and pans, pressure vessels, sanitary fittings, valves, shipping drums, spinning, still tubes, textile dyeing equipment, tubing.

Corrosion Resistance: resists most oxidizing acids and salt spray.

Physical Properties	Metric	English	Comments
Density	8 g/cc	0.289 lb/in ³	

Mechanical Properties

Hardness, Brinell	123	123	Converted from Rockwell B hardness.
Hardness, Knoop	138	138	Converted from Rockwell B hardness.
Hardness, Rockwell B	70	70	
Hardness, Vickers	129	129	Converted from Rockwell B hardness.
Tensile Strength, Ultimate	505 MPa	73200 psi	
Tensile Strength, Yield	215 MPa	31200 psi	at 0.2% offset
Elongation at Break	70 %	70 %	in 50 mm
Modulus of Elasticity	193 - 200 GPa	28000 - 29000 ksi	
Poisson's Ratio	0.29	0.29	
Charpy Impact	325 J	240 ft-lb	
Shear Modulus	86 GPa	12500 ksi	

Electrical Properties

Electrical Resistivity	7.2e-005 ohm-cm	7.2e-005 ohm-cm	at 20°C (68°F); 1.16E-04 at 650°C (1200°F)
Magnetic Permeability	1.008	1.008	at RT

Thermal Properties

CTE, linear 20°C	17.3 μm/m-°C	9.61 μin/in-°F	from from 0-100°C
CTE, linear 250°C	17.8 μm/m-°C	9.89 μin/in-°F	at 0-315°C (32-600°F)
CTE, linear 500°C	18.7 μm/m-°C	10.4 μin/in-°F	at 0-650°C
Specific Heat Capacity	0.5 J/g-°C	0.12 BTU/lb-°F	from 0-100°C (32-212°F)
Thermal Conductivity	16.2 W/m-K	112 BTU-in/hr-ft ² -°F	at 0-100°C, 21.5 W/m°C at 500°C
Melting Point	1400 - 1455 °C	2550 - 2650 °F	
Solidus	1400 °C	2550 °F	
Liquidus	1455 °C	2650 °F	

Figure A.9: Data sheet for the stainless steel 1.4301. Source: [114]

A.7 Python Code for Fitting the CDBS Ratio Curves

```
# -*- coding: utf-8 -*-
"""

Created on Wed May 02 17:46:28 2018

@author: tgigl
"""

import numpy as np
import matplotlib.pyplot as plt
from matplotlib.legend_handler import HandlerLine2D

#enter file name here:
filename = 'C:/Users/tgigl/Desktop/Fit_Anpassung_ab_2_4keV.txt'

# check if same no of entries in each colom
content = open(filename, 'r')
text = content.readlines()
content.close()

for i in range(len(text)):
    j = text[i].split('\t')
    if j[3] == '\n':
        break
if i < len(text):
    new = open('newdata.txt', 'w')
    for k in range(i):
        new.write(str(text[k]))
    new.close()
    data = np.loadtxt('newdata.txt', skiprows=1)
else: data = np.loadtxt(filename, skiprows=1)

E = data[:,0]
Al = data[:,1]
Cu = data[:,2]
LBW_P1 = data[:,3]
LBW_P2 = data[:,4]
LBW_P3 = data[:,5]
```

```

# define fit function
def fitfct(i, start):
    return start*Cu[i] + (1-start)*Al[i]

# optimizes values from 0 to 1 in steps of stepsize/upborder
stepsize = 1
upborder = 10000
allmins = []
for l in range(0, upborder, stepsize):
    start = float(l)/upborder
    summanden = []
    for i in range(len(E)):
        toadd = (LBW_P1[i]-fitfct(i, start))**2
        summanden+= [toadd]
    standabw = np.std(summanden)
    min = ((1.0/len(E))*np.sum(summanden))**0.5
    allmins += [min]

# minimize composition value
result = allmins.index(np.min(allmins))/float(upborder)

#initialize values of fit function
fit = []
for m in range(len(E)):
    fit += [fitfct(m, result)]

#print result
print '_____'
print 'min:' + str(result)
print '_____'

```